In presenting the dissertation as a partial fulfillment of the requirements for an advanced degree from the Georgia Institute of Technology, I agree that the Library of the Institute shall make it available for inspection and circulation in accordance with its regulations governing materials of this type. I agree that permission to copy from, or to publish from, this dissertation may be granted by the professor under whose direction it was written, or, in his absence, by the Dean of the Graduate Division when such copying or publication is solely for scholarly purposes and does not involve potential financial gain. It is understood that any copying from, or publication of, this dissertation which involves potential financial gain will not be allowed without written permission.

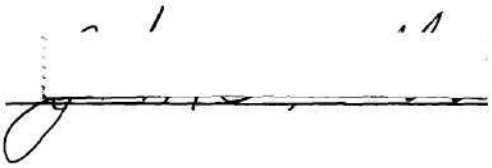

7/25/68

ESTIMATION OF THE FREQUENCY OF LASER VELOCIMETER SIGNALS

A THESIS

Presented to

The Faculty of the Graduate Division

by

John Burton Allen

In Partial Fulfillment

of the Requirements for the Degree

Doctor of Philosophy

in the School of Electrical Engineering

Georgia Institute of Technology

January, 1973

ESTIMATION OF THE FREQUENCY OF LASER VELOCIMETER SIGNALS

Approved:

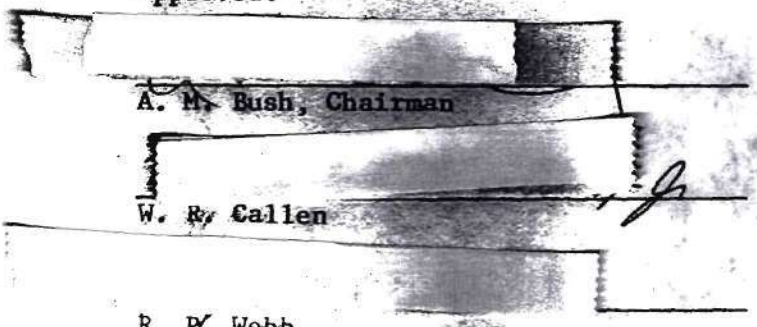

A. M. Bush, Chairman

W. R. Callen

R. P. Webb

Date approved by Chairman: Jan., 17, 1973

ACKNOWLEDGMENTS

There are many individuals who gave me advice and encouragement throughout this thesis and I am hesitant to name any for fear I will not name them all. However, I am especially indebted to Dr. W. T. Mayo who introduced me to the subject of laser velocimeters and suggested that I choose some aspect of the frequency estimation problem as my thesis topic.

Dr. A. M. Bush, my thesis advisor, guided me through the Ph.D. program and gave me advice on many sections of the thesis. I wish to thank the Lockheed-Georgia Company, especially L. M. Boggs and D. M. Meadows, for their cooperation in the experimental aspects of the thesis which were conducted under Research Authorization 4110. The thesis was, in part, motivated by the stimulating courses in statistical communication theory taught to me by Dr. A. M. Bush and Dr. R. H. Pettit. I consider these courses to have been the highlight of my Ph.D. studies.

I wish to thank my wife for her endurance during the time at which I had to study for the last several years and the typing of the early drafts of the thesis.

TABLE OF CONTENTS

TABLE OF CONTENTS (Concluded)

LIST OF TABLES

LIST OF ILLUSTRATIONS

LIST OF ILLUSTRATIONS (Continued)

LIST OF ILLUSTRATIONS (Continued)

LIST OF ILLUSTRATIONS (Continued)

LIST OF ILLUSTRATIONS (Continued)

LIST OF ILLUSTRATIONS (Concluded)

SUMMARY

The objectives of this thesis are to derive a mathematical model for laser velocimeter signals and to find a means to estimate the frequency of the signals. Expressions for the signals from the two types of velocimeters, namely the laser Doppler velocimeter (LDV) and the laser interference velocimeter (LIV), are derived through the use of the Fresnel-Kirchhoff integral. The sources of noise in both systems are identified and their contributions to the total noise are assessed. Velocimeter systems were built and experiments were carried out to verify the signal and noise models. It is shown that under most conditions, velocimeter signals are discrete sinusoidal pulses with Gaussian envelopes and that the noise is white and Gaussian. An estimator, called the "Fourier transform estimator," is motivated and statistically analyzed. The estimator is found to perform well when the velocimeter signals are changing rapidly in frequency and when noise levels are high. Experiments were carried out which demonstrated the estimator's performance.

CHAPTER I

INTRODUCTION

Fluid Velocity Measurement

Need for a Reliable Means to Measure Fluid Velocity

In order to understand the flow around an airfoil in a wind tunnel test section, an aerodynamicist would like to know the pressure, temperature, density, and velocity of the air at every point in the test section. These quantities are in general time varying and may be either deterministic or random. The devices by which these parameters are measured should interfere with or alter the flow as little as possible.

Pressure is generally measured by inserting a small pitot tube into the flow. The tube is either connected to a manometer or a pressure transducer which give a direct readout of the pressure. There is a considerable art in designing the tubes so that they give correct pressure readings and do not change the flow by a significant amount. To make accurate pressure measurements, the effect of the tube on the flow must be estimated and accounted for. Quite often, the ends of the tubes are mounted flush with the model so they do not alter the flow. However, when they are mounted this way, they only measure the pressure at the model's surface.

Temperatures in wind tunnel flows are measured by thermocouple probes. These probes can be made quite small and, like pitot tubes, are

inserted into the flow at the point where temperature is to be measured. Thermocouples also alter the flow and this alteration must be accounted for to obtain good estimates of temperature. Thermocouples can be embedded into the model to measure surface temperature of the model without altering flow. Although there is room for improvement in temperature and pressure measuring techniques, the present techniques are generally thought to be adequate for most steady and time varying flows.

Density is measured by a technique known as "interferometry." A wavefront of collimated coherent light is passed through the tunnel. The beam is then interfered with a beam that has not passed through the tunnel. From the resulting interference pattern, the phase variation imparted to the beam by the flow can be determined. The phase variation is related to index of refraction variation which is in turn related to density. Interferometry has the distinct advantage of not altering the flow. However, the phase variation of the wavefront passing through the tunnel is only related to density if the flow is two-dimensional, i.e., varies only in two dimensions. In the special case of axially symmetric flow, the density can be found from the phase variations by means of the Abel transformation.[1] Statistics of random density variation in three dimensional flows can be found by means of a related technique called "cross-beam Schlieren."[2] Due to the restriction of interferometry to special flow symmetries, there is a pressing need for a device to measure air density in arbitrary flows.

Velocity is the parameter most difficult to measure by conventional

means. The only device which measures velocity directly is the "hot wire anenometer." The hot wire is a very small wire, usually less than one mil in diameter, with a small current flowing through it. This wire is placed in the flow and the cooling effect of the flow alters the resistance of the wire. The resulting variation in the current is directly related to velocity. The hot wire anemometer is very difficult to install due to its small size and its tendency to break. Also, the wire is likely to be broken if there is much dust or particulate in the flow or if the flow is very fast. The quantity measured is velocity magnitude rather than direction. Due to the limitations caused by the fragile nature of the hot wire, it is seldom used in wind tunnel measurements. Because of the inadequacy of the hot wire anemometer, a reliable, non-interfering means of measuring wind tunnel velocities is needed.

Application of Laser Velocimeters to the Fluid Velocity Measurement Problem

The laser velocimeter, when fully developed, has the potential of solving the fluid velocity measurement problem. The velocimeter can make non-interfering measurements of specific velocity components at any point in the test section. It can be made rugged, insensitive to a noisy environment, and easy to operate. The first major problem in the velocimeter development, namely the design of an efficient and stable optical system, has been solved.[3,4,5,10] The problem of estimating velocity from the laser velocimeter signals still remains.

The two principal kinds of laser velocimeters are the laser Doppler

velocimeter (LDV) and the laser interference velocimeter (LIV).[3,6] To use either velocimeter, the wind tunnel must first be "seeded" with small particles such as smoke which move along with the flow. Under certain conditions, a wind tunnel contains enough natural particulate such as dust so that artificial seeding is not necessary.[7] The LDV system measures the velocity by illuminating the flow with a laser beam and detecting the light scattered by the particulate in the flow. The scattered light has a Doppler frequency shift which the velocimeter measures and relates to the particulate or fluid velocity. The LIV measures velocity by creating a very small sinusoidal interference pattern in the test section. As particles move through the interference region, they scatter light whose intensity is proportional to the intensity of the interference pattern at the point where the particle is passing. By detecting and measuring the waveform of the scattered light, the particulate velocity can be determined. Both types of velocimeters have certain advantages and disadvantages which will become apparent.

The LDV system was first presented by Cummins and Yeh.[8] A schematic of the LDV system presented by Foreman[9,11] is shown in Figure 1 and illustrates the basic principles of operation. A continuous wave laser beam is focussed inside the wind tunnel test section by lens L1. Particles passing through the focal region scatter light in all directions. Light scattered through an angle of θ with respect to the original beam is imaged by lens L2 and reflected by mirror M1 to a PMT. The unscattered light is imaged by lens L3 and reflected by mirror M2 and a beam splitter to the PMT. The scattered and unscattered beams interfere at the PMT and

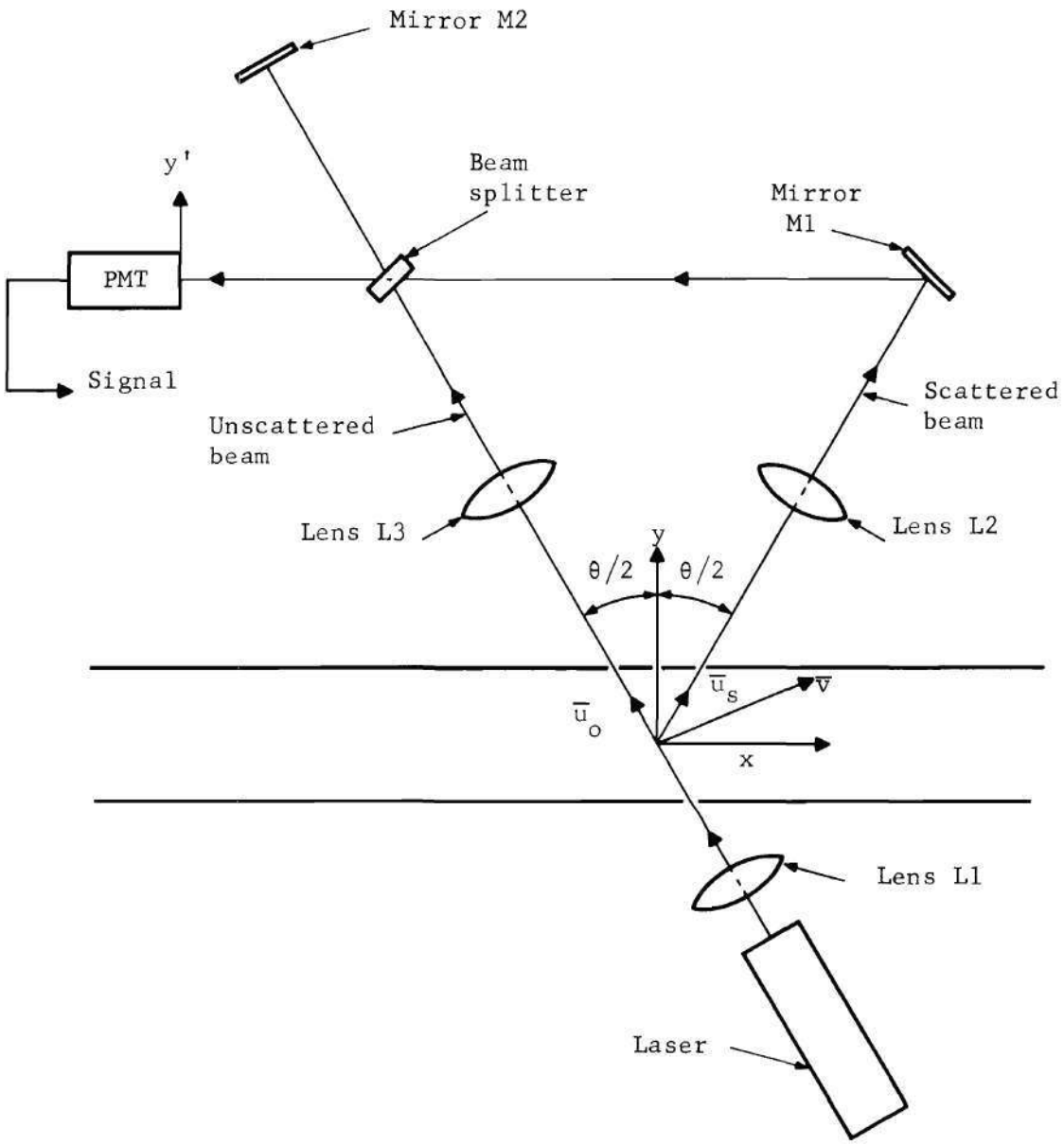

Figure 1. Schematic of the Laser Doppler Velocimeter as described by Foreman[9]

the resulting beat frequency of the mixed signals is the Doppler frequency shift imparted to the light by the velocity of the particles in the flow. The velocity of the air in the test section is given by the well known Doppler relation,[9,11]

$$v_x = f_D\lambda/(2n[\sin\theta/2]) \qquad (1)$$

where v_x is a specific velocity component, λ is the wavelength of the laser, f_D is the Doppler frequency shift, and n is the index of refraction of air.

Although the LDV system of Figure 1 is conceptually workable, it is very difficult to align and very easily misaligned by ambient vibrations common around wind tunnels. In order for the PMT to produce a time varying current, it is necessary that the scattered light from mirror M1 and the reflected light from mirror M2 be parallel when they strike the PMT. Micrometer adjustments are required on the mirrors and beam splitter to achieve parallel beams. Once the mirrors and beam splitter are adjusted, they can be misaligned by vibrations. For these reasons, the LDV system described above is not very practical for wind tunnel measurements although it is an improvement over the hot wire anemometer.

The LDV system shown in Figure 2, proposed by Mayo[3,4] and Brayton,[5] has become standard and is used by most investigators. By means of its simple design and self aligning optics, it is very easy to set up and it operates well around noisy wind tunnels. The beam from the laser strikes a glass plate whose back surface is silvered. Part of the beam (usually five percent) is reflected by the front surface of the plate. The re-

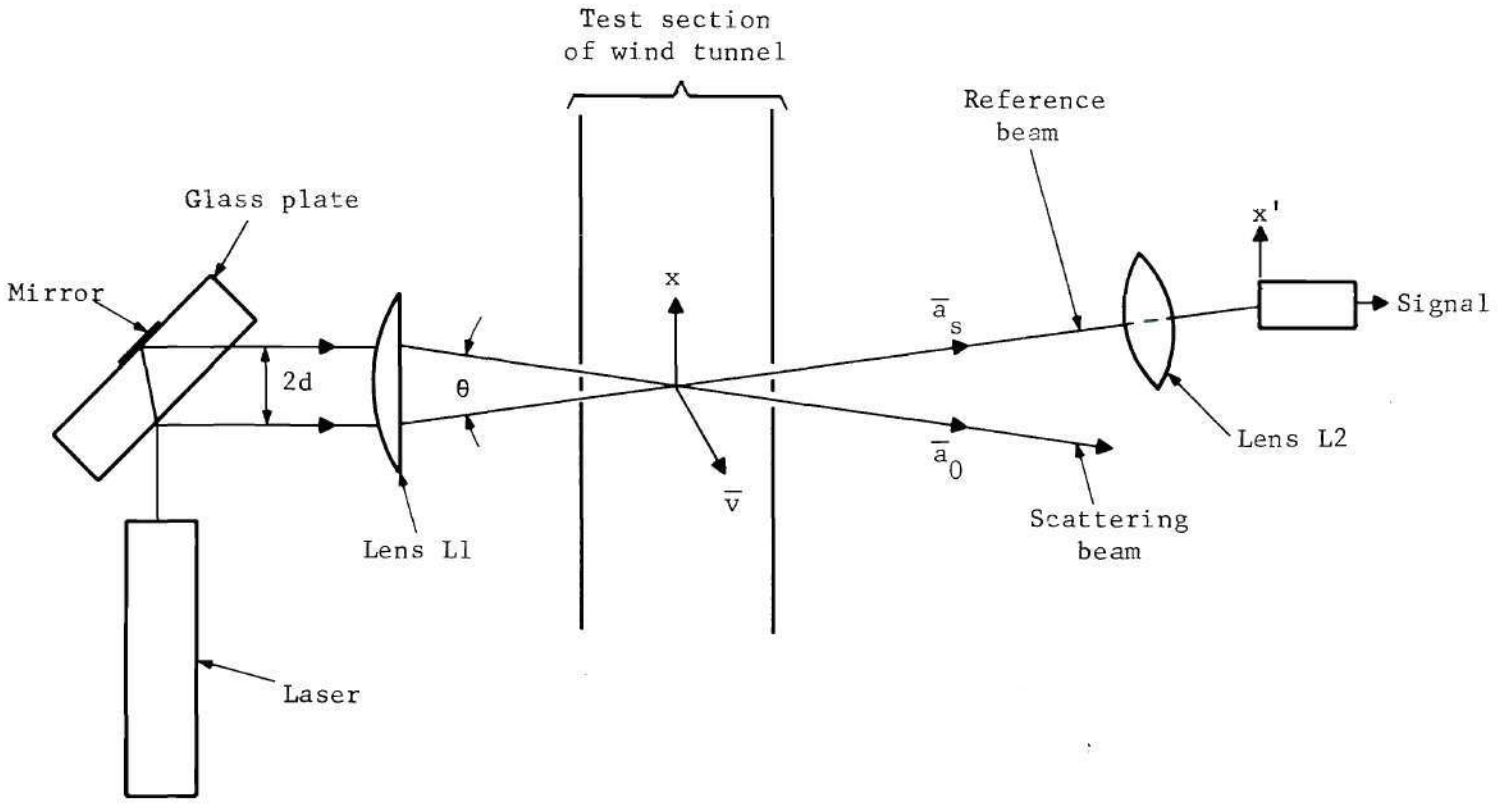

Figure 2. Schematic of Self Aligning LDV System[3,5]

mainder of the beam is transmitted by the first surface of the plate and totally reflected by the second surface. The net result is two beams, one about 20 times stronger than the other, leaving the glass plate. If the sides of the plate are parallel, the two beams are parallel. The two beams pass through lens L1 and are focussed inside the test section in the focal plane of the lens. Since the two beams entering the lens are parallel, they are focussed at the same point. Particles passing through the focal region will scatter light from both beams, but the scattered light from the strong beam will be much stronger than the light scattered from the weak beam. Lens L2 images the focal region of the weak beam to a PMT. Also, light from the strong beam which is scattered by the particles in the direction of the weak beam will also be imaged to the PMT. The images of the scattered and unscattered light interfere with each other at the PMT and produce a current whose frequency is the Doppler frequency shift.

In order for the scattered and unscattered light to be parallel when they strike the PMT, it is necessary that the two beams entering the test section be focussed at the same point. The beams always focus at the same point if the beams entering lens L1 are parallel which is assured by the sides of the glass plate being parallel. Since the sides of the plate are always parallel regardless of vibrations, the system is automatically aligned and insensitive to vibrations. The essential element of the self aligning LDV system is that its alignment depends only on the sides of the glass plate being parallel while the alignment of the LDV system in Figure 1 depends on the beam splitter, and the two mirrors being

precisely aligned and remaining aligned in a noisy environment.

The advent of the self aligning LDV system motivated the discovery of the laser interference velocimeter (LIV) depicted in Figure 3.[3,6,12] The first surface of the glass plate is coated as a beam splitter and the second surface as a mirror so that two equal intensity parallel beams leave the plate. The two parallel beams are equal in intensity in contrast with the LDV system in which one beam is much stronger than the other. The two equal intensity beams are brought to focus at the same point in the wind tunnel forming a sinusoidal interference pattern at that point. The interference pattern has high contrast since the two beams are equal in intensity. When a particle passes through the interference region, light is scattered every time the particle passes through a reinforcement. Hence, the scattered light varies sinusoidally in time at a frequency determined by the geometry of the system and the velocity of the particle. Lens L2 images the scattered light to the PMT. It is shown in Chapter II that the velocity of a specific component, v_x, is given by the relation

$$v_x = f_o \lambda / (2n \sin[\theta/2]) \tag{2}$$

where f_o is the frequency of the received signal.

It should be noted that, although the self aligning LDV system and the LIV system appear similar, there is at least one fundamental difference between them. The LDV system makes use of optical heterodyne detection since the scattered light from the particles is heterodyned by the PMT with the unscattered beam. The LIV system makes use of direct detec-

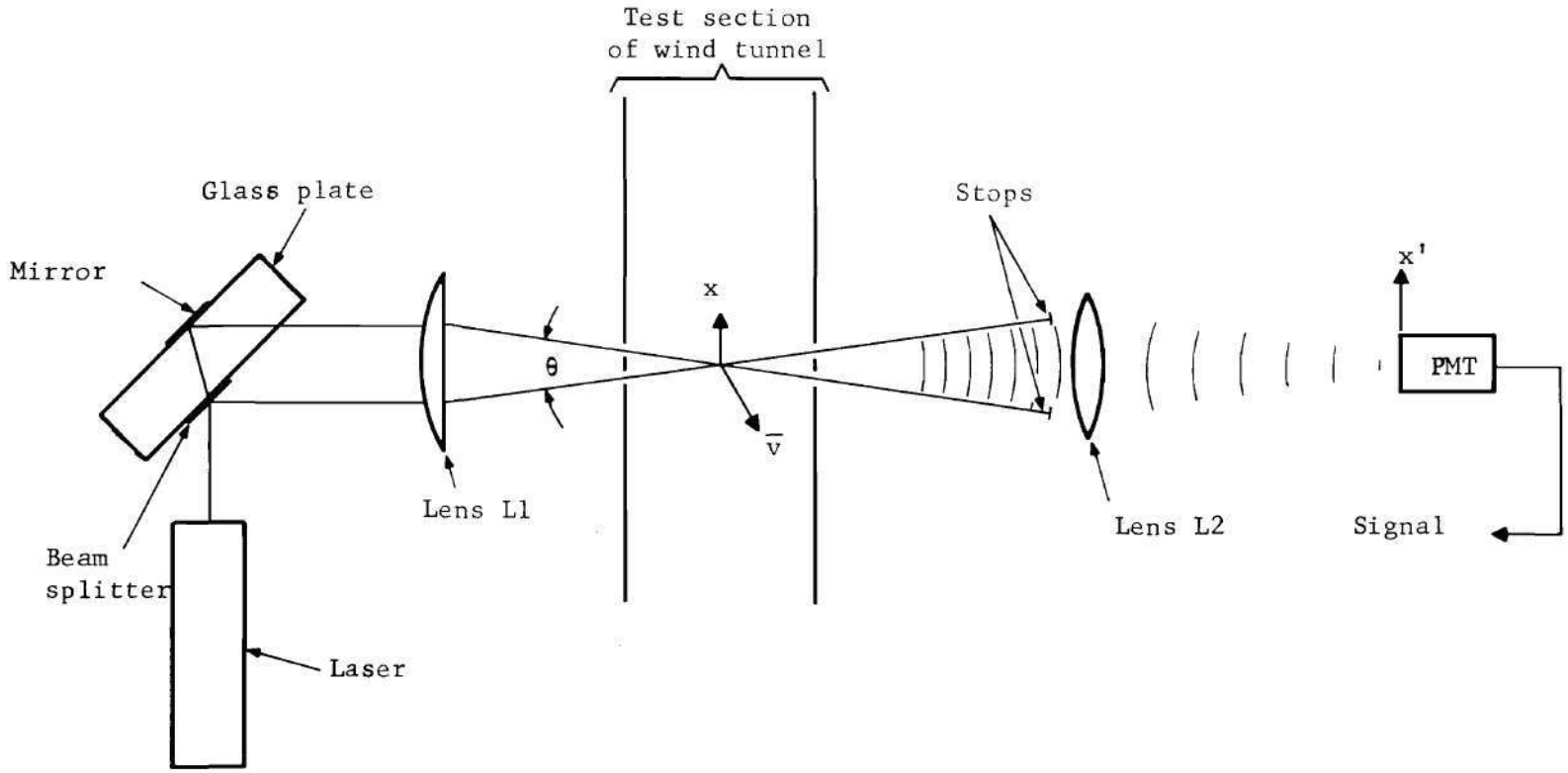

Figure 3. Schematic of a LIV System

tion since the scattered light it detects is time varying in amplitude. Hence, the PMT for LDV systems must be placed so that it intercepts the light scattered in the same direction as the unscattered light as indicated in Figure 2. However, the PMT for the LIV system need only intercept the scattered light. For this reason, the PMT and lens L2 can be placed in any arbitrary direction since light is scattered by the particles in all directions. Due to the many various shapes and locations of wind tunnel test sections, it is extremely convenient at times to place the PMT and lens L2 in arbitrary positions. The LDV system has the advantage of producing a larger output signal due to the conversion gain produced by optical heterodyne detection. When the particles in the flow are small or few in number, the intensity of the scattered light is small. The amplification produced by conversion gain makes the signal portion of the PMT current from the LDV larger than the current from the LIV.

Most of the development work in laser velocimeters has been directed toward the design of a stable, self aligning system which can be used in a real wind tunnel environment. Now that such a system has been developed, the major problem area in the development of a practical velocimeter is the frequency estimation system. This problem is described in more detail in the next section.

The Laser Velocimeter Signal Estimation Problem

Description of Laser Velocimeter Estimation Problem

The output current from the PMT in both the LDV and LIV systems consists of a train of sinusoidal pulses as illustrated in Figure 4. A pulse is produced every time a particle passes through the focal region

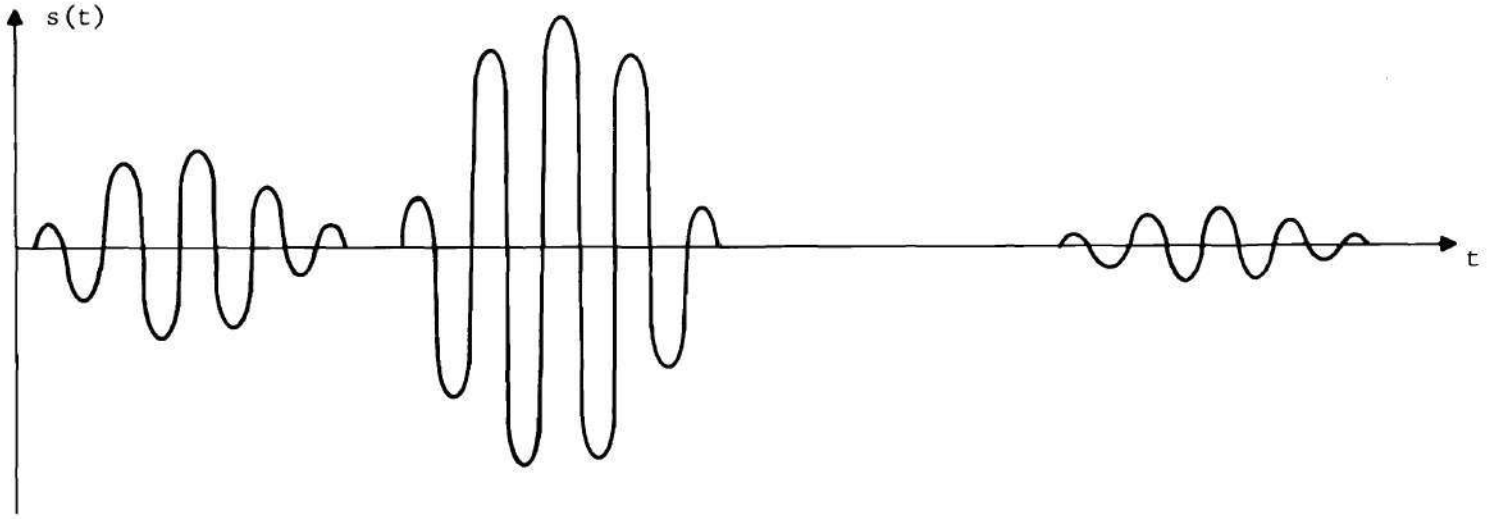

Figure 4. Sketch of a Signal Produced by a Laser Velocimeter

of the two beams. Since the laser beam generally has a Gaussian intensity distribution, the envelope of the pulses is also a Gaussian function. The amplitude of the pulses depends on the size and composition of the particles. In general, the bigger particles produce larger amplitude signals. The particles arrive in the scattering region at random times producing a randomly spaced pulse train. The frequency of the pulses is denoted by f_D for the LDV system and f_o for the LIV system. Although there are some differences between LDV and LIV signals which become apparent in Chapters II and III, the signals from both systems are essentially as described above. The velocimeter estimation problem is the estimation of the frequency f_D or f_o of the pulses.

Relationship to the Pulse-Doppler Estimation Problem

It should be noted that the velocimeter estimation problem is related to the Doppler radar estimation problem. The relationship is most apparent in the case of the LDV system. Both Doppler radar and LDV measure velocity of objects by illuminating them with a coherent beam of radiation and detecting the Doppler frequency shift of the scattered radiation. However, the problems differ from each other in certain significant respects which have a great influence on the estimation systems used. The first difference is that Doppler radar receivers must operate in real time for most applications. In contrast, there is no pressing need for time estimation of laser velocimeter signals since velocimeters are used in experimental wind tunnel tests. Since velocimeter estimators need not be real time, there is more flexibility in their design. In fact, the estimator proposed in this thesis does not operate in real time.

The signal transmitted by Doppler radar systems can be designed to optimize performance. If only velocity information is needed, a very long or continuous signal is produced to give maximum frequency resolution. If position as well as velocity is needed, pulse-Doppler techniques are used in which a specially designed signal is transmitted. The signal is designed so that it is long in duration for good velocity resolution and also has good autocorrelation properties for range resolution. Velocity information only is estimated from the laser velocimeter signal. The location of the particles which scatter light is determined from the geometry of the velocimeter system. Since only velocity information is required of the velocimeter signal, it is desirable for the velocimeter to use long or continuous pulses to obtain good velocity resolution in the same manner as Doppler radar. However, the pulse width is controlled by the size of the scattering volume which is specified by the requirements of the particular wind tunnel tests being carried out. Hence, the velocimeter signal from which the velocity is to be estimated is not optimum according to the principles of radar signal design.

Another important difference between Doppler radar estimation and velocimeter signal estimation is the amount of a priori information available about the shape of the return signal. If a coded pulse (Figure 5) is transmitted by a Doppler radar, its return shape is known within a time delay and a Doppler frequency shift. The delay and frequency shift are estimated from the return by well known correlation techniques. However, the detailed structure of the return signal (Figure 4) from a laser velocimeter is unknown. Not only is the frequency unknown, but the

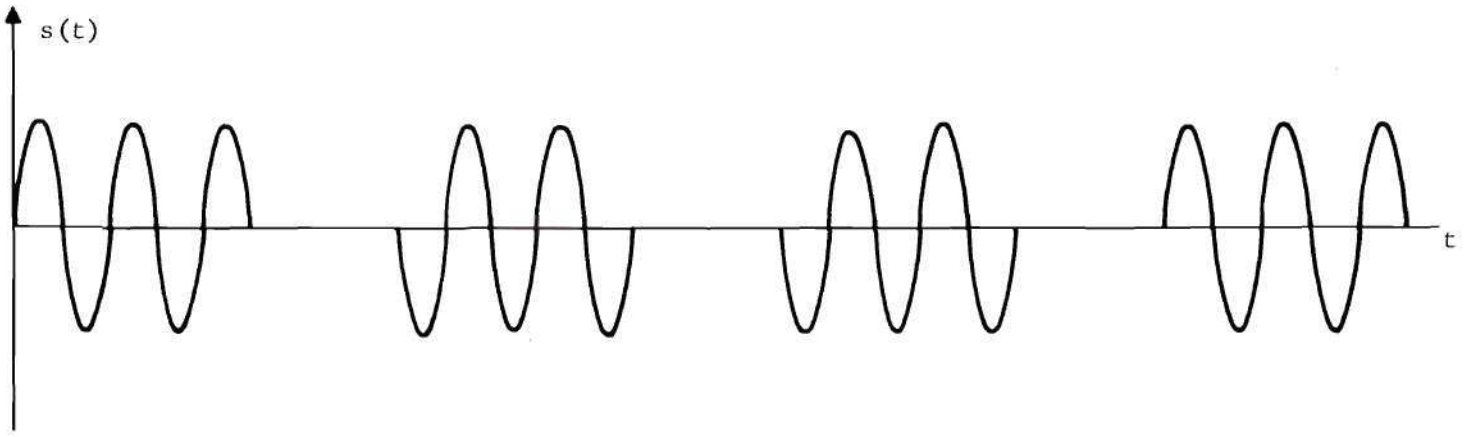

Figure 5. Example of a Coded Pulse Transmitted by a Pulse-Doppler Radar System

relative amplitudes and spacings of the individual pulses are also unknown. Hence, the velocimeter signal cannot simply be correlated with another signal shifted only in frequency and time as is done in pulse-Doppler radar estimation.

The Doppler shift frequencies produced by velocimeters can range from about 100 mHz in the free stream of a supersonic tunnel to about 100 kHz or less in the boundary layer of the airfoil. In low speed wind tunnels, the Doppler frequencies can be as low as 100 Hz. Hence, a laser velocimeter estimator must be capable of estimating frequencies over a much wider frequency range than required for Doppler radar receivers. It is not desirable to heterodyne down high frequency signals in velocimeter systems since the bandwidth to center frequency ratio is relatively high before any heterodyning is applied. If heterodyning is applied, the band width to center frequency ratio becomes much larger making it difficult to estimate the center frequency.

There are flow conditions in wind tunnels in which the flow is very transient. Such conditions occur around shock waves and leading and trailing edges of airfoils. The flow is so transient that it can change from particle to particle or change in less than a millisecond. The rapidly changing nature of certain flows makes it necessary for the estimator to be able to track the changing velocity. In contrast, it is seldom necessary for a Doppler radar to track such a rapidly changing frequency.

Aspects of the Doppler radar estimation and the velocimeter estimation problems are certainly conceptually similar. However, the wide

range of frequencies to be estimated (10,000 to 1), the rapidly changing signal frequency, and the random amplitudes and spacings of the velocimeter returns make the problems very different.

Requirements of a Velocimeter Signal Estimator

Certain requirements of a velocimeter signal estimator are evident from the preceding discussion. The arrival time of the particles in the focal regions of the two beams is a random process. There are instances when many particles are in the focal region at once producing an almost continuous signal. The more common case is the one in which there are few particles present in the test section resulting in gaps between the signal pulses. An estimator must effectively turn itself off when no particle is present or else it will estimate the frequency of noise only. The gaps between the pulses can be thought of as a severe case of fading.

The velocity in a test section can be either steady or time varying as pointed out. In the free stream or in laminar boundary layers, the velocity is steady. Near the trailing or leading edge of the airfoil, the flow is time varying. Therefore, a velocimeter signal estimator should operate well for steady and time varying velocities.

Often the small size of the particles and the small number of particles can make the signal quite small. Also, the photon shot noise, discussed in Chapter III, due to both the scattered and unscattered light can produce a large amount of noise. Under these conditions, signal to noise ratios less than unity are common. A good velocimeter signal estimator should operate satisfactorily when the signal to noise ratios are low.

Flow velccities in wind tunnels can vary widely as pointed out earlier. The free stream flow in a supersonic tunnel can have velocities corresponding to frequencies in the 100 mHz region in the free stream to the 100 kHz region or lower in the boundary layer. It is therefore necessary that the velocimeter estimator operate over a wide frequency range.

Approach Taken in Thesis

The goals of this thesis are to systematically define the velocimeter estimation problem and to establish the feasibility of an estimation technique which will be useful in a number of applications. In Chapter II, mathematical models of LDV and LIV signals were derived and experiments have been carried out to verify the models. The noise sources in velocimeter systems are outlined in Chapter III and the manner in which the noise enters into LDV and LIV systems is discussed. The analysis is supported by experiments. In Chapter IV, an estimator named the "Fourier Transform Estimator" is motivated and analyzed. Chapter V describes the experimental evaluation of the Fourier transform estimator. Steady and time varying flows were produced in a low speed smoke tunnel. LDV and LIV systems were built and the signals produced by these systems were used to test the estimator. The estimator tracked the changing frequency of LDV and LIV signals under high noise conditions with performance superior to conventional estimation techniques. Chapter VI summarizes the thesis and recommends future development of the estimator.

CHAPTER II

SIGNAL MODELS FOR LDV AND LIV SYSTEMS

Introduction

The LDV and LIV systems were described qualitatively in Chapter I. Both systems require the wind tunnel to be seeded with particles which move along with the flow. The LDV system measures the velocity of the particles by illuminating them with a laser beam and measuring the resulting Doppler frequency shift. The LIV system creates a small interference pattern in the wind tunnel. Velocity is determined by measuring the frequency of the waveform of light scattered by the particles as they move through the interference region.

In this chapter, quantitative mathematical models are derived for the signals produced by LDV and LIV systems. A brief general discussion of the signals produced by a laser beam of arbitrary spatial distribution is given first. Then detailed expressions are derived for the most important case, a laser beam with a Gaussian amplitude distribution. Experiments involving both LDV and LIV systems are described. These experiments verify the key features of the mathematical models.

Simplified Analysis of Signals from an LDV System

The following derivations are based on the self aligning LDV system shown in Figure 6. The self aligning LDV system is used since it has become standard in the field[12,13] and its analysis can be extended to other

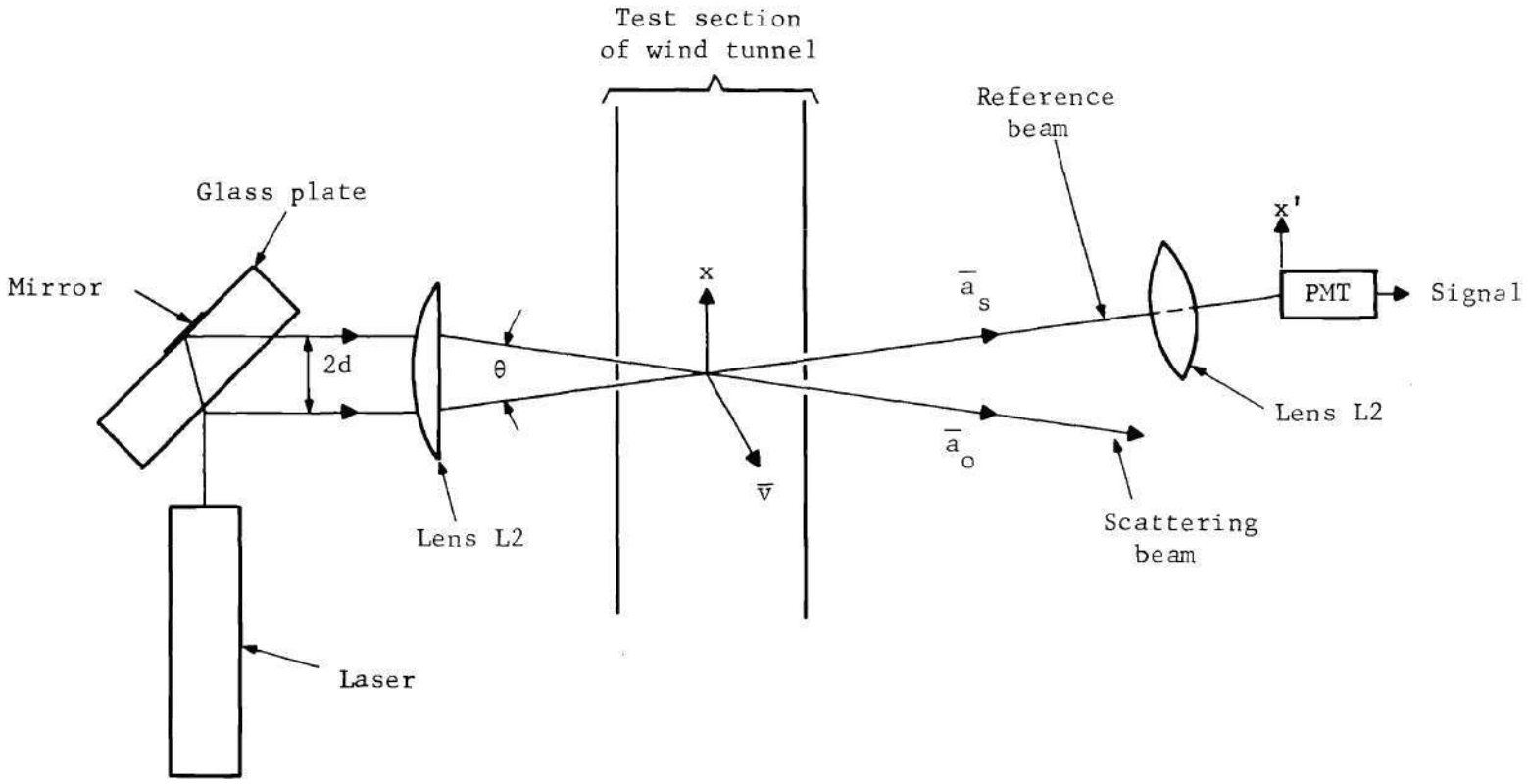

Figure 6. Schematic of Self Aligning LDV System[3,5]

LDV systems. Figure 6 illustrates an LDV system designed to measure the x-component of velocity. Referring to Figure 6, the beam leaving the laser passes through a glass plate with parallel sides and with one side silvered. The net effect of the glass plate is to transform the beam entering the plate into two parallel beams, one about 20 times stronger than the other. Both beams pass through lens L1 and are subsequently focused inside of the wind tunnel test section. The fact that both beams are parallel implies that their focal regions intersect as illustrated. The volume in which the two beams intersect is called the "detection volume" since, as it will be seen, only the velocity of particles passing through this region will be estimated.

Consider the light scattered from the strong beam, called the "scattering beam," in the detection volume. Light scattered from the weak beam, usually called the "reference beam," and light scattered from portions of the scattering beam outside of the detection volume are discussed later. Light scattered from the portion of the scattering beam comprising the detection volume has a Doppler frequency shift f_D given by[11]

$$f_D = \frac{1}{2\pi} (\bar{k}_s - \bar{k}_o)\cdot\bar{v} \qquad (1)$$

where $\bar{k}_s$ is the wave vector of the scattered light, $\bar{k}_o$ is the wave vector of the incident light, and $\bar{v}$ is the velocity of the particle. For velocities encountered in wind tunnels $|\bar{k}_s| \approx |\bar{k}_o|$ and Eq. (1) reduces to

$$f_D = \frac{n}{\lambda} (\bar{a}_s - \bar{a}_o)\cdot\bar{v} \qquad (2)$$

where λ is the wavelength of the laser, n is the index of refraction of air, and $\bar{a}_s$ and $\bar{a}_o$ are unit vectors in the $\bar{k}_o$ and $\bar{k}_s$ directions, respectively. From Eq. (2), the Doppler frequency shift of light scattered from the scattering beam in the direction of the reference beam is

$$f_D = \frac{2nv_x \sin\theta/2}{\lambda} \tag{3}$$

where v_x is the x-component of the particle velocity and θ is the angle between the scattering beam and the reference beam. For air, n is very close to unity so that the above equation is usually written

$$f_D = \frac{2v_x \sin\theta/2}{\lambda}$$

From this equation, the component v_x of the particle velocity can be determined from the Doppler frequency shift f_D as follows

$$v_x = \lambda f_D / 2\sin\theta/2$$

Lens L2 images to a PMT the unscattered light from the reference beam and the light from the scattering beam which is scattered through an angle of θ. The reference beam and the scattered light coherently interfere at the PMT.

Consider light scattered from sources other than the portion of the scattering beam inside of the detection volume. Light scattered from the reference beam to the PMT is not Doppler shifted since its scattering angle is effectively zero. Light scattered from portions of the scatter-

ing beam outside of the detection volume may be neglected for several reasons. First of all, the light in the detection volume is much more intense than elsewhere in the beam. Hence, light scattered from elsewhere is much lower in intensity than light from the detection volume. Since lens L2 is imaging the detection volume to the PMT, light scattered from places other than the detection volume is out of focus and reduced in intensity. Also, it is shown in a number of references,[14,15] that two interfering time modulated beams striking a PMT produce a time varying current only if they are very nearly parallel. It is apparent from Figure 6 that only light scattered from the detection volume is parallel to the reference beam. For this reason, only light scattered from the portion of the scattering beam in the detection volume produces a time varying current. In addition, an aperture is generally placed at the PMT which is the size of the imaged detection volume to block out light from other sources. Therefore, the only Doppler shifted light of consequence at the PMT is produced by particles passing through the portion of the scattering beam in the detection volume.

Let the complex amplitudes of the scattered light and the reference beam in the plane of the PMT be described, respectively, by

$$u_s(x',y',t) = A_s(x',y',t)e^{j2\pi f_D t} \tag{4}$$

and

$$u_r(x',y',t) = A_o(x',y')$$

The intensity $I_d(x',y',t)$ of the field at the PMT is then

$$I_D(x',y',t) = |u_s(x',y',t) + u_o(x',y')|^2 \tag{5}$$

$$= A_s^2(x',y',t) + A_o^2(x',y')$$

$$+ 2A_s(x',y',t)\, A_o(x',y') \cos 2\pi f_D t$$

In general, the intensity of the scattered light is much less than the intensity of the reference beam, hence,

$$|A_s(x',y',t)|^2 \ll 2A_s(x',y',t)\, A_o(x',y') \tag{6}$$

$$\cdot |\cos 2\pi f_D t| \ll |A_o(x',y')|^2$$

The current $i_D(t)$ produced by the PMT is proportional to the integral of the intensity over the surface of the PMT and is given by

$$i_D(t) = K_D \int\int_{\substack{\text{area of} \\ \text{PMT}}} I_D(x',y',t)\, dx'dy' \tag{7}$$

$$= K_D \int\int [A_s^2(x',y',t) + A_o^2(x',y') + 2A_o(x',y')\, A_s(x',y',t)$$

$$\cos 2\pi f_D t]\, dx'dy'$$

$$= i_s + i_D + I_D(t) \cos 2\pi f_D t$$

where K_D is proportional to the gain of the PMT.

It is apparent from Eq. (6) that

$$i_s \ll I_D(t) \cos 2\pi f_D t \ll i_D \tag{8}$$

The current $i_D(t)$ is primarily a dc current with a small ac ripple. The v_x component of the flow can be determined by estimating the frequency of f_D of the ac component and applying Eq. (3).

The coefficient $I_D(t)$ of the cosine term in Eq. (7) is important in the velocimeter signal estimation problem. In order to attack the velocimeter estimation problem, a specific expression for $I_D(t)$ must be obtained in the case of a laser beam with a Gaussian spatial intensity distribution. Since the equations derived up to now cannot be straightforwardly extended to the Gaussian case, a more detailed derivation of this case is now presented.

LDV Systems with Beams of a Gaussian Spatial Intensity Distribution

Although it is conceptually possible to have a laser beam with almost any spatial amplitude distribution, most continuous wave lasers available operate in the TEM_{00} mode and have a Gaussian spatial amplitude distribution. Mayo[3] demonstrates that a Gaussian distribution is optimum for both LDV and LIV systems since a Gaussian beam produces the narrowest bandwidth signal for a given detection volume size. A narrow band signal is desirable since it enables one to get a better estimate of the center frequency f_D. Since Gaussian laser beams are readily available and are optimum for velocimeter application, detailed expressions for the signals produced by velocimeters using Gaussian beams are derived.

In order to simplify the following derivation as much as possible, the analysis is divided into the following sections. First of all, with reference to Figure 7, the amplitude distributions in the focal plane of

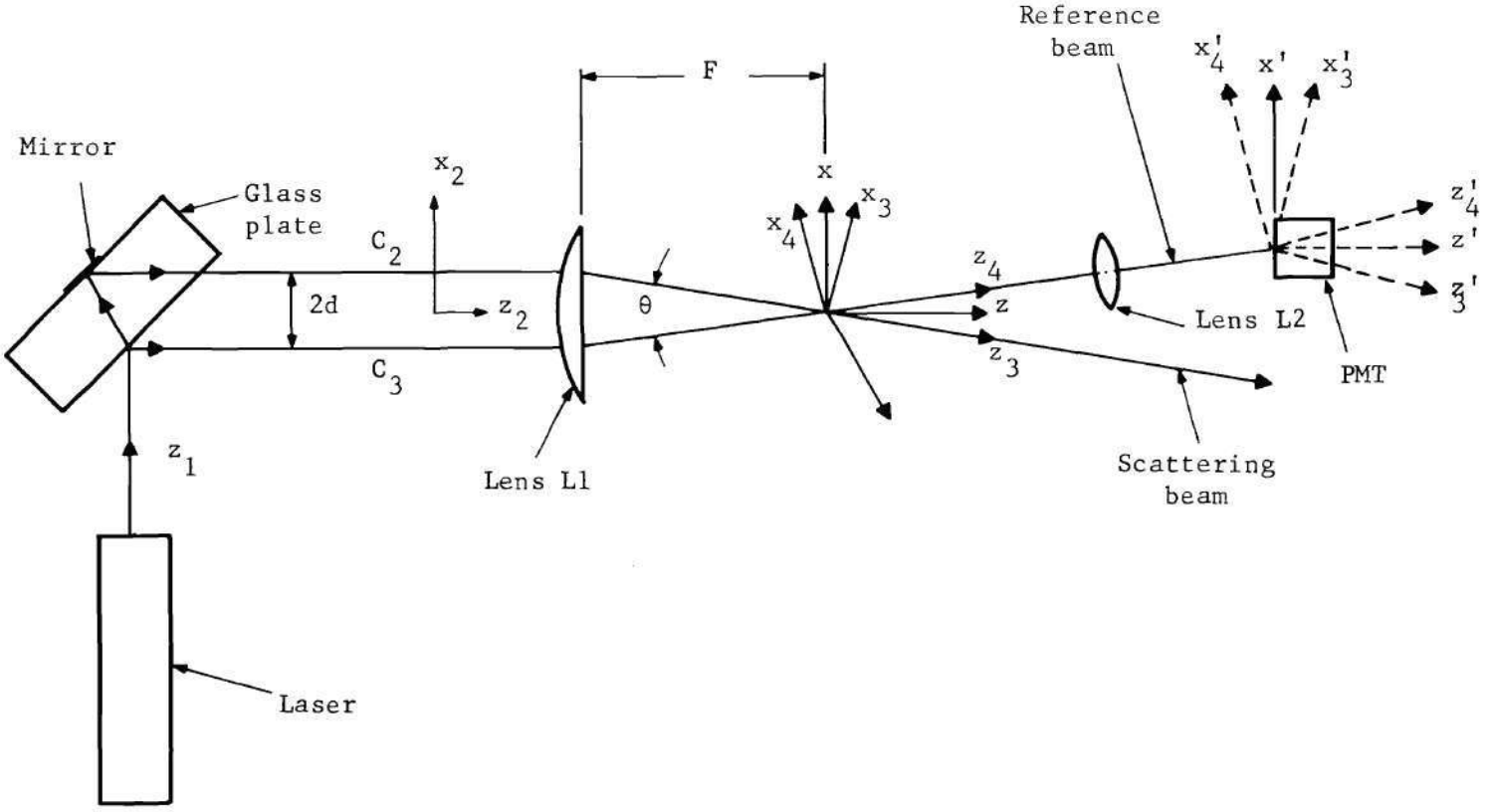

Figure 7. Schematic Used in the Discussion of the Self Aligning LDV System with a Beam from a TEM_{00} Laser

lens L1 are derived. Next, expressions for the light imaged to the PMT surface by lens L2 are presented. Finally, an expression for the current from the PMT is stated and interpreted.

Light Amplitude Distribution in the Focal Plane of Lens L1

Referring to the self aligning LDV system of Figure 7, the amplitude distribution of the beam leaving the laser is given by

$$u_o(x_1,y_1) = \frac{C_1 \, e^{-D(x_1^2+y_1^2)}}{\sqrt{\pi/2D}} \tag{9}$$

where C_1 and D are constants. The two parallel beams leaving the glass plate have amplitude distributions in plane P1 of the front focal plane of lens L1, given by

$$u_{s1}(x_2-d,y_2) = \frac{C_2 \, e^{-D[(x_2-d)^2+y_2^2]}}{\sqrt{\pi/2D}} \tag{10}$$

and

$$u_{r1}(x_2+d,y_2) = \frac{C_3 \, e^{-D[(x_2+d)^2+y_2^2]}}{\sqrt{\pi/2D}} \tag{11}$$

where $u_{s1}(x_2-d,y_2)$ and $u_{r1}(x_2+d,y_2)$ are the scattering beam and reference beam, respectively, separated by a distance 2d. The path length differences of the two beams caused by the glass plate are ignored because they are generally negligible compared to the coherence length of the laser. The path length differences can be compensated by a second glass plate if they become important.[5] In the previous section, it was demonstrated that

$$|u_{s1}(x_2-d,y_2)|^2 \approx 20|u_{r1}(x_2+d,y_2)|^2 \tag{12}$$

The two beams pass through lens L1 and are focused in the detection volume. It can be shown that, if a beam entering a lens is collimated with a Gaussian spatial amplitude distribution, the amplitude distribution of the light leaving the lens is also Gaussian.[3,16] More specifically, if the scattering beam entering the lens has an amplitude distribution given by Eq. (10), it has the following amplitude distribution $u_{s2}(x_3y_3z_3)$ when it leaves the lens[3,16]

$$u_{s2}(x_3,y_3,z_3) = \frac{C_2}{\sqrt{\pi/2\beta(z_3)}} e^{jkz_3} e^{-\beta(z_3)(x_3^2+y_3^2)} \cdot e^{j\frac{\gamma(z_3)}{2}(x_3^2+y_3^2)} e^{-j\delta(z_3)} \tag{13}$$

where

$$\beta(z_3) = \left[G^2\left(1 + \frac{\lambda z_3}{\pi G^2}\right)\right]^{-1} \tag{14}$$

$$\gamma(z_3) = k\left[z_3(1 + [\pi/\lambda z_3 D]^2)\right]^{-1}$$

$$\delta(z_3) = 1/2 \tan^{-1}(\lambda z/\pi G^2)$$

$$G = 2F\sqrt{D}/k$$

$$F = \text{focal length of L1}$$

and the coordinate system (x_3,y_3,z_3) is defined in Figure 7.

By a similar line of reasoning, the reference beam after it has passed through lens L1 is given by

$$u_{r2}(x_4,y_4,z_4) = \frac{C_3}{\sqrt{\pi/2\beta(z_4)}} e^{jkz_4} e^{-\beta(z_4)(x_4^2+z_4^2)} \cdot e^{j\gamma(z_4)(x_4^2+y_4^2)} e^{-j\delta(z_4)} \tag{15}$$

where the (x_4,y_4,z_4) coordinate system is defined in Figure 7.

Amplitude Distribution of Light in the Plane of the PMT

Now that the expressions for the light amplitude in the focal region of lens L1 have been stated, expressions for the light in the PMT plane are obtained. The function of lens L2 is to image the detection volume to the PMT. It is assumed that the imaging is done with unity magnification. If the magnification is not unity, the following results are altered by a scale factor. With unity magnification, essentially all the reference beam passes through L2 and the image $u_r(x_4',y_4',z_4')$ of the portion of the reference beam in the detection volume can be described by*

$$u_r(x_4',y_4',z_4') = u_{r2}(x_4',y_4',z_4') \tag{16}$$

The light scattered to the PMT by particles passing through the detection volume is now derived. Oil smoke, which generally ranges in diameter from 0.01 to 1 micron,[17] was used to seed the flows in the ex-

*Strictly speaking, the magnification is unity only in the x_4' and y_4' directions since a lens images nonlinearly in the z_4' direction. It can be shown that, if the length of the detection volume in the z_4' direction (about .1 mm) is small compared to the focal length of lens L2 (several hundred millimeters), the magnification in the z_4' dimension of the detection volume is differentially close to unity.

periments carried out in this thesis. The light scattered by particles of diameter d in this size range is governed by Rayleigh scattering when the quantity

$$\alpha = \pi d/\lambda \tag{17}$$

is less than 0.3 and by Mie scattering[18] when the quantity α is greater than 0.3. For helium-neon lasers, which have a wavelength of 0.6328 micron, α is 0.3 for a particle diameter of 0.06 micron. Rayleigh scatterers scatter as much light in the forward as in the backward directions whereas Mie scatterers scatter light primarily in the forward direction. It was obvious by viewing the laser velocimeter used in this thesis that much more light is forward-scattered than backward-scattered. Therefore, the signals most dominant in a velocimeter are likely produced by particles larger than 0.06 micron and close to a micron in size.

The mathematics involved in evaluating the expressions which follow are simplified if it is noted that the variation of the amplitude of the light in the detection volume over distances of the same magnitude as the particle diameter is negligible. In the experimental work, the angle θ between the two beams in the detection volume was 2.54°. The fringe spacing p for the LIV system follows as[32]

$$p = \lambda/\sin\theta \tag{18}$$

$$= 14.3 \text{ microns}$$

where $\lambda = 0.6328$ micron. Since the particles have diameters much smaller than p, the amplitude of the light falling on a particle in a given instant is constant in space over the extent of the particle. Since there

are no interference fringes in the LDV system, the amplitude of the light varies more slowly in space in the detection volume of the LDV system than does the light in the LIV system. Therefore, the approximation made above is even more valid for the LDV system.

Consider a particle of diameter d moving through the point (x_3,y_3,z_3) in the detection volume with a velocity $\bar{v} = (v_{x_3},v_{y_3},v_{z_3})$ and a position at t = 0 specified by (x_3^o,y_3^o,z_3^o). The amplitude of the light falling on the particle in the $\bar{z}_3$ plane is given by

$$u_{s3}(x_3,y_3,z_3) = u_{s2}(\bar{x}_3,\bar{y}_3,\bar{z}_3)\text{circ}\,[2r(x_3,y_3)/d] \tag{19}$$

where

$$\bar{x}_3 = x_3^o + v_{x_3}t$$

$$\bar{y}_3 = y_3^o + v_{z_3}t$$

$$\bar{z}_3 = z_3^o + v_{z_3}t$$

$$r(x_3,y_3) = \sqrt{(x-\bar{x}_3)^2 + (y_3-\bar{y}_3)^2}$$

and

$$\text{circ}\,[2r(x_3,y_3/d)] = 1 \quad r(x_3,y_3) \leqq d/2$$

$$= 0 \text{ elsewhere}$$

The particle in plane $\bar{z}_3$ is imaged to the PMT by lens L2. The image is not as bright as the particle itself since the light is scattered by the particle in all directions and only a small portion of the light passes through L2. The amplitude of the particle's image at the PMT, taking into account the loss of light due to scattering, is given by

$$u_s(x_3',y_3',\bar{z}_3) = \varepsilon u_{s3}(x_3',y_3',\bar{z}_3) \tag{20}$$

where $\varepsilon < 1$.

An estimate of the magnitude of ε is now made. The light falling on the oil particle is either absorbed or scattered. Since the oil used was extremely clear, it is assumed that all the light is scattered by the oil droplet. The index of refraction of oil ranges from about 1.4 to 1.5.[42] A computation using Mie theory has been carried out for a 0.5 micron particle with a refractive index of 1.5 in visible light.[18] This computation demonstrates that almost all of the light is forward scattered by the particle into a cone whose half angle is 60°.[18] The lens used to gather the scattered light in the experimental work had a two inch aperture and was positioned about 16 inches from the detection volume. For this arrangement, ε^2 is approximately given by

$$\varepsilon^2 \approx \frac{\text{solid angle subtended by lens}}{\text{solid angle subtended by a } 60^\circ \text{ cone}} \tag{21}$$

$$\approx \frac{\pi 1^2}{\pi(16 \tan 60)^2}$$

$$\approx \frac{1}{770}$$

Current Produced by the PMT

Now that the light amplitude distribution on the PMT surface has been found, the current from the PMT can be obtained. The intensity of the light in the PMT plane is derived and then the current is obtained by integrating the intensity over the PMT surface. The resulting expression

is complicated and simplifications and approximations are made to obtain a more meaningful result.

The intensity I_D of the light in front of the PMT is given by

$$I_D = \left| u_r(x_4', y_4', z_4') + u_s(x_3', y_3', z_3') \right|^2 \tag{22}$$

$$= \left| u_r(x_4', y_4', z_4') \right|^2 + \left| u_s(x_3', y_3', z_3') \right|^2 + u_s^*(x_3', y_3', z_3')$$

$$\cdot\ u_r(x_4', y_4', z_4') + u_s(x_3', y_3', \bar{z}_3')\ u_r(x_4', y_4', z_4')$$

where $(x_3', y_3', \bar{z}_3')$ and (x_4', y_4', z_4') are the same point in different coordinate systems. The current $i_D(t)$ from the PMT is proportional to the time variation of the integral of the intensity over the surface S of the PMT as follows

$$i_D(t) = K_D \int_S\int I_D\ dA' \tag{23}$$

$$= K_D \int_S\int \left| u_r(x_4', y_4', z_4') \right|^2\ dA' + K_D \int_S\int u_s(x_3', y_3', \bar{z}_3')$$

$$\cdot + K_D \int_S\int u_s^*(x_3', y_3', \bar{z}_3)\ u_r(x_4', y_4', z_4')\ dA' + K_D \int_S\int u_s(x_3', y_3', \bar{z}_3')$$

$$u_r^*(x_4', y_4', z_4')\ dA'$$

$$= K_D[I_r + I_s + I_{sr} + I_{sr}^*]$$

where K_D accounts for the PMT quantum efficiency and gain.

The first integral I_r represents the intensity of the reference

beam. Since the integrand is defined in the (x_4', y_4', z_4') system, its evaluation is simplified if the integration is carried out in that system over the surface S_1, the projection of the surface S into the $z_4' = 0$ plane. The integral I_r becomes, with the aid of Eqs. (15) and (16)

$$I_r = \int_{S_1}\int |u_r(x_4', y_4', z_4')|^2 \, dA' \tag{24}$$

$$= \int_{S_1}\int \left(\frac{C_3}{\sqrt{\pi/[2\beta(z_4')]}}\right)^2 e^{-2\beta(z_4')(x_4'^2 + y_4'^2)} \, dx_4' dy_4'$$

$$= C_3^2$$

The integration utilizes the fact that the integrand is a product of two Gaussian functions whose area is unity. As one would expect, the total power in the reference beam is time invariant. The second integral is the intensity in the image of the particle and is a function of time since the particle is moving. The integration is simplified if it is carried out in the projection S_2 of the PMT surface in the z_3' plane. Using Eqs. (19) and (20), the integral is evaluated as

$$I_s = \int_{S_2}\int |u_s'(x_3', y_3', \bar{z}_3')|^2 \, dx_3' dy_3'$$

$$= \epsilon^2 \int_{S_2}\int |u_{s3}(x_3', y_3', \bar{z}_3')|^2 \, dx_3' dy_3'$$

$$= \epsilon^2 \int_{S_2}\int |u_{s2}(\bar{x}_3, \bar{y}_3, \bar{z}_3)\,\mathrm{circ}[2r(x_3', y_3')/d]|^2 \, dx_3' dy_3'$$

$$= \epsilon^2 |u_{s2}(\bar{x}_3, \bar{y}_3, \bar{z}_4)|^2 \int_{S_2}\int \mathrm{circ}^2[2r(x_3', y_3')/d] \, dx_3' dy_3'$$

From Eq. (19), the integral above is the area σ^2 of the cross section of the particle of diameter d which is given by $\pi d^2/4$. Substituting from Eq. (13), I_s becomes

$$I_s = \frac{\varepsilon^2 \sigma^2 C_2^2}{\pi/2\beta(\bar{z}_3)} e^{-2\beta(\bar{z}_3)(\bar{x}_3^2 + \bar{y}_3^2)} \tag{25}$$

The contribution due to I_s is an exponentially shaped current pulse. The magnitude of I_s is now compared to the magnitude of I_r. The exponential factor in I_s is maximum when the argument of exponent is zero which occurs when

$$\bar{x}_3 = \bar{y}_3 = 0 \tag{26}$$

The coefficient of the exponent is maximum when $\beta(\bar{z}_3)$ is maximum which occurs when $\bar{z}_3 = 0$. From Eq. (14)

$$\beta(\bar{z}_3) = 1/G^2 \tag{27}$$

and it follows from Eq. (25) that

$$I_s \leqq \frac{2\varepsilon^2 \sigma^2 C_2^2}{\pi G^2} \tag{28}$$

The value of the bound on I_s given above is now estimated. From Eq. (21)

$$\varepsilon^2 \approx 1/770$$

For a 0.5 micron particle, typical of the sizes used in the experimental work, the cross-sectional area σ^2 is given by

$$\sigma^2 = \pi d^2/4$$
$$= \pi(0.5 \times 10^{-3} \text{ mm})^2/4$$
$$= 0.195 \times 10^{-6} \text{ mm}^2$$

For most LDV systems, $C_2^2 \approx 20C_3^2$ as pointed out earlier in the chapter. From Eq. (14), G is given by

$$G = 2F\sqrt{D}/k \tag{29}$$

F is the focal length of lens L1 which for the experimental work was 24 inches. D is approximately the inverse of the square of the radius of the beam entering lens L1, as is apparent from Eq. (9). Since the beam entering lens L1 in the experiments had a 4 mm radius, a typical value of D is $(4 \text{ mm})^{-2}$. The value of k for a helium-neon laser is $2\pi/\lambda$ where λ = 0.6328 micron. Substituting these values into Eq. (29), one obtains

$$G = 2F\sqrt{D}/k$$
$$= \frac{2(24)(25.4)\sqrt{4^{-2}}}{2\pi/0.6328 \times 10^{-3}}$$
$$= 0.031 \text{ mm}$$

Substituting the above values into Eq. (28), the bound on I_s becomes

$$I_s \leq \frac{2\varepsilon^2\sigma^2 C_2^2}{\pi G^2} \tag{30}$$
$$\leq \frac{2(1/770)90.195 \times 10^{-6})(20C_3^2)}{\pi(0.031)^2}$$
$$\leq 3.36 \times 10^{-6} C_3^2$$

Since I_r is equal to C_3^2, it is clear from the above expression that $I_r >> I_s$.

The third and fourth integrals of Eq. (23) represent the cross products of the scattered light and the reference beam. These terms are the ones which contain the Doppler frequency shifts imparted to the light by the particle velocity. The integration is simplified if it is carried out over the surface S_2 defined earlier as the projection of S into the $z_3' = \bar{z}_3$ plane

$$I_{sr} = \int_{S_2}\int u_s^*(x_3',y_3',\bar{z}_3)\ u_r(x_4',y_4',z_4')\ dx_3'dy_3'$$

Substituting Eqs. (17) and (20) into the above equation, I_{sr} becomes

$$I_{sr} = \int_{S_2}\int \varepsilon u_{s2}^*(\bar{x}_3,\bar{y}_3,\bar{z}_3)\ \mathrm{circ}[2r(x_3',y_3')/d]\ u_r(x_4',y_4',z_4')\ dx_3'dy_3'$$

It is demonstrated earlier in the chapter that the extent of the particle's cross section represented by the circular function in the above equation is small enough that the light falling on it is effectively constant in amplitude over the surface of the particle. With this simplication, I_{sr} becomes

$$I_{sr} = \sigma^2 \varepsilon\ u_{s2}(\bar{x}_3,\bar{y}_3,\bar{z}_3)\ u_r(\bar{x}_4,\bar{y}_4,\bar{z}_4) \qquad (31)$$

where $(\bar{x}_3,\bar{y}_3,\bar{z}_3)$ and $(\bar{x}_4,\bar{y}_4,\bar{z}_4)$ are the same point in different coordinate systems. Note that the first factor is defined in the (x_3,y_3,z_3) system and the second in the (x_4,y_4,z_4) system. In order to further evaluate the term, both factors are expressed in the (x,y,z) coordinate system by

standard analytic geometry.

The transformation into the (x,y,z) is cumbersome and is outlined briefly below. By substituting Eqs. (13) and (15) into the expression for I_{sr}, one obtains

$$I_{sr} = \frac{C_2 C_3 \epsilon \sigma^2}{\sqrt{\pi/[2\beta(\bar{z}_3)\beta(\bar{z}_4)]}} e^{-\beta(\bar{z}_3)[\bar{x}_3^2 + \bar{y}_3^2]} e^{-jk\bar{z}_3} \tag{32}$$

$$\cdot e^{-j\gamma(\bar{z}_3)(\bar{x}_3^2 + \bar{y}_3^2)} e^{j\delta(\bar{z}_3)} e^{-\beta(\bar{z}_4)(\bar{x}_4^2 + \bar{y}_4^2)}$$

$$\cdot e^{jk\bar{z}_4} e^{j\gamma(\bar{z}_4)(x_4^2 + y_4^2)} e^{-j\delta(\bar{z}_4)}$$

Before proceeding further, a few simplifications are made in the phase of the above expression. The strongest contributors to the phase of I_{sr} are the linear phase components $k\bar{z}_3$ and $k\bar{z}_4$. Every time the distance traversed by the particle along the z_3 and z_4 coordinates equals one wavelength, the phase changes by 2π. Another component is $\delta(\bar{z}_3)$ given by Eq. (14) as

$$\delta(\bar{z}_3) = 1/2 \tan^{-1} \frac{\lambda \bar{z}_3}{\pi G^2} \tag{34}$$

Since the value of $\delta(\bar{z}_3)$ changes from $-\pi/2$ to $\pi/2$ as the distance $\bar{z}_3$ traversed ranges from $-\infty$ to ∞, the contribution to the phase of $\delta(\bar{z}_3)$ is negligible compared to the contribution of the linear phase terms. By similar reasoning, the contribution made by $\delta(\bar{z}_4)$ is also negligible. The addition to the phase made by

$$\gamma(\bar{z}_3)(\bar{x}_3^2 + \bar{y}_3^2)$$

is also small. The factor $\gamma(\bar{z}_3)$ is defined in Eq. (14) as

$$\gamma(\bar{z}_3) = k[\bar{z}_3(1 + [\pi/\lambda\ z_3 D]^2)]^{-1} \tag{35}$$

By differentiation with respect to $\bar{z}_3$, the largest value of Eq. (35) can be shown to be D. The largest value of $\bar{x}_3^2 + \bar{y}_3^2$ is the radius squared of the detection volume which, in the experimental work, was 7.39×10^{-3} mm^2. With these estimates, a bound on the contribution to the phase made by Eq. (35) is

$$\gamma(\bar{z}_3)(\bar{x}_3^2 + \bar{y}_3^2) \leq \left(\frac{1}{16\ mm^2}\right)(7.39 \times 10^{-3}\ mm^2) \tag{36}$$

$$= .462 \times 10^{-3}\ rad$$

Therefore the components of the phase due to $\gamma(\bar{z}_3)(\bar{x}_3^2 + \bar{y}_3^2)$ and $\gamma(\bar{z}_4)(\bar{x}_4^2 + \bar{y}_4^2)$ are negligible compared to the phase of the linear terms. Hence the only significant contribution to the phase is produced by the linear phase terms. With these approximations, the expression for I_{sr} becomes

$$I_{sr} = \frac{C_2 C_3 \epsilon \sigma^2}{\sqrt{\pi/2\beta(\bar{z}_3)}\sqrt{\pi/2\beta(\bar{z}_4)}}\ e^{-\beta(\bar{z}_3)[\bar{x}_3^2 + \bar{y}_3^2]} \tag{37}$$

$$e^{-\beta(\bar{z}_4)(x_4^2 + y_4^2)}\ e^{-jk\bar{z}_3}\ e^{jk\bar{z}_4}$$

In order to simplify the phase factors of Eq. (37), the linear phase terms are rotated into the (x,y,z) by using the following standard analytical geometry equations

$$\bar{x}_3 = \bar{z}\,\sin\theta/2 + \bar{x}\,\cos\theta/2 \tag{38}$$

$$\bar{z}_3 = \bar{z}\,\cos\theta/2 - \bar{x}\,\sin\theta/2$$

$$\bar{x}_4 = -\bar{z}\,\sin\theta/2 + \bar{x}\,\cos\theta/2$$

$$\bar{z}_4 = \bar{z}\,\cos\theta/2 + \bar{x}\,\sin\theta/2$$

Substituting the transformations of Eq. (38) into the phase factors of Eq. (37), I_{sr} becomes

$$I_{sr} = \frac{C_2 C_3 \varepsilon \sigma^2}{\sqrt{\pi/2\beta(\bar{z}_3)}\sqrt{\pi/2\beta(\bar{z}_4)}}\, e^{-\beta(\bar{z}_3)(\bar{x}_3^2 + \bar{y}_3^2)} \tag{39}$$

$$e^{-\beta(\bar{z}_4)(x_4^2 + y_4^2)}\, e^{-2jk\bar{x}\,\sin\theta/2}$$

The other cross product term I_{sr}^* is the complex conjugate of I_{sr} and the sum of the two terms becomes

$$I_{sr} + I_{sr}^* = \frac{2C_2 C_3 \varepsilon \sigma^2}{\sqrt{\pi/2\beta(\bar{z}_4)}\sqrt{\pi/2\beta(\bar{z}_3)}}\, e^{-\beta(\bar{z}_3)(\bar{x}_3^2 + \bar{y}_3^2)} \tag{40}$$

$$e^{-\beta(\bar{z}_4)(\bar{x}_4^2 + \bar{y}_4^2)}\, \cos(2k\bar{x}\,\sin[\theta/2])$$

In order to obtain an idea of the shape of the envelope, a few approximations are made in the exponent of Eq. (40). The terms $\beta(\bar{z}_3)$ and $\beta(\bar{z}_4)$, when rotated into the (x,y,z) system, become

$$\beta(\bar{z}_3) = [G^2(1 + (\lambda/\pi G^2)(\bar{z}\,\cos\theta/2 - \bar{x}\,\sin\theta/2))]^{-1} \tag{41}$$

and

$$\beta(\bar{z}_4) = [G^2(1 + (\lambda/\pi G^2)(\bar{z}\cos\theta/2 + \bar{x}\sin\theta/2))]^{-1}$$

The terms, $\beta(\bar{z}_3)$ and $\beta(\bar{z}_4)$, are almost equal since the only difference between them is the sign of the $\bar{x}\sin\theta/2$ term. The maximum values of $\bar{x}$ and $\bar{z}$ are the maximum dimensions of the detection volume along those coordinates. If the particle has coordinates $\bar{x}$ and $\bar{z}$ greater than dimensions of the detection volume, the particle would be outside of the detection volume and no light would be scattered by the particle. It is shown in the experimental section that the value of θ is 2.54° and that the maximum values of $\bar{x}$ and $\bar{z}$ are 0.086 mm and 3.87 mm, respectively. With these values, the maximum values of $\bar{z}\cos\theta/2$ and $\bar{x}\sin\theta/2$ are 3.87 mm and 0.0019 mm, respectively. If the particle's position is such that $\bar{z}\cos\theta/2$ is the dominant term,

$$\beta(\bar{z}_3) \approx \beta(\bar{z}_4) \tag{42}$$

Suppose that the particle's position is such that $\bar{x}\sin\theta/2$ is larger than $\bar{z}\cos\theta/2$. In that case, the term $(\lambda\bar{x}\sin\theta/2)/(\pi G^2)$ is bounded by

$$\frac{\lambda\bar{x}\sin\theta/2}{\pi G^2} \leqq \frac{(0.6328 \times 10^{-3}\ \text{mm})\ (0.086\ \text{mm})}{\pi(0.031\ \text{mm})^2} \tag{43}$$

$$\leqq .018$$

This term is negligible compared to unity and from Eq. (41),

$$\beta(\bar{z}_3) \approx \beta(\bar{z}_4) \approx 1/G^2 \tag{44}$$

In either event, $\beta(\bar{z}_3) \approx \beta(\bar{z}_4)$ and $\beta(\bar{z})$ will be used to denote both terms in the (x,y,z) system in the following analysis.

With the above approximation of $\beta(\bar{z}_3)$ and $\beta(\bar{z}_4)$ and substitution from Eq. (38), the expression for $I_{sr} + I_{sr}^*$ from Eq. (40) reduces to

$$I_{sr} + I_{sr}^* = \frac{4C_2C_3\epsilon\sigma^2}{\pi/\beta(\bar{z})} e^{-\beta(\bar{z})[\bar{z}^2\sin^2\theta/2 - \overline{zx}\sin\theta + \bar{x}^2\cos^2\theta/2 + \bar{y}^2]} \tag{45}$$

$$\cdot e^{-\beta(\bar{z})[\bar{z}^2\sin^2\theta/2 + \overline{zx}\sin\theta + \bar{x}^2\cos^2\theta/2 + \bar{y}^2]}$$

$$\cdot \cos(2k\bar{x}\sin\theta/2)$$

$$= \frac{4C_2C_3\epsilon\sigma^2}{\pi/\beta(\bar{z})} e^{-2\beta(\bar{z})[\bar{z}^2\sin^2\theta/2 + \bar{x}^2\cos^2\theta/2 + \bar{y}^2]} \cos(2k\bar{x}\sin\theta/2)$$

Substituting the velocity terms for $(\bar{x},\bar{y},\bar{z})$, the above expression reduces to

$$I_{sr} + I_{sr}^* = \frac{4C_2C_3\epsilon\sigma^2}{\pi/\beta(z_o + v_z t)} e^{-2\beta(z_o + v_z t)[(z_o + v_z t)^2 \sin^2\theta/2} \tag{46}$$

$$+ (y_o + v_y t) + (x_o + v_x t)^2 \cos^2\theta/2] \cos[2k(x_o +$$

$$+ v_x t)\sin\theta/2]$$

To further simplify the envelope of Eq. (45), assume that the particle passes through the origin of the coordinate system at t = 0 so that

$$x_o = y_o = z_o = 0 \tag{47}$$

Let the x-direction be the direction of the free stream velocity so that in most cases v_x is the largest velocity component, i.e.,

$$v_x \gg v_y \tag{48}$$

$$v_x \gg v_z$$

Also assume that the transverse velocity components v_y and v_z are of equal orders of magnitude. For most LDV systems, θ is only a few degrees so that

$$\sin^2\theta/2 \ll \cos^2\theta/2 \tag{49}$$

With these approximations

$$(v_z t)^2 \sin^2\theta/2 \ll (v_x t)^2 \cos^2\theta/2 \tag{50}$$

and

$$(v_y t)^2 \ll (v_x t)^2 \cos^2\theta/2$$

The factor $\beta(\bar{z})$, given by

$$\beta(\bar{z}) = [G^2(1 + (\lambda/\pi G^2)(\bar{z}\cos\theta/2 + \bar{x}\sin\theta/2))]^{-1}$$

The maximum value of the term $\lambda\bar{x}(\sin\theta/2)/\pi G^2$ with the parameters used in the experimental work is 0.331×10^{-3} and the maximum value of $\lambda\bar{z}\cos\theta/2/\pi G^2$ using those same parameters is 0.341. If both these terms are neglected relative to unity, $\beta(\bar{z})$ becomes

$$\beta(\bar{z}) \approx 1/G^2 \tag{51}$$

With the above approximations and setting $\cos^2\theta/2 \approx 1$, Eq. (46) becomes

$$I_{sr} + I_{sr}^{*} = \frac{4C_2C_3\epsilon\sigma^2}{\pi G^2} e^{-(2/G^2)(v_x t)^2} \cos[2kv_x t \sin(\theta/2)] \qquad (52)$$

Using the definition

$$f_D = \frac{2k(\sin\theta/2)\, v_x}{2\pi} \qquad (53)$$

$$= \frac{2v_x \sin\theta/2}{\lambda}$$

the above expression can be put into the form

$$I_{sr} + I_{sr}^{*} = \frac{4C_2C_3\epsilon\sigma^2}{G^2\pi} e^{-\alpha(2\pi f_D t)^2} \cos 2\pi f_D t \qquad (54)$$

where $\alpha = [2k^2G^2 \sin^2\theta/2]^{-1}$.

The approximations made to arrive at the expression for $I_{sr} + I_{sr}^{*}$ given by Eq. (54) are valid under most wind tunnel tests. It should be noted that the argument of the cosine factor is the portion of the signal which most estimation techniques use in estimating v_x. The approximations used to obtain the argument of the cosine factor, namely the approximations made about $\gamma(\bar{z}_3)$, $\gamma(\bar{z}_4)$, $\delta(\bar{z}_3)$, and $\delta(\bar{z}_4)$ are valid under any conceivable wind tunnel tests. The approximations made regarding the envelope of $I_{sr} + I_{sr}^{*}$ are also valid under a wide variety of conditions but are admittedly weaker approximations than those made regarding the argument of the cosine factor. The purpose of the approximations regarding the envelope is to give a more intuitive feeling about the shape of the envelope. No estimation procedure presented in this thesis makes use of

the dependence of the envelope on v_x to estimate the x-component of velocity.

Now that a simplified form (given by Eq. (54)) for $I_{sr} + I_{sr}^*$ has been derived, a few conclusions are drawn from it. Note that the width of the envelope is dependent on f_D^2. As the Doppler shift increases, the envelope becomes more narrow. In fact, the number of cycles under the envelope is independent of f_D. The number of cycles of the signal being independent of f_D implies that, as the Doppler shift of the signal increases, the bandwidth of the signal becomes wider. Hence, one would expect that it would be more difficult to estimate the frequency of the signal for higher Doppler shifts than for lower Doppler shifts. Also, since the number of cycles is independent of f_D, the energy of the signal decreases as f_D increases. For this reason, one might expect noise to become more of a problem at higher frequencies than at lower frequencies.

The total expression for the PMT current becomes, from Eqs. (23), (24), (25), and (54)

$$i_D(t) = K_D C_3^2 + \frac{2K_D \varepsilon^2 \sigma^2 C_2^2}{G^2 \pi} e^{-\alpha(2\pi f_D t)^2} + \frac{4K_D C_2 C_3 \varepsilon \sigma^2}{G^2 \pi} e^{-\alpha(2\pi f_D t)^2} \cos 2\pi f_D t \tag{55}$$

where approximations have been made to I_s which are similar to those made to the envelope of $I_{sr} + I_{sr}^*$. The second term has the same shape of the envelope of the cosine term. The term I_s already has been shown in Eq. (30) to be negligible compared to C_3^2. Comparing the magnitude of I_s to

$I_{sr} + I_{sr}^*$, one obtains

$$\frac{I_s}{I_{sr} + I_{sr}^*} = \frac{\dfrac{2\epsilon^2\sigma^2 C_2^2}{G^2\pi}}{\dfrac{4C_2C_3\epsilon\sigma^2}{G^2\pi}} = \frac{\epsilon C_2}{C_3} \tag{56}$$

Recalling that $C_2^2 \approx 20C_3^2$ and $\epsilon \approx \frac{1}{\sqrt{770}}$, the above ratio becomes

$$\frac{I_s}{I_{sr} + I_{sr}^*} = \frac{\sqrt{20}}{\sqrt{770}} \tag{57}$$

$$= 0.161$$

The term I_s is low-pass and negligible compared to the dc term I_r and the band-pass term $I_{sr} + I_{sr}^*$. Therefore I_s is henceforth neglected. The final expression for the LDV signal is now given by

$$i_D(t) = K_D C_3^2 + \frac{4K_D C_2 C_3 \epsilon\sigma^2}{G^2\pi} e^{-\alpha(2\pi f_D t)} \cos 2\pi f_D t \tag{58}$$

It should be noted that the coefficient of the cosine term is proportional to the product of the relatively large amplitude of the reference beam and the relatively small amplitude scattered light which follow from Eqs. (13), (15), (20), and (44) as $C_3/\sqrt{\pi G^2/2}$ and $\epsilon C_2/\sqrt{\pi G^2/2}$, respectively. The multiplication of a small signal beam by a large reference beam is known as "optical heterodyne detection"[20] and serves to amplify the cosine signal. The amplification is referred to as "conversion gain."[20] The LDV system therefore makes use of optical heterodyne detec-

tion. It will be seen that it is this feature which distinguishes the LDV system from the LIV system which uses direct detection.

Simplified Analysis of Signals from an LIV System

A schematic of an LIV system is shown in Figure 8.[3] As pointed out in Chapter I, a beam from a cw laser enters a glass plate with parallel sides. Part of the first side is coated as a beam splitter so that two equal intensity beams are formed. One beam reflects from the beam splitter and the other beam passes through the glass and totally reflects off the fully silvered rear surface of the plate. The totally reflected beam passes back through the glass plate and leaves the plate through a portion of the front surface which is anti-reflection coated. The net result is two parallel beams which are equal in intensity.[4] If the difference in optical path length of the two beams caused by the glass plate is not much less than the coherence length of the laser, a second glass plate can be inserted to equalize the path lengths.[5]

The two beams, separated by a distance 2d, are brought to focus inside of the test section by lens L1. The beams, $u_1(x,y,z)$ and $w_1(x,y,z)$ can be described in the focal region of L1 by

$$u_1(x,y,z) = A(x,y,z)\ e^{jk(\sin\theta/2)x} \tag{59}$$

and

$$w_1(x,y,z) = A(x,y,z)\ e^{-jk(\sin\theta/2)x}$$

where θ is the angle between the two beams and $\sin(\theta/2) = d/F$. The intensity $I_I(x,y,z)$ of the interference pattern of the beams is given by

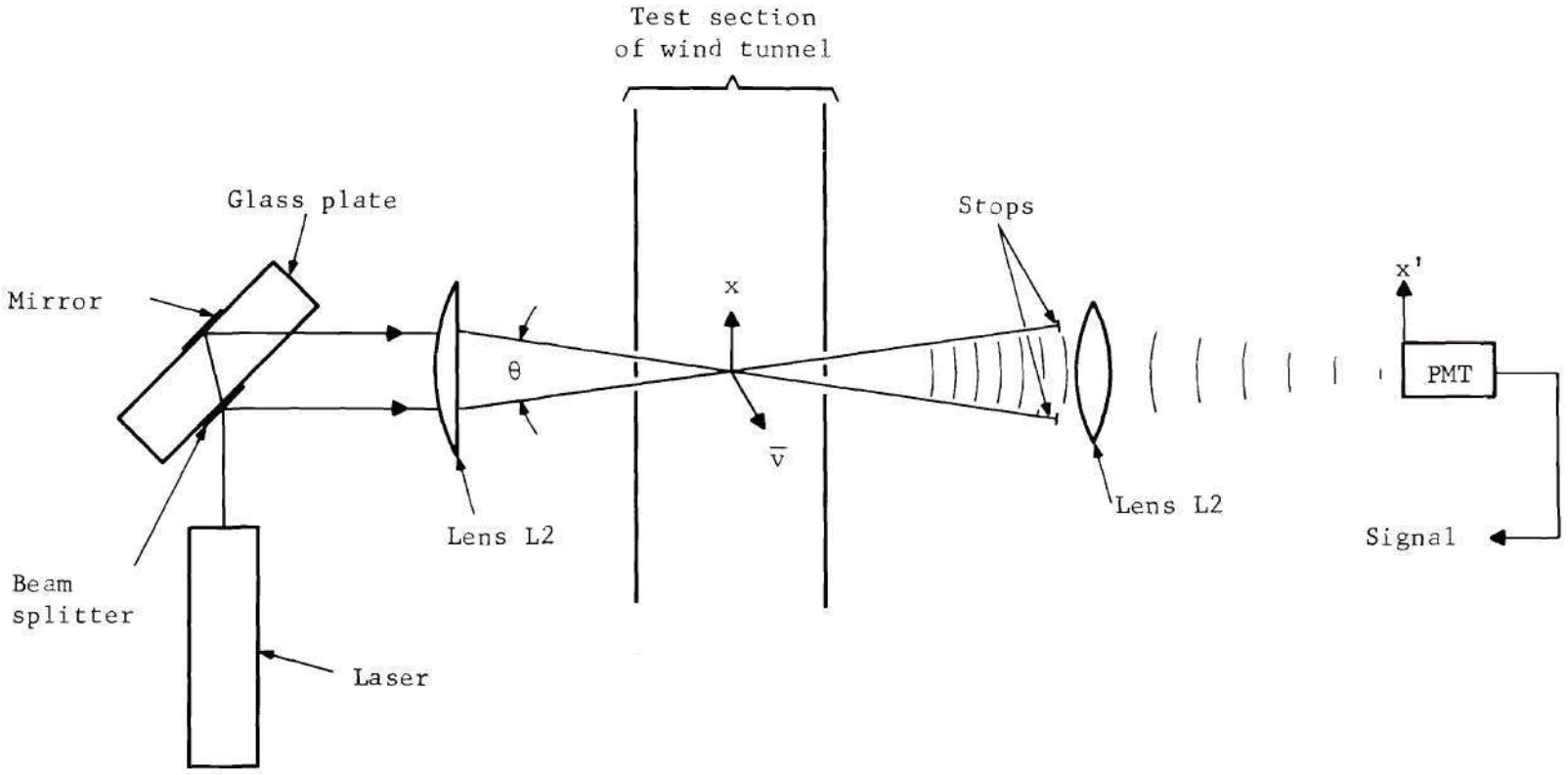

Figure 8. Schematic of a LIV System

$$I_I(x,y,z) = |u_1(x,y,z) + w_1(x,y,z)|^2 \tag{60}$$

$$= 2A^2(x,y,z)\ [1 + \cos\ 2k(\sin\theta/2)x]$$

As is evident from Eq. (57), a sinusoidal interference pattern is formed in the focal region of L1. The focal region where the sinusoidal pattern is formed is called the detection volume of the LIV system.

As a particle passes through the detection volume, it scatters light in all directions. Lens L2 is placed so that it images with unity magnification the light scattered by a particle to the PMT. The PMT is so placed that it is in the image plane of the detection volume. Generally, the imaging is one-to-one as was the case with LDV systems. An aperture is placed in the plane of the PMT which is the same size as the imaged detection volume. The aperture serves to keep out stray light.

Note that the PMT images only light scattered by the particles. The lens is deliberately placed so that it does not image the two scattering beams. In Figure 8, the two scattering beams completely miss L2. Since the signal is contained solely in the scattered light, the image of the unscattered light on the PMT would serve no useful purpose and would produce unwanted photon fluctuation noise. This situation is in contrast to the LDV system where the reference beam is imaged on the PMT. Light scattered by particles passing outside of the detection volume also falls on the PMT surface. Since the light is most intense in the detection volume, the light scattered by particles outside the volume is much lower in intensity than light from particles inside the volume. Also, light from particles outside the volume is out of focus on the PMT surface since

the surface is in the image plane of the volume. In addition, the aperture on the PMT surface would likely block out most of the light from particles outside of the volume. Whatever light reaches the PMT from outside of the detection volume would likely be low pass in nature since the contrast of the interference pattern decreases rapidly as one moves away from the volume.

The time variation of the intensity of the light striking the PMT is proportional to the intensity of the field through which the particle passes. A particle, passing through the detection volume with velocity $\bar{v} = (v_x, v_y, v_z)$ and position given by $(x_o + v_x t,\ y_o + v_y t,\ z_o + v_z t)$, scatters light to the PMT whose intensity I_I follows from Eq. (60) and is proportional to

$$I_I = K2A^2(\bar{x},\bar{y},\bar{z})[1 + \cos(2k \sin\theta/2)\bar{x}t)]] \tag{61}$$

where

$$\bar{x} = x_o + v_x t$$

$$\bar{y} = y_o + v_y t$$

$$\bar{z} = z_o + v_z t$$

The resulting PMT current $i_I(t)$ is the integral of the intensity over the PMT surface and is given by

$$i_I(t) = i_s(t) + i_s(t) \cos 2\pi f_o t \tag{62}$$

where $f_o = 2(\sin\theta/2)v_x/\lambda$. The x-component of velocity is

$$v_x = \lambda f_o / 2\sin\theta/2 \tag{63}$$

Comparing Eq. (7) describing the LDV signal with Eq. (62) describing the LIV signal, one notes that the LDV signal consists of large dc bias and a small ac ripple. The LIV signal consists of a low pass signal and a band pass signal both equal in amplitude.

LIV Systems with Beams of a Gaussian Spatial Intensity Distribution

The analysis of LIV systems with a Gaussian laser beam parallels the analysis of the LDV systems with a Gaussian beam. The LIV discussion is considerably shorter since many analogous results can be directly lifted from the LDV analysis. As in the LDV discussion, let the beam leaving the laser be described by

$$u_o(x_1,y_1) = \frac{C_1 \, e^{-D(x_1^2 + y_1^2)}}{\sqrt{\pi/2D}} \tag{64}$$

where C_1 and D are constants and the coordinate systems are defined in Figure 9. The two beams leaving the glass plate are equal in intensity, separated by a distance 2d and described by

$$u_1(x_2-d,y_2) = \frac{C_4 \, e^{-D[(x_2-d)^2 + y_2^2]}}{\sqrt{\pi/2D}} \tag{65}$$

and

$$w_1(x_2+d,y_2) = \frac{C_4 \, e^{-D[(x_2+d)^2 + y_2^2]}}{\sqrt{\pi/2D}}$$

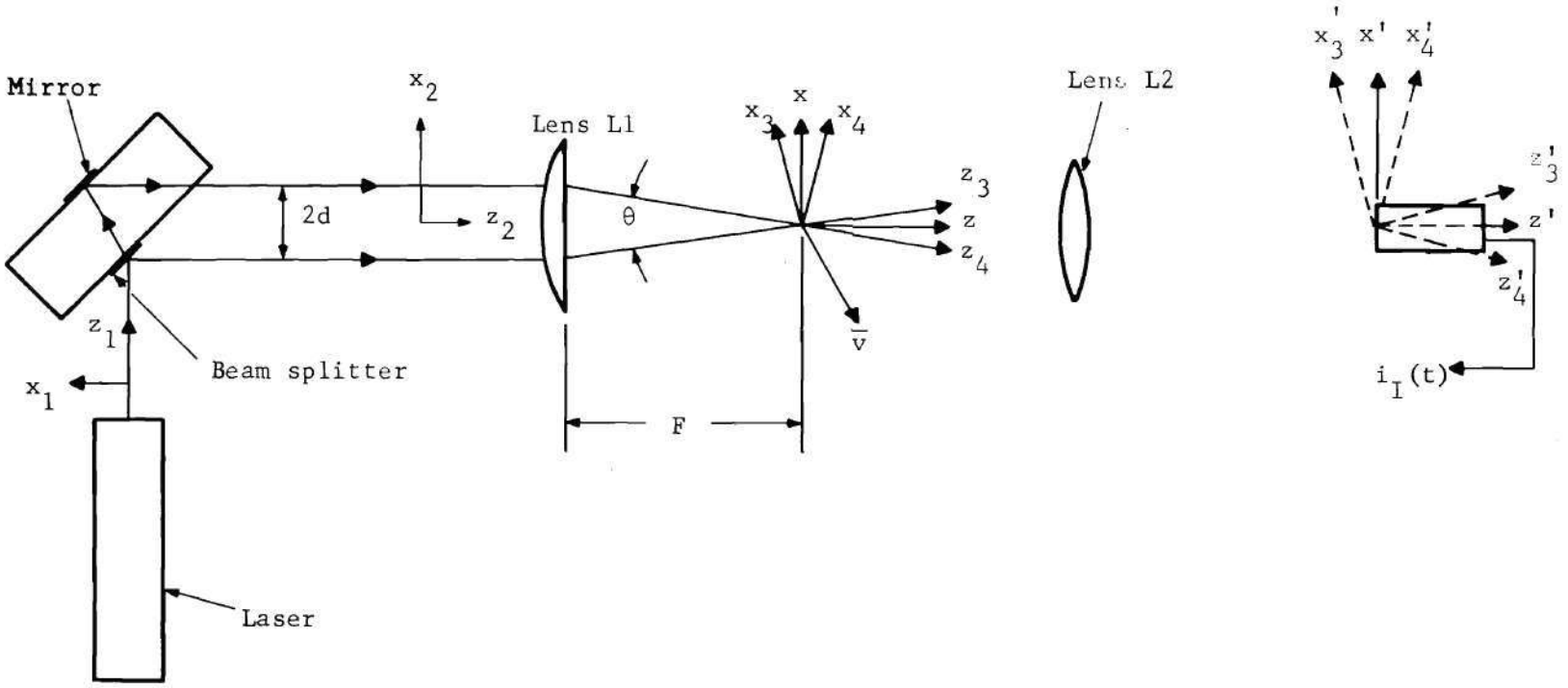

Figure 9. Schematic Used in the Discussion of the LIV System with a Beam from a TEM_{00} Laser

The two beams pass through lens L1 and are brought to focus in the focal region of L1 forming the detection volume. The expressions for the beams after passing through the lens are analogous to Eqs. (12) and (14) and are given, respectively, by

$$u_2(x_3,y_3,z_3) = \frac{C_4\, e^{jkz_3}}{\sqrt{\pi/2\beta(z_4)}}\, e^{-\beta(z_3)(x_3^2 + y_3^2)} \cdot e^{j(\gamma(z_3)/2)(x_3^2 + y_3^2)}\, e^{-j\delta(z_3)} \tag{66}$$

$$w_2(x_4,y_4,z_4) = \frac{C_4\, e^{jkz_4}}{\sqrt{\pi/2\beta(z_4)}}\, e^{-\beta(z_4)(x_4^2 + y_4^2)} e^{j(\gamma(z_4)/2)(x_4^2 + y_4^2)}\, e^{-j\delta(z_4)}$$

The intensity I_{I1} of the light in the detection volume is given by

$$\begin{aligned} I_{I1} &= |u_2(x_3,y_3,z_3) + w_2(x_4,y_4,z_4)|^2 \\ &= |u_2(x_3,y_3,z_3)|^2 + |w_2(x_4,y_4,z_4)|^2 \\ &\quad + u_2(x_3,y_3,z_3)\, w_2^*(x_4,y_4,z_4) + u_2^*(x_3,y_3,z_3) \\ &\quad w_2(x_4,y_4,z_4) \end{aligned} \tag{67}$$

Consider a particle moving through the detection volume with velocity $\bar{v} = (v_{x_3},v_{y_3},v_{z_3})$ in the (x_3,y_3,z_3) system and $\bar{v} = (v_{x_4},v_{y_4},v_{z_4})$ in the (x_4,y_4,z_4) system. The position of the particle at time t is given by $(\bar{x}_3,\bar{y}_3,\bar{z}_3)$ where

$$\bar{x}_3 = x_3^{\circ} + v_{x_3} t \tag{68}$$

$$\bar{y}_3 = y_3^{\circ} + v_{y_3} t$$

$$\bar{z}_3 = z_3^{\circ} + v_{z_3} t$$

Similarly, the position of the particle in the (x_4,y_4,z_4) system is $(\bar{x}_4,\bar{y}_4,\bar{z}_4)$. The intensity I_{13} of the field through which the particle is passing follows from Eq. (67) as

$$I_{I3} = |u_2(\bar{x}_3,\bar{y}_3,\bar{z}_3)|^2 + |w_2(\bar{x}_4,\bar{y}_4,\bar{z}_4)|^2 \tag{69}$$
$$+ u_2^*(\bar{x}_3,\bar{y}_3,\bar{z}_3)\, w_2(\bar{x}_4,\bar{y}_4,\bar{z}_4)$$
$$+ u_2(\bar{x}_3,\bar{y}_3,\bar{z}_3)\, w_2^*(\bar{x}_4,\bar{y}_4,\bar{z}_4)$$

The particle scatters part of the light to lens L2 which images the particle to the PMT. The intensity I_{I3} of the image in front of the PMT is given by

$$I_{I3} = \epsilon^2[\,|u_2(\bar{x}_3,\bar{y}_3,\bar{z}_3)|^2 + |w_2(\bar{x}_4,\bar{y}_4,\bar{z}_4)|^2 \tag{70}$$
$$+ u_2^*(\bar{x}_3,\bar{y}_3,\bar{z}_3)\, w_2(\bar{x}_4,\bar{y}_4,\bar{z}_4)$$
$$+ u_2(\bar{x}_3,\bar{y}_3,\bar{z}_4)\, w_2^*(\bar{x}_4,\bar{y}_4,\bar{z}_4)]\,\mathrm{circ}[2r(x',y')/d]$$

where

$$r(x',y') = \sqrt{(x'-\bar{x})^2 + (y-\bar{y})^2}$$

and

$$\text{circ}[2r(x',y')/d] = 1 \qquad r(x',y') \leqq d/2$$

$$= 0 \text{ elsewhere}$$

The PMT current $i_I(t)$ is given by

$$I_I(t) = K_I \int_S\int I_{I3}\, dx'dy' \tag{71}$$

and K_I is a constant which accounts for the quantum efficiency and gain of the PMT, and S is the surface of the PMT. Substituting Eq. (70) into Eq. (71) and evaluating, $i_I(t)$ becomes

$$\begin{aligned} i_I(t) = K_I\, \epsilon^2\sigma^2[\, &|u_2(\bar{x}_3,\bar{y}_3,\bar{z}_3)|^2 + |w_2(\bar{x}_4,\bar{y}_4,\bar{z}_4)|^2 \\ &+ u_2(\bar{x}_3,\bar{y}_3,\bar{z}_3)\; w_2^*(\bar{x}_4,\bar{y}_4,\bar{z}_4) \\ &+ u_2^*(\bar{x}_4,\bar{y}_4,\bar{z}_4)\; w_2(\bar{x}_4,\bar{y}_4,\bar{z}_4)\,] \\ = K_I[I_u &+ I_w + I_{uw} + I^*_{uw}] \end{aligned} \tag{72}$$

The various terms of Eq. (72) are evaluated in a manner similar to the evaluation of the terms in the expression for $i_D(t)$ given by Eq. (23). From Eqs. (66) and (72) the expressions for I_u and I_w are

$$I_u = \frac{\epsilon^2\sigma^2 C_4^2\, e^{-2\beta(\bar{z}_3)(\bar{x}_3^2 + \bar{y}_3^2)}}{\pi/2\beta(\bar{z}_3)} \tag{73}$$

and

$$I_w = \frac{\epsilon^2\sigma^2 C_4^2\, e^{-2\beta(\bar{z}_4)(\bar{x}_4^2 + \bar{y}_4^2)}}{\pi/2\beta(\bar{z}_4)}$$

From Eqs. (66) and (72), I_{uw} is written as

$$I_{uw} = \frac{2C_4^2 \epsilon^2 \sigma^2}{\pi / \beta(\bar{z}_4)\beta(\bar{z}_3)} e^{-\beta(\bar{z}_3)[\bar{x}_3^2 + \bar{y}_3^2]} e^{jk\bar{z}_3} \cdot e^{-\beta(\bar{z}_4)(\bar{x}_4^2 + \bar{y}_4^2)} e^{-jk\bar{z}_4} \tag{74}$$

recalling from the section on LDV systems that the γ and δ phase terms can be neglected relative to the linear phase terms $k\bar{z}_3$ and $k\bar{z}_4$. Adding I_{uw} to its complex conjugate and rotating the phase of the two terms into the (x,y,z) system, $I_{uw} + I_{uw}^*$ becomes

$$I_{uw} + I_{uw}^* = \frac{4C_4^2 \epsilon^2 \sigma^2}{\pi \beta(\bar{z}_4)\beta(\bar{z}_3)} e^{-\beta(\bar{z}_3)(\bar{x}_3^2 + \bar{y}_3^2)} \cdot e^{-\beta(\bar{z}_4)(\bar{x}_4^2 + \bar{y}_4^2)} \cos k[2\bar{x} \sin\theta/2] \tag{75}$$

The expression for $i_I(t)$ given by Eq. (72) consists of the low-pass terms $I_u + I_w$ of Eq. (73) and the band-pass term $I_{uw} + I_{uw}^*$ of Eq. (75). The only approximations made up to this point involve the phase terms γ and δ and these approximations are shown in the LDV discussion to be very good approximations. Substituting for $\bar{x}$, the cosine factor of the band pass term of Eq. (75) becomes

$$\cos k[2(x_o + v_x t) \sin\theta/2]$$

The frequency f_o of this factor, given by

$$f_o = \frac{2k(\sin\theta/2)\ v_x}{2\pi} \tag{76}$$

is the same as the frequency f_D of the band-pass term of the LDV system given by Eq. (53). The x-component of velocity follows as

$$v_x = \frac{f_o 2\pi}{2k(\sin\theta/2)} = \frac{\lambda f_o}{2\sin\theta/2} \tag{77}$$

The envelope of the LIV signal, like the LDV signal, is a complicated function of all three velocity components. However, the frequency of the band-pass portion is a relatively simple function of the component v_x. All of the estimation procedures described in this thesis estimate v_x by estimating the frequency of the band-pass term.

In order to obtain simplified expressions for the low-pass terms and the envelope of the band-pass terms, the same approximations regarding the detection volume and the particle velocities made in Eqs. (41) through (54) of the LDV discussion are made in this discussion. It is shown in Eq. (44) that

$$\beta(\bar{z}_3) \approx \beta(\bar{z}_4) \approx \beta(\bar{z}) \tag{78}$$

Substituting $\beta(\bar{z})$ for $\beta(\bar{z}_3)$ and $\beta(\bar{z}_4)$ in Eq. (75) and rotating the remainder of the expression into the (x,y,z) system I_u and I_w becomes

$$I_u = \frac{\epsilon^2\sigma^2 C_4^2}{\pi/2\beta(\bar{z})}\, e^{-2\beta(\bar{z})[\bar{z}^2\sin^2\theta/2 - \overline{zx}\,\sin\theta + \bar{x}^2\cos^2\theta + \bar{y}^2]} \tag{79}$$

and

$$I_w = \frac{\varepsilon^2\sigma^2 C_4^2}{\pi/2\beta(\bar{z})} e^{-2\beta(\bar{z})[\bar{z}^2\sin^2\theta/2 + \overline{xz}\sin\theta + \bar{x}^2\cos^2\theta + \bar{y}^2]}$$

If the velocity terms

$$\bar{x} = x_o + v_x t \tag{80}$$

$$\bar{y} = y_o + v_y t$$

$$\bar{z} = z_o + v_z t$$

as substituted into Eq. (79) and the velocity approximations of Eqs. (47) through (51) are made, it follows that

$$I_u \approx I_w \approx \frac{2\varepsilon^2\sigma^2 C_4^2}{\pi G^2} e^{-(2/G^2)(v_x t)^2} \tag{81}$$

The dependence of the envelope of the term $I_{uw} + I_{uw}^*$ on $(\bar{x}_3, \bar{y}_3, \bar{z}_3)$ and $(\bar{x}_4, \bar{y}_4, \bar{z}_4)$ of Eq. (75) is identical to the dependence of the envelope of $I_{sr} + I_{sr}^*$ of Eq. (40) on those same coordinates. If the same approximations made on the envelope of $I_{uw} + I_{uw}^*$ are made on the envelope of $I_{sr} + I_{sr}^*$, it immediately follows from Eqs. (75) and (52) that

$$I_{uw} + I_{uw}^* \approx \frac{4C_4^2\varepsilon^2\sigma^2}{\pi G^2} e^{-(2/G^2)(v_x t)^2} \cos(2k[\sin\theta/2]\, v_x t) \tag{82}$$

Combining Eqs. (81) and (82) and substituting into (72), the PMT current becomes

$$i_I(t) = \frac{4K_I C_4^2\varepsilon^2\sigma^2}{\pi G^2} e^{-(2/G^2)(v_x t)^2} (1 + \cos[2k(\sin\theta/2)\, v_x t]) \tag{83}$$

Defining the following quantities in analogy with Eqs. (53) and (54), $i_I(t)$ becomes

$$i_I(t) = \frac{4K_I C_4^2 \varepsilon^2 \sigma^2}{\pi G^2} e^{-\alpha(2\pi f_o t)} (1 + \cos 2\pi f_o t) \tag{84}$$

where

$$\alpha = [2k^2 G^2 \sin^2 \theta/2]^{-1}$$

$$f_o = \frac{2k(\sin\theta/2)\, v_x}{2\pi}$$

Comparison of LDV and LIV Signal Models

The LDV and LIV signals, although produced by different mechanisms, are mathematically of similar form. Note that both the LDV signal

$$i_D(t) = K_D C_3^2 + \frac{4K_D C_2 C_3 \varepsilon \sigma^2}{G^2 \pi} e^{-\alpha(2\pi f_D t)^2} \cos 2\pi f_D t \tag{85}$$

and the LIV signal

$$i_I(t) = \frac{K_I 4\varepsilon^2 \sigma^2 C_4^2}{G^2 \pi} e^{-\alpha(2\pi f_o t)^2} (1 + \cos 2\pi f_D t) \tag{86}$$

are band-pass signals with Gaussian envelopes and low-pass components. The band-pass components have the same shape, but the amplitudes are different. The ratio of the amplitudes of the LDV band-pass term to the LIV band-pass term is given by

$$\frac{K_D \left[\frac{4C_2C_3\epsilon\sigma^2}{G^2\pi}\right]}{K_I \left[\frac{4\epsilon^2\sigma^2C_4^2}{G^2\pi}\right]} = \frac{K_D\ C_2C_3}{K_I\ \epsilon C_4^2} \tag{87}$$

Recalling that C_1 is the amplitude of the beam from the laser and using the previous estimates of the parameters used in the experimental work, it follows that

$$C_2 \approx \sqrt{0.95}\ C_1 \qquad \epsilon = \frac{1}{\sqrt{770}} \tag{88}$$

$$C_3 \approx \sqrt{0.05}\ C_1 \qquad \sigma^2 = 0.195 \times 10^{-6}\ \text{mm}^2$$

$$C_4 \approx C_1/\sqrt{2} \qquad G = 0.031\ \text{mm}$$

the ratio becomes

$$\frac{K_D\ C_2C_3}{K_I\ \epsilon C_4^2} = \frac{12.1\ K_D}{K_I} \tag{89}$$

If the PMT gains K_D and K_I are equal, the LDV band-pass signal is many times greater than the LIV signal. The amplitude of the LDV signal is larger because of the multiplication of the weak scattered light by the strong reference beam of the LDV system. The conversion gain phenomenon of optical heterodyne receivers is discussed in the LDV section.

Since there is no conversion gain in the LIV system, the LIV signal is many times weaker than the corresponding LDV as pointed out above.

The type of receiver used in the LIV system where there is no reference beam is referred to as a "direct detection receiver."[20] Hence the basic difference between LDV and LIV systems is that the former uses optical heterodyne detection and the latter uses direct detection. The principal advantage of the LDV system is that the received signals are larger due to conversion gain and hence less sensitive PMT's can be used than required for LIV systems. However, the LDV system has a large dc term, namely $K_D C_3^2$, which produces photon fluctuation noise. The photon fluctuation noise added by this term can make the LDV signal to noise ratio worse than the LIV system since there is no large term in the LIV system to produce this noise. Photon fluctuation noise is discussed in detail in the next chapter.

The discussion up to now has considered only one particle passing through the detection volume. In reality, there will be N particles passing through the detection volume during a time interval T. Also, there will be noise present denoted by n(t). Therefore, the general LDV signal $r_{TD}(t)$ can be expressed as

$$r_{TD}(t) = K_D C_3^2 + \sum_{i=1}^{N} B_i \, e^{-\alpha(2\pi f_D)^2 (t-t_i)^2} \cos 2\pi f_D (t-t_i) + n(t) \qquad (90)$$

where B_i is the amplitude pulse produced by the i^{th} particle defined as

$$B_i = \frac{4K_D C_2 C_3 \epsilon \sigma^2}{G^2 \pi}$$

and t_i is the arrival time of the i^{th} particle into the detection volume. In a similar manner, the LIV signal $r_{TI}(t)$ can be written as

$$r_{TI}(t) = \sum_{i=1}^{N} B_i \, e^{-\alpha(2\pi f_D)^2 (t-t_i)^2} (1 + \cos 2\pi f_D (t-t_i)) + n(t) \qquad (91)$$

where B_i is defined for the LIV signal as

$$B_i = \frac{4K_I \varepsilon^2 \sigma^2 C_4^2}{G^2 \pi}$$

The symbol f_D is used here to denote the frequency in both the LDV and LIV systems.

Experimental Evaluation of LDV and LIV Signal Models

Prototype velocimeter systems were set up and signals generated to experimentally verify the mathematical models. The experimental LDV and LIV systems are described and photographs of oscilloscope traces of typical signals are shown. Properties of the signals which are predicted by the mathematical model are pointed out.

Schematics of the LDV and LIV systems are shown in Figures 10 and 25, respectively. The systems are similar as can be seen from the schematics and one system can readily be converted to the other. In order to properly align an LDV system, it is generally set up as an LIV system first and converted to an LDV system. Therefore, the experimental LIV system is first discussed followed by a discussion of the LDV system.

LIV System Description

Due to the fact that the laser was being used in other experiments, the portion of the system from the laser to lens L1 shown in Figure 10 was in one room and the remainder of the system in the next room. The beam passed from one room to the next through a hole in the wall. The

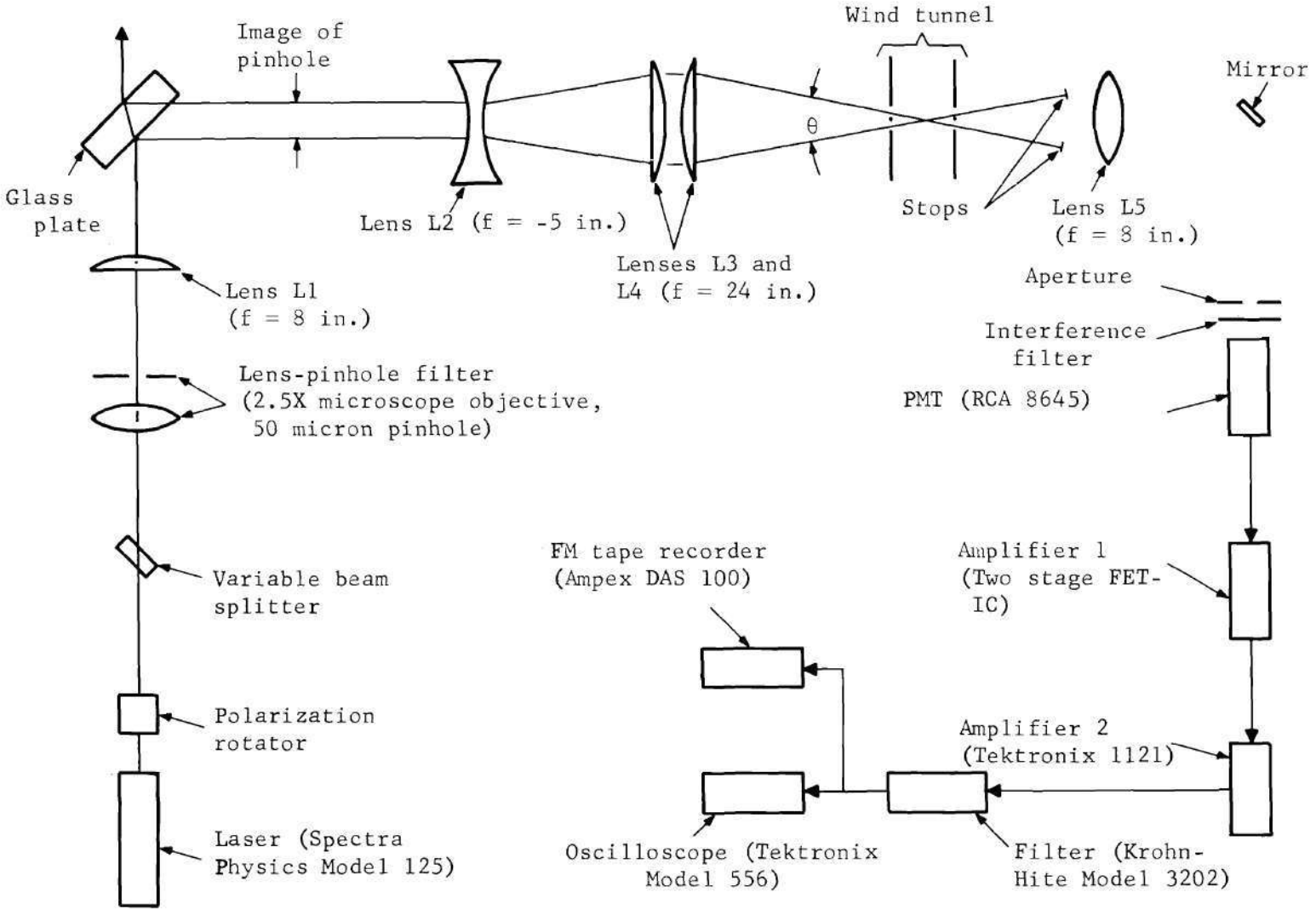

Figure 10. Schematic of the LIV System Used in the Experimental Work

beam from the laser passed initially through a polarization rotator and a variable beam splitter. The polarization rotator was used to rotate the polarization vector so that the fringes in the LIV detection volume had maximum contrast. The variable beam splitter reflected a portion of the laser beam to other experiments and adjusted the intensity of the beam driving the LIV system so that the signal to noise ratio of the system could be varied. The beam was spatially filtered and expanded by the lens pinhole combination following the variable beam splitter. The spatial filter removed imperfections in the shape of the beam and provided a more uniform fringe pattern in the detection volume.

Lens L1 imaged the light in the pinhole to a position between the glass plate and the negative lens L2. The purpose of the glass plate was to create two equally intense and parallel beams. One beam was the reflection from the front surface of the plate and the other beam was the reflection from the rear surface. The two beams were approximately equal in intensity since the beam reflected from the first surface was only a small fraction of the light which passed through the plate. Hence, the beam inside the plate was approximately equal to the beam as it entered the plate. The percentage of the light reflected from the second surface was the same as reflected from the first surface. Since the light beam striking the first surface was approximately equal in intensity to the light striking the second surface, one would expect the two reflected beams to be about equal in intensity. Measurements of the two beams with a photometer indicated that the two beams differed in intensity by about 10 percent. Since the sides of the glass plate were parallel, the two reflected beams were also parallel.

This method is not a very efficient means of generating two parallel beams since most of the light is transmitted through the plate and out of the system. A more efficient means to generate the beams is to make the portion of the front surface of the plate where the beam enters the plate a 50/50 beam splitter and the second surface a totally reflecting mirror. The portion of the front surface, through which the reflected beam from the rear surface exits, is left uncoated. In this way, all of the light goes into the two parallel beams. A plate coated such as this was not available for the thesis.

The image of the pinhole was greatly magnified along the optical axis as well as transverse to the optical axis by lens L1. It is shown in Appendix A that this magnification produces a depth of focus of the pinhole image of about 0.43 meter. The difference in optical path length between the two beams induced by the glass plate was measured to be 0.7 cm. Since the difference in optical path length of the two beams was less than the depth of focus of the pinhole image, the image of the pinhole in both beams was effectively in focus in the same plane transverse to the optical axis.

The two parallel beams passed through lens L2 which was a negative lens whose focal length was three inches. Since the beams entering the lens were parallel, the negative lens diverged the beams and made them appear to be coming from the same point at a distance of one focal length or three inches from the lens. The diverging beams were collimated by lens L3 whose focal length was 24 inches. A lens L4 identical to L3 focused the two beams in the focal plane of L4. The point at which the two beams crossed was the detection volume of the LIV system.

In order for the system to be properly aligned, it was necessary that the detection volume be the image of the pinhole. The detection volume has its smallest dimensions and hence highest spatial resolution when this condition is satisfied. The detection volume is the image of the pinhole if the image of the pinhole created by lens L1 is in the focal plane of lens L2. The two beams appear to intersect in the focal plane of L2 forming a virtual intersection volume. If they also intersect at the point where the pinhole is imaged, all lenses L3 and L4 must do is image the virtual intersection volume to the test section and the detection volume is an image of the pinhole.

Once the LIV system was aligned as described above, the next step was to image with lens L5 and mirror M2 the light scattered by the particles to the PMT. There were several means to do this, but the means selected consisted of placing a ground glass plate in the detection volume. The ground glass plate scattered the light in all directions as particles passing through the detection volume might do. The image of the scattered light was formed with lens L5 on the face of the PMT. In order to filter out light not scattered by the particles, an interference filter preceded by a small aperture the same size as the detection volume image was placed in front of the PMT. When lens L5, mirror M2, and the PMT filters were properly positioned, the ground glass was removed.

The PMT output was amplified and filtered. A preamplifier amplified the PMT signal from a few microamps to the millivolt range. A second amplifier produced a signal whose output was about one volt peak to peak. The output of this amplifier was filtered by a band-pass filter allowing only signals from 200 to 20,000 Hz, the range considered in this thesis,

to pass. The signals were recorded on a seven channel FM recorder for further use.

The Lockheed-Georgia low speed smoke tunnel was used to generate the velocimeter signals. This tunnel is capable of producing flows ranging in velocity from 0.1 to 0.8 ft/sec. Several screens and dampers inside of the tunnel insure that the flow is steady. The tunnel has two 5" x 12" Schlieren quality windows in both sides for the laser beams to pass through. The tunnel is seeded with smoke produced by a heater element and Lionel train smoke solution.

Experiments with the LIV System

Several experiments were conducted with the LIV system described above. First of all, the beam intensity pattern was measured near the laser to make sure that laser was operating in the TEM_{00} mode. The relationship between signal frequency and velocity was determined from the geometry of the system. A densitometer trace of the intensity pattern in the detection volume was made in order to predict the shape of the envelope of the signals. The dimensions of the detection volume were calculated. Oscilloscope traces were made of representative LIV signals and the signal parameters as determined from these traces were compared with the mathematical model.

The mathematical model derived in this chapter assumed the laser to be operating in the TEM_{00} mode which implies that the spatial intensity distribution of the beam is Gaussian. The relative intensity distribution of the laser beam was measured with a Gamma Scientific Model 721 linear photometer. This device in part consists of a 12 mil fiber optical probe mounted on a precision drive. The probe is scanned through the beam

whose intensity is to be measured and the position of the probe can be accurately located by a micrometer. The light passes through the probe to a PMT whose output current is read with an ammeter. The relative intensity as a function of distance across the beam was measured with the photometer and is shown in Figure 11. Note the beam intensity distribution was Gaussian implying that the laser was operating in the TEM_{00} mode.

The frequency f_D of the velocimeter signals is given by Eq. (53) repeated below as

$$f_D = 2v_x(\sin\theta/2)/\lambda \tag{92}$$

Since the two beams entering lens L4 were parallel, the angle θ between them when they left the lens is given by

$$\theta = \tan^{-1} (d/2)/f$$

where d is the distance between the beams and f is the focal length of the lens. The distance d was measured to be 1 1/16 inches and f to be 24 inches with the result that θ was equal to 0.044 radians or 2.54°. With this value of θ and assuming λ is 0.6328 micron, the system sensitivity defined as v_x/f_D was given by

$$v_x/f_D = \lambda/2\sin(\theta/2) \tag{93}$$

$$= \frac{0.0466 \text{ ft/sec}}{\text{kHz}}$$

The relative shape of the intensity distribution of the detection volume was measured in order to determine the expected shape of the velocimeter signal. From Eq. (72), the temporal variation of the velocimeter

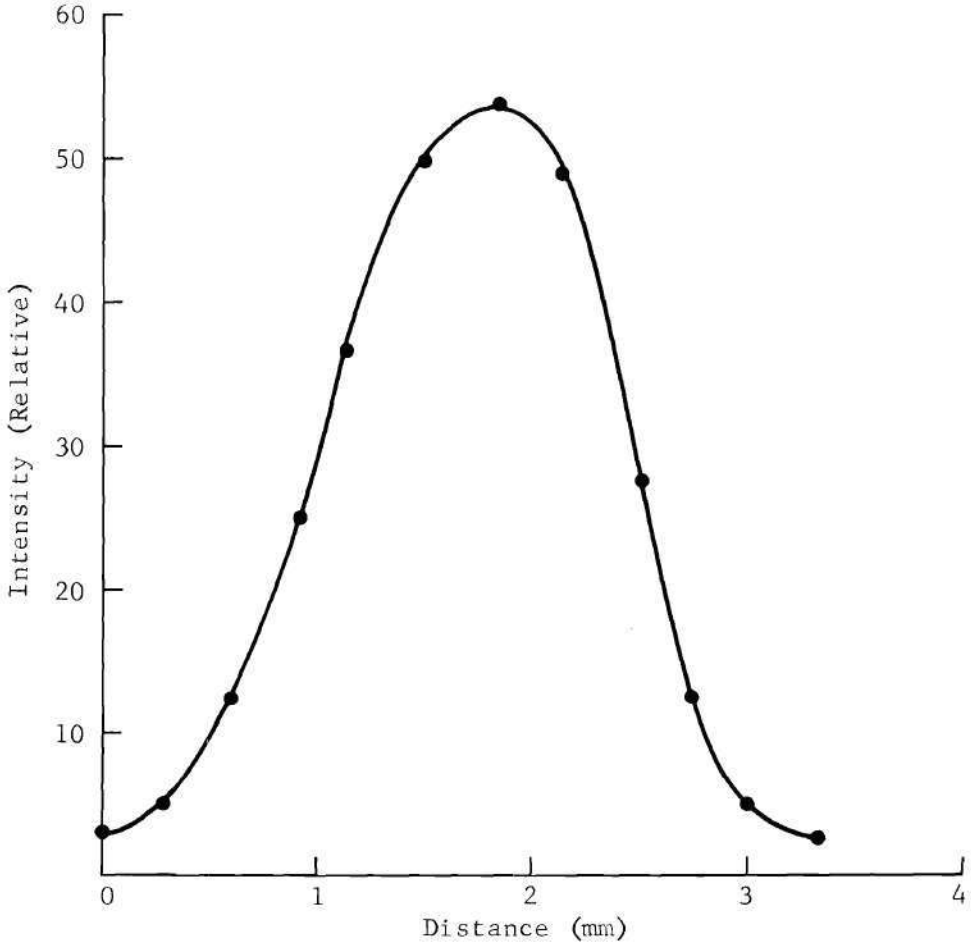

Figure 11. Beam Intensity Pattern of the Laser Used in the Experimental Work

signal is proportional to the spatial variation of the intensity distribution of the detection volume. The detection volume was magnified with a 10X microscope objective and imaged onto a photographic plate producing a photograph of the interference region shown in Figure 12. Note from the photograph that there were approximately 12 interference fringes in the region. A densitometer trace was made from the negative of this photograph and is shown in Figure 13. The intensity variation of the interference region was approximately sinusoidal with a Gaussian envelope which is predicted from the analysis and which is evident from Figure 13.

The dimensions of the detection volume can be estimated by knowing the number of fringes, their period, and the angle θ. The period p of the fringes is calculated in Eq. (18) to be 14.3 microns. Since there were 12 fringes in the volume, the radius r of the volume is approximated

$$\begin{aligned} r &= 6p \\ &= (6)(14.3) \\ &= 85.8 \text{ microns} \end{aligned} \tag{94}$$

The length 1 of the volume can be calculated from the radius as[3]

$$\begin{aligned} 1 &= 2r/\sin(\theta/2) \\ &= 2(85.8)/\sin 1.27^{\circ} \\ &= 7.74 \text{ mm} \end{aligned} \tag{95}$$

Several photographs of representative LIV signals are shown in Figures 14 through 20. The signals were made by running the wind tunnel at speeds from 0.3 to 0.7 ft/sec resulting in signals ranging in frequency about 7 kHz to 15 kHz. Note that most of the signals have about 10-12 cycles

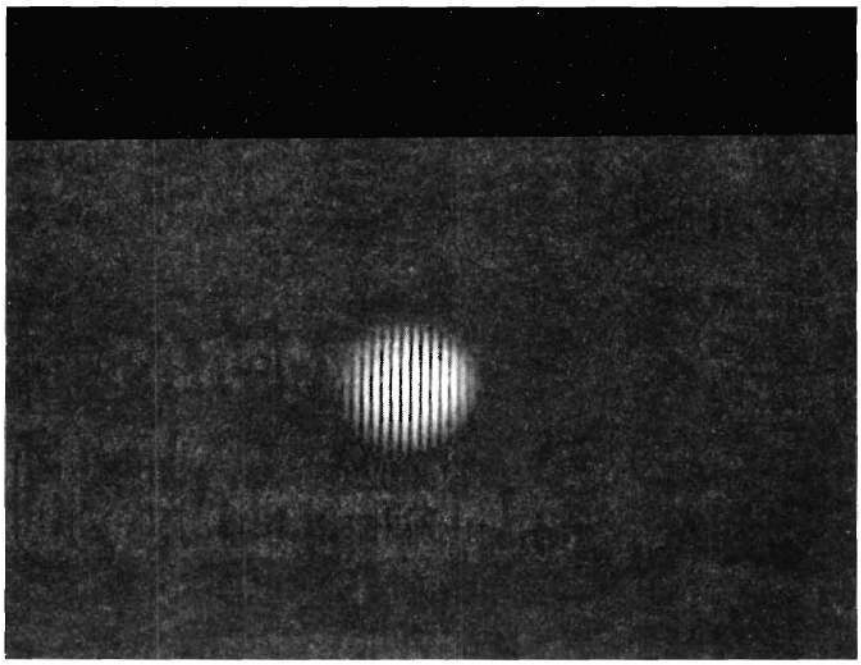

Figure 12. Interference Region of the LIV System

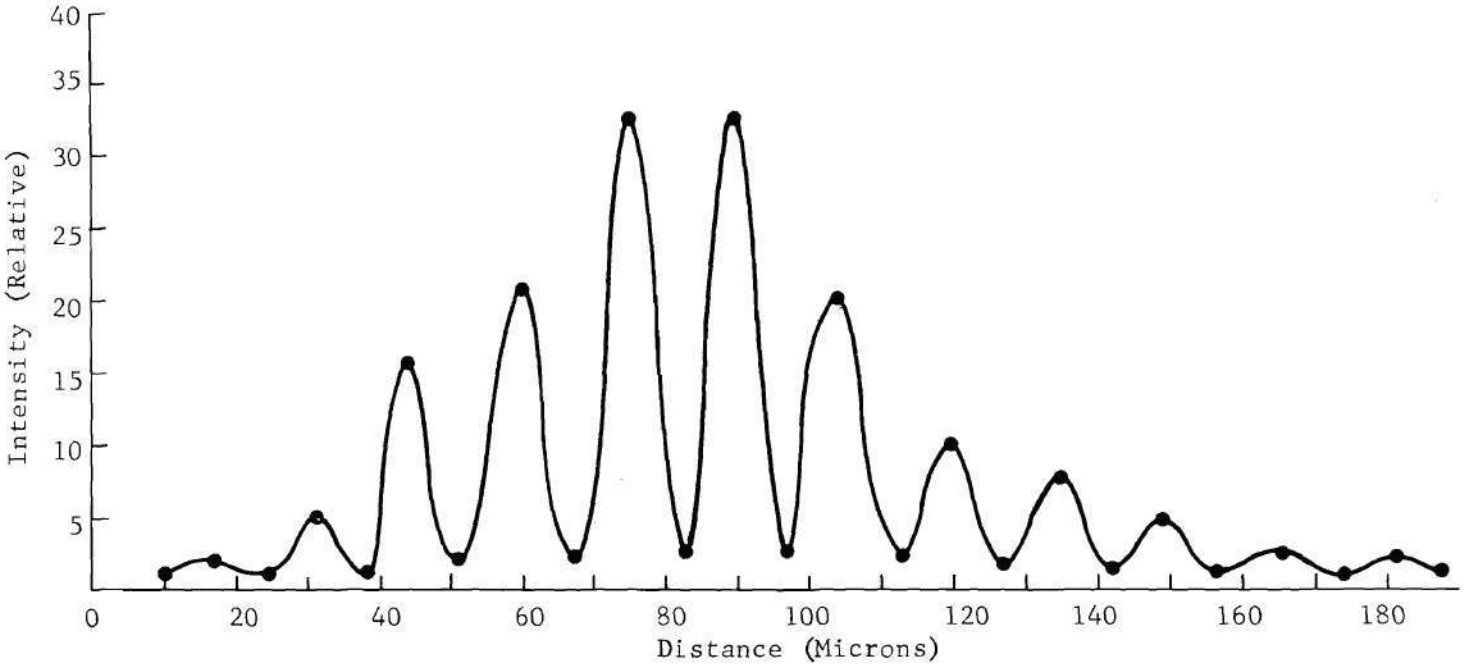

Figure 13. Variation in Intensity of the LIV Interference Region

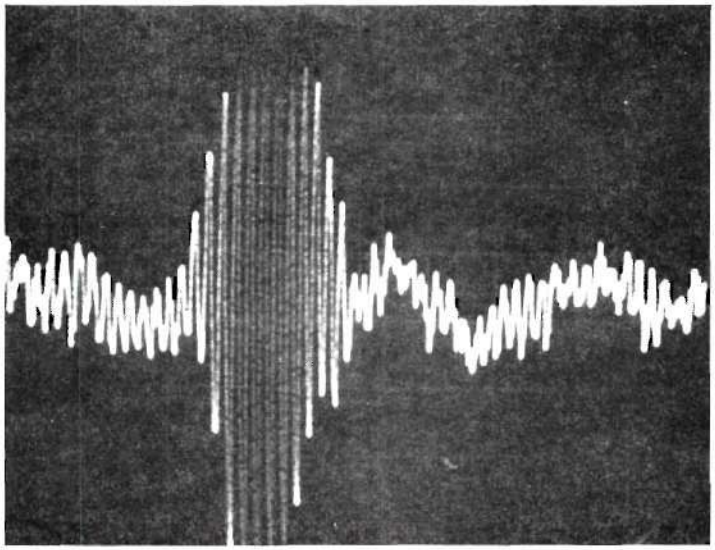

Figure 14. Single LIV Pulse Which Illustrates the Gaussian Envelope of the LIV Signal. (Note that there are 12 cycles under the envelope which is consistent with Figures 12 and 13.)

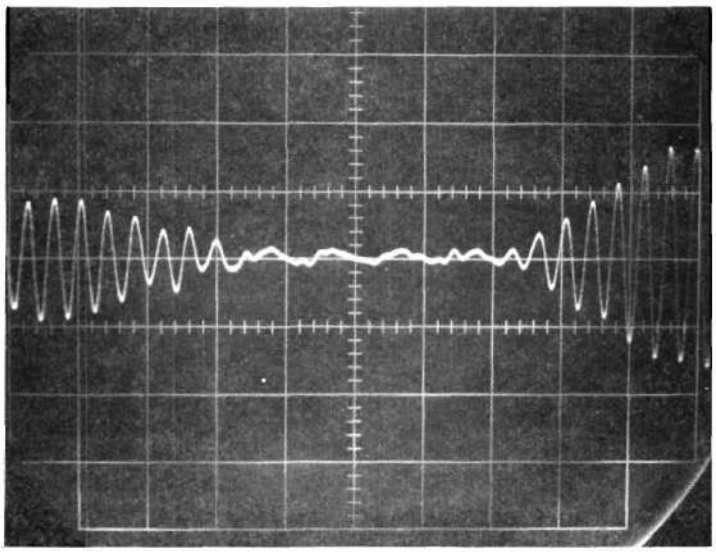

Figure 15. Two Adjacent LIV Pulses of Different Amplitudes Separated in Time Showing the Gaps between Pulses. (As in Figure 14, note the Gaussian envelopes.)

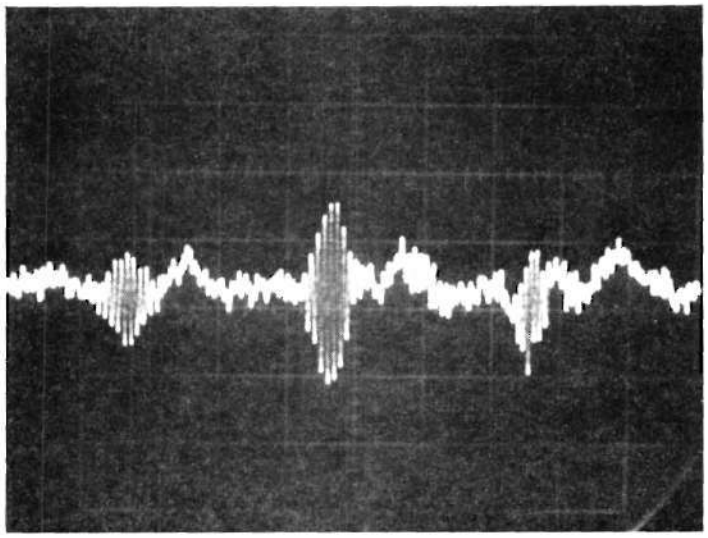

Figure 16. At Least Three LIV Pulses and Possibly More of Lower Amplitudes

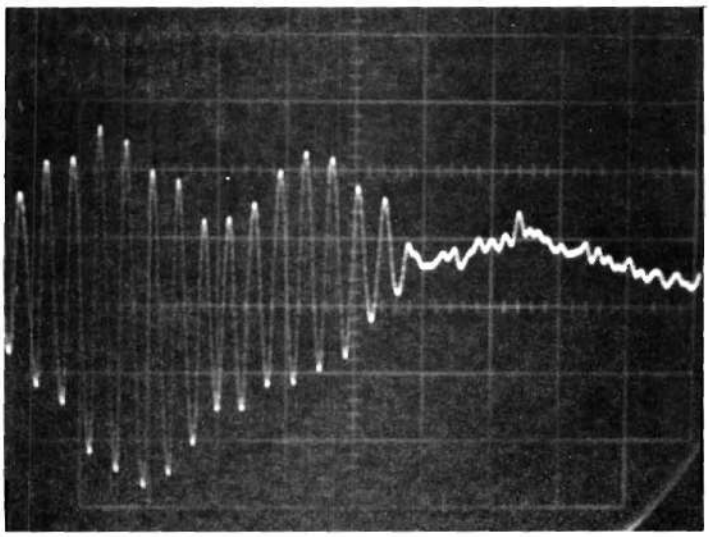

Figure 17. Two Overlapping LIV Pulses

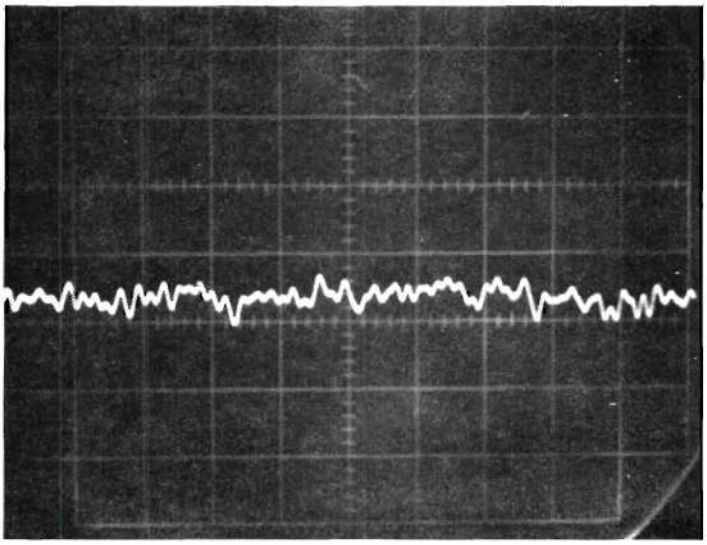

Figure 18. Time Interval During Which No Discernible LIV Was Detected

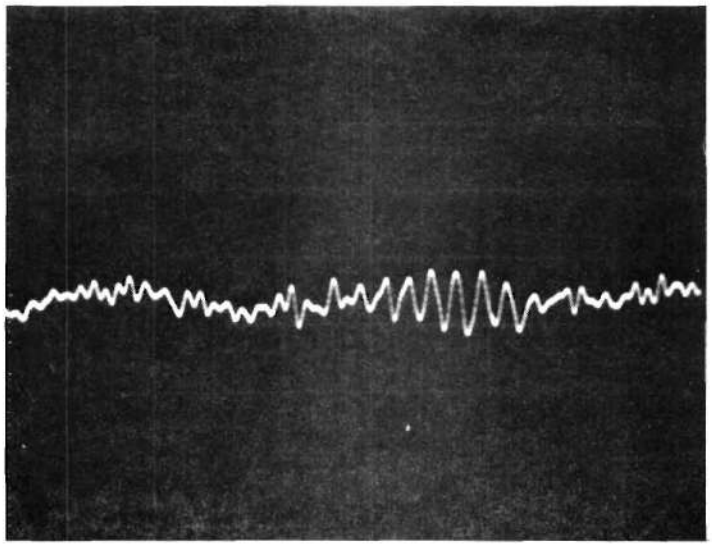

Figure 19. At Least One Low Amplitude LIV Pulse

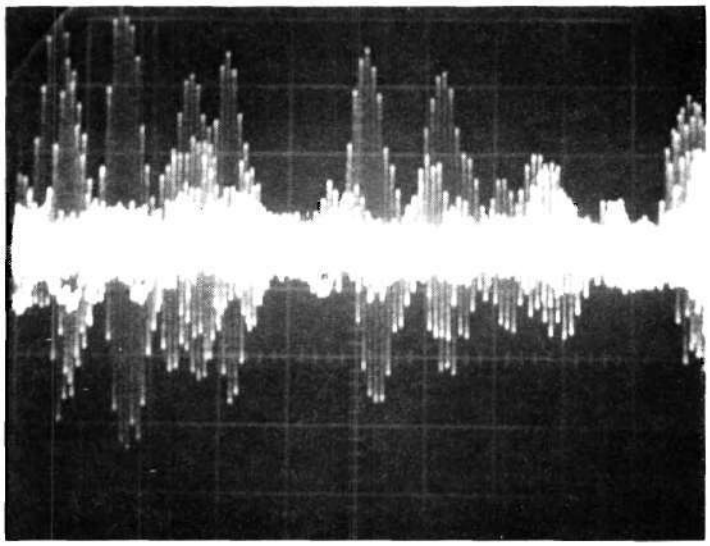

Figure 20. Multiple Sweep Photograph Showing Many LIV Pulses (Note the random amplitudes and arrival times of the pulses.)

per pulse and that the pulses have approximately Gaussian envelopes. The purpose of these figures is to demonstrate that velocimeter signals consist of discrete pulses spaced randomly in time and having Gaussian envelopes. The amplitude of these pulses is random and the number of cycles per pulse is the same as the number of cycles in the intensity distribution of the detection volume shown in Figures 12 and 13.

One of the key features of velocimeter signals is that the number of cycles per pulse is independent of the frequency of the pulse or equivalently the speed of the tunnel. The independence of the number of oscillations and the signal frequency f_o is apparent from Eq. (84) for the LIV signal repeated below as

$$i_I(t) = \frac{K_I \, 4\varepsilon^2\sigma^2 C_4^2}{G^2\pi} \; e^{-\alpha(2\pi f_o t)^2} \; (1 + \cos 2\pi f_o t) \qquad (96)$$

since the argument of the exponential in the envelope is identical to the argument of the cosine factor. This property is illustrated in Figures 21 through 23 which are photographs of velocimeter signals made with the tunnel running at speeds corresponding to frequencies of 5, 10, and 15 kHz. Note that oscillations in each of the pulses are approximately the same even though the signal frequencies are different.

Eq. (90) predicts that the LIV signals have a low pass component due to the Gaussian term. This component is difficult to see in oscilloscope traces of the time domain signals but is quite apparent in the frequency domain. Figure 24 is a photograph of an oscilloscope trace of a spectrum analyser output of 10 kHz LIV signals. The spectrum analyzer was

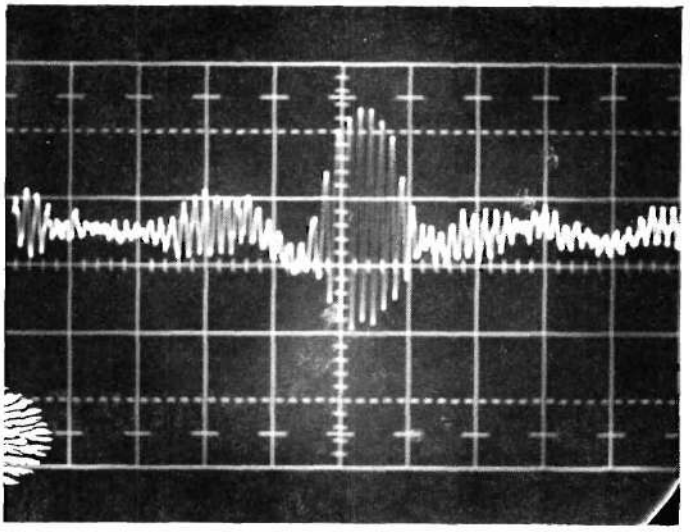

Figure 21. A 5 kHz LIV Pulse with about 11 Cycles

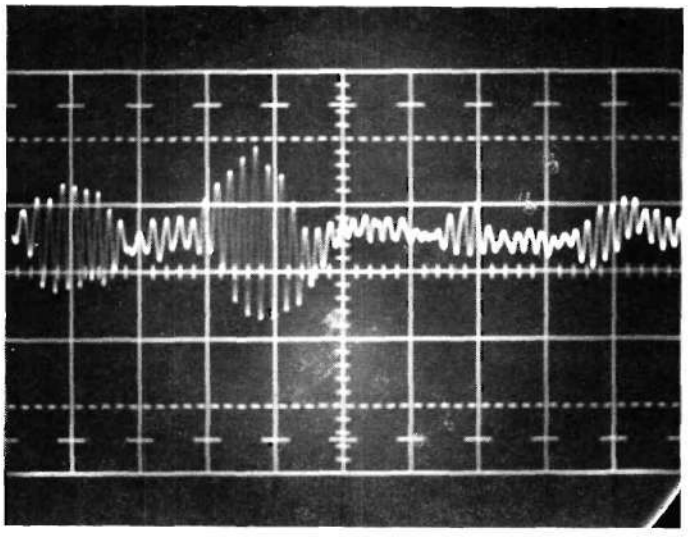

Figure 22. A 10 kHz LIV Pulse with about 12 Cycles

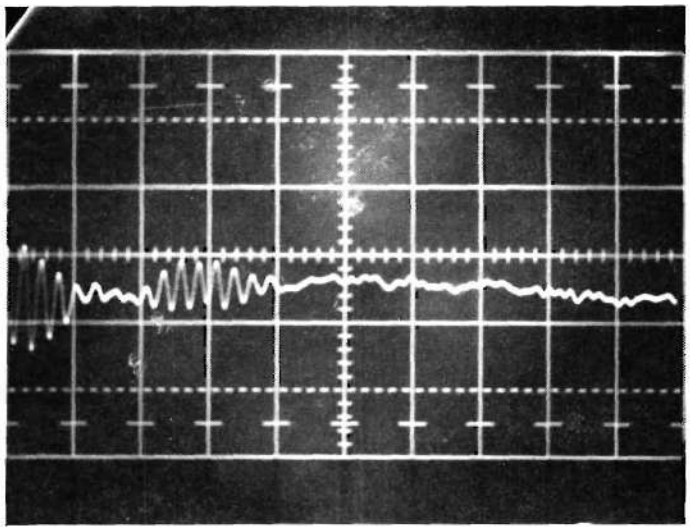

Figure 23. A Low Amplitude 15 kHz LIV Pulse with about 9 Cycles Discernible above the Noise Level

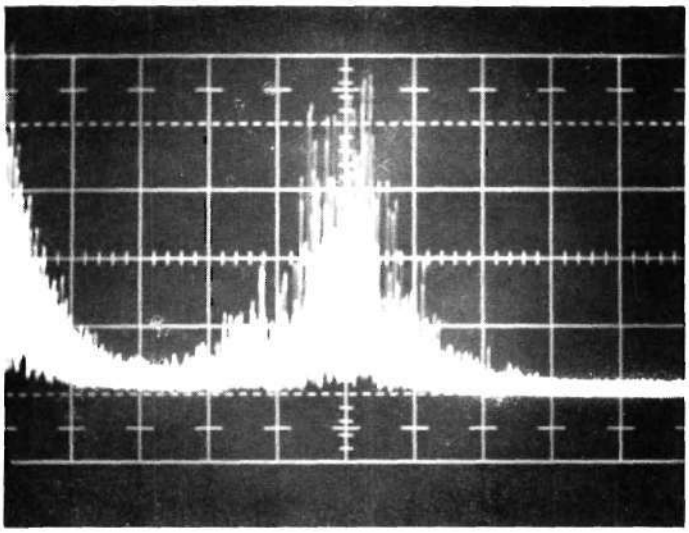

Figure 24. A Spectrum Analyzer Trace from 0 to 20 kHz of a 10 kHz LIV Signal. (Note the band pass component at 10 kHz and the low pass component at dc.)

a 1L5 Tektronix plug-in analyzer used in a Tektronix Model 556 dual plug-in oscilloscope. Note the strong signal corresponding to the cosine term at 10 kHz and the low pass signal near dc due to the low-pass Gaussian term.

LDV System Description

A schematic of the LDV system is shown in Figure 25 and is similar to the LIV schematic shown in Figure 10. The LIV system used in the experiments described in the previous section was converted to an LDV system for the experimental work in this section. The first step in converting the system was to replace the glass plate in the LIV system with a mirror and to place the glass plate a few inches from the mirror at a 45° angle in the beam as indicated. The mirror M1 reflected the beam through a right angle to the remainder of the optical system. The glass plate produced one strong and one weak beam both parallel to each other. The strong beam passed directly through the glass plate and its intensity after it left the plate was about the same as before it entered the plate. A small portion of this beam was reflected internally inside of the plate from the surface of the plate near the negative lens. A portion of this beam was then reflected a second time by the other surface of the glass plate and passed out of the plate parallel to the stronger beam as shown. The weaker beam, after it left the plate, was about five percent of the intensity of the stronger beam. The glass plate effectively produced a strong beam needed for the scattering beam and a weak beam needed for the reference beam in the LDV system.

If the system was properly aligned as an LIV system, the system is only slightly misaligned as an LDV system in that the scattering beam and reference beam almost intersect at their narrowest portion forming the

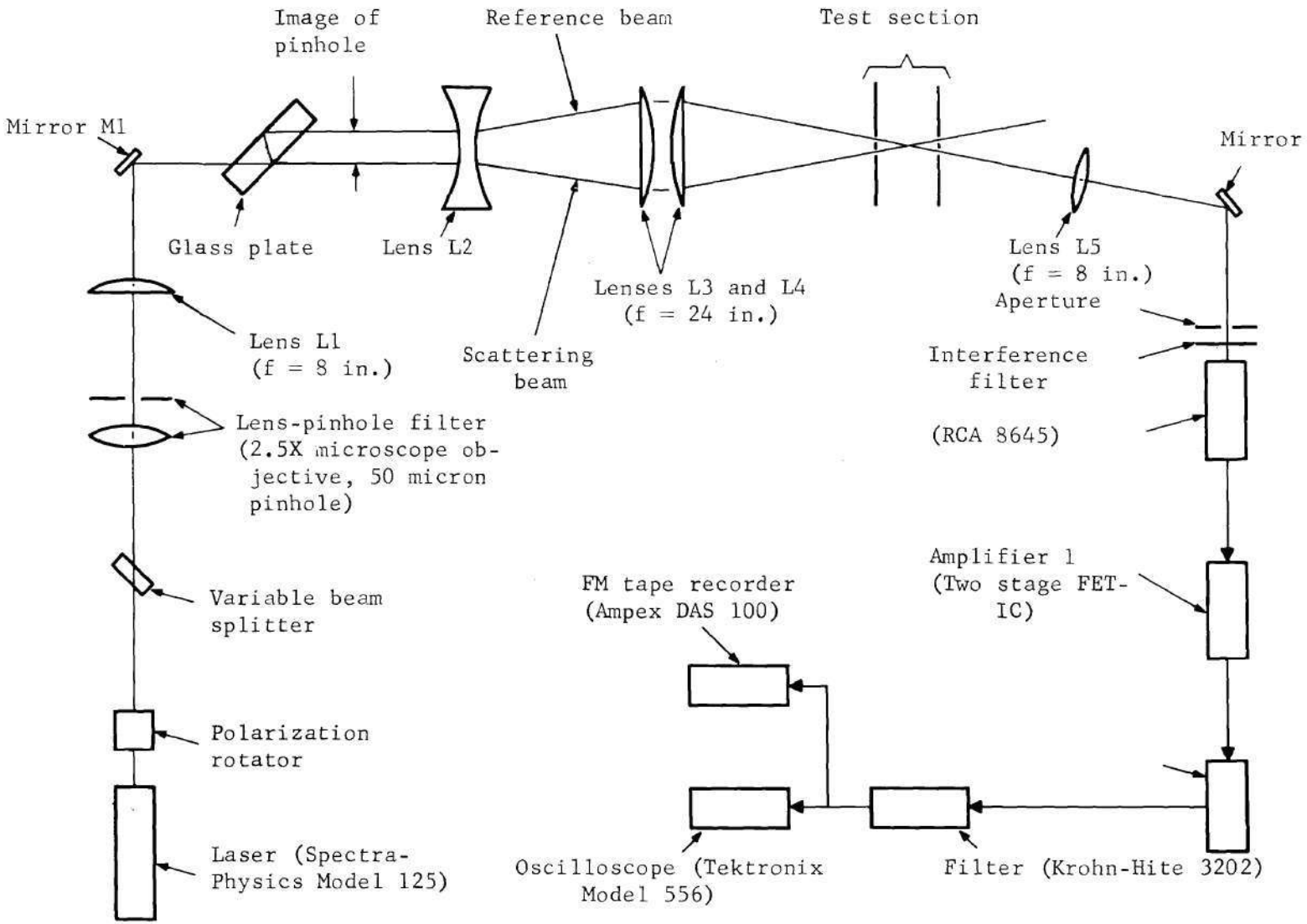

Figure 25. Schematic of the LDV System Used in the Experimental Work

detection volume. Since both beams pass through the glass plate in the LDV system whereas only one beam passed through the plate in the LIV system, the optical path length of the beams in the LDV is slightly greater. The image of the pinhole might not therefore be in exactly the focal plane of the negative lens due to this difference in path length. If the glass plate is very thick, some readjustment may be necessary in order that the image of the pinhole might be in the focal plane of the negative lens. When this slight adjustment is made, the LDV system is aligned.

The only other change made in the LIV system to convert it to an LDV system involved lens L5. In the LDV system, lens L5 must image the portion of the reference beam in the detection volume to the PMT. Therefore, lens L5 was repositioned so that the reference beam was imaged, after reflection from mirror M2, to the PMT. Light scattered by particles from the scattering beam in the direction of the reference beam was also imaged to the PMT. With these minor modifications, the system was set up to operate as an LDV system.

Experiments with the LDV System

The basic signal parameters of the LDV system should also be those of the LIV system since it is apparent from Eqs. (85) and (86) that the band pass portions of signals from the LIV and LDV systems with the same geometry have the same shape signal. Hence, the LDV signals in the experimental work also have Gaussian envelopes with about 12 cycles per pulse and the detection volume dimensions for the LDV system are identical to those of the LIV system.

Representative LDV signals were generated with the LDV system under the same conditions as the signals which were generated with the LIV system.

The tunnel was run at various speeds from 0.3 to 0.7 ft/sec, resulting in signals ranging in frequency from 5 kHz to 15 kHz as before. The photographs of the oscilloscope traces are shown in Figures 26 through 28. First of all, note that there was more noise in the LDV signals than in the LIV signals shown in Figures 14 through 20 and as a consequence it is more difficult to see the individual LDV pulses. The increased noise is explained more fully in the next chapter but essentially it was due to the fact that the reference beam of the LDV system was constantly falling on the PMT producing photon fluctuation noise whether particles were present or not. The only light falling on the PMT in the LIV system was scattered light from the particles which was much weaker than the reference beam in the LDV system.

Figure 26 is an oscilloscope trace of the signal when no light was scattered by the particles. It was taken with the scattering beam blocked in the system so that only the reference beam was striking the PMT. This photograph illustrates the magnitude of the noise in the system produced by the reference beam which was always present with the signal. Figures 27 and 28 show various numbers of LDV pulses. Note that the pulses have Gaussian envelopes and have about 12 cycles per pulse. The heights of the pulses and their spacing are random. Effectively the pulses are the same nature as the LIV pulses except that the LDV pulses are noisier.

It is apparent from Eq. (85) that LDV signals, like LIV signals, have the same number of cycles regardless of the frequency of the signals. This property is illustrated in Figures 29 through 31 which depict 5, 10, and 15 kHz LDV signals. The number of oscillations under each of the pulses is about 12 regardless of the frequency of the pulses.

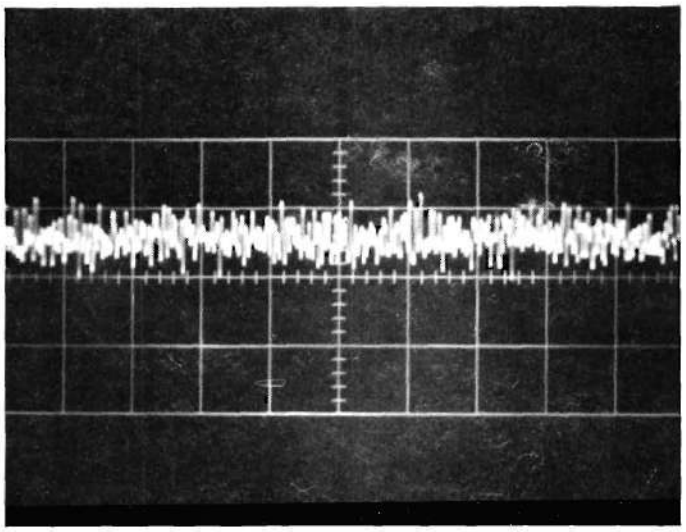

Figure 26. Oscilloscope Trace of an LDV Signal Consisting Solely of Noise Illustrating the High Noise Level of LDV Systems

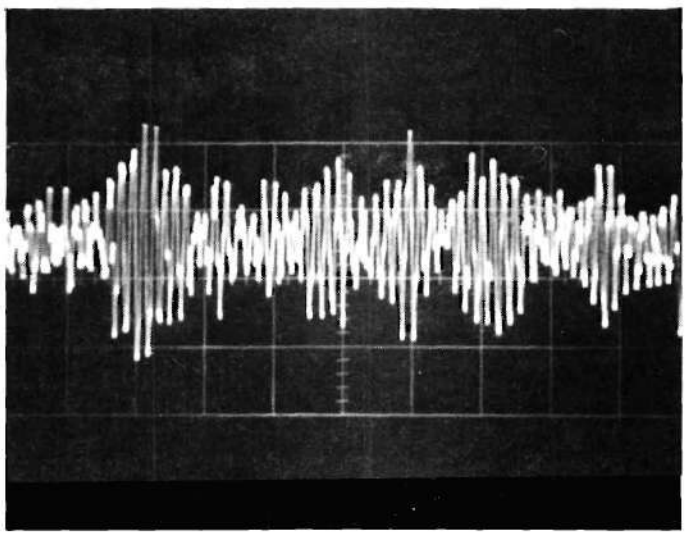

Figure 27. LDV Signal Consisting of at Least Five Pulses (Note that the envelope is approximately Gaussian and there are about 12 cycles per pulse.)

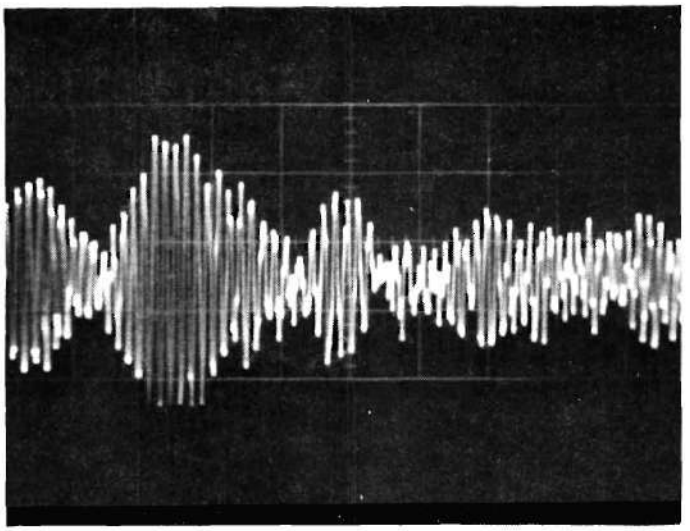

Figure 28. LDV Signal Showing at Least Four Pulses Two of Which Are Overlapping

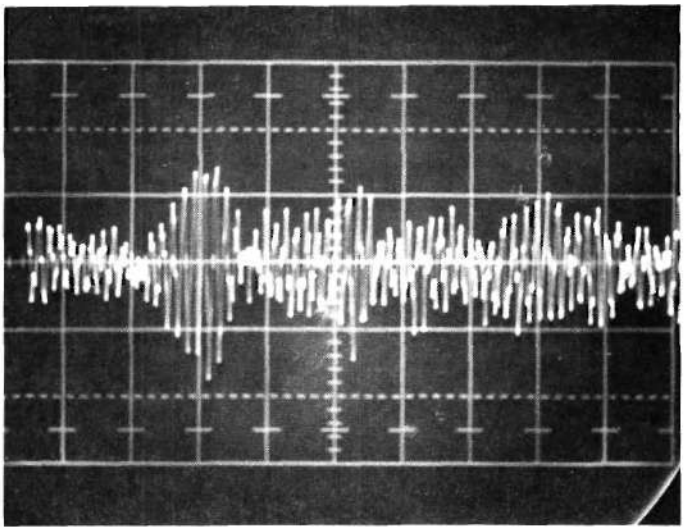

Figure 29. A 5 kHz LDV Signal
(Note that there is at least one clearly discernible pulse with about 10 cycles under its envelope.)

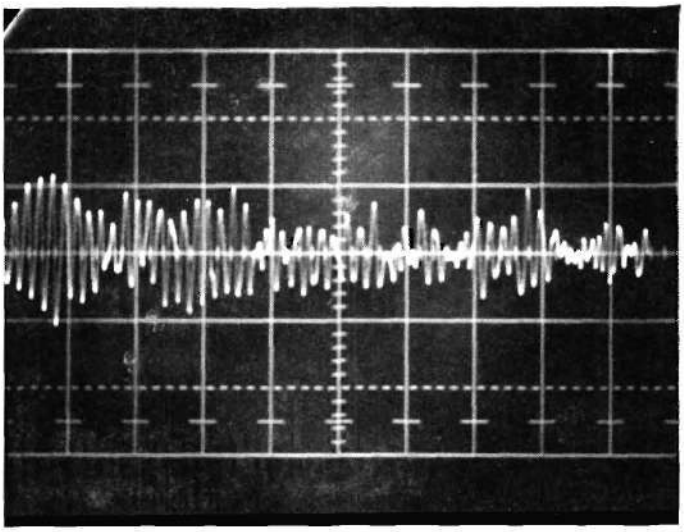

Figure 30. A 10 kHz LDV Signal Showing at Least One Clear Pulse with about 10 Cycles under Its Envelope

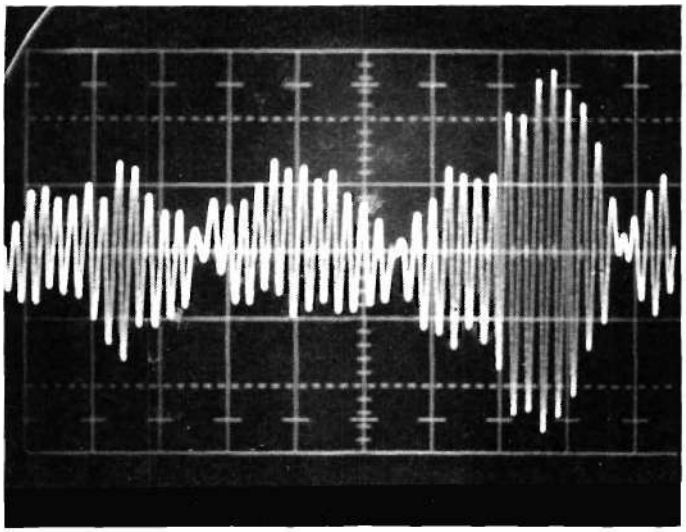

Figure 31. A 15 kHz LDV Showing a Pulse with 12 Cycles under Its Envelope

It is pointed out in the discussion of LDV systems that the LDV signal contains a low-pass term denoted by $K_D I_s$ which is shown in Eq. (57) to be negligible compared to the band-pass term. The fact that this term is negligible is demonstrated by the virtual absence of the low-pass component in the spectrum analyzer trace of a 10 kHz LDV signal shown in Figure 32. The spectrum analyzer used here was identical to the one used to obtain the spectrum of the cosine term centered at 10 kHz, the other components of the spectrum are constant. The apparent rise at dc is due to the dc marker as evident from Figure 33 which is the spectrum analyzer output with no signal applied. Comparing the LIV spectrum of Figure 24 with the LDV spectrum of Figure 32, note that the increased noise of the LDV signals as compared to LIV signals is clearly shown in the spectra of these two signals. The magnitude of the noise in the LDV spectrum in Figure 32 is about five volts whereas the magnitude of the noise of the LIV spectrum is about two volts.

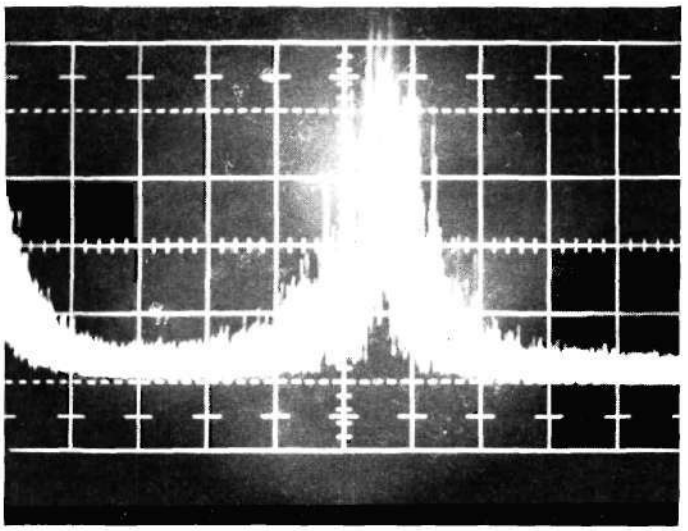

Figure 32. A Spectrum Analyzer Trace from 0 to 20 kHz of a 10 kHz LDV Signal. (Note that the noise is almost white and no dc component is present as in the LIV signal of Figure 25. The apparent rise at dc is due to the dc marker illustrated in Figure 33.)

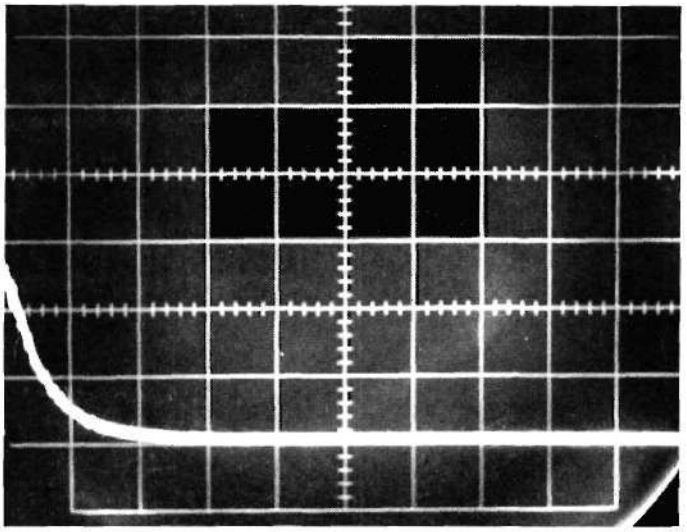

Figure 33. Spectrum Analyzer Trace with No Signal Applied Showing the Marker at dc Which Is Always Present

CHAPTER III

NOISE MODELS FOR LDV AND LIV SYSTEMS

Introduction

In Chapter II, signal models for LDV and LIV systems were derived and experimentally verified. In this chapter, noise models for the systems are presented. First of all, the sources of noise in velocimeter systems are discussed. The manner in which each of these sources affects LDV and LIV systems is then pointed out. It turns out that under most operating conditions, the dominant noise in both systems is white, Gaussian noise. The noise in the experimental velocimeter systems described in the previous chapter was measured to verify the analytical noise models.

Sources of Noise in Velocimeter Systems

The primary kinds of noise in velocimeter systems are photon fluctuation noise, laser intensity fluctuation noise, dark current noise, and thermal noise. Photon fluctuation noise is a white Poisson noise process produced by light falling on the PMT. The light may either be light scattered by the particles, light from the reference beam of the LDV system, or background light caused by stray laser beam reflections from components of the velocimeter system, and room lights. Dark current noise is a white Poisson noise produced by electrons emitted by the photocathode due to thermal excitation. The PMT acts as a low pass filter and effectively filters the Poisson processes so that they become Gaussian processes.

The system which estimates the frequency of the PMT current acts as a filter with a finite bandwidth and further filters the Poisson noise. Since most velocimeter signals fall well within the bandwidth of the filters, the noise is effectively white with respect to the velocimeter signals. Laser intensity fluctuation noise consists of variations in the laser beam intensity caused by excess photon fluctuation noise and current fluctuation noise. Excess photon fluctuation noise is modeled as Gaussian and has a spectrum which is almost constant over the frequencies generated by velocimeters. Current fluctuation noise is low-pass and generally smaller than photon fluctuation noise or excess photon noise. The net effect of the noises associated with the laser beam, namely photon fluctuation noise, excess photon fluctuation noise, and current fluctuation noise, is experimentally shown to be white over the frequency ranges of interest. Thermal noise, produced by the resistors in the amplifiers, is well documented in the literature as white Gaussian noise.

Photon Fluctuation Noise

When a beam of light falls on a PMT, the number of photons striking the PMT per unit time varies from one instant to the next even though the mean number of photons is constant. The random variation in the number of photons about the mean produces a corresponding variation in the number of photoelectrons emitted from the cathode. The resulting noise is called photon fluctuation noise and is a Poisson process. The power spectrum $S'_p(f)$ of the resulting current from the cathode is given by[20]

$$S'_p(f) = q^2\bar{n} + \bar{n}^2 q^2 \delta(f) \qquad (1)$$

$$= qI + I^2\delta(f)$$

where $\bar{n}$ is the mean number of photoelectrons emitted per unit time, q is the charge of one electron, and I is the mean value of the photoelectron current. The spectrum consists of a signal component given by $I^2\delta(f)$ and a white noise component given by qI. It is important to note that the power in the white noise component increases linearly with I while the power of signal component increases as I^2. Therefore, as the laser power is increased, the signal power increases faster than the photon fluctuation noise power resulting in a better signal to noise ratio.

The photoelectrons are accelerated and produce more electrons by secondary emission processes in the multiplier stages of the PMT. Each of the secondary emission electrons created in one multiplier stage produces more secondary emission electrons in the next stage. The initial velocities of the secondary emission electrons created at each stage are not all the same. The variation in initial electron velocities at each multiplier stage limits the bandwidth of the PMT. A photoelectron which might be modeled as a short duration pulse entering the multiplier stages is turned into a longer duration pulse due to the variation in velocity of the secondary emission electrons.[26] The multiplier stages have the effect of a low-pass filter on the photoelectric current.

In realistic situations, the system which estimates the frequency of the PMT current also has a finite bandwidth. The estimator is conceptually preceded by a low-pass filter whose bandwidth is the maximum frequency that the system can estimate. The finite bandwidth in a digital estimator can be limited by the speed of the A-D converters, or the speed at which digital operations can be performed. If the estimator requires that the data first be recorded on magnetic tape or film, the maximum

frequency of the data recorder limits the bandwidth of the estimator. The bandwidth of the estimator described in this thesis is limited by the maximum frequency which can be recorded by an optical data recorder.

The filtering done by both the PMT and the estimator converts the photon fluctuation noise from a white Poisson noise process to a low-pass Gaussian noise process. As a series of randomly spaced delta functions passes through a filter, they are spread out or widened due to the finite bandwidth of the filter. Therefore, the impulses begin to overlap and the Central Limit Theorem predicts the resulting noise to be Gaussian.

Gilbert and Pollak[21] have proven that a series of randomly spaced delta functions governed by Poisson's law becomes a Gaussian process when properly filtered. If the input current $x(t)$ to the filter is a series of randomly spaced delta functions

$$x(t) = \sum_{i=-\infty}^{\infty} q\delta(t-t_i) \tag{2}$$

with the output $z(t)$

$$z(t) = \sum_{i=-\infty}^{\infty} qh(t-t_i) \tag{3}$$

the probability density $p(z)$ of the output is the solution of

$$zp(z) = n_q \int_o^{\infty} \frac{d}{dz} \left(p[z-qh(t)]qh(t)\right) dt \tag{4}$$

where n_q is the number of pulses per second and $h(t)$ is the impulse response of the filter. This equation has been solved for a number of low-

pass and band-pass filters. Gilbert and Pollak[21] have shown that, if $n_q/a \geq 10$, where a is the maximum frequency passed by the filter, p(z) is effectively a Gaussian density when the filter is low pass or band-pass. Therefore, the dark current noise and photon fluctuation noise is effectively Gaussian if the above inequality is satisfied. It is shown further on in this chapter that this inequality is satisfied for LDV and LIV systems studied experimentally in this thesis.

Photon fluctuation noise is white Poisson noise before the noise is filtered. After filtering, the noise becomes low-pass. The power spectrum $S_p(f)$ of the signal from the PMT follows from Eq. (1) and is given by

$$S_p(f) = qG^2I + G^2I^2\delta(f) \qquad \text{for} \quad f < f_c \tag{5}$$

$$= qG^2I + G^2I^2\delta(f) \qquad \text{for} \quad f > f_c$$

where G is the PMT gain and f_c is the maximum frequency of the PMT. Under the proper conditions, as discussed above, the Poisson noise is also converted to Gaussian noise. The PMT used in the thesis was an RCA 8645 which has a fast rise time and is very sensitive in the visible region of the spectrum. Its bandwidth is approximately 160 megahertz.[26] The photon fluctuation noise leaving the PMT is then low-pass with a maximum frequency of about 160 megahertz. From Eq. (93) of Chapter II, a frequency of 160 megahertz corresponds to a velocity v of

$$v = \left(\frac{160 \times 10^3 \text{ kHz}}{1}\right)\left(\frac{0.0466 \text{ ft/sec}}{\text{kHz}}\right) \tag{6}$$

$$= 7456 \text{ ft/sec}$$

which is about Mach 7. The bandwidth of the estimator in this thesis is 20 kHz which is far less than the PMT bandwidth. For a wide variety of flows, especially those at subsonic velocities, the frequencies generated by velocimeters and the bandwidths of their estimator systems are less than the bandwidth of the Poisson noise. Under these conditions, the Poisson noise can be considered white with respect to these systems.

Laser Intensity Fluctuation Noise

Photon fluctuation noise, as described above, is noise produced by random fluctuations in the number of photons striking the PMT even though the mean intensity of the beam remains constant. In contrast, laser intensity fluctuation noise is noise produced by random fluctuations in the mean intensity of the beam. The two primary kinds of laser intensity noise, current fluctuation noise and excess photon fluctuation noise, are briefly described below. An expression for the power spectrum of the resulting noise in the PMT current produced by the intensity fluctuations is presented in terms of the power spectrum of the intensity fluctuations. The net effect of photon fluctuation noise, excess photon fluctuation, and current fluctuation on the power spectrum of the noise from the PMT is experimentally determined for a TEM_{00} helium-neon laser.

The random variation in laser power produced by random fluctuations in the plasma tube current is referred to as current fluctuation noise. Hongo[27] has demonstrated that this noise does not exist at frequencies greater than 250 kHz for helium-neon lasers. He also points out that this critical frequency is related to the metastable life time of the helium atom. His results were verified by an experiment in which he sinusoidally modulated the current driving a helium-neon laser and measured the ampli-

tude of the response of the laser to each sinusoid.

Excess photon fluctuation noise arises from the interaction of various longitudinal modes in the laser. Even though a laser is operating in a single transverse mode (say TEM_{00} mode) it can have many longitudinal modes. Generally, the phases of these modes with respect to each other is random and time varying. Hence, these modes will randomly beat together producing a difference frequency with a broad spectrum which acts as noise. If the longitudinal modes are phase locked together, i.e., their relative phase variations are fixed in time, the spectrum of the noise is a narrow spike or nearly a delta function. In this instance, excess photon fluctuation noise produces no detection problem except at Doppler shifts near the center of the beat frequency. Argon lasers can be readily made to operate in a single longitudinal mode by placing an etalon in the laser cavity. For such a laser, no excess photon fluctuation noise exists.

The center frequency of the noise is given by

$$f = c/2L_c \tag{7}$$

where c is the speed of light, and L_c is the cavity length of the laser. For a typical laser one meter long, f_c = 150 mHz. As indicated above, the resulting noise in a mode locked laser has a very narrow bandwidth and the spectrum is essentially a spike. For a non-mode locked laser, the spectrum $S_E(f)$ can be shown to have a shape given by the expression[22]

$$S_E(f) = \frac{2\tau_c/\pi}{1 + \left(\frac{f-f_c}{1/4\tau_c}\right)^2} \tag{8}$$

where τ_c is the coherence interval of the mode. A typical value of τ_c measured from a Spectra-Physics Argon laser is 3.3×10^{-8} sec.* Substituting this value into Eq. (8), $S_E(f)$ is one fifth of its peak value at 120 mHz when $f_c = 150$ mHz. From the functional form of Eq. (8), the contribution of excess photon fluctuation noise is nearly constant for frequencies less than 100 mHz. The noise is effectively filtered by the PMT and by the frequency estimator system in the same manner as the Poisson noise discussed earlier. The nature of excess photon fluctuation noise is discussed in more detail by Hondara,[22] and is modeled as white Gaussian noise in the analysis of this thesis.

The power spectra of the intensity fluctuations in the beam arising from excess photon fluctuation noise and current fluctuation noise have been described. Mayo[3] has demonstrated that the noise in the PMT current, I, induced by laser intensity fluctuations has a power spectrum $S_I(f)$ given by

$$S_I(f) = I^2 S_n(f) \tag{9}$$

where $S_n(f)$ is the power spectrum of the intensity variations. Note that the power spectrum of the PMT current noise has the same shape as the power spectrum of the intensity fluctuations. Also note that $S_I(f)$is dependent upon I^2 in contrast to the photon fluctuation noise spectrum which is dependent upon I. Because of this dependence, intensity fluctuation noise can in some instances be the dominant noise for low frequency velocimeter signals.[3]

---

*Private communication with Spectra-Physics, Inc.

In order to determine the net effect of the various laser noises, the spectrum of a Spectra-Physics Model 120 helium-neon laser was measured. The spectrum of the laser was measured with a Hewlett-Packard Model 851B spectrum analyzer system as shown in Figure 34. The output of the laser was passed through a variable density filter to control the intensity of the beam. The beam then struck a ground glass plate which diffused the light. The light from the ground glass fell on the PMT whose output was amplified by two Hewlett-Packard Model 461A amplifiers. The amplifier output went to the Hewlett-Packard Model 8551B up converter and Model 851B spectrum analyzer. In order to obtain maximum PMT frequency response, the PMT was operated at 1800 volts and the amplifier gains adjusted so that no saturation occurred.

The measured spectrum of this laser indicated that the noise due to the laser is effectively white. Figure 35 shows the spectrum from zero to nine mHz. The upper trace is the power spectrum and the lower trace is the spectrum analyzer with the PMT covered. The spike at the one centimeter mark is a dc marker produced by the spectrum analyzer. Figure 36 is a trace of the spectrum from zero to 900 kHz and Figure 37 is a trace of the spectrum from zero to 90 kHz. This range was the lowest which could be analyzed with the Hewlett-Packard analyzer so this analyzer was replaced with a Tektronix 1L5 analyzer which has a lower range. Figures 38 and 39 show, respectively, the zero to 90 kHz and zero to 10 kHz ranges. Note that these photographs indicate that the noise due to the laser is approximately white over these frequency ranges.

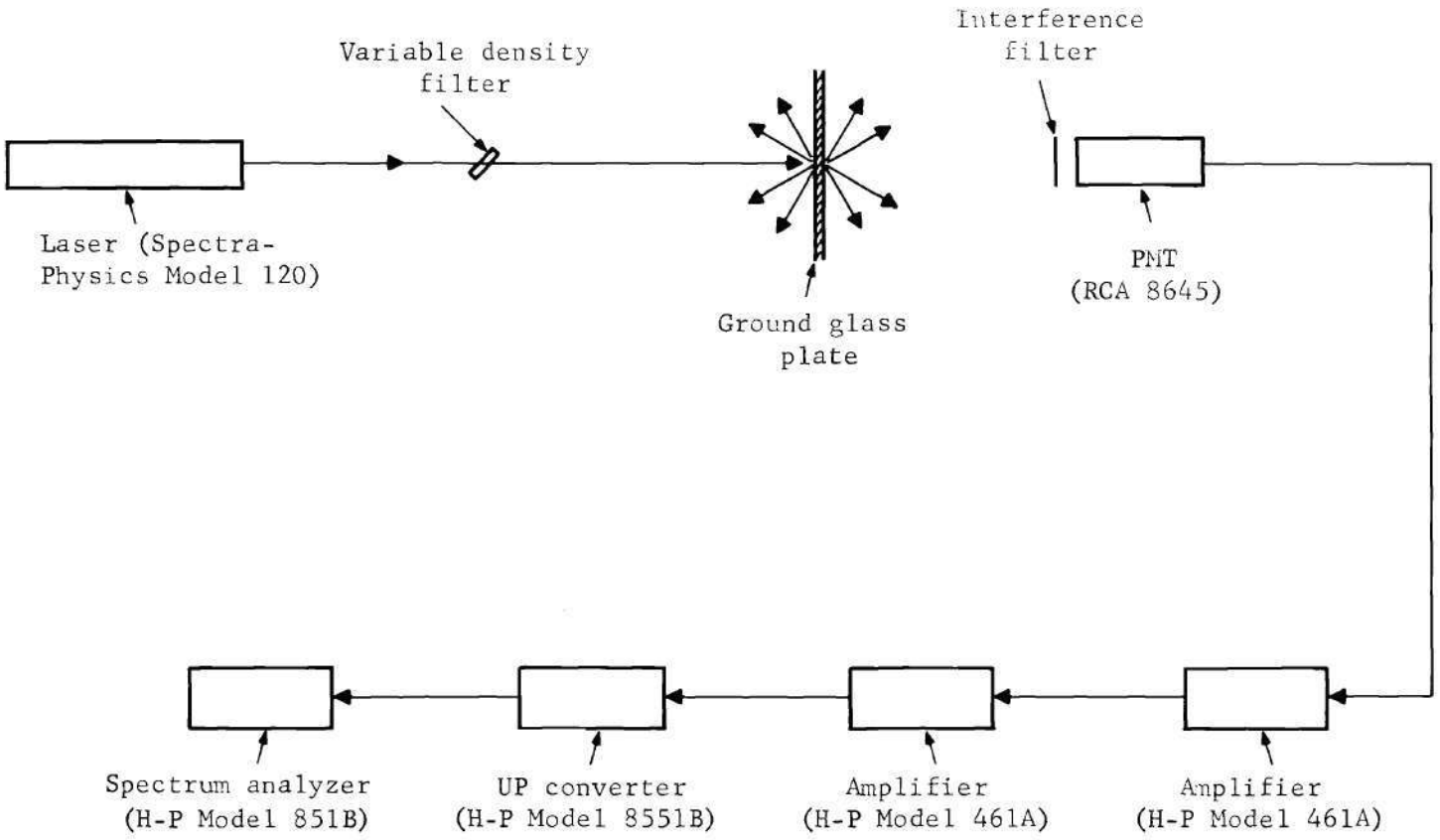

Figure 34. System Used to Measure the Spectrum of the Laser Noise

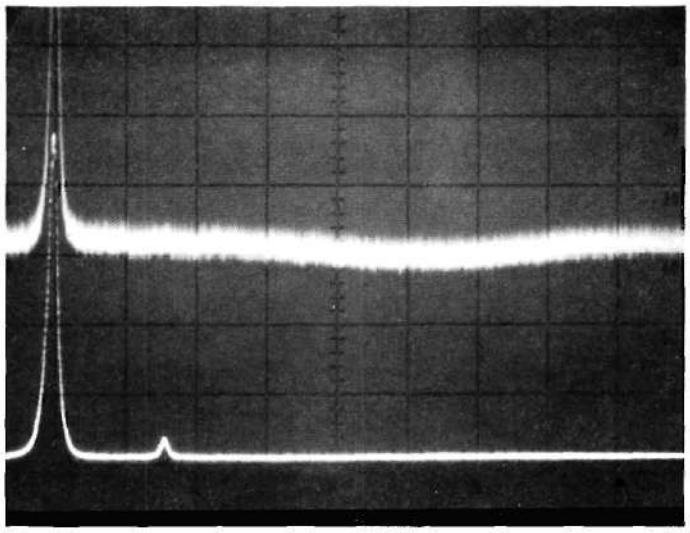

Figure 35. Laser Noise from Zero to Nine mHz (Lower trace is the zero level (output of analyzer with no signal applied).)

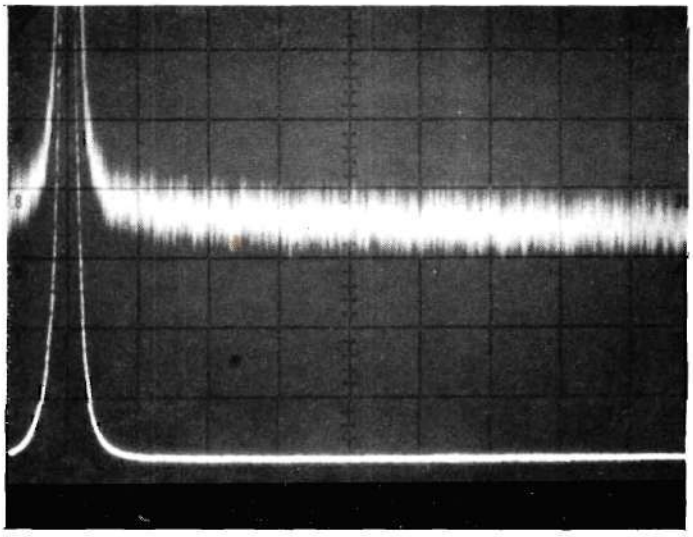

Figure 36. Laser Noise from Zero to 900 kHz

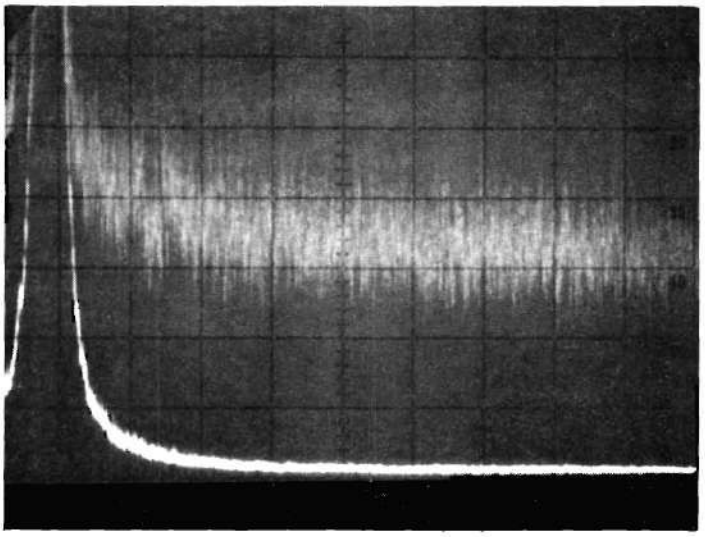

Figure 37. Laser Noise from Zero to 90 kHz Measured by the Hewlett-Packard Spectrum Analyzer

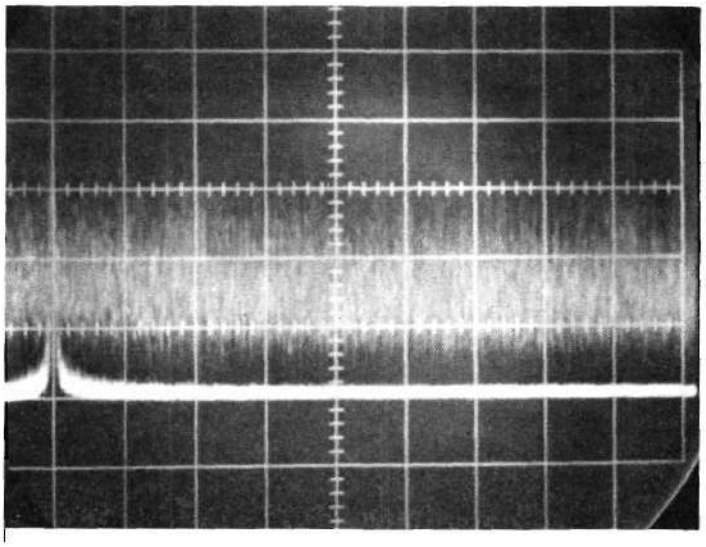

Figure 38. Laser Noise from Zero to 90 kHz Measured by the Tektronix 1L5 Analyzer

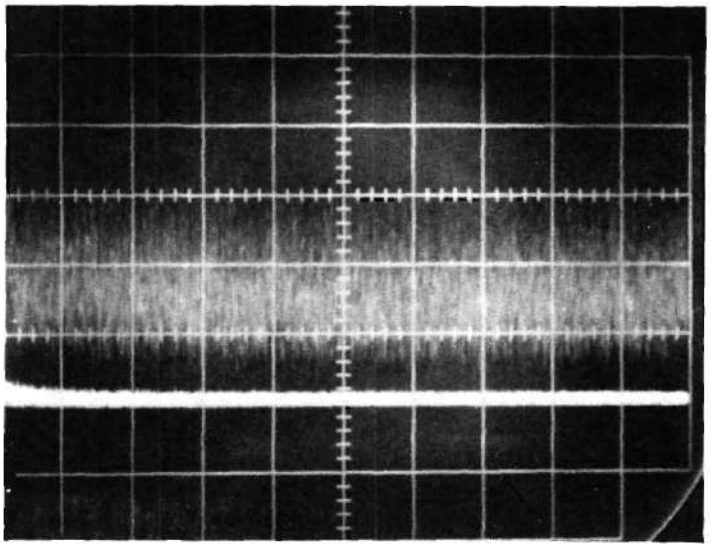

Figure 39. Laser Noise from Zero to 10 kHz Measured with the Tektronix Spectrum Analyzer

Dark Current Noise

Dark current noise arises from electrons which are emitted from the photocathode due to thermal excitation and are not produced by collisions with photons. The number of electrons emitted per unit time is a white Poisson process like photon fluctuation noise. Pratt[20] demonstrates that the power spectrum $S_D'(f)$ of the electrons leaving the cathode is given by

$$S_D'(f) = q^2\bar{n} + \bar{n}^2 q^2\, \delta(f) \tag{10}$$

where $\bar{n}$ is the mean number of electrons emitted per unit time and q is the charge of a single electron. Upon amplification and filtering by the multiplier stages of the PMT, the spectrum $S_D(f)$ of the dark current becomes

$$\begin{aligned} S_D(f) &= G^2 q^2 \bar{n} + G^2 \bar{n}^2 q^2\, \delta(f) \qquad \text{for} \quad f < f_c \\ &= 0 \qquad\qquad\qquad\qquad\quad \text{for} \quad f > f_c \end{aligned} \tag{11}$$

where G is the PMT gain, and f_c is the PMT bandwidth. The spectrum can be rewritten in terms of the current I_E produced by the dark current as follows

$$\begin{aligned} S_D(f) &= GqI_E + I_E^2\, \delta(f) \qquad f < f_c \\ &= 0 \qquad\qquad\qquad\quad f > f_c \end{aligned} \tag{12}$$

where $I_E = Gq\bar{n}$. The spectrum consists of a constant component GqI_E and a dc component $I_E^2\, \delta(f)$. The constant component is the only troublesome component since a dc current in no way interferes with estimation procedures discussed in this thesis.

The electrons emitted from the cathode due to thermal excitation are statistically independent of those emitted due to photon collisions. Since dark current noise and photon fluctuation noise have the Poisson statistics and are independent of each other, they can be effectively lumped together into a single noise component.

Thermal Noise

Thermal noise is produced by resistors in the amplifiers following the PMT. The thermally excited electrons in a resistor give rise to many random voltage pulses across the terminals of a resistor. The Central Limit Theorem predicts the noise to be Gaussian. Since the pulses are short in duration, the noise is also white. Davenport and Root[19] give a complete discussion of noise models for thermal noise while Pratt[20] discusses its effects on optical communication systems.

Effect of Noise on LDV Systems

Now that the prime contributors to the noise in velocimeter systems have been outlined, the effect of the noise sources on LDV systems is discussed. It is shown that the major contributors to the noise are background room and laser light, the LDV reference beam, dark current noise, and thermal noise. Since each of these sources is white and Gaussian, the resultant noise is also white and Gaussian which is verified by measurements made on the experimental LDV system described in Chapter II.

The manner in which the sources of noise contribute to the LDV signal is depicted in Figure 40. The light striking the PMT consists of background light, the reference beam, and the light scattered by the particles. The background light comes primarily from the room lights

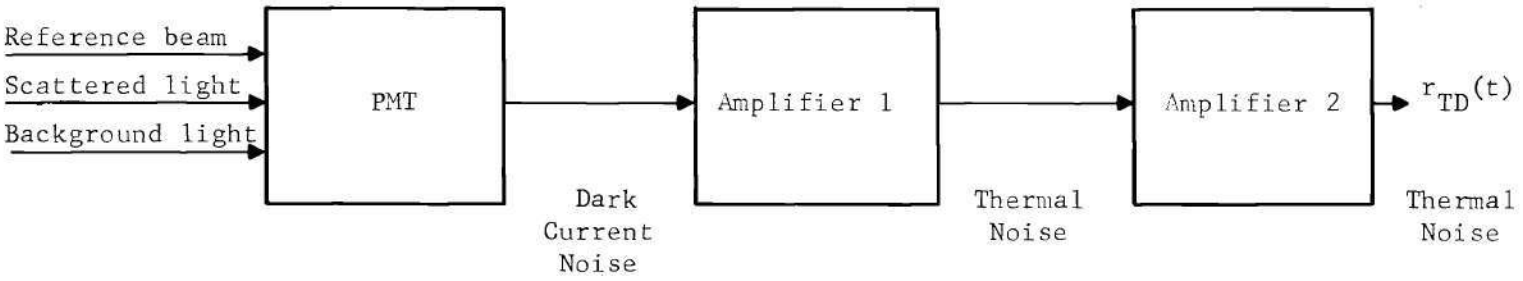

Figure 40. Schematic of LDV Noise Sources

and from stray laser reflections. The effects of the background light were reduced in the experimental work by placing an aperture in front of the PMT at the point where the detection volume was imaged along with an interference filter centered at the laser wavelength. The aperture was the same size and at the same position as the imaged detection volume. This means that scattered light and reference light from the detection volume were in focus at the PMT and stray laser light from other parts of the system was out of focus and therefore reduced in intensity.

It is shown in Eq. (23) of Chapter II that the reference light and the scattered light are optically heterodyned together at the PMT producing an intensity I_D

$$I_D = I_s + I_r + I_{sr} + I_{sr}^* \tag{13}$$

If background light is included, the intensity I_D at the surface of the PMT is

$$I_D = I_s + I_r + I_{sr} + I_{sr}^* + I_B \tag{14}$$

where I_B is the intensity of the background light. Photon fluctuation noise and laser intensity fluctuation noise are produced at the PMT by the light falling on the PMT. The magnitude of the power spectra of these noises is shown in Eqs. (5) and (9) to be dependent on the PMT current I which is proportional to I_D. The intensity I_r of the reference beam is by far the largest component of I_D. The reference beam is about five percent of the total laser power and is focused directly on the PMT. For this reason, I_r is much greater than the intensity I_B of the background light,

i.e.,

$$I_r \gg I_B \tag{15}$$

of the background light. Also, it follows from Eqs. (30) and (57) of Chapter II that

$$I_r \gg I_{sr}^{*} + I_{sr} \tag{16}$$

and

$$I_r \gg I_s$$

Therefore, the power spectrum of the photon fluctuation noise and the laser intensity fluctuation noise depend primarily on I_r. Since I_r is constant, these noises have time invariant spectra and hence are statistically stationary.

Dark current noise and photon fluctuation noise have been shown to be Poisson shot noise processes. Effectively, the PMT filters the shot noise due to its non-infinite bandwidth. It was demonstrated earlier that the filtered shot noise is Gaussian if $n_q/a \geq 10$ where a is the filter bandwidth and n_q is the number of electrons per second passing through the filter. This condition was satisfied by the LDV system used in this thesis and by most other LDV systems. The PMT used was an RCA 8645 and was selected because of its wide bandwidth, low dark current, and high sensitivity at laser wavelengths. Since the bandwidth of the PMT is 160 mHz,[26] the condition for Gaussian noise becomes

$$\begin{aligned} n_q &\geq 10a \\ &\geq 10(160 \times 10^6) \\ &\geq 1.6 \times 10^9 \text{ photoelectrons/sec} \end{aligned} \tag{17}$$

Since quantum efficiency η of the tube is six percent at the wavelength of the helium-neon laser, the required number n_k of photons per second is

$$\begin{aligned} n_p &\geq 10a/\eta \\ &\geq \frac{1.6 \times 10^9}{0.06} \\ &\geq 2.66 \times 10^{10} \text{ photons/sec} \end{aligned} \tag{18}$$

The power P' of a laser needed to produce photons at the required rate follows from Planck's law as

$$\begin{aligned} P' &\geq \frac{10a\, h\nu}{\eta} \\ &\geq \frac{(2.66 \times 10^{10})(6.624 \times 10^{-34})(3 \times 10^{11})}{0.6328 \times 10^{-3}} \\ &\geq 8.36 \times 10^{-6} \text{ mw} \end{aligned} \tag{19}$$

If a typical helium-neon laser with a power output of 20 milliwatts is used to drive the LDV, the power in the reference beam is five percent of the total power or one milliwatt. The threshold of 8.36×10^{-6} milliwatts is easily exceeded and the Poisson noise is effectively Gaussian. Argon lasers with one watt output power can be used in LDV systems providing 50 mw for the reference beam.

In addition to the filtering done by the PMT, the estimator system also filters the signal. If the estimation system is designed for subsonic velocities, it has a frequency cut off at frequencies corresponding to speeds of about 1000 ft/sec. From Eq. (93) of Chapter II, 1000 ft/sec

corresponds to a frequency cut off at

$$\left(\frac{1000 \text{ ft/sec}}{1}\right)\left(\frac{\text{kHz}}{0.0466 \text{ ft/sec}}\right) = 21.4 \text{ mHz} \tag{20}$$

Taking into account this filter, the threshold power P" required to convert the Poisson noise to Gaussian noise is reduced to

$$P'' = \frac{21.4 \text{ mHz}}{160 \text{ mHz}} \, p' = 1.12 \times 10^{-6} \text{ mw} \tag{21}$$

It is shown in Chapter V that the system used in the experimental work had an upper frequency limit of 20 kHz further reducing the threshold power to

$$P''' = \frac{20 \text{ kHz}}{160 \text{ mHz}} \, p' = 1.045 \times 10^{-9} \text{ mw} \tag{22}$$

The current $i_{1D}(t)$ from the PMT with noise taken into account follows from this discussion and Eq. (91) of Chapter II as

$$I_{1D}(t) = \sum_{i=1}^{N} B_i \, e^{-\alpha(2\pi f_D)^2 (t-t_i)^2} \cos 2\pi f_D (t-t_i) + n_{Do}(t) \tag{23}$$

where $n_{Do}(t)$ is white Gaussian noise and it is assumed that the dc component $K_D \, C_3^{\,2}$ is removed by a very narrow filter at dc. The laser noise produced by $K_D \, C_3^{\,2}$ still remains and is included in $n_{Do}(t)$. The signal $i_{1D}(t)$ now goes to the two amplifiers. The amplifiers following the PMT amplify the current $i_{1D}(t)$ and add thermal noise to it. Denoting the gain of the first amplifier by G_1 and the gain of the second by G_2, the current $r_{TD}(t)$ from the second amplifier follows from Eq. (23) as

$$r_{TD}(t) = G_1 G_2 \sum_{i=1}^{N} B_i \, e^{-\alpha(2\pi f_D)^2 (t-t_i)^2} \cos 2\pi f_D (t-t_i) \qquad (24)$$

$$+ G_1 G_2 \, n_{Do}(t) + G_1 n_1(t) + n_2(t)$$

where $n_1(t)$ and $n_2(t)$ are thermal noises added by the two amplifiers, respectively. Since all the prime contributors to the noise, namely $n_{Do}(t)$, $n_1(t)$, and $n_2(t)$ are white Gaussian noise, the LDV signal can be written as

$$r_{TD}(t) = \sum_{i=1}^{N} B_i \, e^{-\alpha(2\pi f_D)^2 (t-t_i)} \cos 2\pi f_D (t-t_i) + n(t) \qquad (25)$$

where $n(t)$ is white Gaussian noise and B_i has been amended to include G_1 and G_2.

In order to experimentally verify the noise model, measurements were made on the LDV system described in Chapter II to determine which sources contributed the noise and to determine the power spectrum of the noise. The contribution to the noise of each element in the LDV system of Figure 25 was measured. The results of measurements are tabulated in Table 1. The noise from amplifier two with no applied input was 0.01 volt. When amplifier one was connected to amplifier two, the output of amplifier two became 0.1 volt. The PMT was connected to the system with its surface covered from the light and no change in the output current was noted as the voltage applied to the PMT was varied from 0 to 1600 volts. The dark current is therefore negligible in the 0 to 1600 volt range used in all the experimental work. Figure 41 shows the power

Table 1. Summary of Contributions of Noise Sources to Experimental LDV System

Elements	RMS Noise Voltage
Amplifier two	0.01 v
Amplifier one and Amplifier two, in series	0.01 v
PMT (0 to 1600 v), Amplifier one and Amplifier two, in series	0.01 v

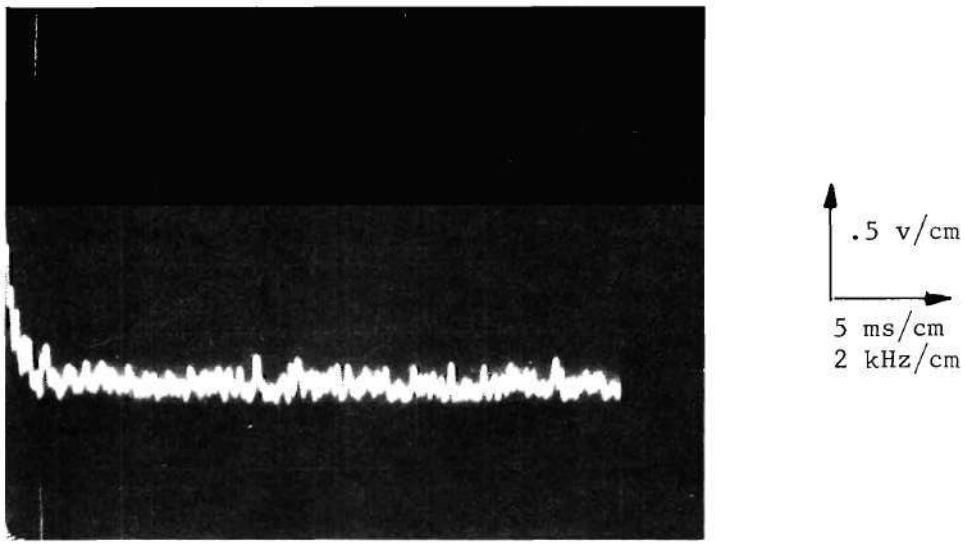

Figure 41. Power Spectrum from Zero to 20 kHz of the Noise from the LDV Detection System

spectrum of the noise from amplifier two with the elements connected in series as described above. The spectrum was measured over the 0 to 20 kHz range with a Tektronix Model 1L5 plug-in spectrum analyzer. Note that the noise is approximately white over this frequency range which was used in the experimental work. Therefore, in the detection system used in the experimental work, the noise was essentially white and the prime contributors to the noise were the two amplifiers. The PMT produces little noise in comparison to the amplifiers.

The reference beam was allowed to fall on the PMT and the output noise voltage increased to 0.35 volt indicating that the laser noise produced by the reference beam was much greater than the detection system noise. Figure 42 shows the power spectrum of the noise with the reference beam falling on the PMT. It is seen that this noise is white over the range from 0 to 20 kHz. When the room lights were turned on, the noise from the filter increased negligibly. Since the noise level with the reference beam was 0.35 volt as compared to 0.1 volt without the beam, it can be concluded that the dominant source of noise in the system was white Gaussian noise created by the laser noises in the reference beam.

Effect of Noise on LIV Systems

The noise sources which are present in LDV systems are also present in LIV systems although their relative contributions to the total noise are different in LIV systems as compared to LDV systems. The LDV signal has a large dc component I_r which controls the magnitude of the laser related noises. However, the LIV signal is composed of two equal

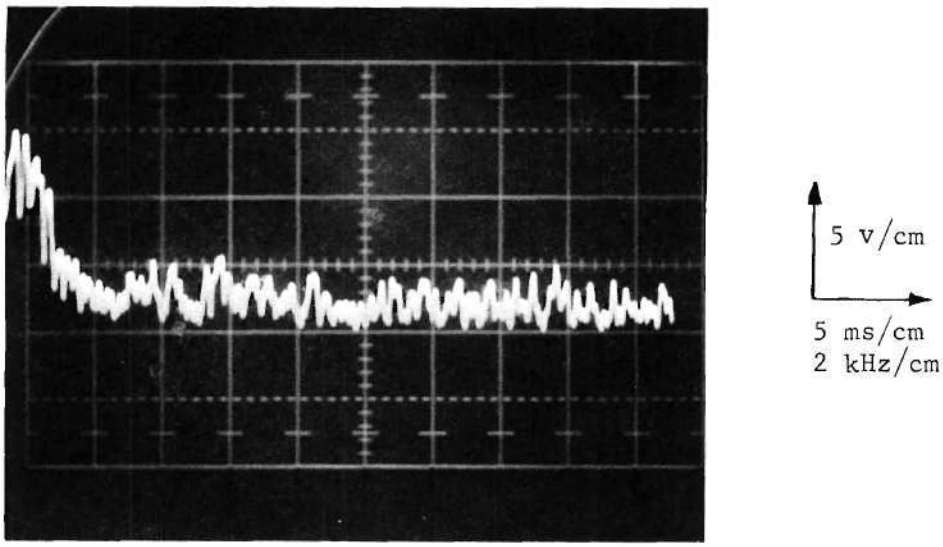

Figure 42. Power Spectrum from Zero to 20 kHz of the LDV Noise with the Reference Beam Falling on the PMT

intensity components which have been demonstrated in Chapter II to be much smaller than I_r. It is the absence of a large dc component in the PMT current of the LIV system which makes the relative magnitudes of the noise contributed by various sources in LIV systems different from their relative magnitudes in LDV systems. However, the dominant noise in the LIV system, like the LDV system, still turns out under most conditions to be white Gaussian noise.

Figure 43 is a schematic of the noise sources in the LIV system. The system from the PMT to the second amplifier shown in the figure is the same detection system used in the LDV. The light falling on the PMT consists of light scattered by the particles and background light. The intensity at the PMT surface due to the scattered light was shown in Eq. (72) of Chapter II to be

$$I_I = I_u + I_w + I_{uw} + I_{uw}^* \tag{26}$$

Taking into account background light intensity I_B, the total intensity I_I' at the PMT is

$$I_I' = I_u + I_w + I_{uw} + I_{uw}^* + I_B \tag{27}$$

The resulting PMT current $i_{II}'(t)$ becomes

$$i_{II}'(t) = K_I\ (I_u + I_w + I_B + I_{uw} + I_{uw}^*) + n_{Io}(t) \tag{28}$$

where $n_{Io}(t)$ is the noise produced by the laser beams and by the dark current.

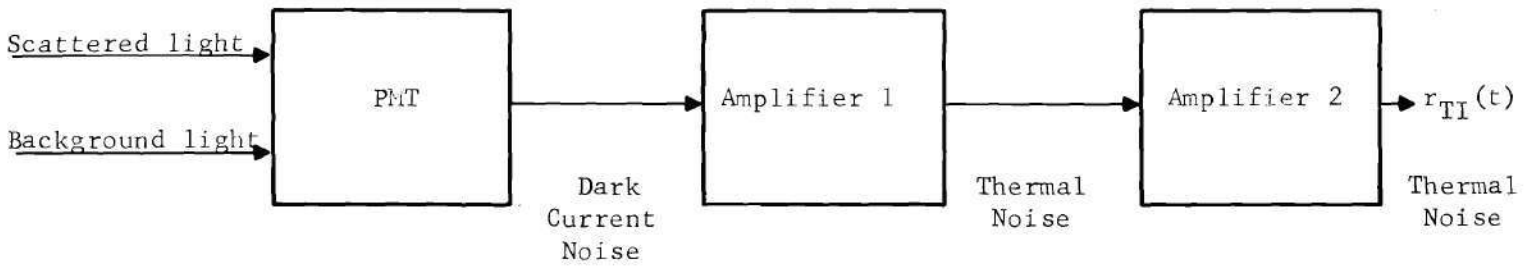

Figure 43. Schematic of LIV Noise Sources

Even though the intensity of the light at the PMT is less in the LIV system as compared to the LDV system, the intensity is still high enough under most conditions to convert the Poisson noise due to the dark current and photon fluctuations into Gaussian noise. The magnitude of the $I_u + I_w$ term follows from Eq. (81) of Chapter II as $4\epsilon^2\sigma^2C_4^2/G^2\pi$. In order to estimate the magnitude of $I_u + I_w$, it is assumed that a 20 mw helium-neon laser is used and that the intensity of the two beams in the LIV system is 10 mw. Using the typical values of ϵ^2, σ^2, and G^2 given in Eq. (88) of Chapter II, the magnitude of $I_u + I_w$ becomes

$$\frac{4\epsilon^2\sigma^2C_4^2}{G^2\pi} = \frac{4(1/770)(0.195 \times 10^{-6})(10)}{(0.031)^2(\pi)} \tag{29}$$

$$= 3.36 \times 10^{-6} \text{ mw}$$

The threshold power required to convert Poisson to Gaussian for the experimental work was shown to be 1.045×10^{-9} mw in Eq. (22). Therefore, in the experimental work, the noise was clearly Gaussian. For estimators designed to operate in any subsonic flows, the threshold power was shown in Eq. (21) to be 1.12×10^{-6} mw. The condition for Gaussian noise is fulfilled in this case also, but not by a margin as large as in the case of the experimental work. Readily available argon lasers which are capable of providing 500 mw to the two beams of the LIV system can also be used. With such a laser, the magnitude of $I_u + I_w$ would be about 1.68×10^{-5} mw, far exceeding the threshold of 1.12×10^{-6} mw required for estimators designed for subsonic flows. With an argon laser, the power

requirement of 8.36×10^{-6} mw for flows up to 7456 ft/sec is also satisfied. It should be noted that the intensity term I_B also contributed photon fluctuation noise and that its contribution has been neglected in the above calculation. It is shown later in this chapter that the noise produced by I_B can be much greater than the noise produced by $I_u + I_w$. If the criterion for Gaussian noise produced by $I_u + I_w$ is fulfilled, the criterion will certainly be fulfilled for the combination of I_B and $I_u + I_w$.

The requirements for Poisson noise to be converted to Gaussian are easily satisfied for the experimental work done in this thesis. In addition, the requirement is satisfied for an estimator whose bandwidth is just wide enough to accept signals from any subsonic flow. If an argon laser is used to drive the velocimeter, the noise is Gaussian for almost any flow. However, if the velocimeter is driven by a low power laser, and if the estimator is designed to operate at frequencies corresponding to supersonic speeds, the Poisson case might be achieved if the background light is low enough.

After the current leaves the PMT, it is amplified by the two amplifiers shown in Figure 43. The PMT current in Eq. (28) can be extended to the case of N particles by substitution from Eq. (91) of Chapter II as follows

$$i_I(t) = \sum_{i=1}^{N} (B_i+1)\, e^{-\alpha(2\pi f_D)^2 (t-t_i)^2} \cos 2\pi f_D (t-t_i) + n_{ID}(t) \qquad (30)$$

The background intensity I_B is generally constant in time and produces a dc current. Since the dc PMT current can be removed by a very narrow

filter placed at dc, it is neglected. It is important to note, however, that the noise produced by I_B is not filtered out and is incorporated in $n_{ID}(t)$. The signal $r_{TI}(t)$ which leaves amplifier two is

$$r_{TI}(t) = G_1G_2 \sum_{i=1}^{N} (B_i+1)\, e^{-\alpha(2\pi f_D)^2(t-t_i)^2} \cos 2\pi f_D(t-t_i) \qquad (31)$$

$$+ G_1G_2\, n_{ID}(t) + G_2 n_1(t) + n_2(t)$$

where G_1, G_2, $n_1(t)$, and $n_2(t)$ have the same definitions as given in the discussion of LDV noise. This equation is rewritten as the following

$$r_{TI}(t) = \sum_{i=1}^{N} (B_i+1)\, e^{-\alpha(2\pi f_D)^2(t-t_i)^2} \cos 2\pi f_D(t-t_i) + n_I(t) \qquad (32)$$

The definition of B_i has been amended to include G_1G_2, and $n_I(t)$ is the sum of all the noise terms.

There are two modes of operation of the LIV system which are considered in this thesis. The noise due to the background light is the dominant noise in one mode and the thermal noise due to the amplifiers is the dominant in the second mode. The background noise mode is the most common mode of operation in most wind tunnel environments. It is difficult and inconvenient to sufficiently darken a room in which a large wind tunnel is operating to remove background light due to room lights. Also, the position of the PMT is dictated by the geometry of the tunnel and model and cannot always be placed where there are no stray laser beams. Laser beam reflections from the wind tunnel windows and from the lenses

in the velocimeter system also produce background light and were observed in the experimental work and considerable alignment was needed to keep them away from the PMT. The background light is stronger than the scattered light from the particles and hence fulfills the Gaussian criterion as discussed earlier. The background light is constant in intensity and hence the power spectrum of the noise which depends on the intensity of the light is not time varying. Therefore, the mode of operation in which noise due to background light dominates is characterized by white Gaussian noise.

In the second mode of operation, it is assumed that by some means the background light is reduced enough that background noise is no longer the dominant source of noise. The intensity of the light scattered by the particles to the PMT is very small as discussed earlier in the chapter. The magnitude of the power spectrum of the $G_1G_2\ n_{ID}(t)$ component of $n_I(t)$ is dependent on the intensity of light at the PMT, as is pointed out in the discussions on photon fluctuation and laser intensity fluctuation noise. Hence, if the light intensity at the PMT is small, the component $G_1G_2\ n_{ID}(t)$ could be quite small compared with the thermal noise component produced by the amplifiers. In this case, the dominant noise in $n_I(t)$ would be thermal noise which is white and Gaussian.

The noise model proposed for LIV systems was verified with the experimental LIV system described in Chapter II. The noise due to the detection system alone was measured to be 0.1 volt in the LDV system which was the same detection system used in the LIV system. The noise from the LIV system was measured with no lights on in the room and was also found

to be 0.1 volt. Under these conditions, background noise is negligible compared to the thermal noise from the amplifiers. The only other source of noise under these conditions is noise associated with the laser light scattered by the particles to the PMT. In order to estimate the amount of noise produced by the scattered light, the ratio R of the power in the signal to the power in the photon fluctuation noise follows from Eq. (5) as

$$R = \frac{G^2 I^2}{qG^2 I \Delta f} \tag{33}$$

$$= \frac{I}{q\Delta f}$$

$$= \frac{\bar{n}}{\Delta f}$$

where Δf is the bandwidth of the system and $\bar{n}$ is the number of photoelectrons per second emitted from the PMT. In the experimental work, Δf was limited by the recording system to be 20 kHz. The power of the scattered light was estimated to be 3.36×10^{-6} mw in Eq. (29). It follows that $\bar{n}$ is given by

$$\bar{n} = \frac{\eta\ (3.36 \times 10^{-6}\ \text{mw})}{h\nu} \tag{34}$$

$$= \frac{(0.06)(3.36 \times 10^{-9})(0.6328 \times 10^{-3})}{(6.624 \times 10^{-34})(3 \times 10^{11})}$$

$$= 6.40 \times 10^{8}\ \text{photoelectrons/sec}$$

With a value for $\bar{n}$, the ratio of Eq. (33) becomes

$$R = \frac{6.40 \times 10^{8}}{20 \times 10^{3}} \tag{35}$$

$$= 3.20 \times 10^{4}$$

The ratio of the power in the signal to the power in the photon fluctuation noise is 3.20×10^{4}. Since the rms value of the signal was about one volt, the rms voltage of the photon fluctuation noise was about

$$\frac{1 \text{ volt}}{\sqrt{R}} = \frac{1}{\sqrt{3.20 \times 10^{4}}} \tag{36}$$

$$= 0.0056 \text{ volt}$$

which is much less than the rms voltage of the thermal noise which was 0.1 volt. The laser intensity fluctuation noise was specified by the manufacturer to be less than one percent of the beam intensity. Since the PMT current is proportional to light intensity, the rms voltage of the noise should be about 0.01 volt when the rms voltage of the signal is one volt. Hence, the laser intensity fluctuation noise is also negligible compared to the thermal noise of the amplifiers.

In order to demonstrate the mode of operation in which background noise was a factor, the room lights were turned on. The rms voltage of the noise increased to 0.15 volt. Figure 44 is a spectrum analyzer trace of the noise with the lights on which shows the noise to have been still approximately white. The white lights were covered with yellow filters. This reduced the background noise level enough that the overall noise was slightly over 0.1 volt. Background noise can be reduced greatly by using

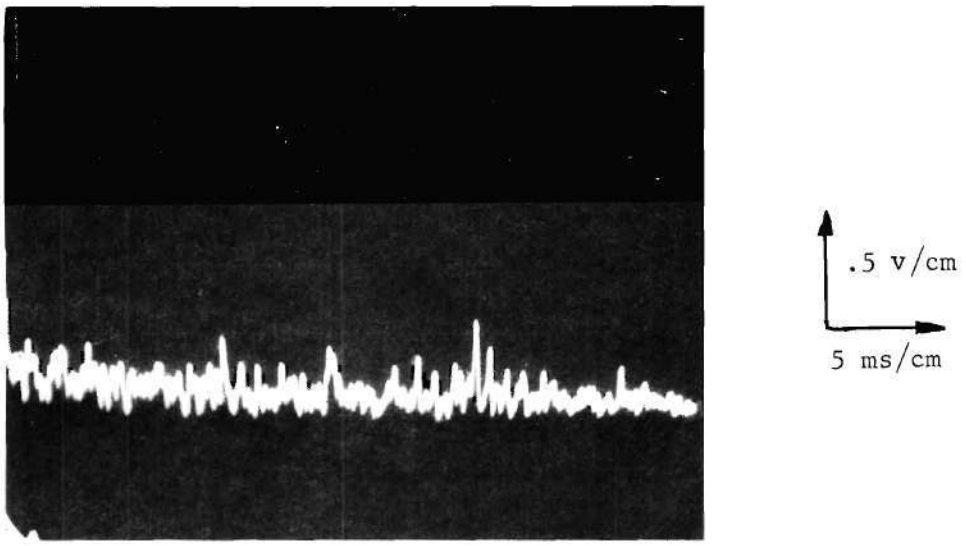

Figure 44. Power Spectrum from Zero to 20 kHz of the LIV Noise with the Room Lights on

colored filters. The background noise due to laser reflections was negligible in the experimental work since the geometry of the tunnel and airfoil allowed the PMT to be located where there were no laser reflections. There are instances in which the PMT might have to be located where there are laser reflections and these reflections will produce background noise.

There is a possible third mode of operation which has not yet been discussed in which both the noise due to background light and due to thermal noise is negligible. Suppose that the LIV system is so well aligned and the optics are so clean that no stray laser light falls on the PMT. Also, let the experiments be carried out in total darkness so that there is no background light due to stray laser beams or room lights. Assume too that the amplifiers are noise free and the PMT is cooled to eliminate dark current. Under these conditions, the only noise present would be the photon fluctuation noise and laser intensity fluctuation noise associated with the light scattered from the particles. The calculations from Eqs. (17) through (22) indicate that this noise is still Gaussian rather than Poisson for typical size lasers and smoke particles, and velocimeter signal estimators designed for operation in subsonic flows. However, if smaller particles are present, the photon fluctuation noise could be Poisson. Since there is no other noise present, the signals from infinitesimally small particles are detectable. The power spectra for the laser noises as given by Eqs. (5), (8), and (9) are all dependent on the intensity at the PMT. The intensity at the PMT in this case is time varying with no large and dominant component such as I_r in the LDV systems or I_B in other LIV systems. Therefore, the spectra of these noises is time

varying which means that the noise is nonstationary. Since this case has not been experimentally achieved in this thesis or reported in the literature to the author's knowledge, it is not further discussed.

CHAPTER IV

THE FOURIER TRANSFORM ESTIMATOR

Introduction

In the preceding chapters, the signal and noise models for LDV and LIV systems were derived. In this chapter, a procedure called the "Fourier transform estimator," to estimate the frequency of velocimeter signals, is described. The estimator is shown to perform well when the frequency of the signal is rapidly changing and the noise level is high. A means to implement the estimator is suggested and a statistical analysis of its performance is carried out.

Motivation and Description of the Fourier Transform Estimator

In Eqs. (86) and (87) of Chapter II, it is demonstrated that the LDV signal $r_{TD}(t)$ and the LIV signal $r_{TI}(t)$ can be written, respectively, as

$$r_{TD}(t) = \sum_{i=1}^{N} B_i \, e^{-\alpha(2\pi f_D)^2 (t-t_i)^2} \cos 2\pi f_D (t-t_i) + n(t) \qquad (1)$$

and

$$r_{TI}(t) = \sum_{i=1}^{N} B_i \, e^{-\alpha(2\pi f_D)^2 (t-t_i)^2} (1 + \cos 2\pi f_D (t-t_i)) + n(t) \qquad (2)$$

where B_i is the amplitude of the i^{th} pulse, t_i is the arrival time of the pulse, f_D is the frequency of the pulse, and N is the number of pulses

during a given time interval T. The dc component in $r_{TD}(t)$ is omitted because it can be filtered out by a very narrow band-stop filter at dc. The interval T is chosen to be small enough that all the pulses have the same frequency f_D. It is shown in Chapter III that n(t) under a wide variety of experiments, including the experiments carried out in this thesis, can be modeled as white Gaussian noise.

One means to estimate the frequency of velocimeter signals is to simply perform the Fourier transformation of the received signal and take the frequency estimate to be the frequency at which the transform is maximum. The Fourier transforms of $r_{TD}(t)$ and $r_{TI}(t)$ are shown in Appendix D to be, respectively,

$$R_D(f,f_D) = \int_o^T r_{TD}(t)\ e^{-j2\pi ft}dt \tag{3}$$

$$= \frac{1}{2f_D\sqrt{\pi\alpha}} \sum_{i=1}^{N} B_i\ e^{-j2\pi f_D t_i} \left\{\exp - \left[\frac{(f-f_d)^2}{4\alpha f_D^{\ 2}}\right] + \exp - \left[\frac{(f+f_D)^2}{4\alpha f_D^{\ 2}}\right]\right\} + N_T(f)$$

$$R_I(f,f_D) = \int_o^T r_{TI}(t)\ e^{-j2\pi ft}dt \tag{4}$$

$$= \frac{1}{2f_D\sqrt{\pi\alpha}} \sum_{i=1}^{N} B_i\ e^{-j2\pi f_D t_i} \left\{2\ \exp - f^2/4\alpha f_D^{\ 2} + \exp - \left[\frac{(f-f_D)^2}{4\alpha f_D^2}\right] + \exp - \left[\frac{(f+f_D)^2}{4\alpha f_D^2}\right]\right\} + N_T(f)$$

where $N_T(f)$ is the Fourier transform of the portion n(t) of the incoming signal which is T seconds long. It is apparent from Eq. (3) that $R_D(f,f_D)$ has its maximum values at $f = \pm f_D$ in the noiseless case, i.e., n(t) = 0. If the exponential centered at the origin in Eq. (4) is discounted, $R_I(f,f_D)$ also has its maximum value at $f = \pm f_D$ in the noiseless case.

The estimator should perform well at high noise levels since the signal is concentrated about $\pm f_D$ in the transform while the noise is spread uniformly along the frequency axis. The time resolution can be made arbitrarily high by making T small. This means that the estimator can track the velocity of rapidly changing flows. As N increases, the amplitudes of the signal portions of Eqs. (3) and (4) increase relative to noise portion. In other words, the performance of the estimator improves as more particles pass through the detection volume during T. As the particles become bigger or more reflective, B_i increases with the result that the signal portion of Eqs. (3) and (4) increases relative to the noise portion. In addition to the estimator being intuitively workable, it can be motivated from the statistically optimum estimator for the LDV system. Appendix B states the optimum estimator and shows its relationship to the Fourier transform estimator.

Implementation of the Fourier Transform Estimator

Coherent optical data processing techniques, already used in a number of applications,[28,29] present a reliable and quick means to perform the Fourier transform operation. The signal is recorded as an amplitude transmission variation on photographic film. Then the film is illuminated by a coherent beam of light which modulates the beam with the information

on the film. The light from the film passes through a lens which performs the Fourier transform operation. Optical data are especially convenient in this application since the incoming signals can be as high as 100 mHz and the most promising means to record such high frequency signals are film recorders. Magnetic tape recorders, not having the high storage capacity of photographic film, cannot record frequencies above a few megahertz.

The data are recorded on film as illustrated by the schematic in Figure 45. The incoming signal is inverted by an amplifier and is passed into a light modulator which modulates a collimated beam of light. The light from the modulator is focused by a lens onto a moving strip of film which is mechanically driven in the focal plane of the lens. The exposure of the film varies as the intensity of the modulated light beam and produces a variable exposure line on the film. The film, when developed, has an amplitude transmission variation related to the exposure by an amplitude transmission-exposure (T-E) curve shown in Figure 46. The average intensity of the beam is chosen to bias the signal in the center of the linear portion and the amplitude of the modulation is chosen to keep the recorded signal within the linear region of the curve. Generally, the center of the linear portion of the curve is at a transmission of 0.5 and the linear region extends from a transmission of 0.2 to 0.8. As the incoming signal increases positively, the light intensity decreases and the transmission of the film increases. The purpose of the inverting amplifier is to take into account the negative slope of the T-E curve.

The light beam being modulated can be a coherent beam such as a

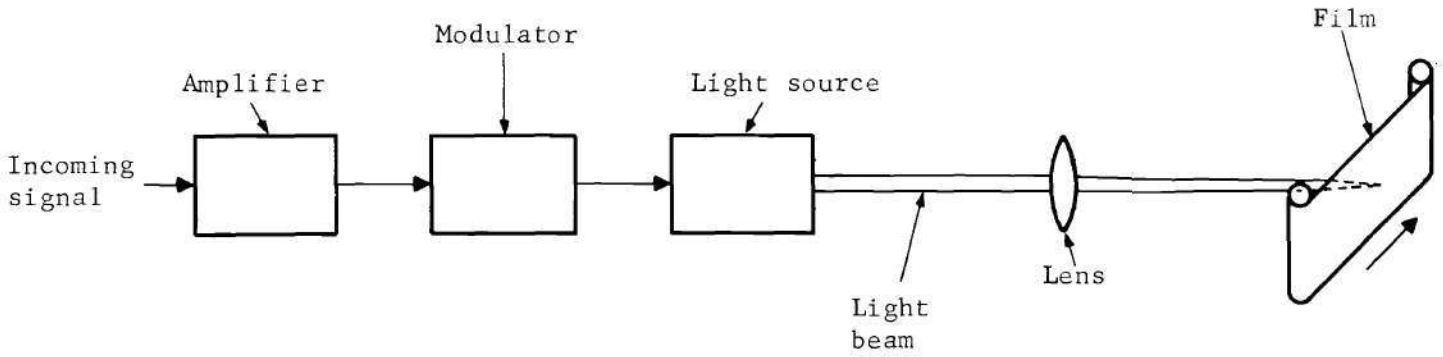

Figure 45. Schematic of a System to Write Data as Amplitude Variations on Film

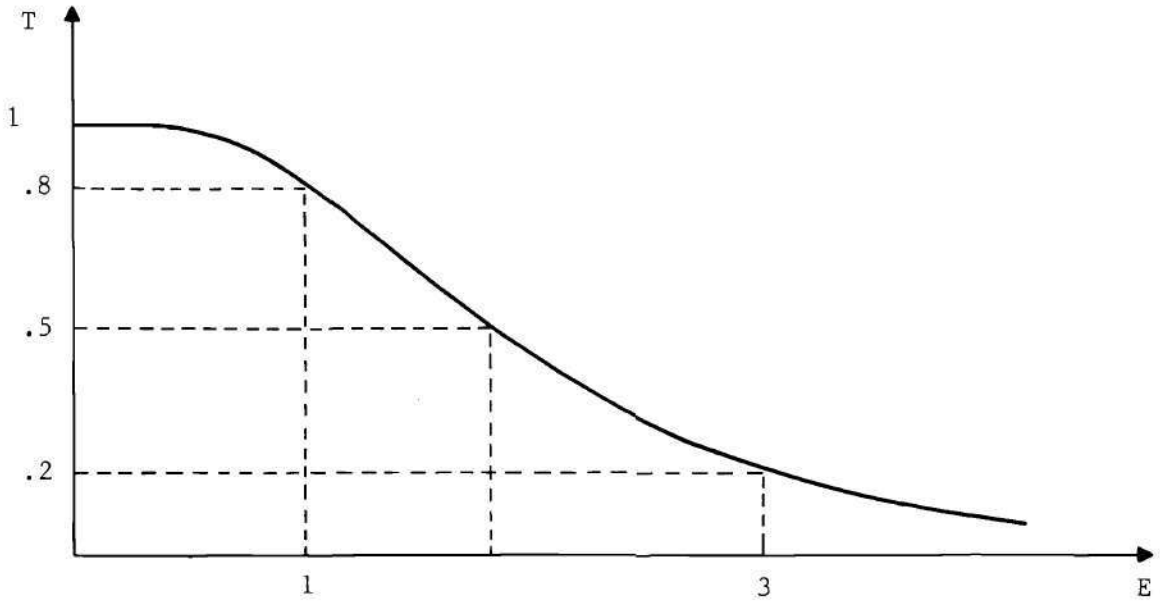

Figure 46. Typical Amplitude Transmission vs. Exposure (T-E) Curve for High Resolution Film

laser beam and the modulator can be a Pockel's cell. Alternatively, a light modulating galvanometer with a coherent or incoherent beam could be used. The lens is usually a one dimensional lens which focuses the beam down to a narrow line rather than a circular spot. The advantage of using a line rather than a spot is that the line spreads the data out over a larger area allowing a larger beam to be used in the subsequent data processing system. Generally, high resolution film such as holographic film with resolution in excess of 2000 lines/mm is used. A commercial unit utilizing a laser, a Pockel's cell, a one dimensional lens, and holographic film is described in reference 30. The dynamic range of the system is the ratio of the intensity of the largest linearly recordable signal to the smallest detectable signal and is generally 30 db. The limiting factor in dynamic range is film grain noise. The width of the line focused on the film limits the spatial frequency of the amplitude transmission pattern which can be written on the film to a density of about 200 lines per mm.

The signal, having been recorded on film, is processed by the optical data processing system shown in Figure 47. A collimated beam of light from a cw laser illuminates the film whose amplitude transmission is given by $r_{TD}(t)$ or $r_{TI}(t)$ where t is now considered to be a spatial dimension. The light leaving the film has a complex amplitude proportional to the amplitude transmission of the film. It is shown in a number of references[31,32] that the complex amplitude of the light in the focal plane of the lens is $R_D(f,f_D)$ or $R_I(f,f_D)$ where f is the spatial

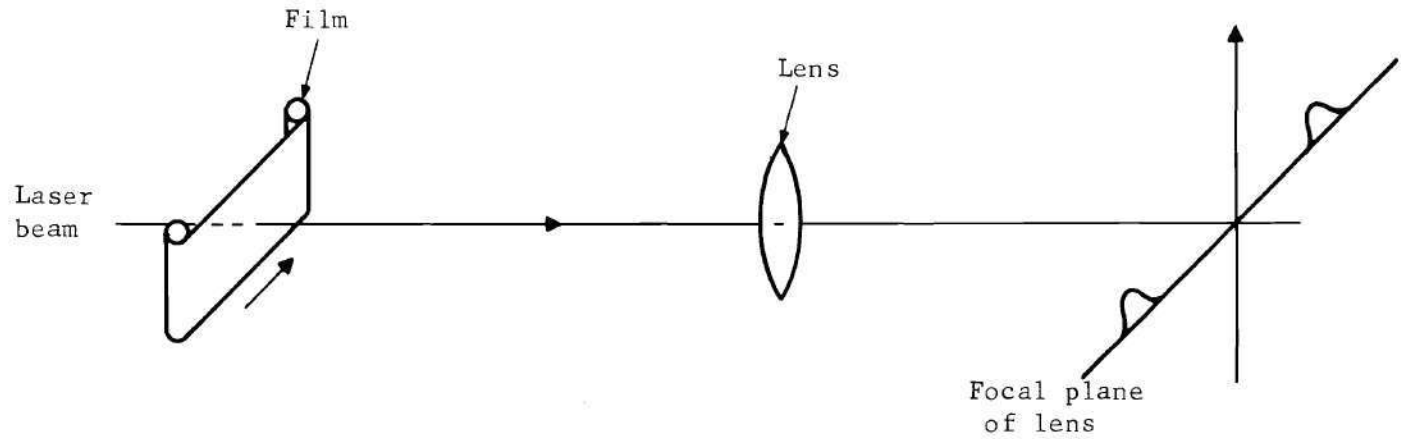

Figure 47. Optical Implementation of the Fourier Transform Estimator

dimension in the focal plane.* The phase of the light is usually not very important since light detectors sensitive only to intensity are placed to the right of the lens. An aperture of width T is placed in the plane of the film to control the length of the sample over which the Fourier transform is taken. The choice of T depends on the resolution in time to which the frequency is to be estimated. A light detector, such as a photomultiplier tube preceded by a slit, is used to measure the intensity of the light at each position in the focal plane. By noting the position f where the light intensity is maximum, an estimate of f_D is obtained.

Figure 48 is a schematic of a laser velocimeter system utilizing optical data processing techniques. The system consists of a data recorder section, a velocimeter section, and an estimator section. The light from the laser strikes the beam splitter. Part of the light goes through the beam splitter and drives the laser velocimeter. The rest of the light passes through a Pockel's cell which modulates the light beam. When the data are ready for processing, a mirror is inserted into the system which directs the beam to the data reduction section. Currently, the only available commercial film requires developing. However, "real

---

*The complex wavefront in the right focal plane of the lens is an exact Fourier transform of the signal recorded on film only if the light beam illuminating the film is collimated and the film is placed in the left focal plane. There are several other configurations which produce a wavefront to the right of the lens whose amplitude is the amplitude of the Fourier transform of the signal on the film.[32] However, the phase of the wavefront is not always the phase of the Fourier transform. Since the estimator only locates the maximum value of the transform, the phase of the transform is unimportant and these other configurations can be used if convenient.

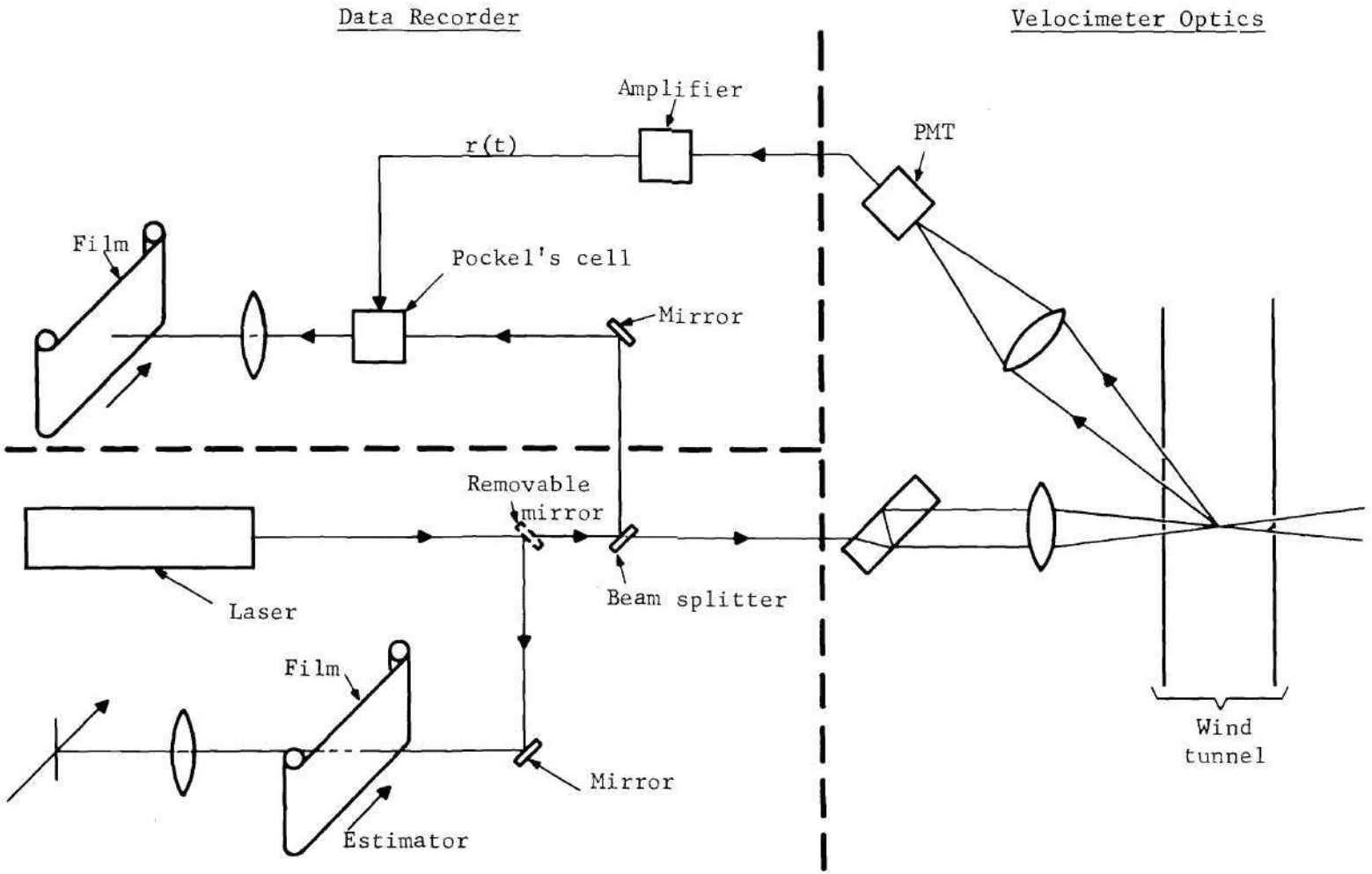

Figure 48. Schematic of Velocimeter Optics, Data Recorder, and Estimator Combined into One Unit

time" film which does not need developing is now being investigated by a number of organizations. Such a real time film would eliminate the delay time required for developing. The proposed system has the potential of being a portable, inexpensive, self-contained unit which can be easily moved from one tunnel to another.

Bound on the Risk of the Fourier Transform Estimator

A bound on the risk with respect to a uniform cost function is derived for the LDV and LIV signals when the noise is white and Gaussian. The analysis is carried out in terms of a signal $r_T(t)$ given by

$$r_T(t) = s(t,f_D) + n(t) \tag{5}$$

where $n(t)$ is white Gaussian noise and $s(t,f_D)$ is given by

$$\sum_{i=1}^{N} B_i \, e^{-\alpha(2\pi f_D)^2(t-t_i)^2} \cos 2\pi f_D(t-t_i) \tag{6}$$

if the signal is from an LDV system and by

$$\sum_{i=1}^{N} B_i \, e^{-\alpha(2\pi f_D)^2(t-t_i)^2} (1 + \cos 2\pi f_D[t-t_i]) \tag{7}$$

if the signal is from an LIV system. There are several unknowns in the above expressions, but the only one of any importance is f_D. The time interval T over which the estimate is to be made is chosen to give the required resolution in time. In effect, time is quantized into segments

of duration T and f_D is estimated for each segment. There is no practical reason to estimate the arrival time t_i of each particle. The estimate of f_D is made by noting the frequency at which the Fourier transform of the signal is maximum. The magnitude of the maximum value of the transform is dependent on t_i, B_i, and N, but its location on the frequency axis is not. For these reasons, f_D is the only parameter which is estimated and the bound on the risk of the estimator is found as a function of t_i, B_i, and N. The dependence of bound on N shows the advantages of using heavy seeding or many particles in the flow as compared to few particles in the flow or light seeding. As the number of particles increases, more signal becomes available and the bound should decrease. The dependence of the bound on B_i shows the advantages of using big or highly reflective particles. The signal amplitude increases as the particles become more reflective or bigger and the bound should again decrease. Although f_D could be modeled as Gaussian in turbulent flows, the mean and variance of the density are usually unknown. Since the statistics of f_D are difficult to determine beforehand, all frequencies will be assumed as equally likely to occur, i.e., f_D is assumed to be uniformly distributed between 0 and the maximum frequency f_{max} that can be estimated with the velocimeter. With this assumption, the probability density $p(f_D)$ becomes

$$p(f_D) = \frac{1}{f_{max}} \qquad 0 \leq f \leq f_{max} \tag{8}$$

$$= 0 \text{ elsewhere.}$$

The expression for the risk V of the Fourier transform estimator

follows from the definition of risk given by Van Trees[33] and is

$$V = \int_{-\infty}^{\infty} C[f_D, \hat{f}_{DF}(\bar{R})]\ p(\bar{R}/f_D)\ p(f_D)\ d\bar{R}df_D \tag{9}$$

The components of the vector $\bar{R}$ are the values of the Fourier transform at various points on the frequency axis. Since the frequency axis is a continuum of points, the Fourier transform is observed at frequency intervals of Δf. The interval Δf is chosen to be $1/T$ as dictated by the Sampling theorem.[34] The estimate made by the proposed estimator is denoted by $\hat{f}_{DF}(\bar{R})$ and is the frequency corresponding to the largest component of $\bar{R}$. The actual frequency of the signal is f_D. The conditional probability of $\bar{R}$ with respect to f_D is $p(R/f_D)$. The cost function $C[f_D, \hat{f}_D(\bar{R})]$ is uniform and is given by

$$\begin{aligned} C[f_D, \hat{f}_D(\bar{R})] &= 1 \qquad \hat{f}_D(\bar{R}) \neq f_D \\ &= 0 \qquad f_D(\bar{R}) = f_D \end{aligned} \tag{10}$$

In other words, equal cost is assigned to all incorrect estimates and zero cost is assigned to the correct estimate.

A bound to the risk V is now derived. By substituting Eq. (8) into Eq. (9), V becomes

$$V = \frac{1}{f_{max}} \int_{-\infty}^{\infty} \int_{o}^{f_{max}} C[f_D, \hat{f}_{DF}(\bar{R})]\ p(\bar{R}/f_D)\ df_D d\bar{R} \tag{11}$$

The frequency f_D is now quantized into intervals of Δf where Δf is $1/T$.

Approximating the integral over f_D in Eq. (11) by a summation, V is given by

$$V = \frac{\Delta f}{f_{max}} \sum_{i=1}^{M} \int_{-\infty}^{\infty} C[k\Delta f, \hat{f}_{DF}(\bar{R})]\ p(\bar{R}/k\Delta f)\ d\bar{R} \tag{12}$$

$$= \frac{1}{M} \sum_{i=1}^{M} \int_{-\infty}^{\infty} C[k\Delta f, \hat{f}_{DF}(\bar{R})]\ p(\bar{R}/k\Delta f)\ d\bar{R}$$

where $f_{max} = M\Delta f$. If the cost function defined in Eq. (11) is substituted into the integral, the expression for V becomes

$$V = \frac{1}{M} \sum_{i=1}^{M} \int_{\bar{R}_o} p(\bar{R}/k\Delta f)\ d\bar{R} \tag{13}$$

The region $\bar{R}_o$ is defined as the region of the observation space in which the estimate $\hat{f}_{DF}(\bar{R})$ is not equal to $k\Delta f$ when the actual signal frequency is $k\Delta f$. In other words, the integral of Eq. (13) is the probability of error of the estimator when a signal of frequency $k\Delta f$ is received. Since the estimate is the frequency at which the Fourier transform is maximum, Eq. (13) can be rewritten as

$$V = \frac{1}{M} \sum_{k=1}^{M} P[\text{any} |R_\ell| > |R_k| k \neq \ell] \tag{14}$$

R_ℓ is the value of the Fourier transform at the frequency $\ell\Delta f$ and $P[\cdot]$ denotes probability. By definition, the probability above is equal to

$$P[\text{any} |R_\ell| > |R_k|\ k \neq \ell] = P[(|R_1| > |R_k|) \bigcup (|R_2| > |R_k|) \tag{15}$$

$$\ldots (|R_\ell| > |R_k|) \ldots (|R_M| > |R_k|)]\ \ell \neq k$$

Since several R_ℓ can be greater than R_k the events $(|R_\ell| > |R_k|)$ are not mutually exclusive. Hence the following inequality results

$$P[\text{any } R_\ell > R_k,\ k \neq \ell] \leq P[|R_1| > |R_k|] + P[|R_2| > |R_k|] \tag{16}$$
$$+ \ldots + P[|R_\ell| > |R_k|] + \ldots + P[|R_M| > |R_k|] \qquad k \neq \ell$$

Substituting (16) into (14), a bound on V is obtained

$$V \leq \sum_{\substack{k=1 \\ k \neq \ell}}^{M} \sum_{\ell=1}^{M} P[|R_\ell| > |R_k|] \tag{17}$$

It should be noted that the bound of Eq. (17) differs from the exact value of V only in that several R_ℓ could be larger than R_k. However, if the signal to noise ratio is high enough, the chances that several R_ℓ are greater than R_k become small. Hence, as the signal to noise ratios increase, the bound becomes asymptotically close to V.

The bound on the risk given by Eq. (17) is now evaluated. The probability density $p(|R_\ell|/k\Delta f)$ is derived and then used to obtain $P[|R_\ell| > |R_k|]$. It follows from Eqs. (6) and (7) that R_i is given by

$$R_\ell = |D(\ell\Delta f, k\Delta f)\ e^{j\phi} + N_T(\ell\Delta f)| \tag{18}$$

If the signal is from an LDV system,

$$R_\ell = R_D(\ell\Delta f, k\Delta f) \tag{19}$$

(continued)

$$D(\ell\Delta f, k\Delta f) = \frac{1}{2k\Delta f\sqrt{\pi\alpha}} \left| \sum_{i=1}^{N} B_i \, e^{-j2\pi(k\Delta f)t_i} \right| \left\{ \exp - \left[\frac{(\ell-k)^2}{4\alpha k^2} \right] \right.$$

$$\left. + \exp - \left[\frac{(\ell+k)^2}{4\alpha k^2} \right] \right\}$$

$$\phi = \angle \left(\sum_{i=1}^{N} B_i \, e^{-j2\pi k\Delta f t_i} \right)$$

If the signal is from an LIV system,

$$R_\ell = R_I(\ell\Delta f, k\Delta f) \tag{20}$$

$$D(\ell\Delta f, k\Delta f) = \frac{1}{2k\Delta f\sqrt{\pi\alpha}} \left| \sum_{i=1}^{N} B_i \, e^{-j2\pi k\Delta f t_i} \right| \left\{ 2 \exp - \left[\frac{\ell^2}{4\alpha k^2} \right] \right.$$

$$\left. + \exp - \left[\frac{(\ell-k)^2}{4\alpha k^2} \right] + \exp - \left[\frac{(\ell+k)^2}{4\alpha k^2} \right] \right\}$$

$$\phi = \angle \left(\sum_{i=1}^{N} B_i \, e^{-j2\pi k\Delta f t_i} \right)$$

The only difference in the two sets of definitions is the low-pass Gaussian term in the LIV signal. In deriving the density $p(R_\ell/k\Delta f)$, the first term of Eq. (18) can be thought of as deterministic and the second as random. The probability density of $N_T(\ell\Delta f)$ is found and used to determine $p(R_\ell/k\Delta f)$.

Since the expression for $N_T(\ell\Delta f)$ given by

$$N_T(\ell\Delta f) = \int_o^T n(t)\ e^{-j2\pi\ell\Delta ft}dt \tag{21}$$

considers only the portion of n(t) between 0 and T, n(t) is assumed periodic over all time with period T. With the periodic assumption, n(t) can be expressed by a Fourier Series of period T as follows[36]

$$n(t) = \sum_{q=1}^{\infty} a_q \cos(2\pi q\Delta ft) + b_q \sin(2\pi q\Delta ft) \tag{22}$$

$$a_q = \frac{2}{T}\int_o^T n(t)\cos 2\pi q\Delta ft\ dt$$

$$b_q = \frac{2}{T}\int_o^T n(t)\sin 2\pi q\Delta ft\ dt$$

Since n(t) is Gaussian and mean zero, a_q and b_q are also Gaussian and mean zero. The variance of a_q is given by

$$< a_q^{\,2} > = \frac{4}{T^2}\int_o^T\int <n(t_1)\ n(t_2)>\cos(2\pi q\Delta ft_1)\ \cos(2\pi q\Delta ft_2) \tag{23}$$

$$\times\ dt_1 dt_2$$

The noise n(t) is white and therefore its autocorrelation is

$$< n(t_1)\ n(t_2) > = \frac{N_o}{2}\ \delta(t_1 - t_2) \tag{24}$$

Utilizing the sifting properties of the delta function, $< a_q^{\,2} >$ becomes

$$<a_q^2> = \frac{4}{T^2}\int_o^T\int \frac{N_o}{2}\,\delta(t_1 - t_2)\,\cos(2\pi q\Delta f t_1)\,\cos(2\pi q\Delta f t_2)\,dt_1 dt_2 \qquad (25)$$

$$= \frac{2N_o}{T^2}\int_o^T \cos^2(2\pi q\Delta f t_1)\,dt_1$$

$$= \frac{N_o}{T}$$

By a similar analysis, $< b_q^2 >$ is given by

$$< b_q^2 > = \frac{N_o}{T} = < a_q^2 > \qquad (26)$$

The coefficients a_q and b_r are also uncorrelated and hence independent as can be seen by evaluating

$$< a_q b_r > = \frac{4}{T^2}\int_o^T\int < n(t_1)\,n(t_2) > \cos 2\pi q\Delta f t_1\,\sin 2\pi r\Delta f t_2\,dt_1 dt_2 \qquad (27)$$

$$= \frac{2N_o}{T^2}\int_o^T\int \delta(t_1 - t_2)\,\cos 2\pi q\Delta f t_1\,\sin 2\pi r\Delta f t_2\,dt_1 dt_2$$

$$= \frac{2N_o}{T}\int_o^T \cos 2\pi q\Delta f t_1\,\sin 2\pi r\Delta f t_2\,dt_1 dt_2$$

$$= 0$$

Having found the statistics of the Fourier coefficients, the statistics of $N_T(\ell\Delta f)$ follow by substituting Eq. (22) for n(t) into the expression (18) for $N_T(\ell\Delta f)$ as follows

$$N_T(\ell\Delta f) = \int_o^T n(t)\ e^{-j2\pi\ell\Delta ft}\ dt \tag{28}$$

$$= \sum_{q=1}^{\infty} a_q \int_o^T \cos(2\pi q\Delta ft)\ e^{-j2\pi\ell\Delta ft}\ dt$$

$$+ b_q \int_o^T \sin(2\pi q\Delta ft)\ e^{-j2\pi\ell\Delta ft}\ dt$$

By substituting $e^{-j[2\pi\ell\Delta ft]} = \cos 2\pi\ell\Delta ft + j \sin 2\pi\ell\Delta ft$ into Eq. (26) and using standard integration tables,[37] $N_T(\ell\Delta f)$ becomes

$$N_T(\ell\Delta f) = \sum_{q=1}^{\infty} \frac{a_q T}{2}\left[\text{sinc } 2\pi\Delta f(\ell-q)\ T/2 + \text{sinc } 2\pi\Delta f(\ell+q)\ T/2\right] \tag{29}$$

$$+ \frac{jb_q T}{2}\left[\text{sinc } 2\pi\Delta f(\ell-q)\ T/2 + \text{sinc } 2\pi\Delta(\ell+q)\ T/2\right]$$

Observe that the only terms in the above summation which make a contribution to $N_T(\ell\Delta f)$ are the terms for which $q = \ell$. All of the terms q for which $q \neq \ell$ have a zero crossing at the frequency $\ell\Delta f$. With this in mind, $N_T(\ell\Delta f)$ can be written as

$$N_T(\ell\Delta f) = \frac{a_\ell T}{2} - j\,\frac{b_\ell T}{2} \tag{30}$$

Since a_ℓ and b_ℓ are both Gaussian with zero mean and equal variance and also statistically independent, it follows that the amplitude of $N_T(\ell\Delta f)$ is Rayleigh distributed and that the phase of $N_T(\ell\Delta f)$ is uniformly distributed from 0 to 2π.[34]

With the probability density of $N_T(\ell\Delta f)$ determined, the probability density $p(|R_\ell|/k\Delta f)$ can be readily obtained. Substituting Eq. (28) into (16), R_ℓ becomes

$$R_\ell = D(\ell\Delta f, k\Delta f)\ e^{j\phi} + \frac{a_\ell T}{2} - j\,\frac{b_\ell T}{2} \tag{31}$$

The real part of R_ℓ is Gaussian with a mean of $D(\ell\Delta f, k\Delta f)$. The imaginary part of R_ℓ is zero mean Gaussian with the same variance as the real part. It is demonstrated in a number of references[38,39] that the probability density of the amplitude of such a random variable is a Rician density given by

$$p(|R_\ell|/k\Delta f) = \frac{4|R_\ell|}{N_o T}\left\{\exp - \left[\frac{|R_\ell|^2 + D^2(\ell\Delta f, k\Delta f)}{N_o T/2}\right]\right\} \cdot I_o\left(\frac{4D(\ell\Delta f, k\Delta f)\ |R_\ell|}{N_o T}\right) \tag{32}$$

The expression for $p(|R_\ell| > |R_k|)$ is found by integrating the above probability densities as follows

$$P[|R_\ell| > |R_k|] = \int_o^\infty p(|R_k|/k\Delta f) \int_{|R_k|}^\infty p(|R_\ell|/k\Delta f)\ d|R_\ell| d|R_k| \tag{33}$$

The above integral has been evaluated by Stien[40] and is given by

$$P(|R_\ell| > |R_k|) = \left[Q(\sqrt{g_\ell}, \sqrt{h_k}) - \frac{1}{2}\exp\left(-\frac{g_\ell + h_k}{2}\right) I_o(\sqrt{g_\ell, h_k})\right] \tag{34}$$

(continued)

$$g_\ell = \frac{D^2(\ell\Delta f, k\Delta f)}{N_o T/2}$$

$$h_k = \frac{D^2(\ell\Delta f, k\Delta f)}{N_o T/2}$$

$$Q(\sqrt{g_\ell}, \sqrt{h_k}) = \int_{h_k}^{\infty} \exp - \left[\frac{g_\ell + x^2}{2}\right] I_o(x\sqrt{g_\ell}) \; x \; dx$$

The bound on V from Eq. (16) is the summation of the probabilities $P(|R_\ell| > |R_k|)$ and is given by

$$V \leqq \sum_{\substack{k=1 \\ k \neq \ell}}^{M} \sum_{\ell=1}^{M} P(|R_\ell| > |R_k|) \tag{35}$$

$$\leqq \sum_{\substack{k=1 \\ k \neq \ell}}^{M} \sum_{\ell=1}^{M} \left[Q(\sqrt{g_\ell}, \sqrt{h_k}) - \frac{1}{2} \exp\left(-\frac{g_\ell + h_k}{2}\right) I_o(\sqrt{g_\ell h_k})\right]$$

A few conclusions regarding the performance of the estimator can be made by studying the bound on V given by Eq. (35). The bound depends strongly on g_ℓ and h_k and it is shown in Appendix C that the bound becomes arbitrarily small as g_ℓ and h_k increase. As the amplitudes B_ℓ of the pulses increase, the signal becomes stronger relative to the noise. From Eqs. (18, 19, and 34), it is apparent that g_ℓ and h_k increase with B_i and the bound therefore decreases. As the noise power N_o decreases, the bound also decreases. When the number of particles N during the interval T increases, more signal becomes available. The bound is also seen to decrease as N becomes large. The parameter α determines the bandwidth of the signal. A small value of α means a narrow bandwidth

signal and it is easier to estimate the frequency of a narrow band signal as compared to a wide band signal. It is also clear from Eqs. (18, 19, and 34) that the bound decreases as α decreases. As T becomes large, the definitions of g_ℓ and h_k indicate that they decrease and the bound increases. This behavior shows that increasing T without increasing N degrades the estimator's performance. As T is increased, only noise is brought into the signal unless the number of particles N is also increased.

Signal to Noise Ratio

In order to evaluate the performance of the estimator operating on data with various noise levels, it is convenient to define a signal-to-noise ratio S_N. This quantity should be easy to measure and be indicative of the relative strengths of the signal and the noise. The incoming signal from which S_N is determined is given by Eq. (5) as

$$r_T(t) = s(t,f_D) + n(t) \tag{36}$$

The proposed definition of S_N is

$$S_N = \frac{\int_{-f_H}^{f_H} |S(f,f_D)|^2 df}{\int_{-f_H}^{f_H} |N_T(f)^2 df} \tag{37}$$

The quantities $S(f,f_D)$ and $N_T(f)$ are the Fourier transforms of portions of $s(t,f_D)$ and $n(t)$ which are T seconds long and f_H is the upper frequency cut-off of the estimator. The quantity S_N is the ratio of the area under

the square of the Fourier transform of the signal to the area under the square of the Fourier transform of the noise or equivalently the ratio of signal energy to noise energy. The numerator and denominator of S_N can be measured by optically performing the Fourier transform of the incoming signal $r_T(t)$ and measuring the intensity of the light in the Fourier transform plane of the lens. The procedure for experimentally measuring S_N is described in Chapter V.

It is shown in Appendix D that the area under the Fourier transform of the signal $S(f,f_D)$ is given by

$$\int_{-f_H}^{f_H} |S(f,f_D)|^2 df = \sqrt{\frac{2}{\pi\alpha}} \left(\frac{3}{2f_D}\right) \sum_{i=1}^{N} B_i^2 \tag{38}$$

if the signal is from an LIV system and by

$$\int_{-f_H}^{f_H} |S(f,f_D)|^2 df = \sqrt{\frac{2}{\pi\alpha}} \left(\frac{1}{2f_D}\right) \sum_{i=1}^{N} B_i^2 \tag{39}$$

if the signal is from an LDV system. The denominator of S_N is a random variable since $n(t)$ is random. The mean value of the denominator of S_N is given by

$$< \int_{-f_H}^{f_H} |N_T(f)|^2 df > = \int_{-f_H}^{f_H} < |N_T(f)|^2 > df \tag{40}$$

It is shown by Davenport and Root[41] that for large T

$$< |N_T(f)|^2 > \simeq \frac{N_o T}{2} \tag{41}$$

since n(t) is white noise. Substituting Eq. (39) into Eq. (38), the mean value of the denominator becomes

$$< \int_{-f_H}^{f_H} |N_T(f)|^2 df > = N_o T f_H \tag{42}$$

From Eqs. (37, 38, 39, and 42), S_N is approximately equal to

$$S_N \approx \frac{\sqrt{\frac{2}{\pi\alpha}} [3/2f_D] \sum_{i=1}^{N} B_i^2}{N_o T f_H}$$

for LIV signals and

$$S_N \approx \frac{\sqrt{\frac{2}{\pi\alpha}} [1/2f_D] \sum_{i=1}^{N} B_i^2}{N_o T f_H} \tag{43}$$

for LDV signals. The signal to noise ratio increases as the signal amplitudes B_i increase. As α and f_D decrease, the signal's duration is longer and S_N increases. Increasing N, the number of particles recorded in length L, also increases S_N. The ratio S_N decreases as N_o, the spectrum of the noise, increases.

CHAPTER V

EXPERIMENTAL EVALUATION OF ESTIMATOR

Introduction

The Fourier transform estimator is derived in Chapter III and its performance analysed in Chapter IV. This chapter describes the experimental evaluation of a prototype of the estimator. First of all, the LDV and LIV signals which were generated by the velocimeters described in Chapter II were recorded as amplitude transmission variations on photographic film. The recording of the data on film was carried out by means of an optical data recorder whose prime components are a light modulating galvanometer and a precision film drive. The transfer function of the data recording system and the noise produced by it were experimentally determined. The prototype estimator was constructed with standard optical components and its performance in estimating the frequency of various velocimeter signals was determined. The signals were steady and time varying LDV and LIV signals under various noise conditions and particle concentrations. It was demonstrated that the estimator was capable of tracking time varying and steady flows with high noise and low particle concentrations.

Recording of the Velocimeter Signals on Film

Description of Recording System

The velocimeter signals, recorded on magnetic tape as described

in Chapter II, were recorded as amplitude transmission variations on photographic film with the system depicted in Figure 49. The FM tape recorder played back the recorded signals into a power amplifier. The power amplifier was necessary because the tape recorder did not provide enough current to drive the light modulating galvanometer. The light modulating galvanometer is a Bach-Auricon Modulite TD-70 galvanometer. Essentially, the galvanometer produces a slit of light whose width varies in proportion to the current supplied by the amplifier. The slit is then focused by a lens mounted in the front of the galvanometer assembly. When the slit is wide due to a large signal from the amplifier, the focal region of the lens is bright since a great deal of light passes through the wide slit. When the slit is narrow due to a small signal from the amplifier, the focused beam is dim since little light passes through the slit. Hence the intensity of the focused slit varies in proportion to the signal to be recorded.

The film is mounted in a holder which is fastened to a precision drive mechanism which translates the film. The position of the galvanometer is adjusted so that the focused light beam falls in the same plane as the film. As the drive mechanism moves the film, the intensity of the focused beam is varied by the signal to be recorded producing a varying exposure on the film. When developed, the amplitude transmission of the film is proportional to the signal played by the tape recorder.

The film chosen was Agfa-Gevaert 10E56 film which is a high resolution holographic film.* A high resolution film is desirable in this

*Agfa Gevaert 10E56 film was chosen primarily because of its high resolution, low noise, and speed characteristics. The resolution of the

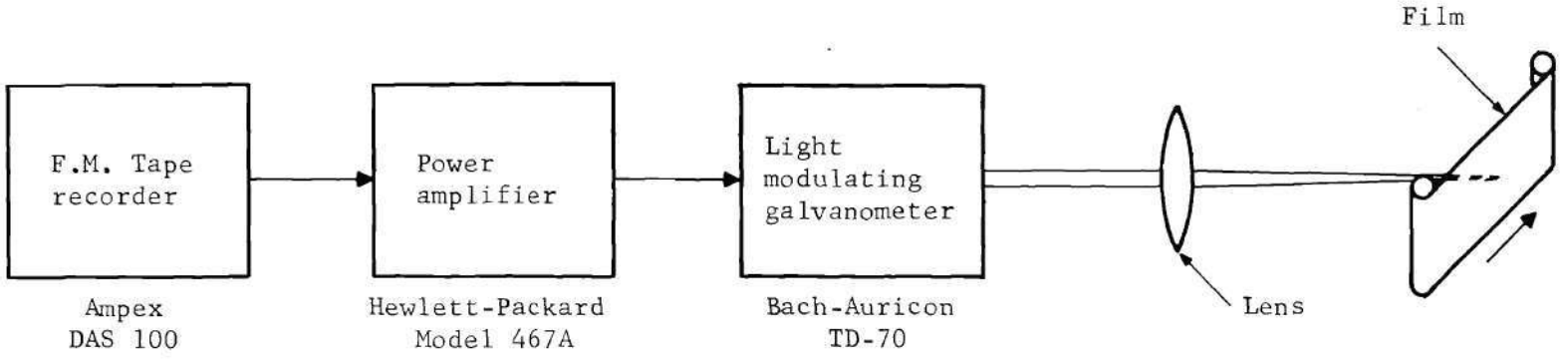

Figure 49. Schematic of System Used in the Experimental Work to Record Velocimeter Signals on Film

application because of its wide transfer function and low grain noise. This film, according to the manufacturer, has a transfer function which is flat to 2000 lines/mm. The mechanism which moves the film is the drive from a Nuclear Science and Engineering Mossbauer Effect Analyser. The drive is a well built precision drive which can move the film at speeds which can be varied continuously from .01 mm/sec to 15 mm/sec.

The beam from the galvanometer was too large to write data on film at the high spatial frequencies desired in this application. Therefore, the beam was reduced by a 16X microscope objective fastened to the front of the galvanometer. The beam after reduction was 21 microns wide and 3 mm high. After the film was exposed, it was developed for 5 minutes in D-19 developer at 68 $^{\circ}$F followed by 30 seconds in a stop bath and five minutes in a fixer solution. In order to obtain repeatable results, it was necessary to control the temperature of the developer within a quarter of a degree.

Before the system could be used to record data, it was necessary to adjust it so that the recording on the film was linear. The essential element governing the linearity was the photographic film. The exposure of the film is related to the amplitude transmission of the film by the amplitude transmission-exposure (T-E) curve shown for Agfa-Gevaert 10E56

---

film is quoted by the manufacturer to be 2000 lines/mm. Although data are not recorded in this thesis at spatial frequencies greater than 100 lines/mm, the high resolution of this film insures that the film transfer function is flat at least out to 100 lines/mm. Also, high resolution film implies that the film grain size is small which means that the film grain noise is minimal. Of the films whose resolutions are in the order of 2000 lines/mm (e.g. E-K 649F, Agfa 8E56, etc.) 10E56 requires the least exposure (50 ergs/cm^2) to produce an amplitude transmission of 0.5.

in Figure 50. From Figure 50, one can see that the center of the linear portion of the T-E curve occurs at a value of 0.5 in transmission and that the linear portion of the curve extends roughly from transmissions of 0.25 to 0.75. The exposure varies by a ratio of three to one over the linear portion of the curve. In order to insure a linear recording, the exposure must be biased in the center of the T-E curve and the ratio of maximum to minimum exposures cannot be larger than three to one.

The transmission of the film was biased at 0.5 as follows. An arbitrary but convenient film drive speed of 7.5 mm/sec was chosen and a piece of film was exposed in the system with several different voltages on the light bulb in the galvanometer. No signal was applied to the galvanometer. The transmission of the film was measured with a densitometer and the voltage on the bulb which produced a transmission of 0.5 was noted. The recorder was operated at this voltage and film speed which insures that the system is biased in the center of the T-E curve.

Next, the amplifier was set so that the transmission of the film fell between 0.25 and 0.75. A low frequency sinusoidal signal was recorded on the tape recorder and played back through the system. The amplitude of the signal was chosen so that it was as large as the amplitude of the velocimeter signals to be recorded. A microscope was set up in front of the galvanometer and focused on the variable aperture slit. The observer could watch the slit open and close when the low frequency signal was applied. The gain of the power amplifier was adjusted until the ratio of the maximum to minimum slit width was three to one. Therefore the ratio of maximum to minimum exposure was three to one and the signal remained in the linear portion of the T-E curve.

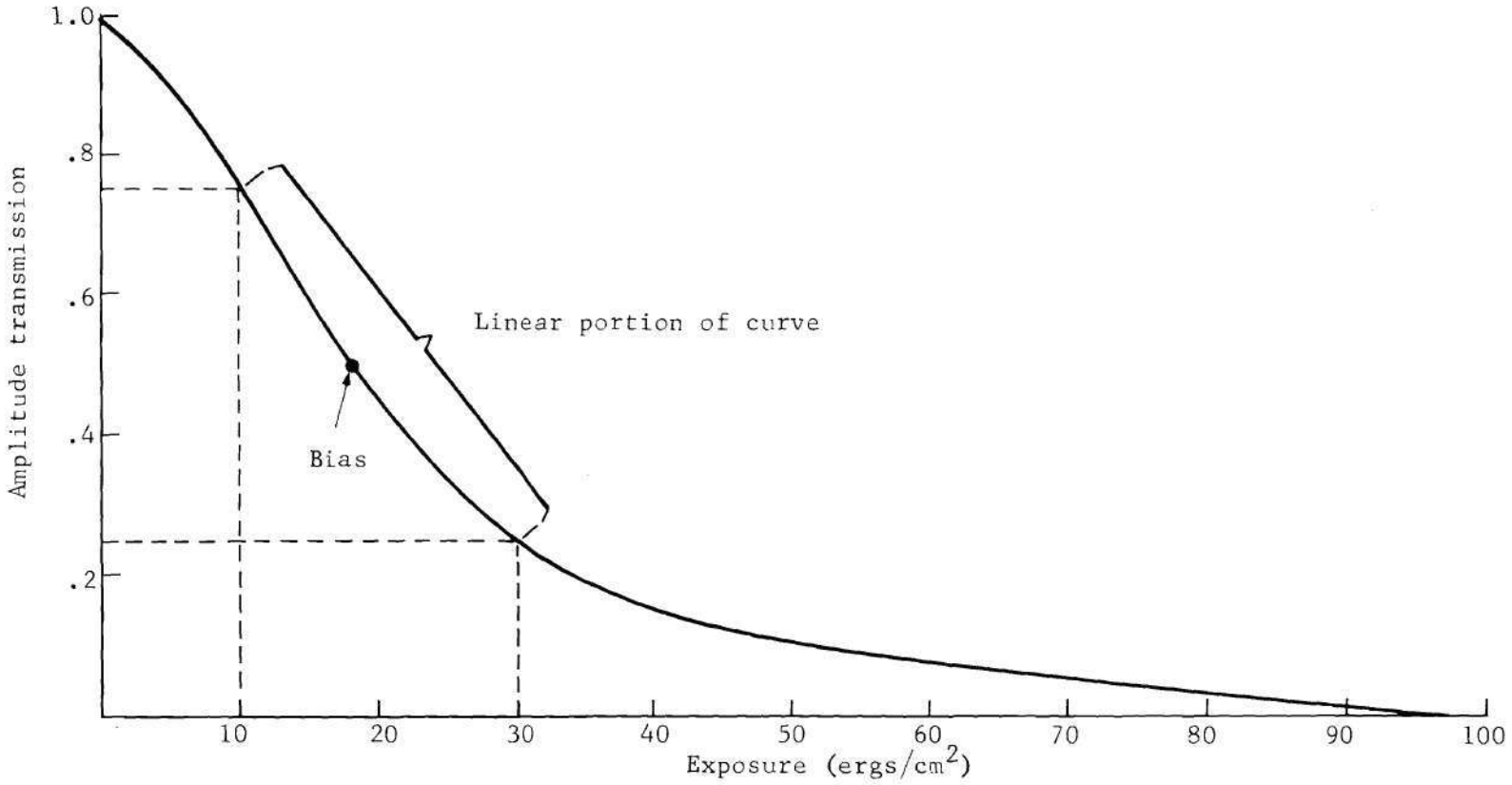

Figure 50. Amplitude Transmission vs. Exposure (T-E) Curve for Agfa-Gevaert 10E56 Film

Measurement of the Transfer Function of the Data Recorder

Once the system was assembled and adjusted for linearity as described above, its transfer function was measured. The inputs to the system were signals which were recorded on the tape recorder and the outputs were the amplitude transmission variations on the film. First of all, the transfer function for the entire system was measured. Then the transfer function of each component was measured and the results related to the transfer function of the entire system.

The transfer function for the entire system was obtained by playing sine wave signals of different frequencies through the system and measuring the variations in the response to the frequencies. Sine waves of equal amplitude and of frequencies listed in Table 2 were recorded on the tape recorder. The amplitude of the sine waves was the same as the amplitude of the low frequency signal used to check the system linearity. The velocimeter signals ranged in frequency from 2.4 kHz to 24 kHz and were recorded at a tape speed of 60 ips. The signals were played back into the film recorder at a tape speed of 1 7/8 ips reducing the frequency range to 75 Hz to 750 Hz and accounting for the frequencies selected in Table 1.

Once the sine waves were recorded on the tape recorder, they were played into the system exposing the film. The film was developed as described earlier producing sinusoidal amplitude transmissions of various frequencies on the film. The spatial frequencies f_x of the sine waves are related to their temporal frequency f and the film drive velocity v as follows

Table 2. Signals Used to Determine Transfer Function of Data Recording System

Signal Frequency at 60 ips kHz	Signal Frequency at 1 7/8 ips Hz	Signal Spatial Frequency cycles/min	Relative Response
24.0	750	100	.78
21.6	675	90	.80
19.2	600	80	1.00
16.8	525	70	.80
14.4	450	60	1.20
12.0	375	50	1.40
9.6	300	40	2.20
7.2	225	30	3.80
4.8	150	20	6.00
2.4	75	10	10.30

$$f_x = f/v \tag{1}$$

and are tabulated in Table 2.

The optical data processor described later in this chapter was used to measure the variation in response of the system to the different frequency sine waves. The physical implementation of the processor is described in detail in that section and is not repeated here. The procedure for measuring the response is described schematically in Figure 51. A beam of light from a laser was expanded and filtered by a lens-pinhole combination. Lens L1 collimated the beam. Each sine wave on the film in plane P1 was successively illuminated with a beam of collimated laser light which passed through the lens L2 as shown. The wavefront of light in the focal plane P2 of the lens had a complex amplitude which was the Fourier transform of the sine wave amplitude transmission of the film. Since the film was biased at an amplitude transmission of 0.5, a dc component had effectively been added to the signal producing a bright spot of light at the focus in P2. The bright spot of light results since the Fourier transform of a constant is a delta function. Therefore plane P2 consisted of one bright spot of light at the origin due to the dc component and two bright spots at equal distances from the origin due to the sine wave transmission of the film. The distance of the spots from the origin was proportional to the spatial frequency of the sine waves. In reality, the bright spots were sin x/x functions due to the finite duration of the signals, but as the duration of the signals increased, the sin x/x function approached a delta function.

Now that the Fourier transform of the sine waves had been generated,

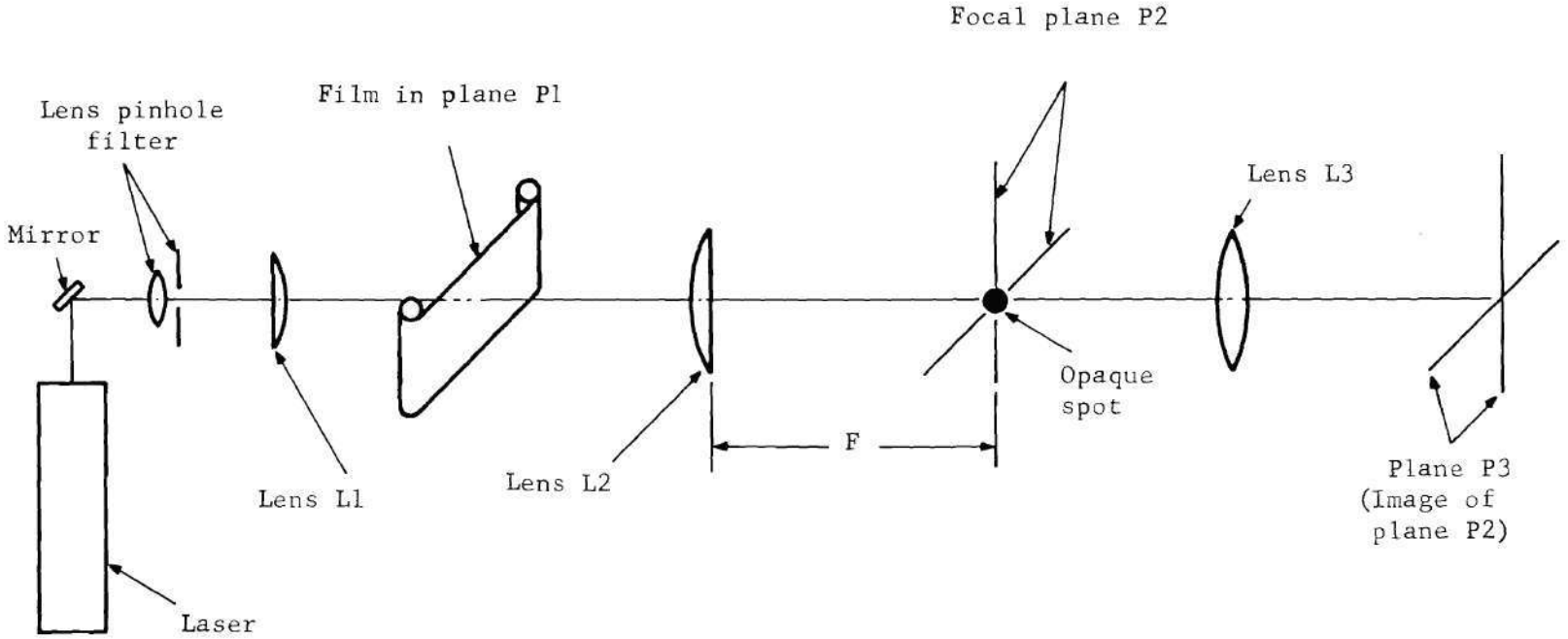

Figure 51. Schematic of System to Measure the Intensity of the Sine Waves Recorded on Film

the intensity of the transform was measured with a photometer yielding an estimate of the square of the magnitude of the system transfer function.* The dc component was very intense and produced so much stray light that it was difficult to measure the intensity of the transform in plane P2. For this reason, an opaque spot was placed at the dc component which effectively blocked it out. Lens L3 imaged plane P2 to plane P3 where the intensity of the transform could be measured. The opaque spot acted as a high-pass filter and plane P3 differed from P2 only in that the dc component was not present in P3.

Table 2 presents the relative intensity of the Fourier transforms at their peak and Figure 52 is a graph of these data as a function of spatial frequency. An estimate of the relative variation of the amplitude squared of the transfer function has been made rather than an estimate of the absolute value of the amplitude of the function. It is seen later on in the chapter that the relative variation of the magnitude squared of the transfer function is all that is really needed. Note that the transfer function is low-pass and that its amplitude squared at 80 cycles/mm is one tenth of its value at 10 cycles/mm. Even though the inputs at 80 cycles/mm are greatly attenuated, a usable response is still obtained at that frequency.

The components of the system shown in Figure 49 are analyzed to

---

*Although the signals were recorded in what appeared to be a linear portion of the T-E curve, some harmonic distortion was evident. A harmonic was observed for each sine wave signal recorded and the intensity of the harmonic was generally about three percent of the fundamental.

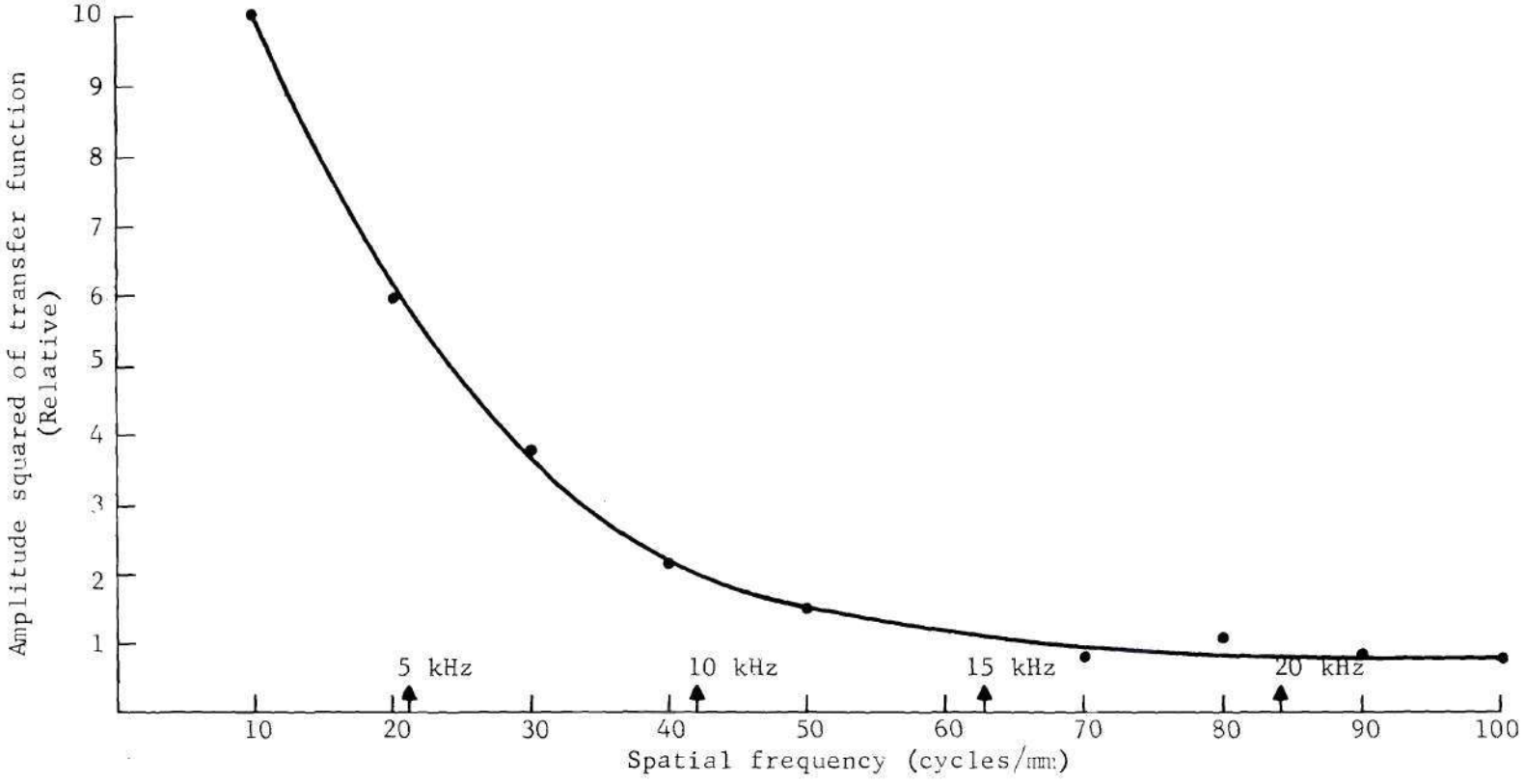

Figure 52. Plot of the Relative Magnitude Squared of the Transfer Function of the Recording System

explain the behavior of the transfer function. The transfer functions of the tape recorder and power amplifier were measured and found to be constant over the range from dc to one kHz. The transfer function of the light modulating galvanometer is defined to be the transfer function whose input is the current applied to the galvanometer and whose output is the time variation of the intensity of the light in the focused beam which exposes the film. Sine wave currents in the range from dc to one kHz were applied to the galvanometer and the time variation of the light beam was measured with the photometer. No variation of output amplitude was noted in this frequency range. The film has a spatial frequency response out to 2000 lines/mm and has a very flat transfer function from dc to 100 lines/mm.

The drop off of the system transfer function cannot be explained in terms of the component transfer functions described above since all the components have flat transfer functions over the frequency range considered. The one system component which has not been discussed is the shape of the writing beam on the focused slit and it is this component which explains the low pass behavior of the system transfer function. Intuitively, one would expect that a narrow beam (i.e. like a delta function) is capable of writing sine waves of a high spatial frequency whereas a coarse beam cannot write high spatial frequency sine waves. To be more precise, consider Figure 53 which shows the line width transfer function whose input if $f_1(t)$, the time variation of the intensity of the slit, and whose output is the exposure $f_2(x)$ of the film as a function of displacement x on the film. The point x is given by

$$x = vt$$

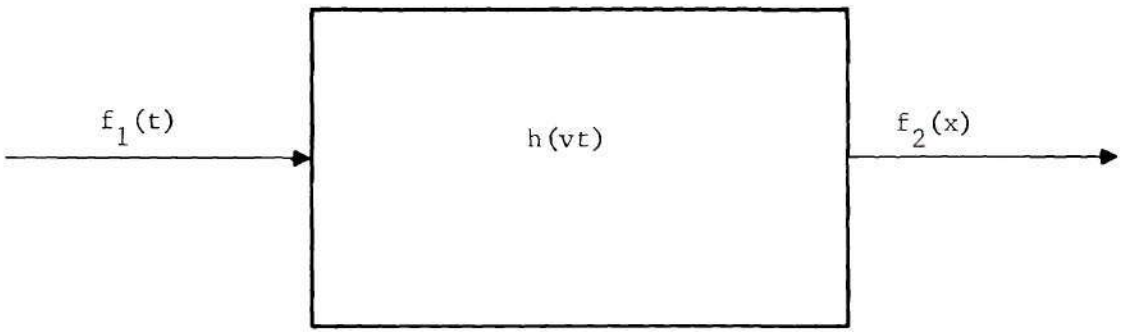

Figure 53. Linear System Whose Input Is the Signal $f_1(t)$ Which Is to be Recorded and Whose Output $f_2(x)$ Is the Exposure of the Film

where v is the velocity of the film drive. The exposure $f_2(x)$ at a point x on the film is related to $f_1(t)$ by a convolution integral as follows

$$f_2(x) = \int_{-\infty}^{\infty} f_1(t')\, h(v[t'-x/v])\, dt' \qquad (2)$$

where h(vt) is the intensity of the line at the point x. If the line of light h(vt) which exposes the film is very narrow, i.e., a delta function, then

$$f_2(x) = f_1(x/v) \qquad (3)$$

and all spatial frequency components are recorded. If the line is of nonzero width, some of the higher frequency components may not be recorded. In the extreme case, if h(vt) is a constant, only the dc component of $f_1(t)$ is recorded. The amplitude of the line used to expose the film was measured by magnifying it with a 10X microscope objective and measuring the intensity of the magnified image with the photometer. A plot of the relative amplitude of the line is shown in Figure 54. Note that the line is approximately Gaussian in shape and has a width of about 21 microns. The bandwidth of the transfer function should be approximately the inverse of the width of the impulse response or 47.5 cycles/mm. From the graph of the transfer function squared in Figure 51, one can see that its width is about 47.5 cycles/mm.

Noise Produced by the Data Recorder

The tape recorder, the amplifier, and the galvanometer added noise to the signal eventually recorded on film. A photograph of an oscilloscope

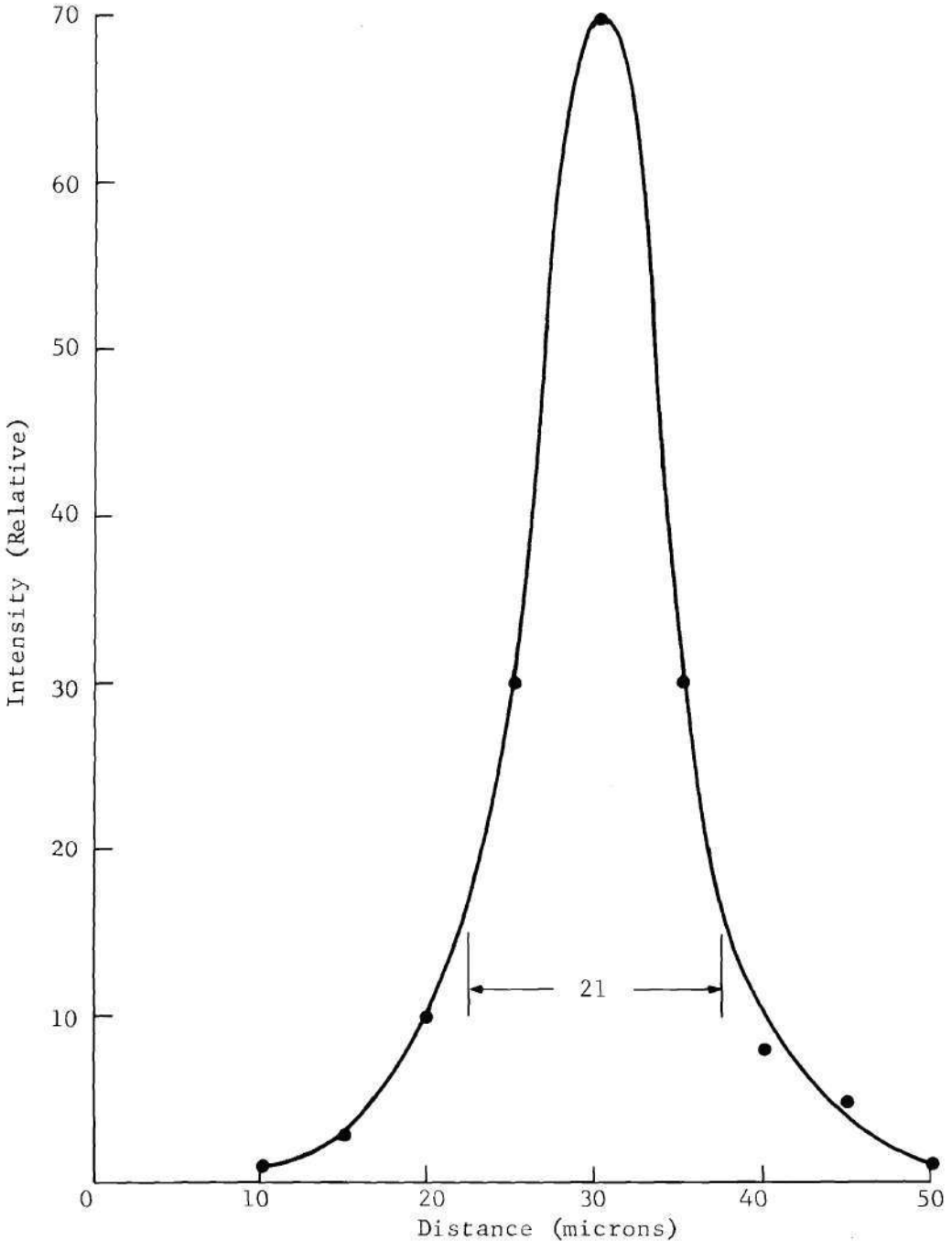

Figure 54. Relative Intensity Distribution of the Writing Line as Measured with the Photometer

trace of the tape recorder noise is shown in Figure 55. The one Hz signal whose peak to peak amplitude was one volt is shown in this figure with the voltage amplified to emphasize the noise. The sweep rate is 5 ms/cm so that only a small portion of the sine wave is shown on the trace. Note that the peak to peak amplitude of the noise is about 0.04 v/cm which is about four percent of the peak to peak value of the signal. Although the tape recorder adds some noise to the system, its contribution is still small compared to the preamplifier of the velocimeter which contributed about 0.1 volts peak to peak of white noise.

The noise produced by the power amplifier was measured by observing the response of the amplifier to a noise free one volt peak to peak sine wave signal from a signal generator. The signal from the tape recorder was not used because the tape recorder noise might be confused with the amplifier noise. The signal had an output peak to peak value of 0.29 v and the only observable noise was a 60 Hz noise whose peak to peak amplitude was 0.004 volts or 1.4 percent of the signal.

The noise produced by the galvanometer was measured by feeding the one Hz signal from the signal generator into the galvanometer and measuring the variation in intensity of the writing line with the photometer. Figure 56 is the oscilloscope trace of the signal into the galvanometer and Figure 57 is the output trace from the photometer. No measurable noise was detected from the galvanometer which might be expected since the galvanometer is a low impedance device. The slight noise visible on the signal in Figure 59 was traced to noise in the photometer output. Also note that the galvanometer appears to have been quite linear as well

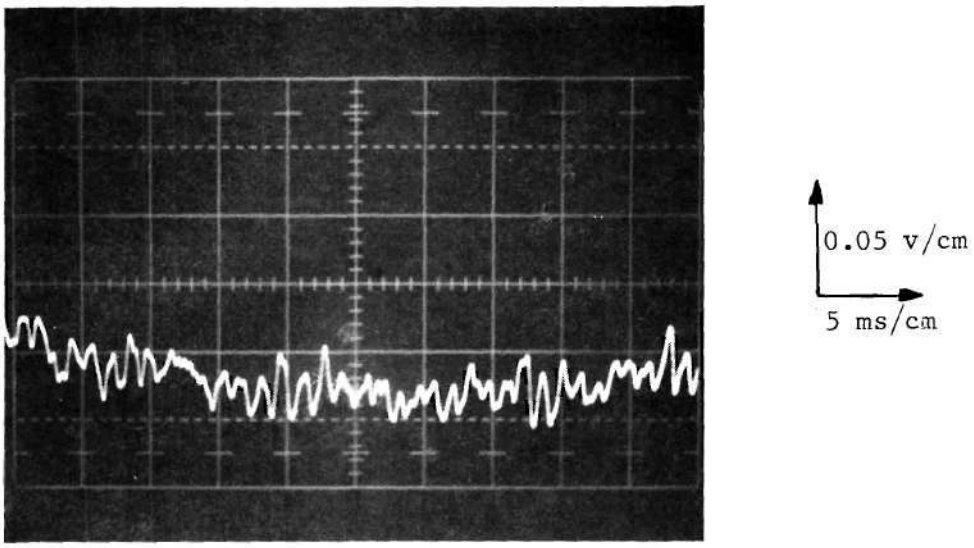

Figure 55. Oscilloscope Trace of Tape Recorder Noise

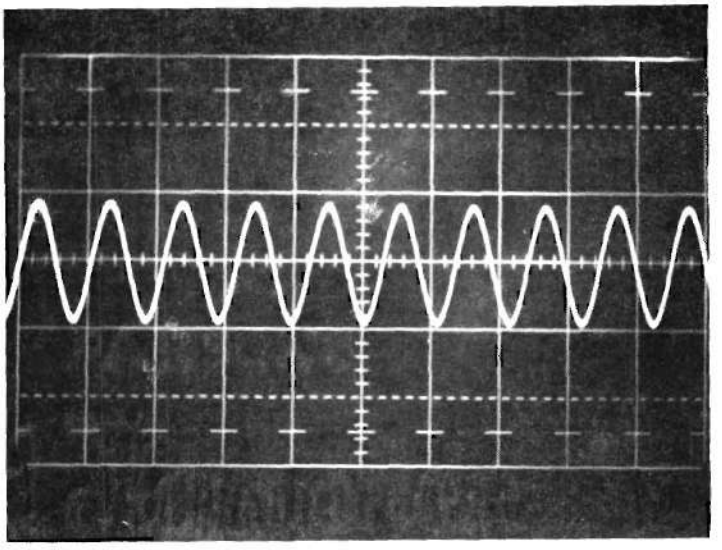

Figure 56. Oscilloscope Trace of Signal from Oscillator Which Was Fed Into the Light Modulating Galvanometer

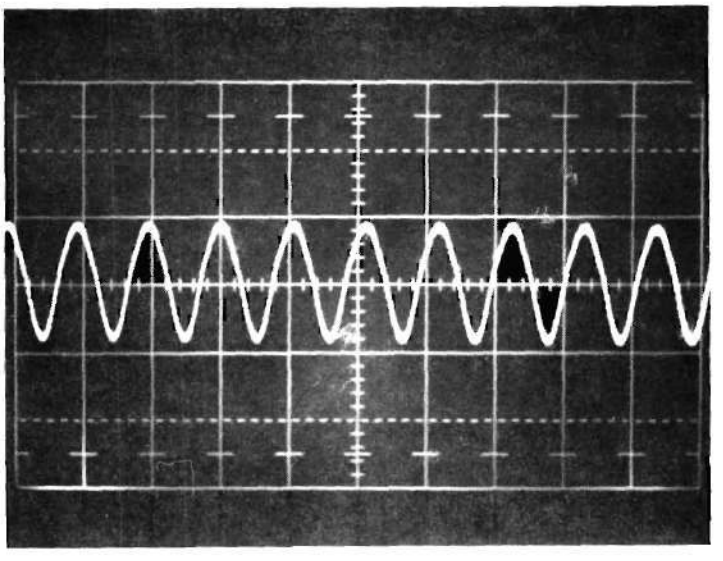

Figure 57. Oscilloscope Trace of Galvanometer Output When Signal of Figure 56 Is Applied

as noise free since the output signal is a sine wave whose shape is the same as the input.

The data recording system appears to be relatively noise free except for the low pass noise contributed by the tape recorder. Its noise was low pass and less than half the value of the noise produced by the velocimeter detection system.

Estimation of the Frequency of the Signals with a Prototype Estimator

The following experiments were designed to demonstrate the capability of the proposed estimator in estimating the frequency of velocimeter signals in steady and time varying flows under representative noise conditions. First of all, the prototype, or breadboard estimator, is described in detail and its sources of internal noise are indicated. Then the performance of the estimator on the velocimeter signals is discussed.

Description of Estimator

Figure 58 shows a schematic of the estimator and lists the equipment used. The light source was a Spectra-Physics Model 125 helium neon laser whose output power was 50 mw at 6328 A. The beam from the laser passed through a variable beam splitter which was used to control the intensity of the beam. A lens and pinhole filter (LPF) combination expanded the beam and filtered out any spatial noise present. The lens was a 10X microscope objective and the filter was a hole 10 microns in diameter. The beam from the LPF was collimated with a 24 inch focal length lens which had a three inch diameter. A film holder with a capability of translating the film horizontally and transverse to the optical axis was placed in the collimated beam in plane P1. Since the velocimeter data

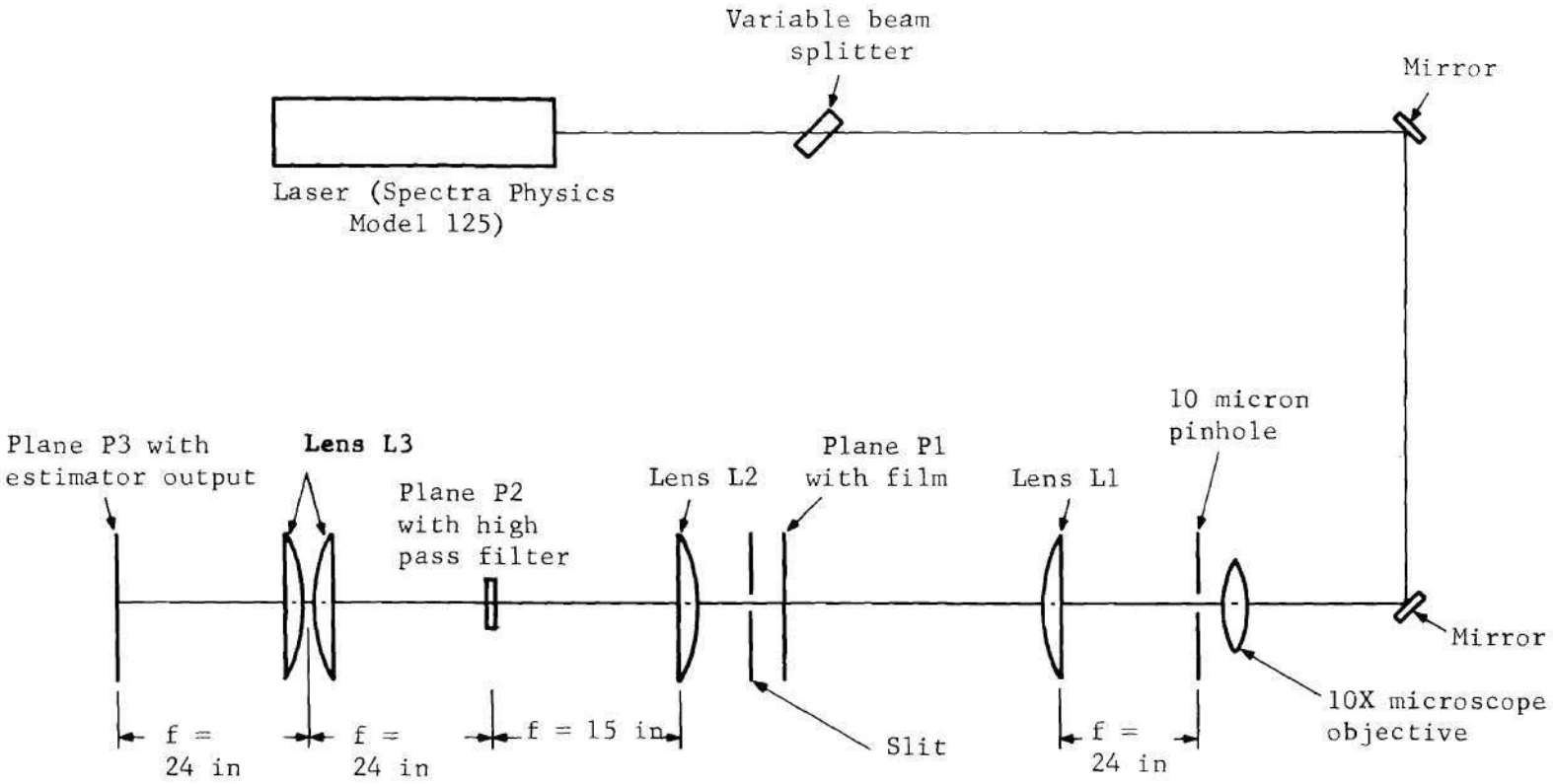

Figure 58. Schematic of the Estimator Used in the Experiments

were written as lines 3 mm wide on 4" X 5" glass plates, a slit 3 mm wide was placed after the film plate to block out any light not illuminating the signal. A four inch diameter and 16 inch focal length lens was placed as close as possible to the slit and was the lens which performed the Fourier transform operation.* The Fourier transform was formed in plane P2.

Once that the Fourier transform of the signal had been performed, it was necessary to read out the intensity of the transform with the photometer. Since the dc component of the signal was added during the recording process by biasing the film at a transmission of 0.5, it could be filtered out without loss of information. Also, it produced reflections in the photometer which could cause the photometer to give erroneous readings. The dc component was filtered out by placing an opaque spot about 3 mm wide at the dc component. The spot acted as a high pass filter. Plane P2 was then imaged with unity magnification by the lens combination L3 to plane P3. The imaging lenses were two collimators placed together as shown. The diameter of the collimators was five inches and focal length was 24 inches. Plane P3 contained the Fourier transform of the signal without the dc component.

The photometer was the Gamma Scientific Model 721 linear photometer used in Chapter II to measure the intensity distribution of the beam from the laser. The photometer had a 12 mil fiber optic probe mounted on a micrometer driven slide enabling the probe to be translated precisely in plane P3. The probe led to a PMT whose current was read with an ammeter.

---

*Since the light begins to diffract immediately after it illuminates the data, the lens should be placed as close as possible to the film and slit so that all the light passes through the lens and not around it.

A variable neutral density filter was present between the fiber optic probe and PMT so that intense light beams could be read by the photometer.*

The high pass filter determined the lower frequency limit of the estimator and the FM tape recorder determined the upper limit. The high pass filter was 3 mm wide and it extended equally into the positive and negative frequencies. The relationship[31,32] between spatial frequency f_x and displacement x_1 in the transform plane is given by

$$f_x = x_1/\lambda F \tag{4}$$

where F is the focal length of the lens. Therefore, the lower spatial frequency limit f_{LOx} is given by

$$f_{LOx} = \frac{1.5 \text{ mm}}{(.6328 \times 10^{-3} \text{ mm})(24 \text{ in})(25.4 \text{ mm/in})} \tag{5}$$

$$= 3.88 \text{ cycles/mm}$$

From Eq. (1), the spatial frequency f_{LOx} corresponds to a temporal frequency f_L' given by

$$f_L' = f_{LOx}\, v \tag{6}$$

$$= \left(\frac{3.88 \text{ cyc.}}{\text{mm}}\right)\left(\frac{7.5 \text{ mm}}{\text{sec}}\right)$$

$$= 29.1 \text{ Hz}$$

*The transfer function of the data recording system discussed earlier in this Chapter was measured with the system described above. The film with the sine wave transmission variations was placed in plane P1 and their Fourier transform measured with the photometer in plane P3.

Since the tape recorder was played into the film recorder at 1 7/8 ips and the velocimeter data were recorded at 60 ips, the lowest velocimeter frequency estimated, denoted by f_L, was actually

$$f_L = \frac{60}{1\ 7/8} f_L', \tag{7}$$

$$= 930 \text{ Hz}$$

It should be pointed out that the lower frequency limit of 930 Hz was not a fundamental lower limit, but dictated by the size of the high-pass filter. Actually, the high-pass filter should be the size of the dc component produced by the film bias. Assuming a plane wave of constant amplitude illuminated the data, the dc component had a width Δx_1[32] given by

$$\Delta x_1 = \frac{2\lambda F}{L} \tag{8}$$

where L is the length of the data which were illuminated. If L is one inch, Δx_1 becomes

$$\Delta x_1 = \frac{(2)(.6328 \times 10^{-3} \text{ mm})(24 \text{ in})}{1 \text{ in}}$$

$$= 30.4 \times 10^{-3} \text{ mm}$$

This distance corresponds to a spatial frequency f_{x_1} of

$$f_{x_1} = x_1/\lambda F \tag{9}$$

$$= \frac{30.4 \times 10^{-3} \text{ mm}}{.6328 \times 10^{-3} \text{ mm (16 in)(25.4 mm/in)}}$$

$$= .118 \text{ cycles/mm}$$

and a temporal frequency f' of

$$f' = f_{x_1} v \tag{10}$$

$$= \left(\frac{.118 \text{ cycles}}{\text{mm}}\right)\left(\frac{7.5 \text{ mm}}{\text{sec}}\right)$$

$$= 8.85 \text{ Hz}$$

The corresponding velocimeter frequency f given by

$$f = \frac{60}{1\ 7/8} f' \tag{11}$$

$$= 284 \text{ Hz}$$

In reality, the dc component probably could not have been this small due to lens aberations and low pass noise in the optical system. However, a smaller high-pass filter could likely have been used if one had been available for the experimental work. It is difficult to make a small high-pass filter for this application since such a filter must be

quite narrow and hence quite fragile. It must also be mounted in a holder with micrometer drives so that it can be placed exactly at the dc component. Most importantly, it must have a low reflectance since the bright dc component falling on the filter can scatter light which would act as noise into the system.

The upper frequency limit of the system was 20 kHz since that frequency was the highest the FM recorder running at 60 ips could record. Another factor which limited the upper frequency was the width of the writing line of the film recorder. If 100 cycles/mm is chosen from Figure 53, as the upper frequency limit, the highest temporal frequency f_H' which would have been recorded is

$$f_H' = f_{Hix}\, v \tag{12}$$

$$= \left(\frac{100 \text{ cycles}}{\text{mm}}\right)\left(\frac{7.5 \text{ mm}}{\text{sec}}\right)$$

$$= 750 \text{ Hz}$$

The above frequency corresponds to a velocimeter frequency of

$$f_H = \left(\frac{60}{1\ 7/8}\right)(750 \text{ Hz}) \tag{13}$$

$$= 24 \text{ kHz}$$

The light modulating galvanometer available for this thesis had an incoherent light source. Data recorders with coherent light sources have

more narrow writing lines and have been built with the capability of recording data in excess of 200 cycles/mm,[30] allowing higher frequencies to be recorded. Since f_L and f_H are proportional to the speed of the film drive as shown in Eq. (1), higher frequencies can be recorded by increasing the film drive speed v.

Noise Produced by the Estimator

The estimator itself added some low-pass noise which was produced by dust and scratches on the optical components and by specular reflections from the optical components. The noise produced by specular reflections was eliminated by slightly tilting the lenses in the system throwing the reflections out of the optical system. Also black pieces of paper were inserted in various locations of the system blocking out the reflections. The noise due to the dust was reduced by carefully cleaning the lenses.

The dust on the collimating lens L1, the transforming lens L2, and the imaging lens L3 contributed noise to the system. Elements between L1 and the laser contribute no noise since their noise was eliminated by the lens-pinhole filter. Generally, the dust particles can be modeled as small discs whose diameter is in the vicinity of 100 microns. The optical system effectively performed a Fourier transform on these particles, as it did on the data. The Fourier transform of a disc is a first order Bessel function whose diameter is given by[32]

$$D = \frac{2.44\ \lambda F}{d} \tag{14}$$

where d is the diameter of the disc and F is the focal length of the transforming lens. If d was 100 microns and F was 24 inches, the width

of the noise in the Fourier transform plane P2 was

$$D_{x_i} = \frac{(2.44)(.6328 \times 10^{-3} \text{ mm})(24 \text{ in})(25.4 \text{ mm/in})}{100 \times 10^{-3} \text{ mm}} \tag{15}$$

$$= 9.4 \text{ mm}$$

From Eq. (4) it is seen that noise from dust particles could have extended to spatial frequencies f_D as high as

$$f_D = D_{x_1}/\lambda F \tag{16}$$

$$= \frac{(9.4 \text{ mm})}{(.6328 \times 10^{-3} \text{ mm})(24 \text{ in})(25.4 \text{ mm/in})}$$

$$= 24.3 \text{ cycles/mm}$$

Noise due to dust particles on the downstream side of L2 and on L3 did not undergo the Fourier transform operation and are more difficult to analyze. The fact that a great deal of the noise was due to dust particles was demonstrated by focusing a microscope on the light due to noise in the Fourier transform plane and following the light back to its origin. In each case, the light was found to be eminating from a dust particle. The noise due to the dust particles and optical imperfections was measured by inserting a piece of film with no data recorded on it into the optical system and measuring the light intensity in plane P3. The film contained only the bias. A plot of the light intensity in plane P3 was made with

the photometer and is shown in Figure 59.

Estimation of the Frequency of Signals from Steady Flows

Estimation Procedure. The general procedure employed in estimating the frequency of the signals from the steady flows was the following. The film with the signals recorded on it was placed in plane P1 of Figure 59. The slit following the film was 3 mm high so that only light illuminating the signal passed through L2. The length L of the slit was one inch which means that T, the duration of the signal used in the frequency estimate, was

$$T = (L/v)\ (1\ 7/8\ /60) \tag{17}$$

$$= \left(\frac{25.4\ \text{mm}}{7.5\ \text{mm/sec}}\right)\left(\frac{1\ 7/8}{60}\right)$$

$$= .106\ \text{sec}$$

The intensity of the Fourier transform in plane P3 was read out with the photometer. The photometer, mounted on a micrometer drive, provided readings in intensity every millimeter. The relationship between the distance along the f_x axis in plane P3 and the frequency of the velocimeter signals was calibrated from the signals used to determine the film recorder's transfer function and found to be 1.2 mm/kHz. The measurements made with the photometer contained the noise present with the velocimeter signals before the data were recorded on magnetic tape, the small amount of low-pass noise added by the tape recorder and the system noise added by the estimator. The system noise added by the estimator is primarily

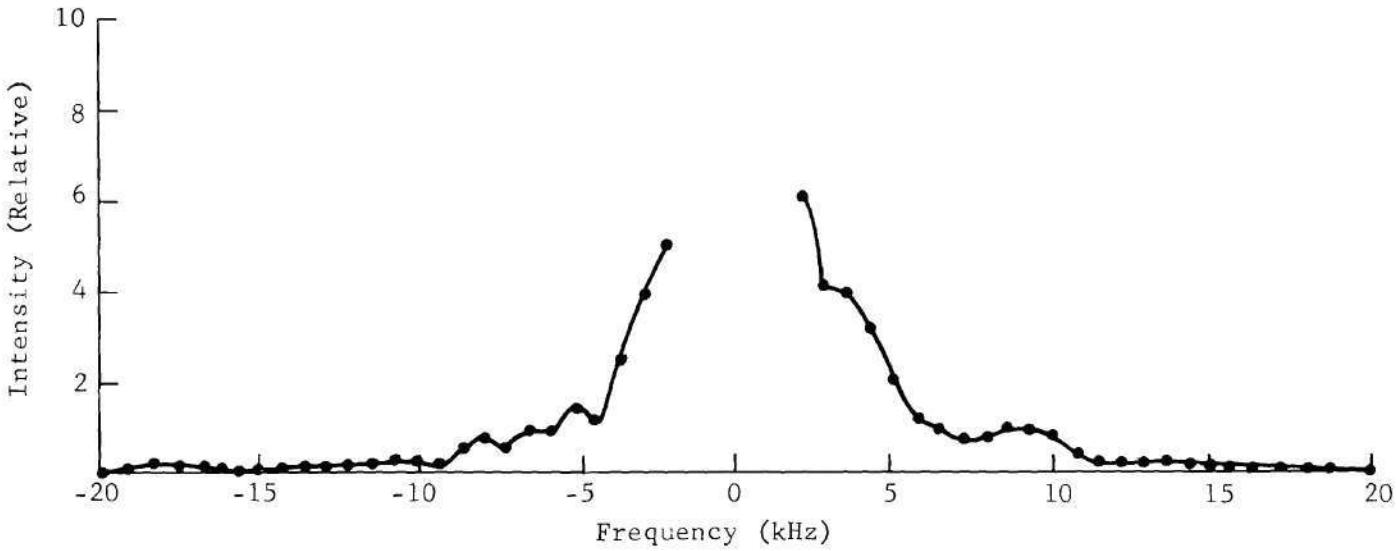

Figure 59. Plot of the Relative Intensity of the Noise in Plane P3 of the Estimator

caused by dust particles and imperfections in the optical components and remains essentially the same regardless of the particular data being processed. Therefore this noise can be thought of as deterministic rather than random. The readings of the system noise shown in Figure 60 were subtracted from readings of the intensity of the Fourier transforms of the signals.

The higher frequencies of the recorded signals were attenuated due to the film recorder transfer function shown in Figure 53. To compensate for the attenuation, the intensity of the Fourier transform was divided by the square of the recorder transfer function. Since the film recorder was modeled as a linear system, its effects could be eliminated by dividing its output by its transfer function. In summary, the velocimeter signals from steady flows were reduced by subtracting out the deterministic noise added by the estimator and by dividing by the transfer function squared of the data recorder. Table 3 illustrates the data reduction procedure at some representative points for the 10 kHz steady flow signals considered in the discussion below.

Low Noise Velocimeter Signals from a Steady Flow. The performance of the estimator on low noise signals generated from various steady flows was determined. Since the experimental LIV system was shown in Chapters II and III to have less noise than the LDV system, the LIV system was used to generate the low noise signals. The tunnel was run without any model in it which resulted in the test section flow being uniform and time invariant. The smoke generator was adjusted to give a strong LIV signal as displayed on the oscilloscope. The tunnel was run at velocities

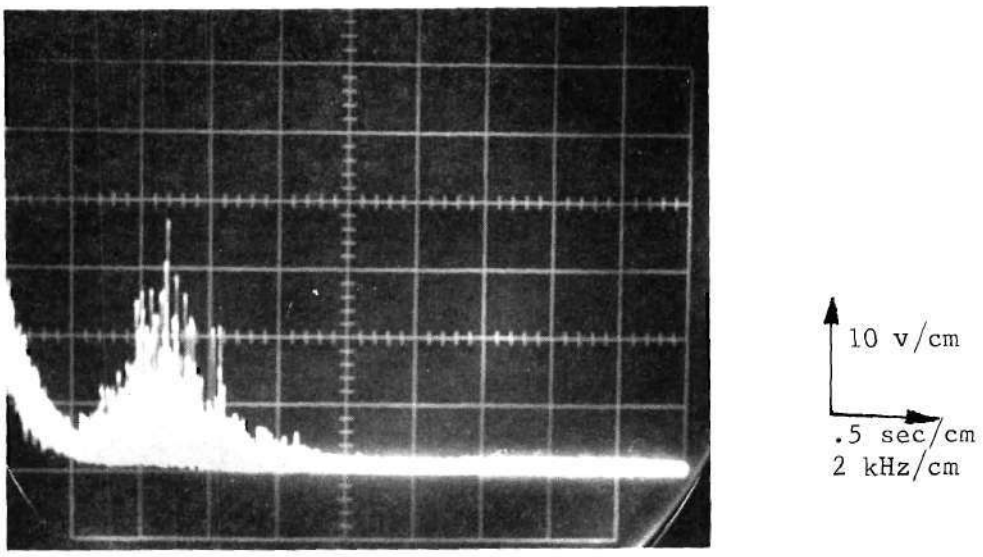

5 kHz Steady Flow Signal

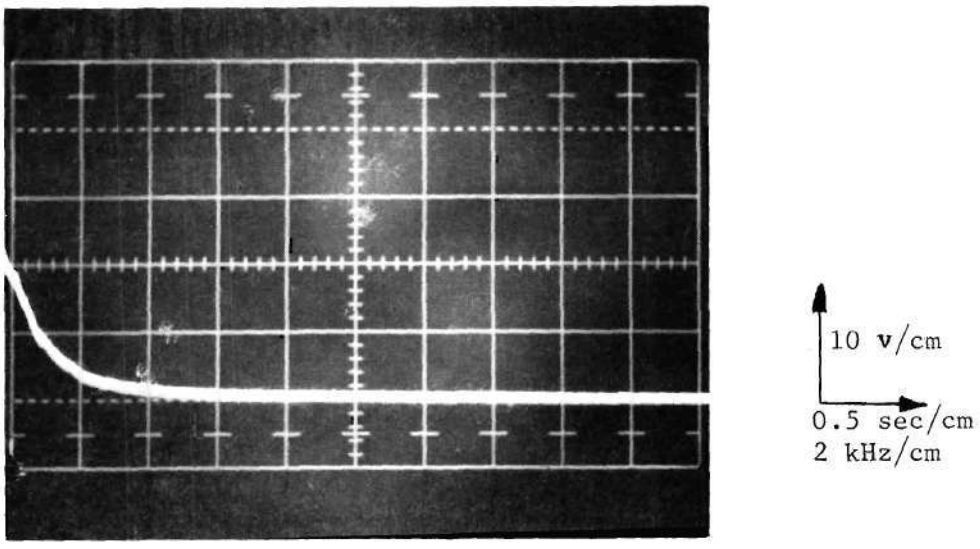

Tracer Signal (no input applied)

Figure 60. Spectrum Analyzer Trace of Steady Flow 5 kHz Velocimeter Signal (top photograph) with Low Noise

Table 3. Example of Data Reduction Procedure to Reduce Steady Flow Velocimeter Signals. (Signal center frequency is 10 kHz and data are plotted in Figure 64.)

Frequency		Signal and Noise $r_T(t)$	Deterministic Noise $n_o(t)$	$r(t) - n_o(t)$	Transfer Fcn of Film Recorder Squared $\|H(\omega)\|^2$	Division by $\|H(\omega)\|^2$ (Reduced Data in Final Form)
Relative	kHz					
			Left Side of Frequency Origin			
7	5	4.0	2.5	1.5	4.9	.306
10	7.1	2.5	.6	1.9	2.8	.68
11.5	8.2	35.0	.65	34.35	2.2	15.6
13.0	9.3	2.5	.2	2.3	1.6	1.44
			Right Side of Frequency Origin			
7	5	3.2	2.1	1.1	4.9	.22
10	7.1	2.0	.8	1.2	2.8	.43
12	8.6	38.0	1.0	37.0	1.9	19.5
13	9.3	15.0	1.0	14.0	1.6	8.75

corresponding to frequencies of 5, 10, and 15 kHz and LIV signals were recorded during these runs. Figures 60, 61, and 62 show spectrum analyzer traces made of the recorded LIV signals. A Tektronix Model 1L5 spectrum analyzer was used to measure the spectra.

The signals were then recorded on film and operated on by the estimator using the procedures described in the previous section. Figures 63, 64, and 65 show the plots of the intensity of the output of the estimator measured with the photometer as a function of displacement along the frequency axis in the plane P3. Note that the outputs of the estimator peaked at the proper frequency for the 5, 10, and 15 kHz signals, respectively, indicating that the estimator correctly estimated the frequency of the low noise LIV signals.

Note that it is considerably easier to locate the center frequency of the signals from the output of the estimator as compared to the spectrum analyzer traces. The estimator produced narrow and sharp peaks at the proper frequency while the spectrum analyzer produced broad and jagged curves making it more difficult to locate the center frequency.

It should be noted that the output of the estimator as shown in the figures is not perfectly symmetrical about the origin. Since the LIV signals are real and the output of the estimator is effectively the Fourier transform of the input signal, one would expect the output to be symmetrical since the amplitude of the Fourier transform of a real function is symmetrical. The lack of perfect symmetry in the experimental data results from the combined effects of several factors. The thickness variations in the emulsion and the glass plate backing of the film gave

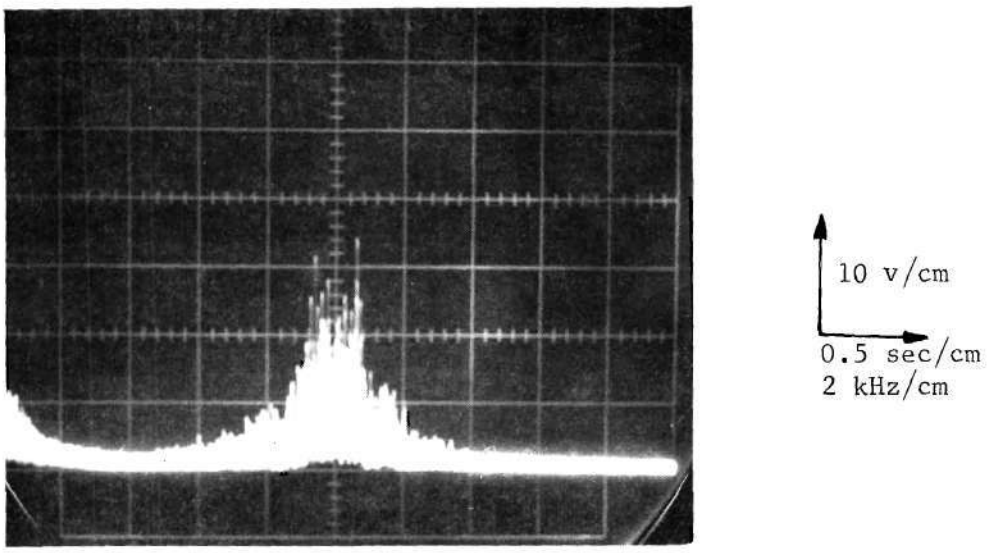

Figure 61. Spectrum Analyzer Trace of Low Noise 10 kHz Velocimeter Signal from a Steady Flow

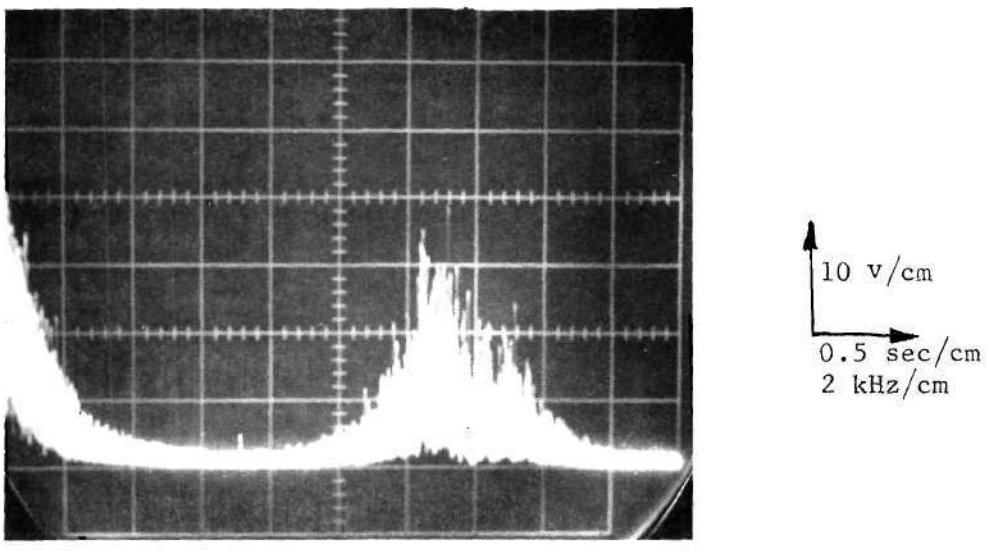

Figure 62. Spectrum Analyzer Trace of Low Noise 15 kHz Velocimeter Signal from a Steady Flow

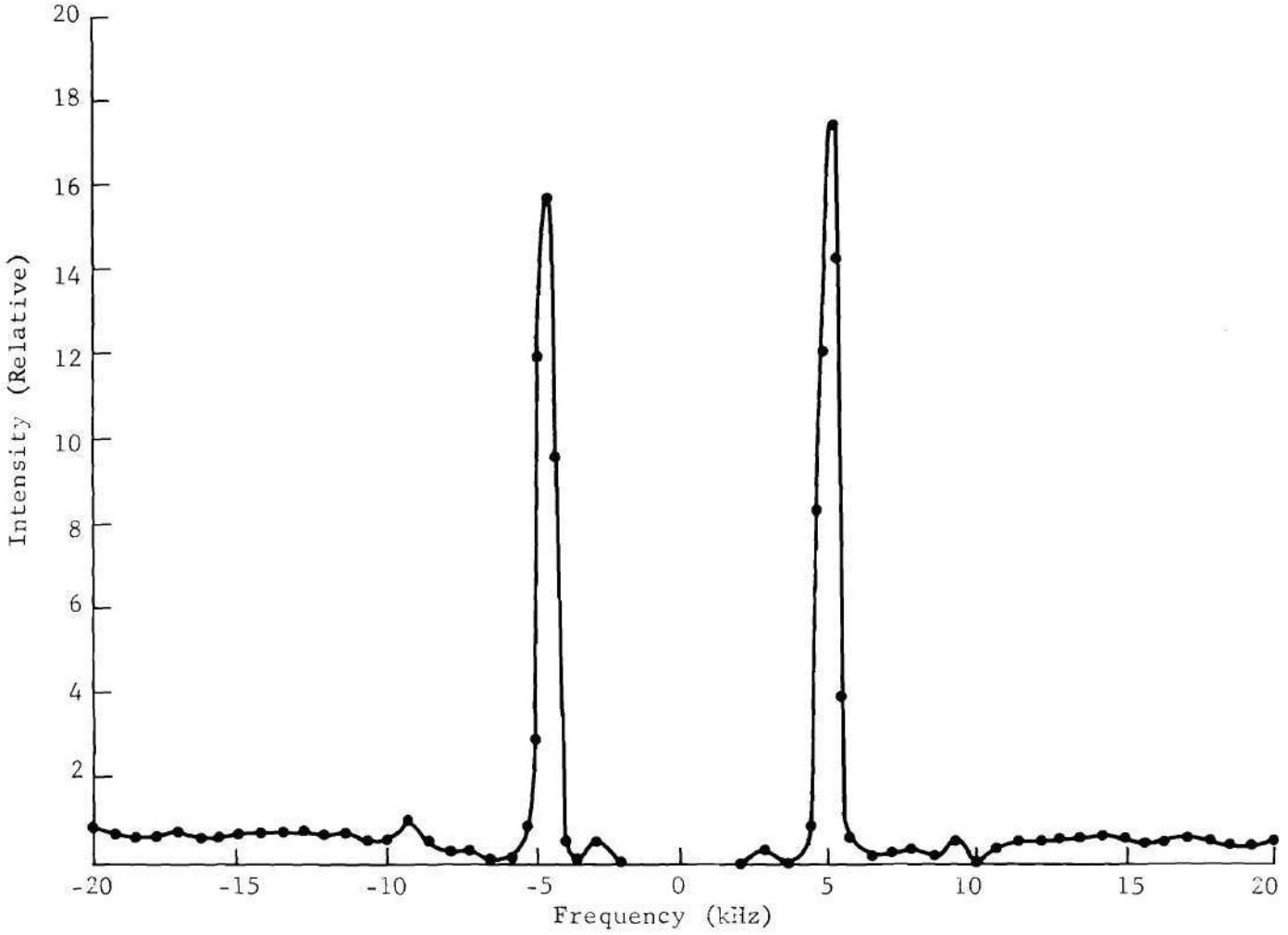

Figure 63. Estimator Output for a Low Noise 5 kHz Velocimeter Signal from a Steady Flow

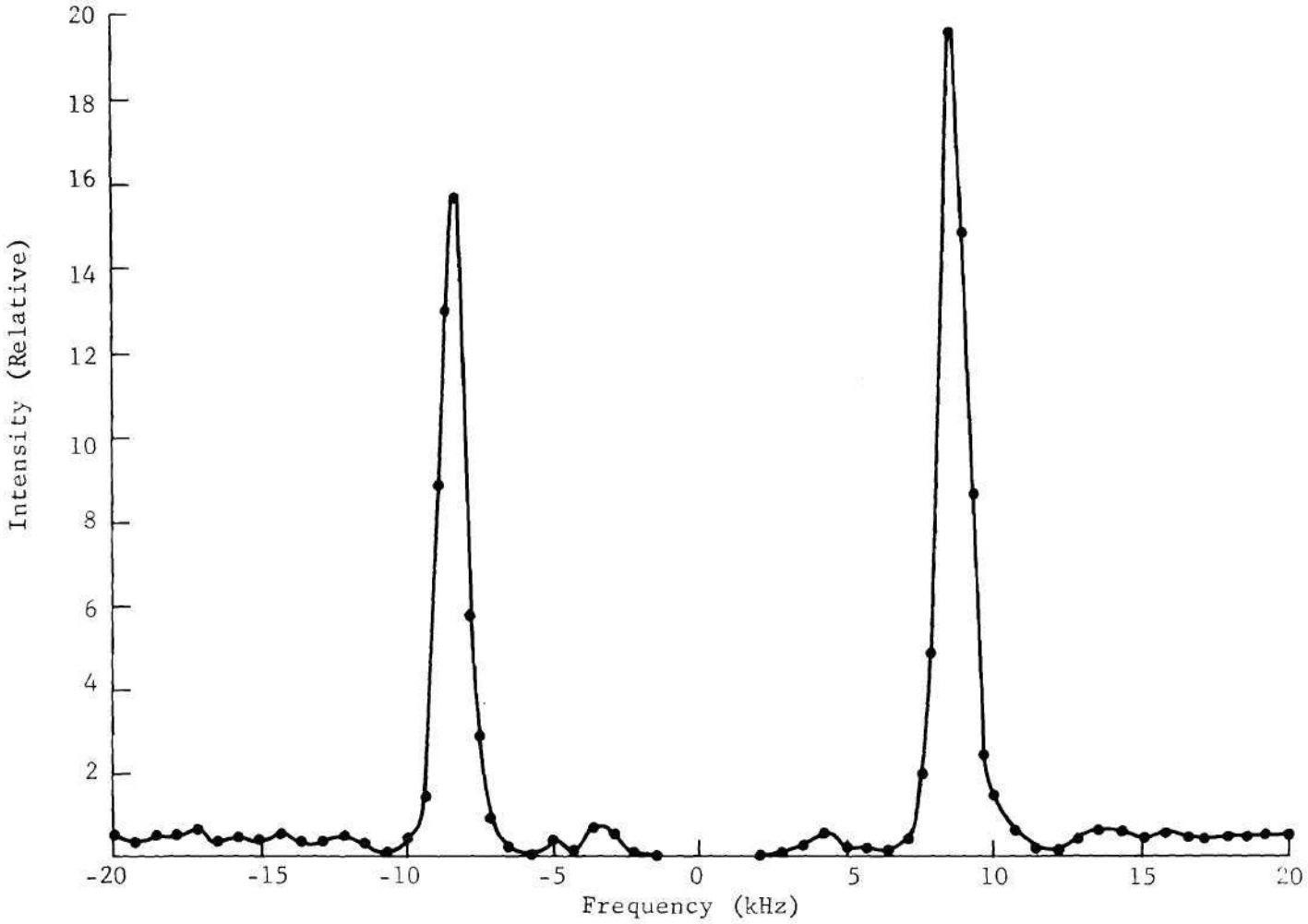

Figure 64. Estimator Output for a Low Noise 10 kHz Velocimeter Signal from a Steady Flow

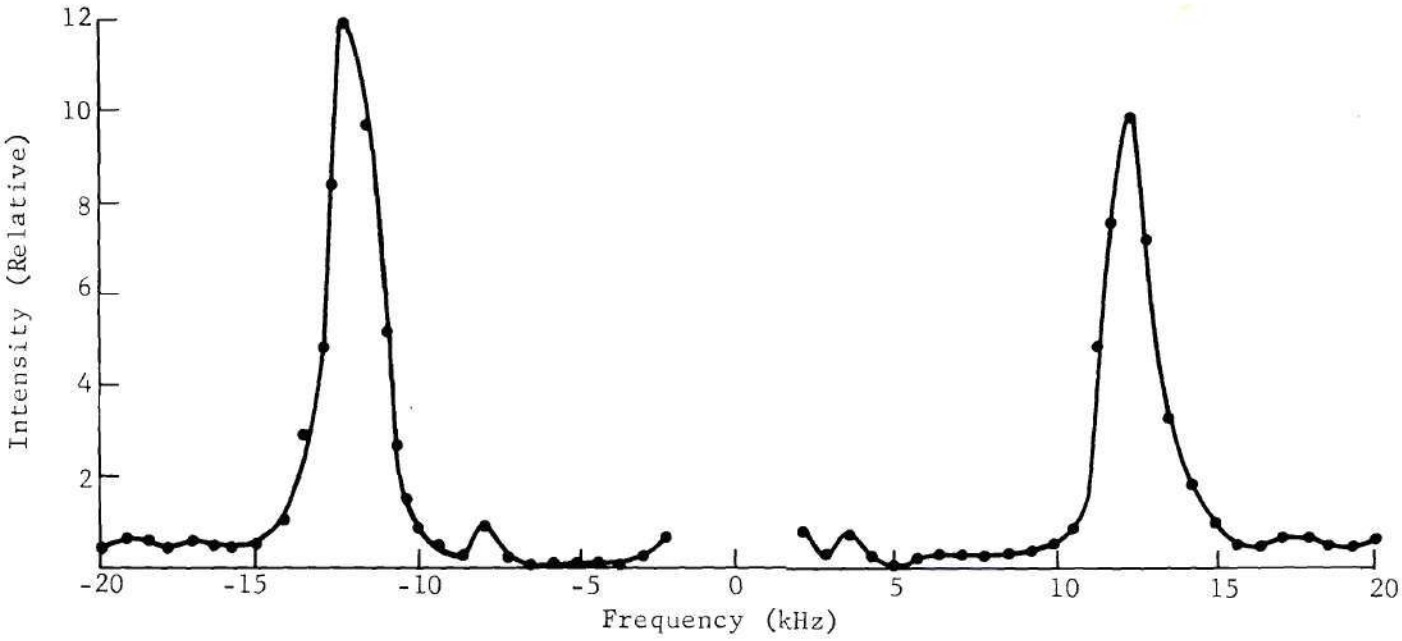

Figure 65. Estimator Output for a Low Noise 15 kHz Velocimeter Signal from a Steady Flow

the light beam passing through the film some spurious phase information. The estimator then performed a Fourier transform of a complex function which might not have had a symmetrical amplitude. The other sources also produced phase noise. The lenses had some thickness variations which contributed phase noise to the signal. Also, the lenses were slightly cocked off axis to keep stray reflections from falling in the transform plane. The tilting of the lenses contributed to the slight asymmetry. The lack of perfect symmetry did not significantly hamper the performance of the estimator.

LDV and LIV Signals. The signal and noise models of Chapters II and III for the LDV and LIV systems indicated that effectively the signals from both systems are of the same nature. The LIV signal has a low-pass component not present in the LDV signal and which gives little or no frequency information. Often, the low-pass component is filtered out either by the velocimeter detection system or by the frequency estimator. The analysis of the estimator in Chapter IV predicts that the estimator performs as well on the LDV signals as the LIV signals of the same noise level.

In order to compare the estimator's performance on LDV and LIV signals, representative signals were recorded from both systems with a steady flow in the tunnel whose velocity corresponded to a frequency of 10 kHz. Figures 66 and 67 are spectrum analyzer traces of the LDV and LIV signals, respectively. Note that both signals are 10 kHz and that the noise level is low. Figures 68 and 69 are plots of the output of the estimator for these signals. Note that the estimator output peaked at

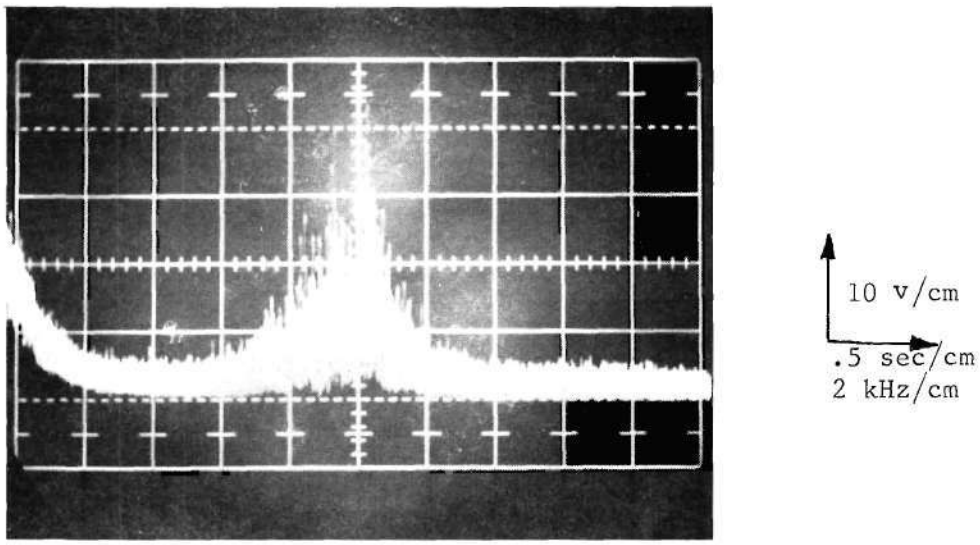

Figure 66. Spectrum Analyzer Trace of a Low Noise 10 kHz LDV Signal from a Steady Flow

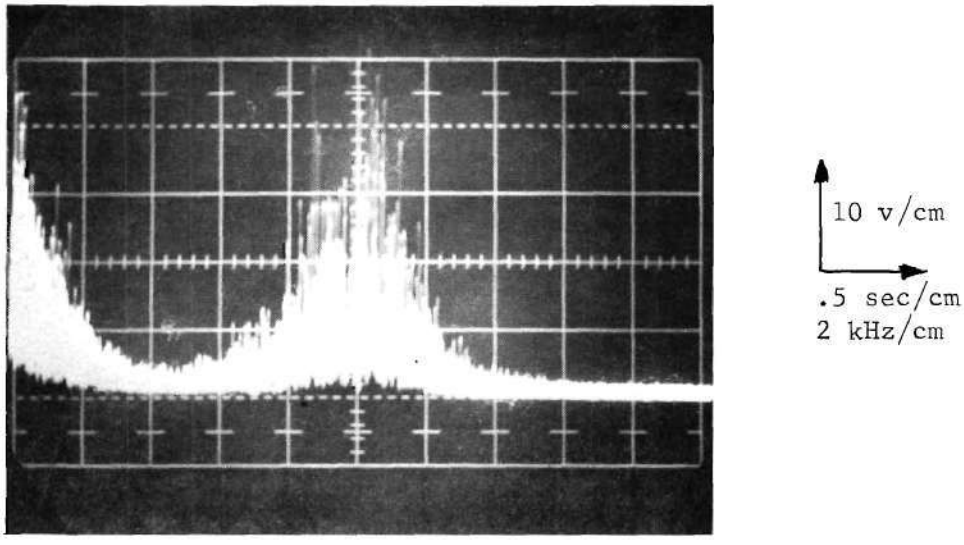

Figure 67. Spectrum Analyzer Trace of a Low Noise 10 kHz LIV Signal from a Steady Flow

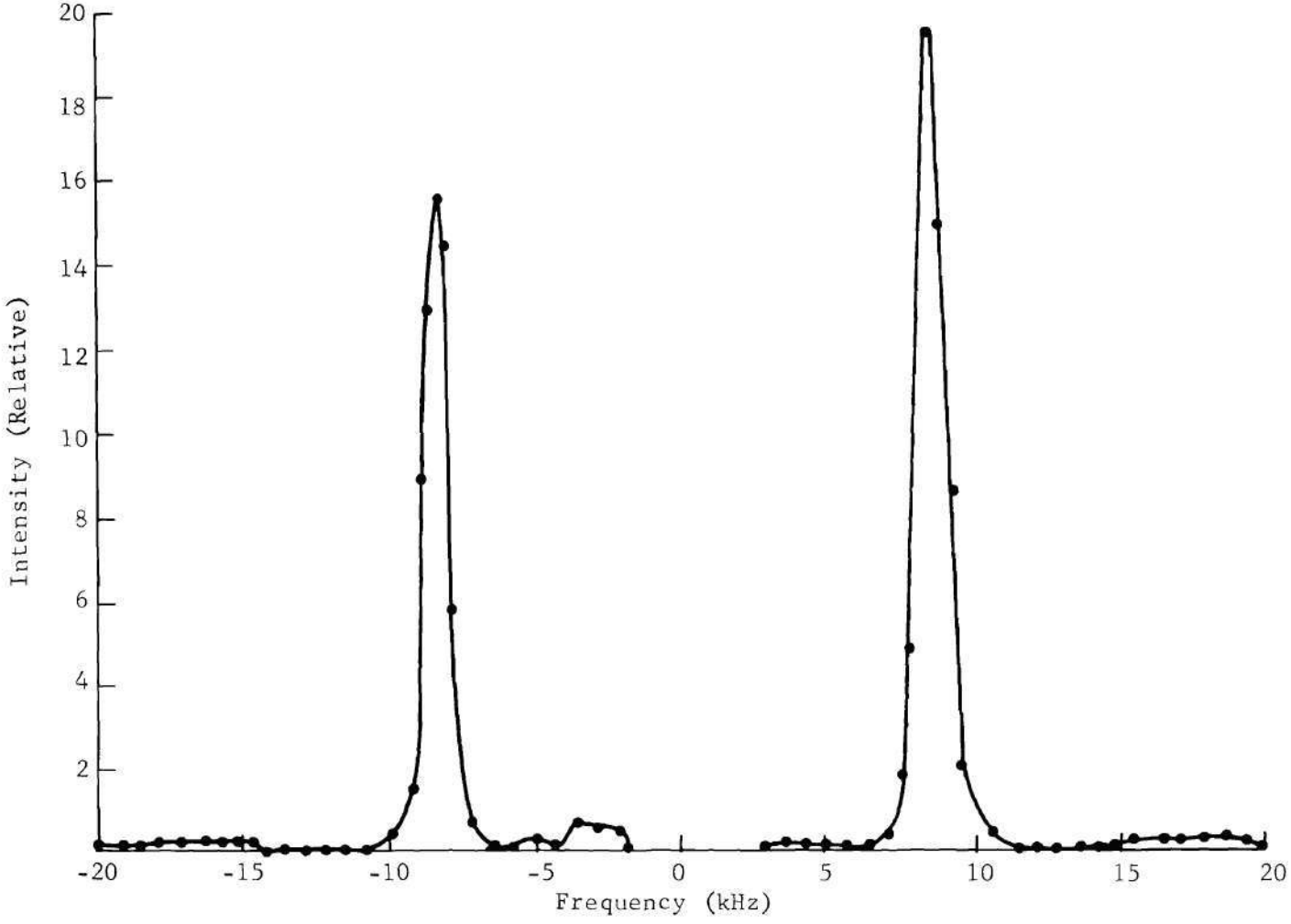

Figure 68. Estimator Output for a Low Noise 10 kHz LIV Signal from a Steady Flow

Page missing from thesis

the proper frequency of 10 kHz and that the output plot is about the same for both signals. Hence the performance of the estimator on LDV signals was about the same as its performance on LIV signals.

Dense and Sparse Steady Signals. It was shown in Eqs. (31) and (32) of Chapter IV that the estimator's performance should be better on signals from flows with dense particles compared to signals from flows with sparse particles. Since more particles means effectively more signal, one would expect the estimator's performance to improve as the particle concentration becomes greater. In order to evaluate the relative performance of the estimator on dense and sparse particle flows, two sets of signals were generated with the LIV system and the wind tunnel running with a steady flow producing signals of 10 kHz frequency. First of all, the smoke generator was adjusted for maximum output producing a great deal of smoke in the tunnel. Figure 70 is a photograph of a signal under these conditions. Note that there are many pulses on this trace indicating the particle concentration is high. Next, the smoke generator was adjusted so that very little smoke was introduced in the tunnel. A trace of signal generated under these conditions is shown in Figure 71. There are only a few small pulses on this trace indicating that the particle concentration was low. Spectrum analyzer traces of the dense and sparse signals are shown in Figures 72 and 73, respectively. As expected, the denser signal gives a stronger spectrum than the sparse signal.

The output of the estimator for the dense particle signal is shown in Figure 74 and for the sparse signal in Figure 75. Note that the output of the estimator for the dense particle flows was over twice as great as

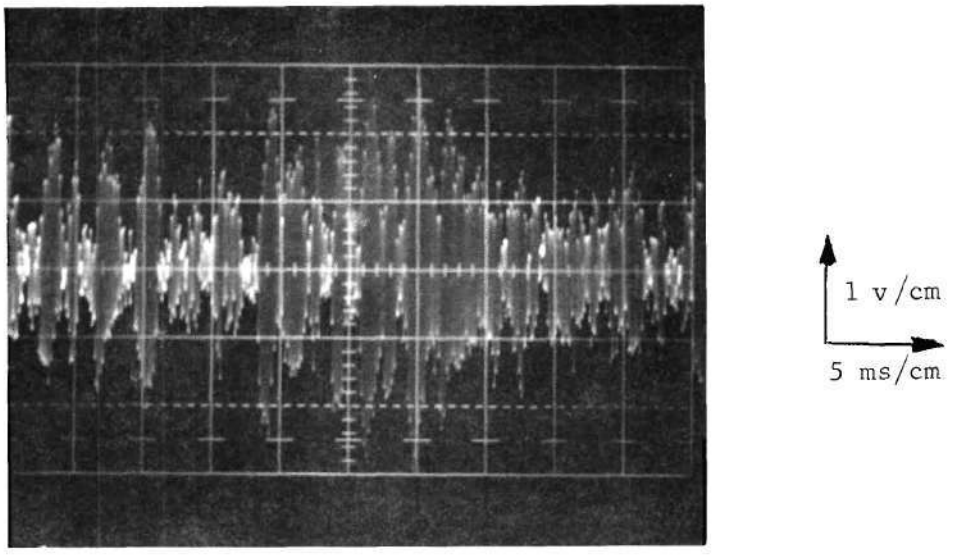

Figure 70. LIV Signal from a Steady Flow with a Dense Smoke Concentration. (Note that many pulses are present.)

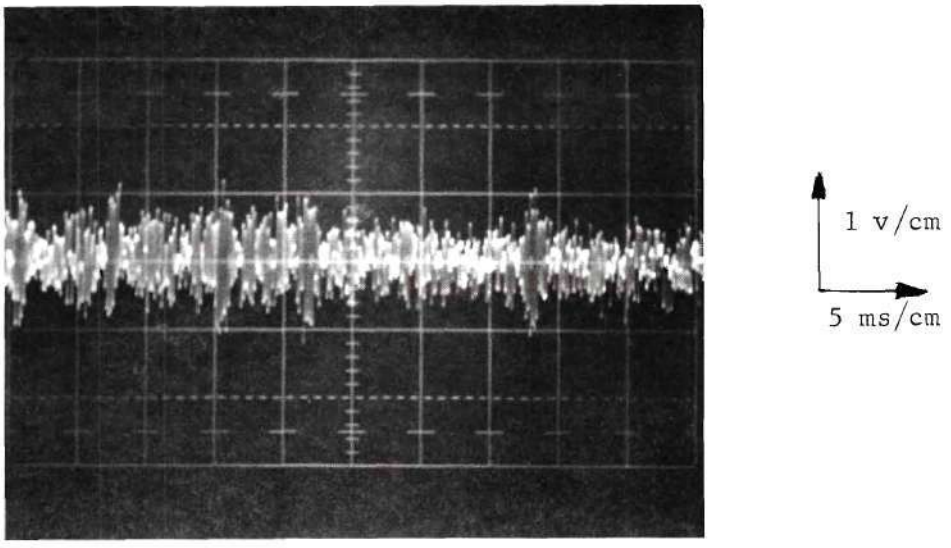

Figure 71. LIV Signal from a Steady Flow with a Sparse Smoke Concentration. (Note that few pulses are present.)

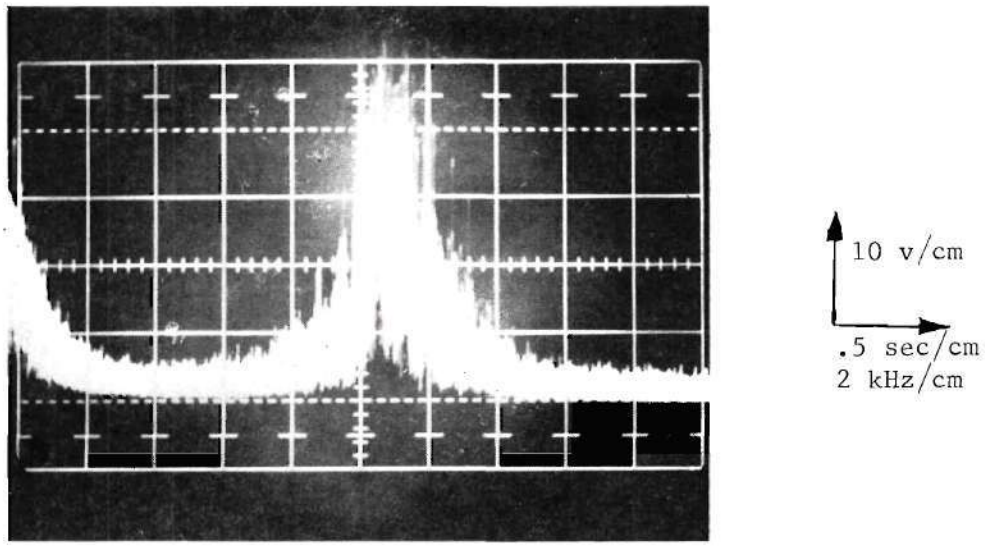

Figure 72. Spectrum Analyzer Trace of 10 kHz LIV Signal from a Steady Flow with Dense Smoke Concentration

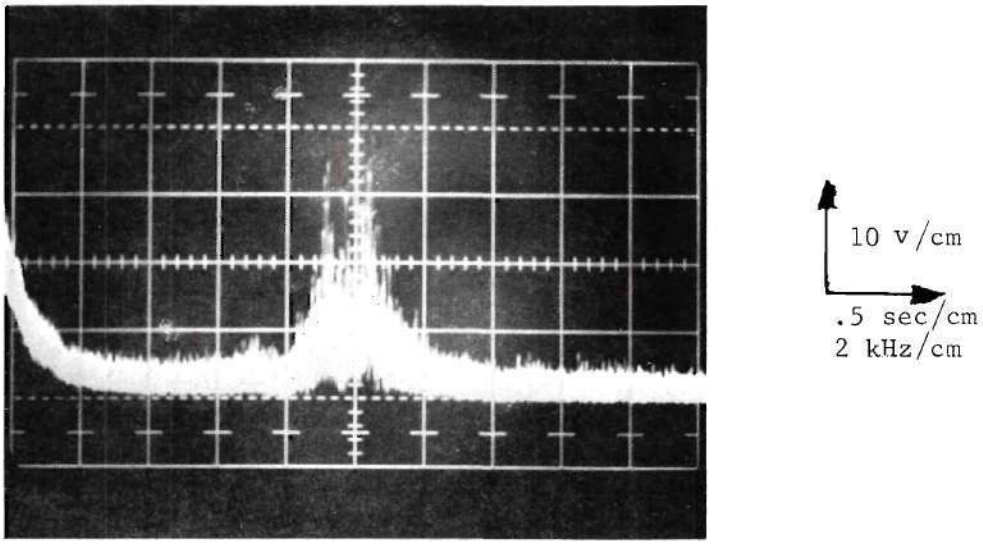

Figure 73. Spectrum Analyzer Trace of a 10 kHz LIV Signal from a Steady Flow with a Sparse Smoke Concentration (0 to 20 kHz)

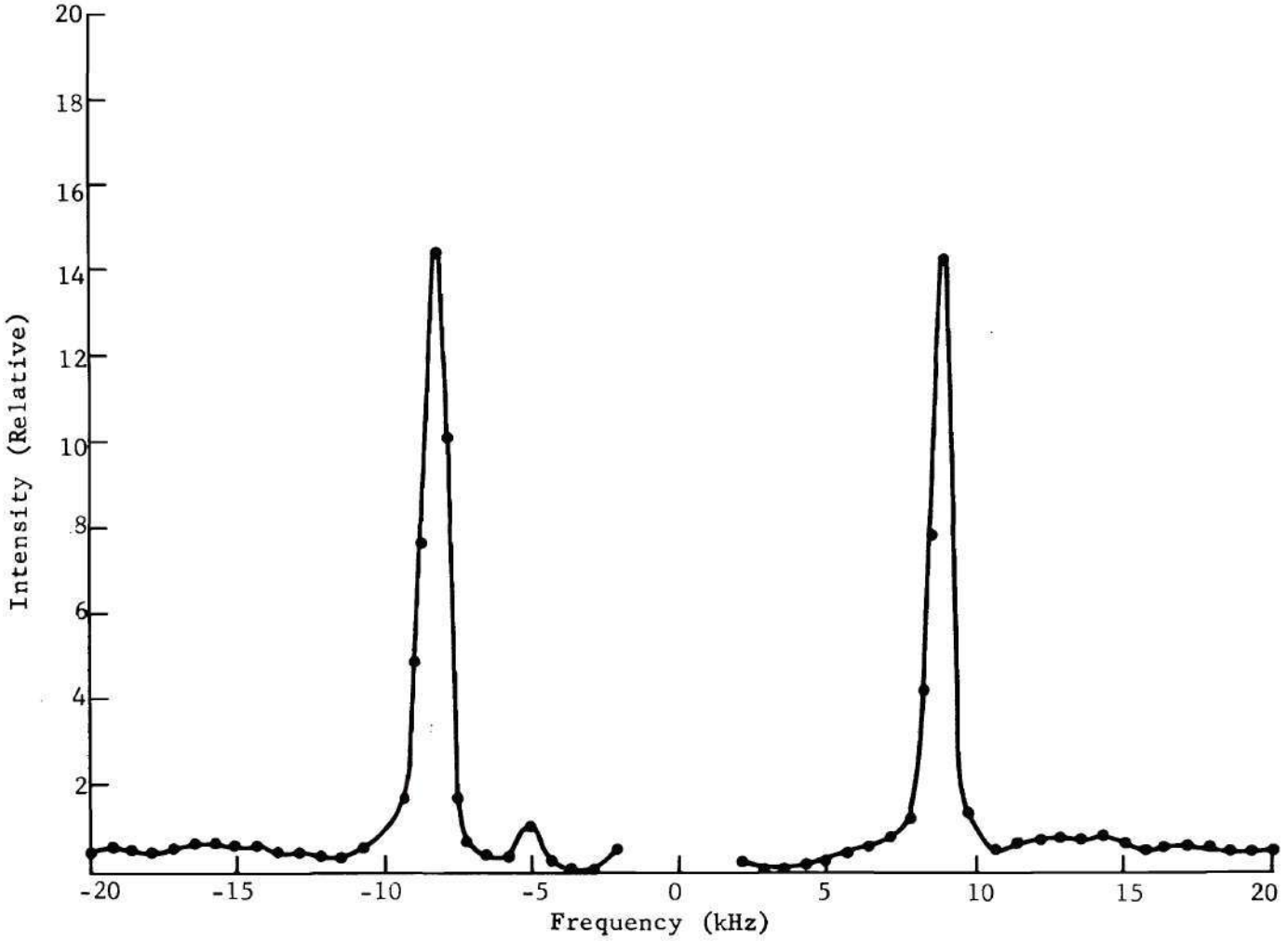

Figure 74. Estimator Output from a 10 kHz LIV Signal Produced by a Steady Flow with a Dense Smoke Concentration

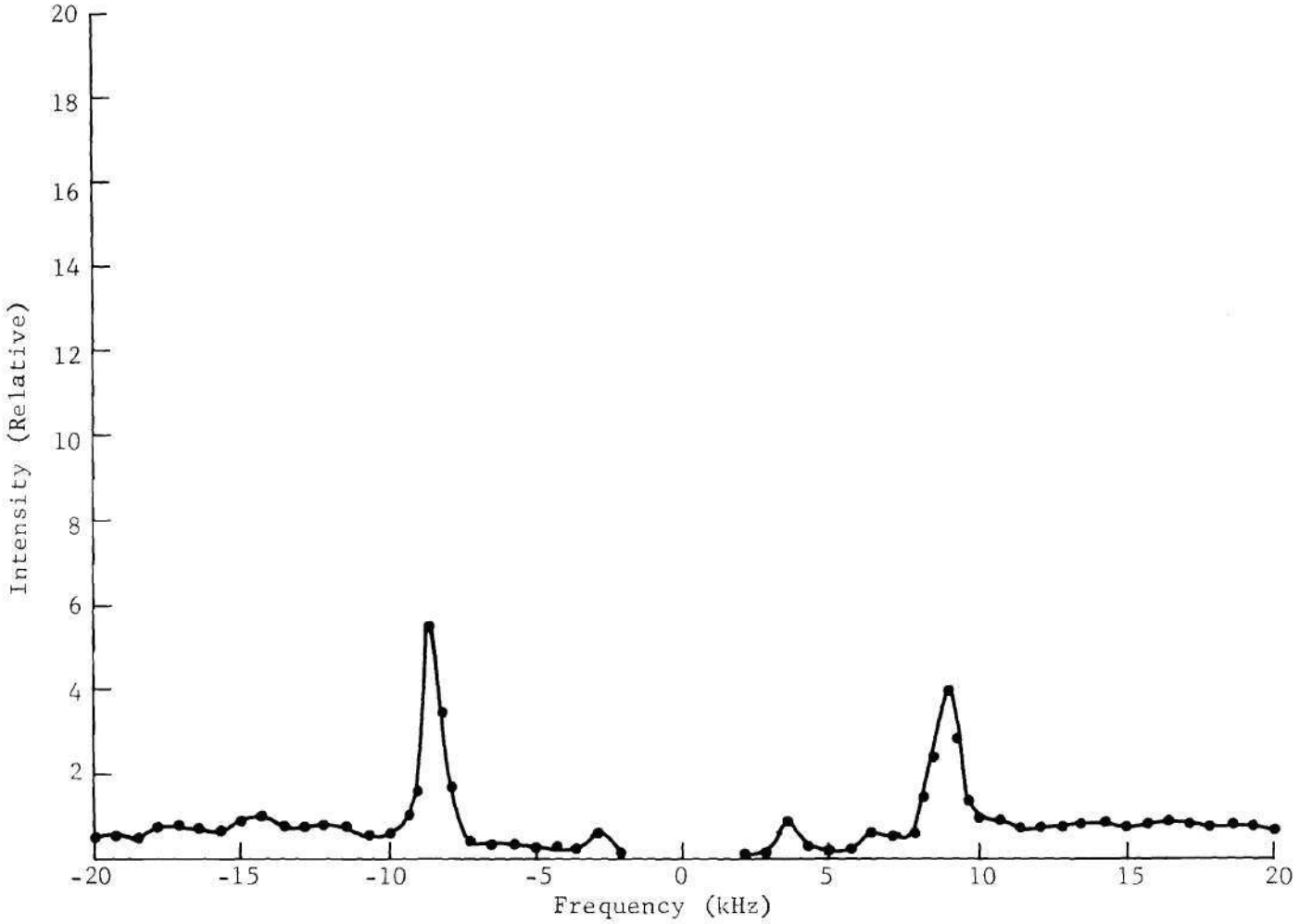

Figure 75. Estimator Output from a 10 kHz LIV Signal Produced by a Steady Flow with a Sparse Smoke Concentration

the output for the sparse particle flows. The performance is consistent with Eqs. (31) and (32) of Chapter V which predict that the performance of the estimator improves as N, the number of particles passing through the volume during the interval T, increases.

Steady Flow High Noise Velocimeter Signals. Up to now, the estimator has shown some improvement in performance over the spectrum analyzer in that the output peaks of the estimator, the location of which determines signal frequency, have been easier to locate than the peaks of the spectrum analyzer. The improvement in performance became more apparent when the noise level of the signals was high. In order to generate high noise signals, the LDV system was set up around the tunnel and the flow adjusted until 10 kHz signals were produced. Then the laser power was reduced by adjusting the variable beam splitter shown in Figure 58. The PMT voltage was increased in order to maintain the strength of the output waveform. It is shown in Eq. (1) of Chapter III that the photon fluctuation noise spectrum is dependent on the intensity of the light on the PMT or the magnitude of the PMT current while the signal spectrum is dependent on the intensity or current squared. Therefore, the reduction of the overall intensity through the reduction of the laser power decreased the signal to noise ratio.

Figure 76 is a photograph of the output of the LDV system under the high noise conditions described above. It is difficult to find any pulses in this signal although the spectrum analyzer trace of the signal shown in Figure 76 indicates that the pulses are there. Although the noise is high, the trace shows some signal around 10 kHz. In order to compare this signal

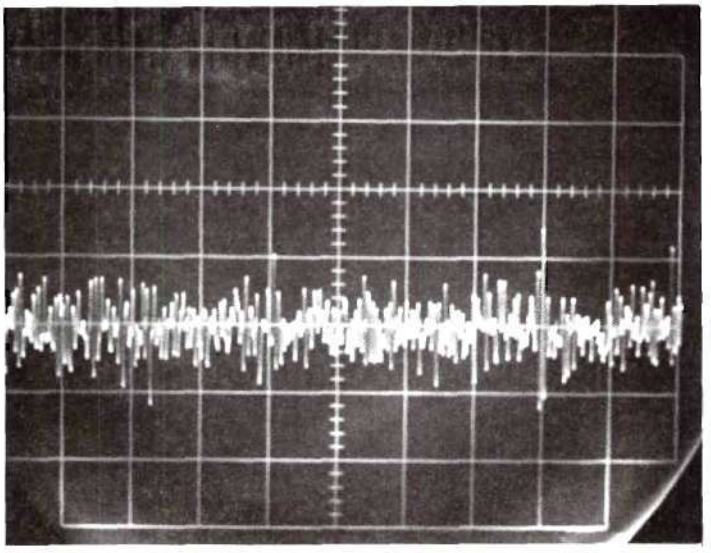

Figure 76. Signal and Noise in a 10 kHz LDV Signal from a Steady Flow When the Noise Is High

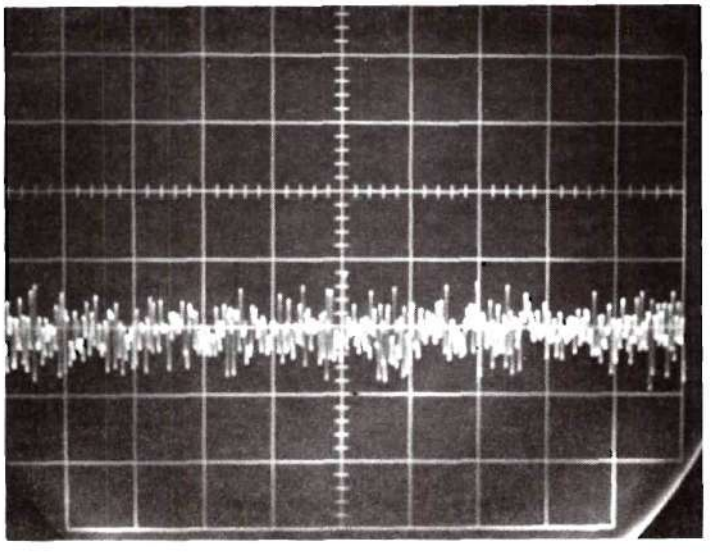

Figure 77. Noise Alone in a 10 kHz LDV Signal

with a signal consisting of noise only, the scattering beam was blocked so that no signal pulses could be generated. Figure 77 shows a trace of this signal consisting of noise only. Note that the noise only signal looks almost the same as the signal in Figure 78. Figure 79 is a spectrum analyzer trace of the noise only signal which shows that the noise is white and demonstrates that no 10 kHz signal pulses are present.

Figure 80 is the output of the estimator with the high noise signal. The output shows two clearly defined peaks at 10 kHz. These peaks are much sharper and easier to locate than the spectrum analyzer peaks of Figure 79. The signal-to-noise ratio as defined in Eq. (37) of Chapter IV is given by

$$S_N = \frac{\int_{-f_H}^{f_H} |S(f,f_D)|^2 \, df}{\int_{-f_H}^{f_H} |N_T(f)|^2 \, df} \qquad (18)$$

which effectively says that the signal to noise ratio is the ratio of the area under the Fourier transform squared of the noise divided by the area under the Fourier transform squared of the signal. The ratio S_N can be approximated from the graph of Figure 80 since this graph is the amplitude squared of the Fourier transform of the signal and noise. The numerator of S_N is estimated by integrating graphically the portion of Figure 80 which is the noise and the denominator is estimated by integrating graphically the portion which is the signal. The estimate of S_N is .48 which says that there is about twice as much noise energy as signal energy.

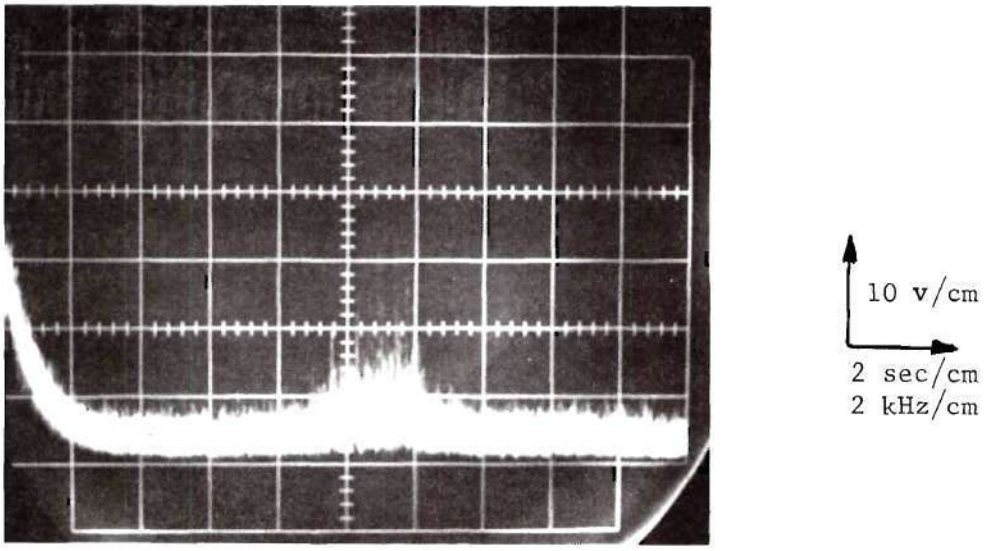

Figure 78. Spectrum Analyzer Trace of Signal and Noise in the High Noise Case

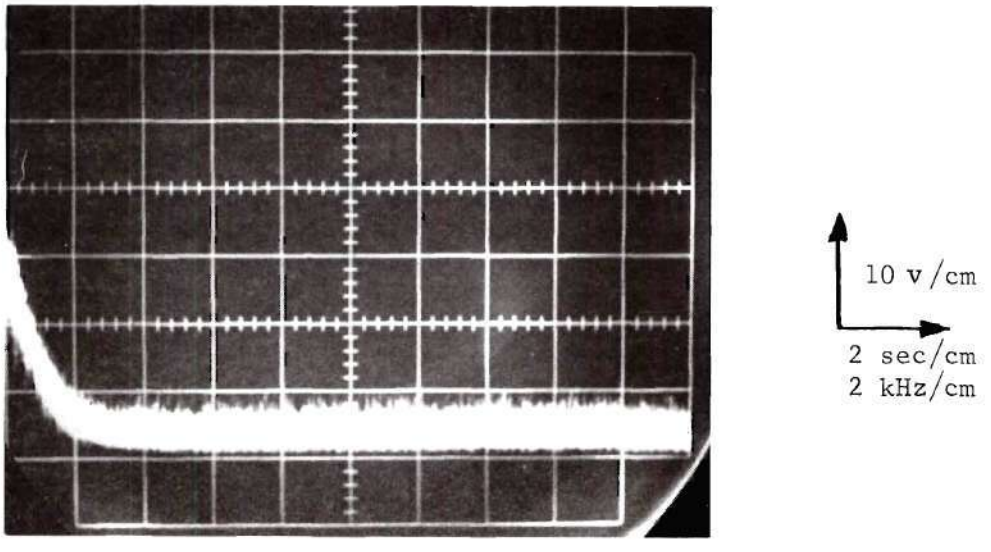

Figure 79. Spectrum Analyzer Trace of Noise Alone in the High Noise Case

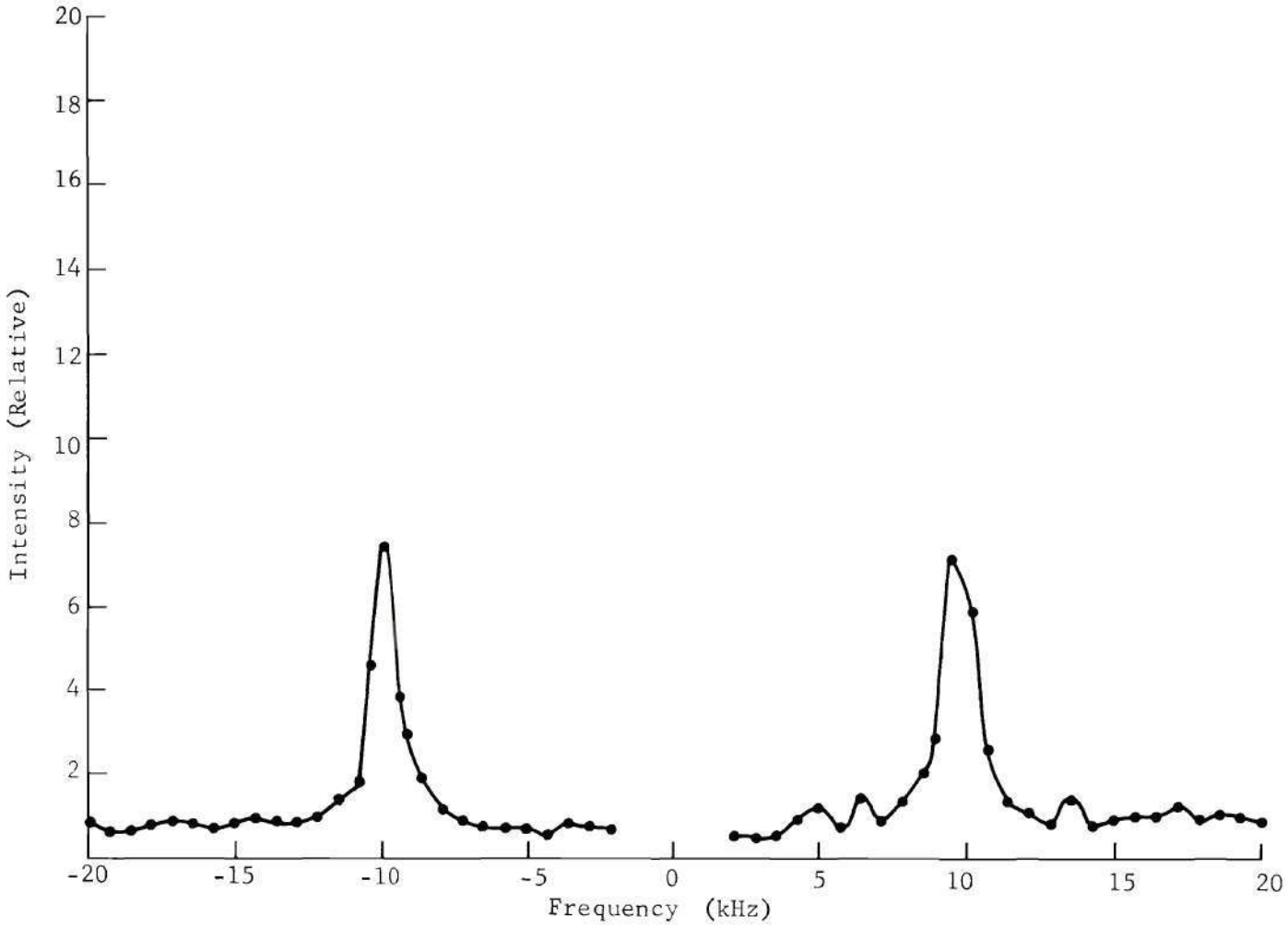

Figure 80. Estimator Output for the High Noise LDV Input

Estimation of the Frequency of Signals from Time-Varying Flows

Once that the performance of the estimator had been demonstrated on steady flows, its performance on time-varying flows was demonstrated. The time-varying flows were generated by placing a motor driven oscillating airfoil in the wind tunnel. The airfoil was one foot long, three inches wide, and about a tenth of an inch thick. The foil oscillated about its center periodically through an angle of about 20°. The rate of oscillation was continuously variable from one to three oscillations per second. The velocimeter detection volume was positioned at a distance of one half inch downstream from the airfoil in the center of the test section. The component parallel to the free stream velocity was measured with the velocimeter in the following tests.

The time variation of the flow behind the airfoil depended on the free stream velocity, the rate of oscillation of the airfoil, the distance behind the airfoil at which the velocity was measured, and the angle through which the airfoil oscillated. An attempt was made to keep all the above parameters constant during the tests and vary only the rate of oscillation of the airfoil. Initially, the airfoil centerline was placed parallel to the flow and the free stream velocity adjusted until 10 kHz steady signals were produced. The flow behind the airfoil was reasonably steady when the airfoil was not oscillating. The airfoil was then adjusted so that it swung 10° above the centerline and 10° below the centerline producing a total swing of 20°. The tests were run over a period of several weeks and at times the airfoil had to be removed from the tunnel. It was difficult to tell whether the airfoil was properly replaced and

conditions exactly duplicated.

Although the time variation of the flow in the detection volume is difficult to predict precisely, certain features can be expected. The flow velocity varies approximately periodically with the same period as the oscillation of the airfoil. If the airfoil is oscillating rapidly, a turbulent component is superimposed on the periodic variation. The turbulent component was clearly observed in the experiments with the airfoil oscillating at 3 Hz and was apparent to a lesser degree in all the time-varying experiments. It is desirable to sample the velocity as often as possible to determine the degree of turbulence and the precise shape of the periodic component.

These experiments tell under what conditions a linear model can be applied to predict the velocity variation in the detection volume. If the flow velocity is sinusoidal with the same frequency as the oscillating airfoil, a linear model would be valid. If the flow is turbulent or if the output is not sinusoidal, a nonlinear model would have to be used. The linearity of the flow can be explored by scanning the detection volume throughout the region of interest.

Estimation Procedure. Since the signals were from time-varying rather than steady flows, the operation of the estimator was slightly different for these experiments as compared to previous experiments. The signals were recorded as before on magnetic tape and then onto photographic film. The film was inserted in plane P1 of the estimator shown in Figure 58. The aperture in front of the film in the steady flow experiments was one inch long allowing an estimate to be made on a .106 second interval

of the signal. Since the signals were steady, a .106 second resolution in time was adequate to describe the signal. When the flow is time varying, it is necessary to reduce the time inverval over which the estimate is made or equivalently to increase the resolution in time.

The aperture was chosen as short as possible to give good time resolution but was also sufficiently long to give good frequency resolution. In order to obtain good frequency resolution it is necessary that the aperture be wide enough to always contain the entire pulse regardless of the frequency of the pulse. If the pulses from the velocimeter contain N cycles, and if the frequency of the pulse is f, the duration of the pulse is N/f. If the lowest frequency considered is also f_L, the duration of the longest pulse is N/f_L. A time duration of N/f_L seconds corresponds to a distance d on the film of

$$d = (vN/f_L)(60/1\ 7/8) \tag{19}$$

Hence the aperture must be d mm long if it is to contain the entire pulse. For the parameters of this system d becomes

$$d = \frac{(7.5\ \text{mm/sec})(12)(60)}{930\ \text{Hz}\ (1\ 7/8)} \tag{20}$$

$$= 3.1\ \text{mm}$$

The lowest frequency of estimation is derived in Eq. (7) and N was shown to be 12 in Chapter II. The aperture was set at 3.1 mm, which corresponded to a resolution T in time given by

$$T = N/f_L \qquad (21)$$
$$= 12/930 \text{ Hz}$$
$$= .0129 \text{ sec}$$

which is equal to the duration of the longest pulse.

The film in plane P1 was mounted on a micrometer drive so that the position of the film in front of the aperture was precisely known. The film was incrementally driven by the aperture and the length of the increments depended on the number of frequency estimates that were needed to define the signal. The photometer with the 12 mil probe was mounted in the output plane P3 as it was in the tests on steady flows. For each successive position of the signal in the input plane, the location of maximum intensity in the output plane was determined with the photometer. The frequency of the increment of the signal in front of the aperture was computed by using the same conversion factor as used in the experiments with steady flows, namely 1 kHz/1.2 mm. The frequency estimates are presented in terms of plots of signal frequency as determined from the micrometer readings in the output plane P3 versus the time at which that estimate was made as determined from the micrometer readings in the input plane P1. It is estimated that the micrometer in the output plane could be read accurately to one half millimeter over a range from 1.2 to 24 mm yielding 46 resolvable estimates in frequency. The range from 1.2 to 24 millimeters corresponds to the frequency range of 930 Hz to 20 kHz.

Since the signal frequency was constant in the steady flow experiments, it was quite easy to obtain spectrum analyzer traces from the Tektronix 1L5 for comparison with the estimator. However, the spectrum

analyzer could not track the time-varying signal well enough to give much indication of how the signal frequency varied in time. The spectrum analyzer by its very nature is designed to estimate the spectrum or frequency of steady rather than frequency varying signals. The incoming signal is mixed with an oscillator signal which sweeps the incoming signal in frequency by a filter. The output of the filter is displayed on a screen and the position on the screen of the maximum response indicates the signal frequency. It is necessary that the sweep time T_S be long enough to allow the signal to remain at the filter for its duration in order to have good resolution in frequency. The duration of the longest signal is N/f_L and hence the sweep time T_S should be chosen to allow the signal pulse to remain at the filter for N/f_L seconds to insure that the entire signal is at the filter at once. Assuming that there are M frequencies resolvable by the filter from f_L to the highest frequency in the range, T_S must be at least

$$T_S \geq MN/f_L \tag{22}$$

seconds long for each pulse to be assured of remaining by each filter for its entire duration of N cycles. Therefore, the sampling time, i.e., the time interval at which the frequency can be sampled, is constrained to be at least MN/f_L seconds. It is estimated M = 40, i.e., there are forty resolvable positions on the oscilloscope screen displaying the spectrum analyzer trace. Using these values, T_S, the sweep time or sampling time becomes

$$T_S = MN_o/f_{LO} \tag{23}$$

$$= \frac{(12)(40)}{930}$$

$$= .516 \text{ sec}$$

The sampling interval of .516 sec is not short enough to yield any significant information of the .75, 1, or 3 Hz signals.

Low Noise Time-Varying Signals. Low noise time-varying signals were generated with the LIV system and the airfoil oscillating at .75 Hz and 3.0 Hz. As pointed out in the section on steady flows, LIV signals were used in the low noise experiments because they had less noise than LDV signals. The signals were recorded on magnetic tape and then on film and were inserted into the estimator. The .75 Hz signals were sampled at the rate of 15 times per second or once every .067 second. To obtain this sampling rate, the film was moved in increments of 16 mm which corresponded to time intervals of .067 sec. Figure 81 shows the frequency variation as a function of time for the .75 Hz oscillation. Note that the velocity was approximately periodic with a period of .75 Hz. The flow was almost sinusoidal, but had distinct character at the maximum and minimum velocities. Since the waveform of each period was almost the same, very little turbulence was present.

The 3 Hz oscillating flow was sampled at a rate of 80 samples per second which implied that the film had to be moved in increments of 3 mm. The flow velocity and frequency as a function of time are shown in Figure 82. The inertia of the air was too great for it to oscillate at the same

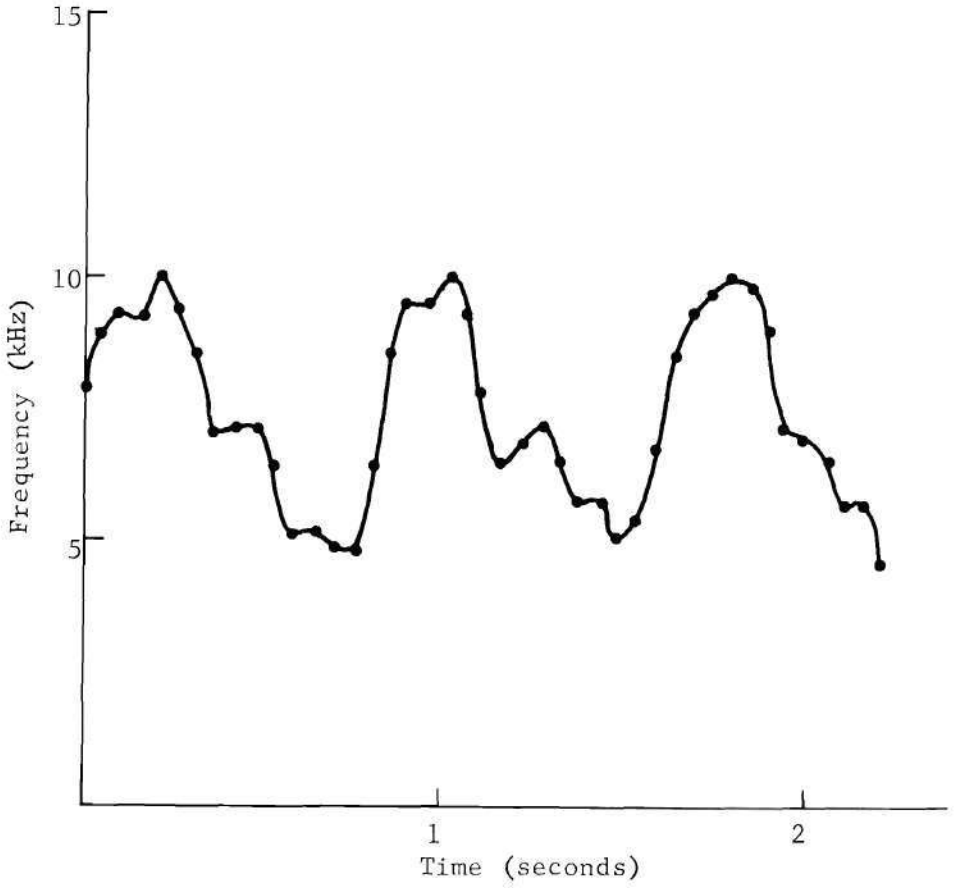

Figure 81. Time Variation of Frequency of a Low Noise LIV Signal When the Airfoil Oscillated at .75 Hz

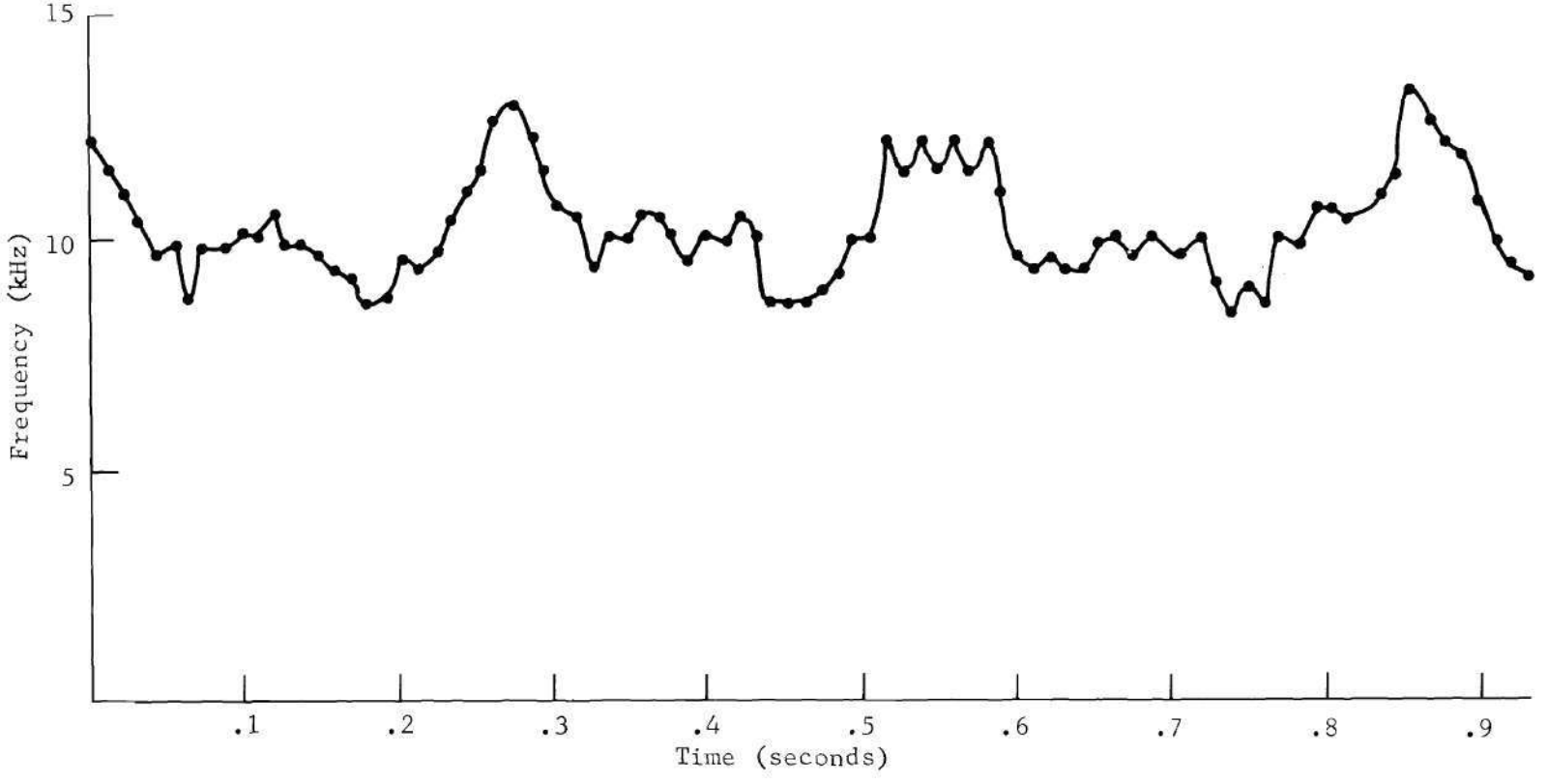

Figure 82. Time Variation of Frequency of a Low Noise LIV Signal When the Airfoil Oscillated at 3 Hz

frequency as the airfoil. Note that some periodic nature was present with an approximate frequency of 2.7 Hz. A considerable amount of turbulence was present, however, since the waveform was not the same for each period. Qualitatively, the experimental results are what one would expect. The flow velocity "follows" the oscillation of the airfoil at low frequencies (.75 Hz) but not at high frequencies (3 Hz).

Time-Varying Flows with Low Particle Concentrations. The low concentration or sparse particle case is a very important case since it can be difficult or undesirable to seed wind tunnels with large particle concentrations. High speed wind tunnels in which a lot of air is passed would require a huge amount of smoke to maintain a large concentration of particles in the test section. A considerable amount of modification would be required to modify a wind tunnel for such a large seeding. Also, excessive quantities of smoke may dirty the wind tunnel windows degrading velocimeter performance and may clog up pitot tubes used for pressure measurements. For these reasons, it is desirable to have an estimator which works well on flows with low particle concentrations.

To attain low particle concentrations, the smoke generator was adjusted so that the signals on the oscilloscope screen from the LIV system were very sparse. The concentration of smoke was so low that no smoke was visible in the tunnel. The airfoil oscillated at one Hz and data were recorded on magnetic tape and then on photographic film as before. Since the particle concentration was so low, estimates were made at every position on the film that a pulse was present. The film was translated and when a signal appeared in the output plane an estimate was made. Hence

the sampling interval was irregular and varied in contrast to the low noise experiments described previously.

The plot of frequency versus time for this experiment is shown in Figure 83. Note that the flow had a period of about 1 Hz although the waveform varied from period to period. The variation from one period to the next shows that the flow was to some extent turbulent. Since the velocity seems to have had an unequal duty cycle, i.e., the frequency was less than 10 kHz for a longer time than it was greater than 10 kHz, the velocity is not sinusoidal. The linearity approximation may not have held in this experiment as well as in some of the previous ones.

Time-Varying Signals with High Noise. The time-varying signals with high noise were generated in a manner similar to the steady signals with high noise. The LDV system was set up around the tunnel and laser power reduced while the PMT voltage was increased to maintain the strength of the output electrical signal. The net result was a decrease in the signal to noise ratio due to an increase in photon fluctuation noise. Once the laser power and PMT voltages were set, the airfoil was made to oscillate at one Hz and signals were recorded on the tape recorder and then on photographic film.

The noise in the high noise time-varying signal was comparable to the noise in the high noise steady signals. Figure 84 is a photograph of the signal and noise and Figure 85 is a photograph of the noise alone. Figure 85 was made with the scattering beam blocked so that no signal could be generated. Note that there is not very much difference between signal and noise and the noise alone indicating that the signal was quite

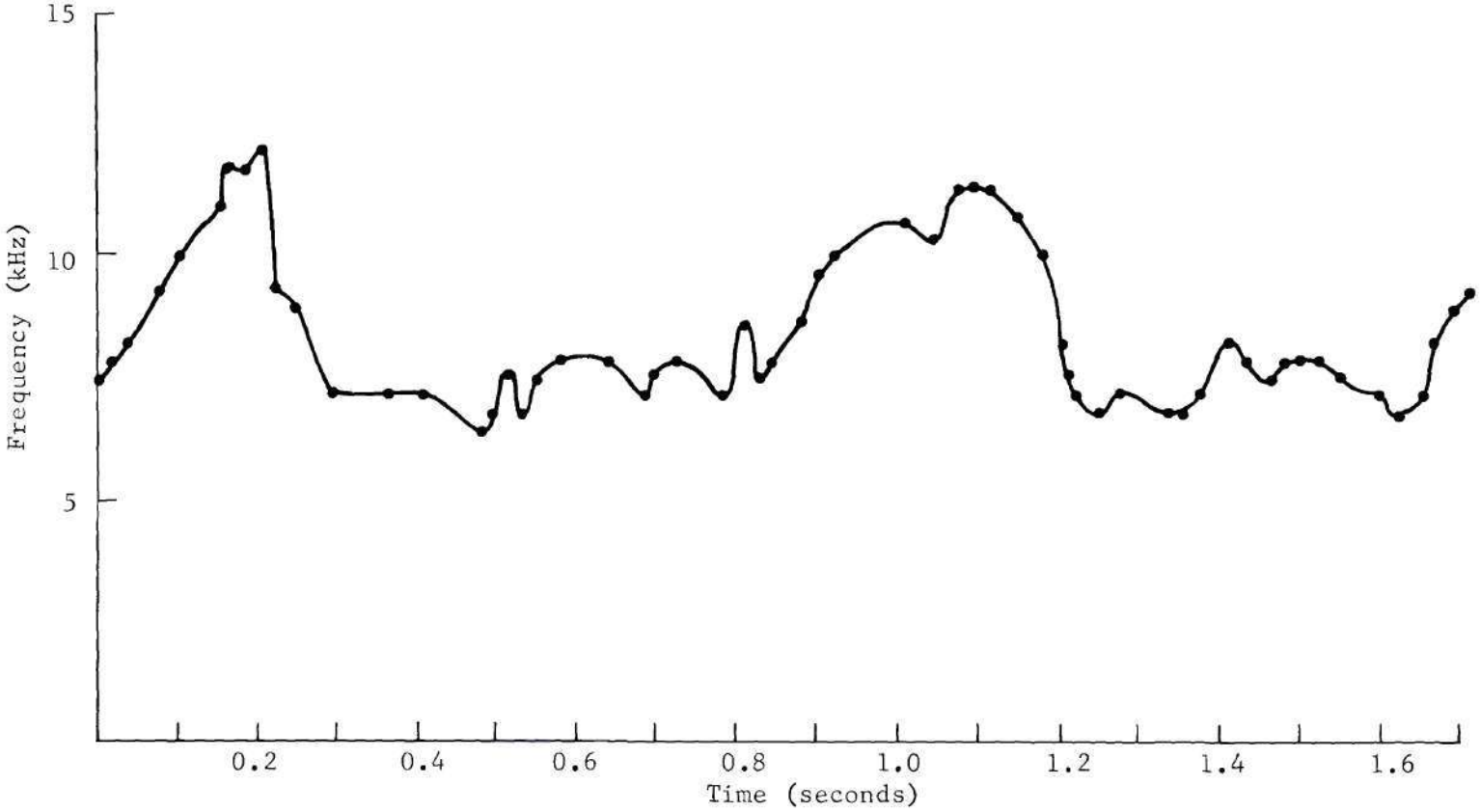

Figure 83. Time Variation of Frequency of a Low Noise LIV Signal When the Particle Concentration Is Sparse. (The airfoil oscillated at 1 Hz.)

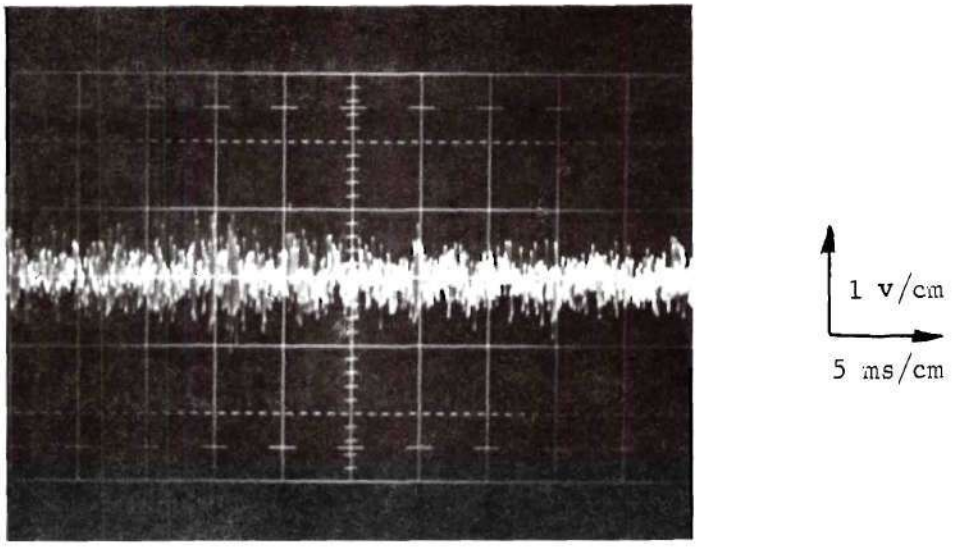

Figure 84. Trace of LDV Signal and Noise Generated from a Time-Varying Flow Under High Noise Conditions

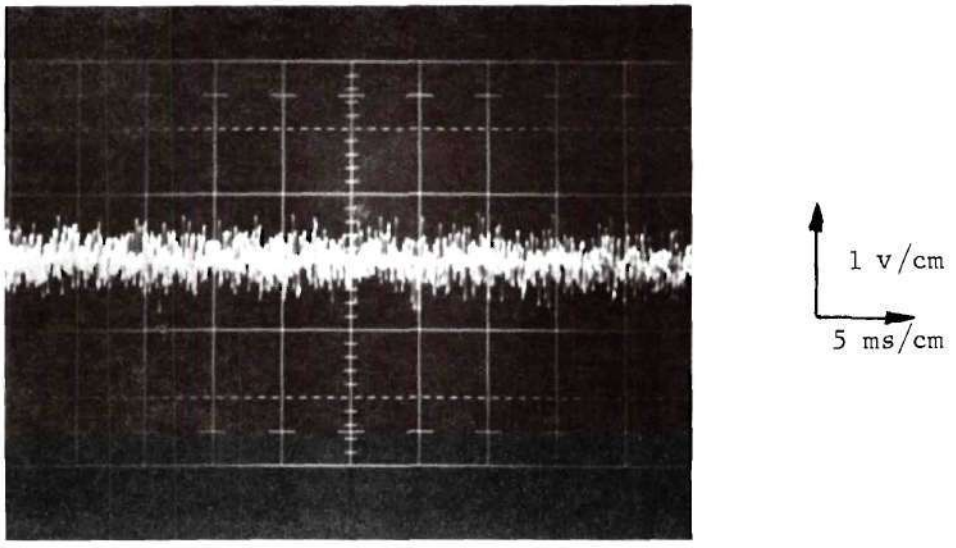

Figure 85. Trace of LDV Noise Alone

small. Figure 86 is a plot of the output signal of the estimator when the frequency was 10 kHz. The signal to noise ratio S_N defined in Eq. (37) of Chapter IV was computed from this graph by taking the ratio of the area under the signal portion of the graph to the area under the noise portion. The value of S_N was .4 indicating that there was 2.5 times more noise energy than signal energy. Figure 87 is a plot of the frequency variation of the signal as measured by the estimator. Note that the variation is approximately sinusoidal with a frequency of one Hz.

Discussion of Experimental Results and Comparison with Other Estimators

The purpose of the preceding experiments was to demonstrate the capability of the Fourier transform estimator concept to estimate the frequency of a wide variety of velocimeter signals with performance superior to conventional approaches. The flows dealt with were steady and time-varying flows with various noise levels and particle concentrations. The estimator performed well with all these flows proving its capability to estimate frequencies of high noise signals with rapidly varying flow velocities.

The first set of experiments showed that the estimator could accurately estimate the frequency of low noise velocimeter signals from steady flows. The estimator's performance was a little better than the spectrum analyzer in that the estimator produced narrow pulses whose centers could be accurately located to determine frequency while the spectrum analyzer produced a somewhat broader pulse whose center was more difficult to

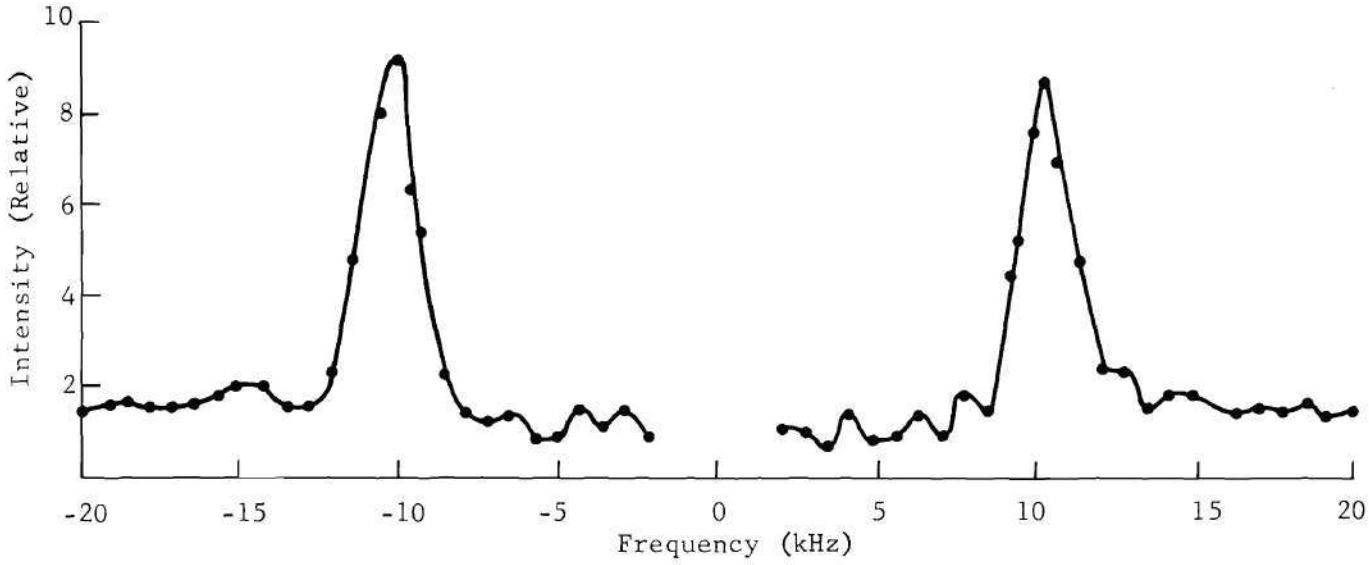

Figure 86. Output of the Estimator When the High Noise Time-Varying LDV Signal Was Applied

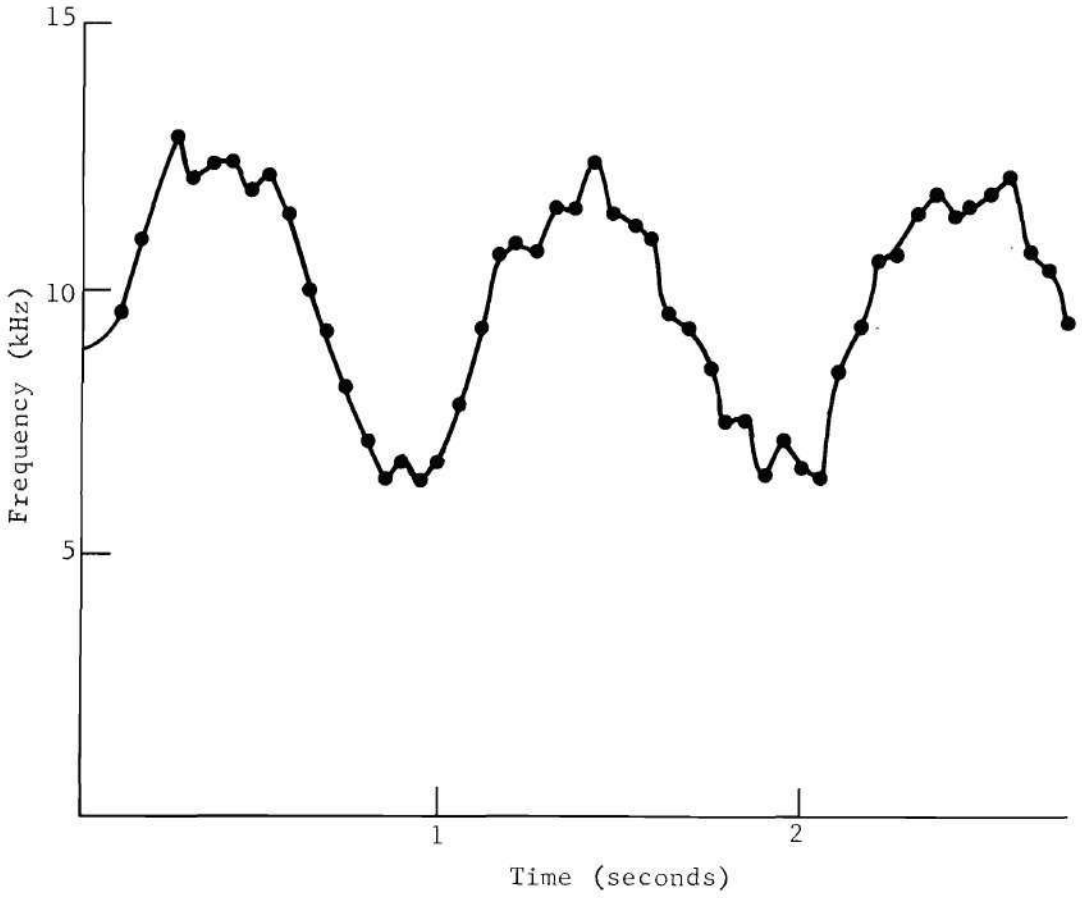

Figure 87. Time Variation of the Frequency of the High Noise LDV Signal When the Airfoil Oscillated at 1.05 Hz

determine. The estimator clearly worked better than the spectrum analyzer when the steady velocimeter signal had a high noise level. The spectrum analyzer trace was irregular and slightly higher at the correct frequency while the estimator had a clear and distinct pulse with a peak at the positions corresponding to the proper frequency. The oscilloscope traces of the signals in time showed an FM discriminator such as zero crossing detector would not work at all on the high noise signal since it is difficult to see any difference between the trace of signal and noise and the trace of noise alone.

The estimator tracked the low noise time-varying flows well enough to give meaningful information about the degree of nonlinearity and turbulence in the flows. Frequency estimates at the rate of 15 per second were made on a time-varying flow produced by an airfoil oscillating at .75 Hz. Estimates at the rate of 80 per second were made on the flow produced by an airfoil oscillating at 3 Hz. The maximum time resolution for the estimator was .0129 second or 80 samples per second. The spectrum analyzer was of no use in these experiments since its sampling interval was .516 second corresponding to less than 3 samples per second.

The resolution in frequency of the estimator was limited to about 45 different frequencies due to the fact that the micrometer driving the probe could only read positions accurately to .5 millimeter. This was the best drive available for the thesis. However, micrometers accurate to .05 millimeter are easily attainable. Such a micrometer would yield about 460 possible different estimates in frequency over the range of 930 Hz to 20 kHz. The large number of resolvable frequencies illustrates the ad-

vantage of the estimator over a parallel filter bank. A parallel filter bank is limited to a finite number of discrete frequency estimates over a given range while the proposed estimator effectively gives a continuum of estimates over the range.

The estimator demonstrated its ability to estimate frequencies when concentrations of particles were quite low. During this experiment, the estimator made an estimate of every pulse during a time interval of about two seconds for a total of 82 estimates. Since the frequency of each pulse was estimated, maximum use was made of the signal available. The flow was generated by the airfoil's oscillating at one Hz and the estimator showed that some turbulence was present. The low particle concentration case is very important since it is desirable to have as few particles as possible in the flow.

The experiment with high noise time-varying signals demonstrated the estimator's ability to estimate time-varying frequency under high noise conditions. The noise was so great that it was again difficult to distinguish between traces of noise alone and signal and noise together indicating that an FM discriminator could not estimate the frequency at all.

CHAPTER VI

SUMMARY, CONCLUSIONS, AND RECOMMENDATIONS

The objectives of this dissertation were to develop mathematical models for laser Doppler velocimeters and laser interference velocimeters. Then, an estimation technique which performed well with high noise signals and signals whose frequency was rapidly changing was presented. Although only a "breadboard" estimator was built for this dissertation, the design can be engineered into a useable and practical instrument.

Summary and Conclusions

Chapter I showed the relationship of the laser velocimeter to the general problem of wind tunnel measurements. Ideally, the aeronautical engineer would like to know the pressure, temperature, density, and velocity at every point in a wind tunnel test section. Devices exist to give pressure, temperature, and density measurements but no suitable means exist to measure velocity. The hot wire anemometer can measure velocity, but it is difficult to use and calibrate and is very easily broken. In addition, the hot wire interferes with and changes the flow velocity. The laser velocimeter has the potential of being a self calibrating, reliable, easy-to-use, and non-interfering means of measuring wind tunnel velocities.

In Chapter II, the operation of laser interference velocimeters and laser Doppler velocimeters was explained in detail. Mathematical

models of the signals produced by the velocimeters driven by lasers operating in the TEM_{00} mode were derived through the use of the Fresnel-Kirchhoff integral. It was found that signals from both types of velocimeters are discrete sinusoidal pulses with Gaussian envelopes. Both types of velocimeters were built and experiments were carried out to verify the signal models.

The problem of noise in velocimeter systems was discussed in Chapter III. The sources of noise and their relative contributions to the total noise in both types of velocimeters were discussed. Experiments were carried out to verify the predictions regarding noise. The noise in the laser Doppler velocimeter is primarily produced by the reference beam falling on the PMT and is white Gaussian noise. The noise in the laser interference velocimeter is produced by background light and thermal noise in the amplifiers and is also white Gaussian noise.

The "Fourier transform estimator" was presented in Chapter IV. Effectively, the estimator performs a Fourier transformation on the incoming signal. The frequency at which the transform is maximum is taken as the estimate of the signal frequency. A means to implement the estimator was suggested which makes use of optical data processing techniques. A bound on the risk of the estimator was derived.

The experimental verification of the estimator was carried out in Chapter V. A breadboard estimator was built and representative velocimeter signals were generated in a low speed wind tunnel. The estimator was shown to be capable of tracking the rapidly changing frequency of signals under the high noise conditions.

Recommendations

The feasibility of the Fourier transform estimator has been demonstrated in this dissertation. The remaining job is to design an instrument based on this principle which an aerodynamicist can use. The data recorder should use a laser beam so that signals can be written on the film at high spatial frequencies. The laser beam in the recorder can be modulated with an electro-optic modulator which has bandwidths up to 100 mHz. A matrix of solid state detectors can be placed in the output plane of the estimator to locate the spatial frequency where the intensity is maximum.

APPENDICES

APPENDIX A

DEPTH OF FIELD OF THE GAUSSIAN BEAM USED IN THE EXPERIMENTS

The depth of field of the image of the pinhole created by lens L1 of Figures 10 and 25 can readily be calculated from the expressions derived by Kogelnik and Li.[16] The pinhole itself is 50 microns in diameter and its distance from L1 is 9.5 inches. The image of the pinhole is 250 inches from the lens giving a magnification M of

$$M = \frac{250}{9.5}$$

$$= 26.3$$

The pinhole image then has a diameter D given by

$$D = (26.3)\ (50 \text{ microns})$$

$$= 1.32 \text{ mm.}$$

Kogelnik and Li[16] demonstrate for Gaussian laser beams that the radius squared $w^2(z)$ of the beam at a distance z from the image plane is given by

$$w^2(z) = w_o^2\left(1 + \left[\frac{\lambda z/2}{\pi w_o^2}\right]^2\right)$$

where w_o is the radius of the image of the pinhole which in this case is .66 mm. If the depth of field is taken to be the distance that the beam

area increases by no more than one percent, the depth of field z follows from

$$\left(\frac{\lambda z/2}{\pi w_o}\right)^2 = .01$$

$$z = \frac{.2\pi w_o^2}{\lambda}$$

Substituting the parameters of the experiment into the above relation, z becomes

$$z = \frac{(.2)(\pi)(.66)^2}{.6328 \times 10^{-3}}$$

$$= .43 \text{ meter}$$

APPENDIX B

STATICALLY OPTIMUM ESTIMATOR FOR THE LDV SYSTEM AND ITS RELATIONSHIP TO THE FOURIER TRANSFORM ESTIMATOR

It is demonstrated in Chapter II and III that the signal from an LDV system can be modeled as a summation of sinusoidal pulses in white Gaussian noise. Eq. (25) of Chapter III states the LDV signal as

$$r_{TD}(t) = \sum_{i=1}^{N} B_i \, e^{-\alpha(2\pi f_D)^2 (t-t_i)^2} \cos 2\pi f_D (t-t_i) + n(t) \qquad (1)$$

where, as defined earlier, B_i is the amplitude of each pulse, t_i is the arrival time of the pulse, f_D is the frequency of the pulse, and N is the number of pulses during a given interval T. The interval T is chosen to give the required time resolution in the estimation of f_D. It is assumed that T is short enough that all the pulses have the same frequency f_D. The noise term n(t) is white, Gaussian noise whose spectrum has a value of $N_o/2$. The above signal $r_{TD}(t)$ can be written in a compact form more convenient for analysis as follows

$$r_{TD}(t) = s(t,\bar{A}) + n(t) \qquad (2)$$

$$s(t,f_D) = \sum_{i=1}^{N} B_i \, e^{-\alpha(2\pi f_D)^2 (t-t_i)^2} \cos 2\pi f_D (t-t_i)$$

$$\bar{A} = (f_D, B_1, \ldots, B_N, t_1, \ldots, t_N, N)$$

The vector $\bar{A}$ contains all the unknowns as components and is referred to as the unknown vector.

There are several optimum estimator structures which can be derived depending on the a priori assumptions made about $\bar{A}$. If $\bar{A}$ is chosen to be a random variable, and a priori statistics assigned to the components of $\bar{A}$, a maximum a posteriori estimate of $\bar{A}$ results. If $\bar{A}$ is considered unknown but nonrandom and hence no statistics assigned to it, the optimum estimator is a maximum likelihood estimator. A hybrid estimator could be derived in which some of the parameters are assumed random and some are not.

Under cases of turbulent flow, f_D might be modeled as Gaussian. The arrival times of the particles, $t_1, \ldots, t_N$, could be assumed uniform over the interval T and N could be modeled as a Poisson random variable. However, the particles quite often travel in bursts if the smoke generator for the tunnel sends out puffs rather than a uniform stream of smoke making the assumptions of uniformly distributed arrival times questionable. The amplitudes of the pulses are a function of a number of parameters, mainly the sizes and reflectivities of the particles producing the pulses. To accurately describe the a priori statistics of the pulses would require very complicated expressions and would likely involve nonstationary probability densities. Often, very little information is known about the size and reflectivity of the seeding particles or about the characteristics of the particulate dispenser, all of which are important in determining the a priori statistics. Although f_D can be modeled at times as Gaussian, the mean and variance of that Gaussian density are usually unknown. Since the a priori statistics are difficult to

determine, the maximum a posteriori estimator which depends on the a priori statistics is not derived for this problem.

Instead, the maximum likelihood estimator which assumes no a priori statistics is the estimator derived. This estimator assumes that all of the components of $\bar{A}$ are unknown, and that no information is available regarding their statistical behavior. The maximum likelihood estimator generates a function called the "likelihood function" and chooses as its estimate the value of the unknown which maximizes this function. If the noise is white Gaussian noise, the estimate which maximizes the likelihood function can also be shown to be the estimate which maximizes the function $L(\hat{\bar{A}})$ defined as[43]

$$L(\hat{\bar{A}}) = 2 \int_o^T r_{TD}(t)\, s(t,\hat{\bar{A}})\, dt - \int_o^T s^2(t,\hat{\bar{A}})\, dt \qquad (3)$$

Various values of $\hat{\bar{A}}$ are substituted into Eq. (3) and the one which maximizes it, denoted by $\bar{A}_0$, is the maximum likelihood estimate of $\bar{A}$. The operation specified by Eq. (3) is shown schematically in Figure 88. Effectively, the incoming signal $r_{TD}(t)$ is correlated with a noiseless replica $s(t,\hat{\bar{A}})$ of the signal. A threshold equal to the energy of the replica is subtracted from the correlation. The estimate $\hat{\bar{A}}$ which controls the shape of the replica $s(t,\hat{\bar{A}})$ is varied over all possible $\hat{\bar{A}}$ and the value of $\hat{\bar{A}}$ which maximizes $L(\hat{\bar{A}})$ becomes the maximum likelihood estimate.

Although the maximum likelihood estimator is conceptually simple, it is difficult to implement practically. Since the number of pulses in the interval T as well as the spacings and amplitudes of the pulses are unknown, many different samples of $s(t,f_D)$ must be generated on order to

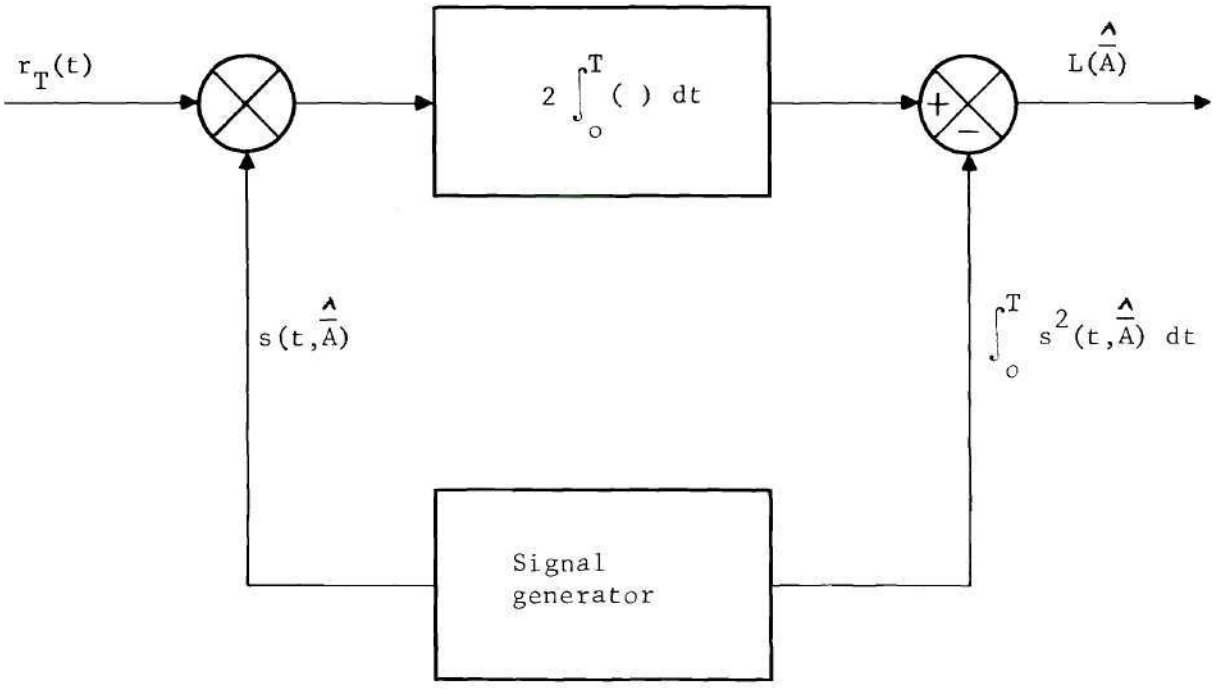

Figure 88. Schematic of the Maximum Likelihood Estimator of $\overline{A}$

find the one which maximizes $L(\hat{\underline{A}})$. In addition to the large number of samples of $\hat{\underline{A}}$ which must be generated, f_D may be in the megahertz range generating a considerable amount of data for processing. One approach in implementing the estimator is to construct a filter bank with filters which have an impulse response corresponding to each $s(t,\hat{\underline{A}})$. Such a filter bank would be far too large to practically construct. Data rates in the megahertz range would rule out a digital computer implementation of Eq. (3).

The filter bank approach is used in the pulse Doppler radar problem whose relationship to the velocimeter estimation problem was discussed in Chapter I. Such an approach is feasible in the pulse Doppler problem because the pulse train which is transmitted is only unknown within an arrival time and a frequency shift. The relative amplitudes and spacings of the pulses in the train are known in contrast to the velocimeter problem. The knowledge of the relative amplitudes and pulse spacings reduces the number of possible $s(t,\hat{\underline{A}})$ and hence the number of filters required for the bank.

Although the maximum likelihood estimator is not buildable, it does have several favorable features. The interval T can be made as short as desired to obtain velocity measurements to the desired time resolution. Each pulse in the interval T contributes to the estimate of $\bar{A}$ making efficient use of all the available data. By the fact that it is a maximum likelihood estimator, it is the optimum estimator in extracting the signal from the noise.

Now that the maximum likelihood estimator has been stated, its

structure is studied to see if it can be simplified into a more practical or buildable system. Since f_D is primarily what is being estimated, assume for the moment that all of the other components of $\bar{A}$, namely $(B_{l_r}, \ldots, B_N, t_1, \ldots, t_N, N)$ are known. The function $L(\bar{A})$ becomes $L_1(f_D)$ in terms of f_D as follows

$$L_1(\hat{f}_D) = 2 \int_o^T r_{TD}(t)\ s(t,\hat{f}_D)\ dt - \int_o^T s^2(t,\hat{f}_D)\ dt \tag{4}$$

The function $L_1(\hat{f}_D)$ consists of two terms as shown in the above equation. The first term will be referred to as the "correlation term" and the second as the "threshold term." Both terms are examined to see if one of the terms can be eliminated without much loss in performance.

The dependence of the correlation and threshold terms on $\hat{f}_D$ is determined. The incoming signal $r_{TD}(t)$, given by

$$r_{TD}(t) = s(t,f_D) + n(t) \tag{5}$$

where f_D is the signal frequency, is substituted into the correlation term yielding

$$2 \int_o^T r_{TD}(t)\ s(t,\hat{f}_D)\ dt = 2 \int_o^T [s(t,f_D) + n(t)]\ s(t,\hat{f}_D)\ dt \tag{6}$$

$$= 2 \int_o^T s(t,f_D)\ s(t,\hat{f}_D)\ dt + 2 \int_o^T s(t,\hat{f}_D)\ n(t)\ dt$$

Substituting the expressions for $s(t,f_D)$ and $s(t,f_D)$ given by Eq. (4)

into the correlation term and evaluating, the dependence on f_D can be shown to be of the form

$$\frac{e^{-\frac{1}{4\alpha}\left(\frac{(\hat{f}_D - f_D)^2}{\hat{f}_D^2 + f_D^2}\right)}}{\sqrt{\alpha(\hat{f}_D^2 + f_D^2)}}$$

In the vicinity of f_D, the correlation term depends on f_D both exponentially as $(\hat{f}_D - f_D)^2$ and inversely as $1/\hat{f}_D$. The dependence of threshold term on $\hat{f}_D$ is found by substituting the expression for $s(t,\hat{f}_D)$ of Eq. (4) into the threshold term. Upon evaluation, the threshold term is shown to vary as $1/\hat{f}_D$. Details of the dependence of the correlation and threshold terms on $\hat{f}_D$ are discussed in Appendix C.

Since the correlation term depends both exponentially and inversely on $\hat{f}_D$ while the threshold term depends only inversely on $\hat{f}_D$, one can conclude that the correlation term has a stronger influence on the value of $\hat{f}_D$ that maximizes $L_1(\hat{f}_D)$ than the threshold term. With the correlation term turning out to be dominant, a possible suboptimal but simpler estimate of $\hat{f}_D$ is that value of $\hat{f}_D$ which maximizes $L_2(\hat{f}_D)$ defined by

$$L_2(\hat{f}_D) = \int_{-\infty}^{\infty} s(t,\hat{f}_D)\, r_{TD}(t)\, dt \tag{7}$$

Applying Parsevals Theorem to Eq. (7), the following is obtained

$$L_2(\hat{f}_D) = \int_{-\infty}^{\infty} R(f,\hat{f}_D)\, S^*(f,\hat{f}_D)\, df \tag{8}$$

where $R_D(f,f_D)$ and $S(f,\hat{f}_D)$ are the Fourier transforms of $r_{TD}(t)$ and $s(t,\hat{f}_D)$, respectively.

Although there are several ways to select an $\hat{f}_D$ so that $L_2(\hat{f}_D)$ is large, it is clear that the selection must be such that $R(f,f_D)$ and $S(f,\hat{f}_D)$ are nonzero over the same frequency range. The functions $R(f,f_D)$ and $S(f,\hat{f}_D)$ are shown in Appendix D to be Gaussian in shape as depicted in Figure 89. It is clear from the figure that one choice of $\hat{f}_D$ is $\hat{f}_{DF}$, the value of f for which $R(f,f_D)$ is maximum. If there is no noise, $\hat{f}_{DF}$ is the correct answer f_D. With the choice $\hat{f}_{DF}$, the functions $S(f,\hat{f}_{DF})$ and $R(f,\hat{f}_{DF})$ are nonzero over the same range of frequencies and $L_2(\hat{f}_{DF})$ should be large. In other words, to estimate the frequency of the incoming signal $r_{TD}(t)$, simply take its Fourier transform and find out which value of f makes it maximum. This method is the "Fourier Transform method" described in Chapter IV.

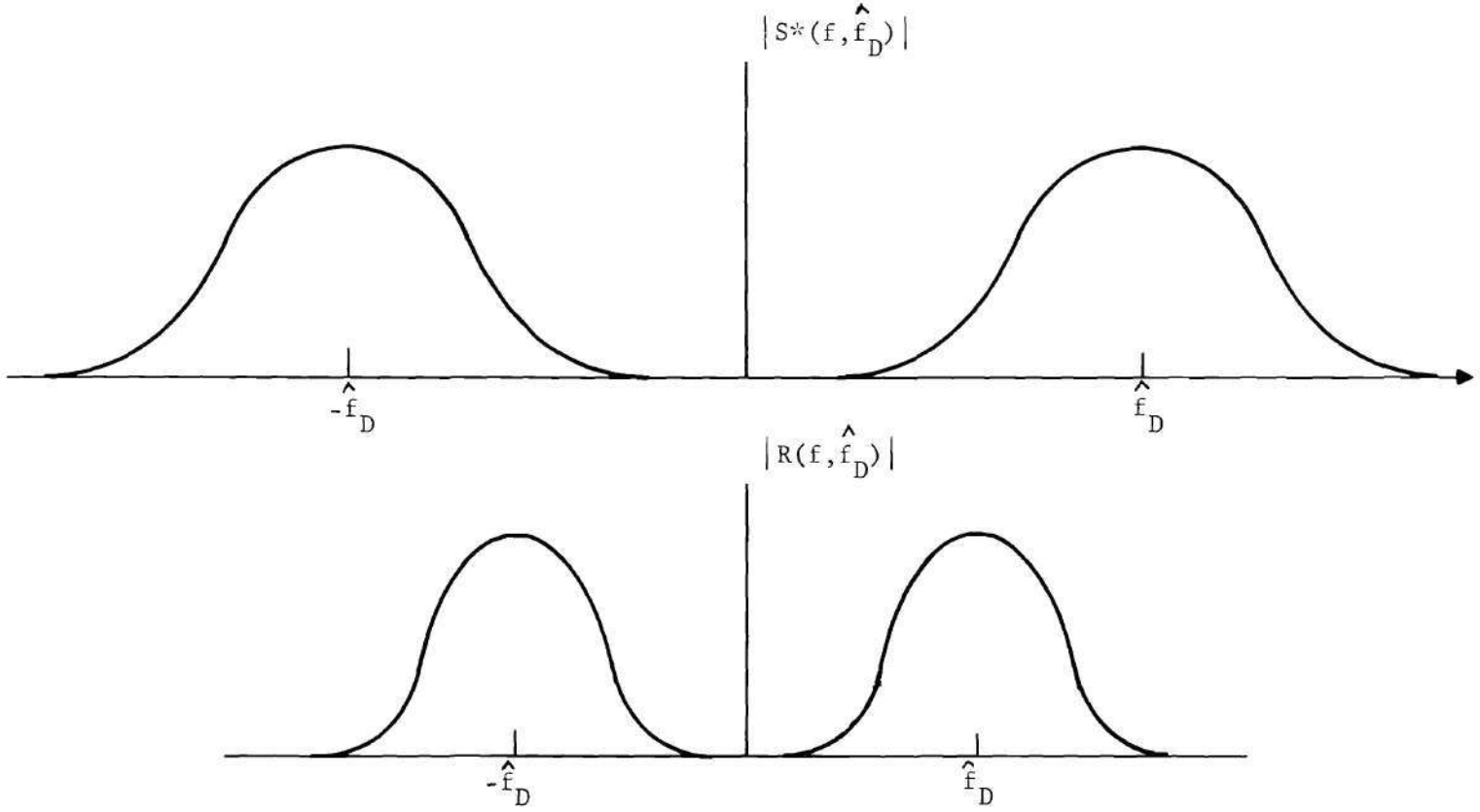

Figure 89. Sketches of the Shapes of $|S^*(f,\hat{f}_D)|$ and $|R(f,\hat{f}_D)|$

APPENDIX C

DEPENDENCE OF f_D OF THE CORRELATION AND THRESHOLD TERMS OF THE OPTIMUM ESTIMATOR

The dependence of the correlation term and the threshold term on the estimate f_D is determined. The correlation term S follows from Eq. (6) of Appendix B as

$$S = 2\int_o^T s(t,f_D)\ s(t,\hat{f}_D)\ dt + 2\int_o^T n(t)\ s(t,\hat{f}_D)\ dt \qquad (1)$$

$$= \qquad S_1 \qquad + \qquad S_2$$

Since n(t) is a Gaussian process, S is a Gaussian random variable with a mean equal to S_1. It is assumed that the variance of S is small enough that S can be adequately represented by its mean S_1. The term S_1 is evaluated by substituting the expression for $s(t,\hat{f}_D)$ given by Eq. (2) of Appendix B into Eq. (1) as follows

$$S_1 = \int_{-\infty}^{\infty} \left(\sum_{i=1}^{N} B_i\ e^{-\alpha(2\pi\hat{f}_D)^2(t-t_i)^2} \cos 2\pi\hat{f}_D(t-t_i) \right) \qquad (2)$$

$$\cdot \left(\sum_{i=1}^{N} B_i\ e^{-\alpha(2\pi f_D)^2(t-t_i)^2} \cos 2\pi f_D(t-t_i) \right) dt$$

The limits of the integral have been changed from 0 and T to $-\infty$ and ∞ which is equivalent to assuming that each pulse is entirely contained in

the (0,T) interval. In other words, no pulse is half in and half out of the interval.

In order to evaluate the expression of Eq. (2), an approximation is made. Note that the two factors in Eq. (2) are summations of discrete, short duration, sinusoidal pulses. The arrival times of the corresponding pulses in each summation are the same. The only difference in the two summations is that the pulse frequency in the first factor is f_D and in the second factor is $\hat{f}_D$. If it is assumed that the pulses are sparse enough that they are non-overlapping, the cross product terms of the integrand of (2) are much smaller than the products of the corresponding terms. With this approximation, S_1 is given by

$$S_1 \approx \sum_{i=1}^{N} \int_{-\infty}^{\infty} B_i^2 \, e^{-\alpha[(2\pi\hat{f}_D)^2 + (2\pi f_D)^2][t-t_i]^2} \cdot \cos 2\pi\hat{f}_D(t-t_i) \cos 2\pi f_D(t-t_i) \, dt \tag{3}$$

When the two cosine terms of the integrand of Eq. (4) are multiplied together, a sum and difference frequency term results. If f_D is anywhere near the value of f_D, the contribution of the difference frequency to the integral is much greater than the contribution of the sum frequency. Assuming that the contribution of the sum frequency to the integral is smaller than that of the difference frequency, S_1 becomes

$$S_1 \approx \sum_{i=1}^{N} \frac{1}{2} \int_{-\infty}^{\infty} B_i^2 \, e^{-\alpha[(2\pi\hat{f}_D)^2 + (2\pi f_D)^2][t-t_i]^2} \cdot \cos(2\pi\hat{f}_D - 2\pi f_D)(t-t_i) \, dt \tag{4}$$

Since the limits of the integral are $-\infty$ and ∞, t_i can be omitted and Eq. (4) becomes

$$S_i = \frac{1}{2}\left(\sum_{i=1}^{N} B_i^2\right)\int_{-\infty}^{\infty} e^{-\gamma t^2} \cos\hat{\omega} t \, dt \tag{5}$$

where

$$\gamma = \alpha[(2\pi\hat{f}_D)^2 + (2\pi f_D)^2]$$

$$= 2\pi\hat{f}_D - 2\pi f_D$$

Equation (5) is a standard integral and is given by formula 4 page 480 of reference 24 as

$$S_1 = \frac{1}{2}\left(\sum_{i=1}^{N} B_i^2\right)\left[\sqrt{\frac{\pi}{\gamma}} \exp\left(\frac{-\delta^2}{4\gamma}\right)\right] \tag{6}$$

$$= \frac{1}{4}\left(\sum_{i=1}^{N} B_i^2\right)\sqrt{\frac{1}{\alpha(f_D^2 + \hat{f}_D^2)\,\pi}}$$

$$\cdot \exp - \left[\frac{(\hat{f}_D - f_D)^2}{4\alpha(\hat{f}_D^2 + f_D^2)}\right]$$

The dependence of S_1 on $\hat{f}_D$ can be expressed as

$$\frac{\exp - \{(\hat{f}_D - f_D)^2/4\alpha(\hat{f}_D^2 + f_D^2)\}}{\sqrt{\alpha(\hat{f}_D^2 + f_D^2)}} \tag{7}$$

The threshold term is the same as the correlation term if $\hat{f}_D$ is set equal to f_D. If $\hat{f}_D$ is set equal to f_D in Eq. (8), the threshold term is immediately seen to depend on $1/f_D$.

APPENDIX D

EVALUATION OF $R_D(f,f_D)$ AND $R_I(f,f_D)$

The functions $R_D(f,f_D)$ and $R_I(f,f_D)$ are determined and then some expressions involving these functions are evaluated. First of all, $R_I(f,f_D)$ is evaluated followed by the evaluation of $R_D(f,f_D)$. By definition, $R_I(f,f_D)$ is given by

$$R_I(f,f_D) = \int_0^T r_{TI}(t)\, e^{-j2\pi ft}\, dt \tag{1}$$

$$= \int_0^T \sum_{i=1}^{N} B_i\, e^{-\alpha(2\pi f_D)^2 (t-t_i)^2} [1 + \cos 2\pi f_D (t-t_i)]\, e^{-j2\pi ft}\, dt$$

$$+ \int_0^T n(t)\, e^{-j2\pi ft}\, dt$$

$$= S_1(f,f_D) + N_T(f)$$

The expression for $r_{TI}(t)$ is given by Eq. (2) of Chapter IV. In order to determine $S_1(f,f_D)$, the limits on the integral in Eq. (1) are changed from 0 and T to $-\infty$ and ∞. The change in limits is equivalent to assuming that the N pulses occurring during the interval T lie entirely within T. No pulse lies partly in and partly out of the interval. Recalling that translation in the time domain implies a phase shift in the frequency domain, $S_I(f,f_D)$ can be written as

$$S_I(f,f_D) = \left(\sum_{i=1}^{N} B_i\, e^{-j2\pi f t_i}\right) \int_{-\infty}^{\infty} (1 + \cos 2\pi f_D t)\, e^{-\alpha(2\pi f_D t)^2} \cdot e^{-j2\pi f t}\, dt \tag{2}$$

Noting in Eq. (2) that $\cos 2\pi f_D t$ effectively heterodynes $e^{-\alpha(2\pi f_D t)^2}$ up to the frequency f_D, the expression for $S_I(f,f_D)$ becomes

$$S_I(f,f_D) = \sum_{i=1}^{N} B_i\, e^{-j2\pi f t_i} \left[G(f-f_D) + G(f+f_D) + 2G(f)\right] \tag{3}$$

where G(f) is the Fourier transform of $e^{-\alpha(2\pi f_D t)^2}$.

In order to evaluate G(f), the expression[25]

$$\mathcal{F}\left[\frac{1}{\sqrt{2\pi}\sigma} e^{-t^2/2\sigma^2}\right] = \exp - \left[2\pi^2\sigma^2 f^2\right] \tag{4}$$

is used. Using this formula with

$$\frac{1}{2\sigma^2} = \alpha(2\pi f_D)^2 \tag{5}$$

G(f) becomes

$$G(f) = \sigma\sqrt{2\pi}\,\mathcal{F}\left[\frac{1}{\sqrt{2\pi}} e^{-t^2/2\sigma^2}\right] \tag{6}$$

$$= \sigma\sqrt{2\pi}\, \exp(-2\pi^2\sigma^2 f^2)$$

Solving for σ in Eq. (5) and substituting into Eq. (7), the following expression for G(f) results

$$G(f) = \sqrt{\frac{\pi}{\alpha(2\pi f_D)^2}} \cdot \exp - \left(\frac{f^2}{4\alpha f_D^2}\right) \tag{7}$$

Substituting Eq. (7) into Eq. (3), $S_I(f,f_D)$ becomes

$$S_I(f,f_D) = \left(\sum_{i=1}^{N} B_i\, e^{-j2\pi f t_i}\right)\sqrt{\frac{\pi}{\alpha(2\pi f_D)^2}} \cdot \left[2\exp(-f^2/4\alpha f_D^2)\right. \tag{8}$$

$$\left. + \exp - \frac{(f-f_D)^2}{4\alpha f_D^2} + \exp - \frac{(f+f_D)^2}{4\alpha f_D^2}\right]$$

The expression for $R_I(f,f_D)$ becomes, from Eqs. (8) and (1),

$$R_I(f,f_D) = \left(\sum_{i=1}^{N} B_i\, e^{-j2\pi f t_i}\right)\sqrt{\frac{\pi}{\alpha(2\pi f_D)^2}}\left[2\exp(-f^2/4\alpha f_D^2)\right. \tag{9}$$

$$\left. + \exp\left[- (f-f_D)^2/4\alpha f_D^2\right) + \exp - (f+f_D)^2/4\alpha f_D^2 + N_T(f)\right.$$

By definition, $R_D(f,f_D)$ is given by

$$R_D(f,f_D) = \int_o^T r_{TD}(t)\, e^{-j2\pi f t}\, dt \tag{10}$$

$$= S_D(f,f_D) + N_T(f)$$

Substituting the definition of $r_{TD}(t)$ given by Eq. (1) of Chapter III into Eq. (10), $R_D(f,f_D)$ becomes

$$R_D(f,f_D) = \int_o^T \left(\sum_{i=1}^{N} B_i \, e^{-\alpha(2\pi f_D)^2 (t-t_i)^2} \cos 2\pi f_D (t-t_i) \right) \cdot e^{-j2\pi ft} \, dt + N_T(f) \tag{11}$$

Noting that Eq. (11) differs from Eq. (1) only in that Eq. (11) is the Fourier transform of a band-pass term while Eq. (1) is the Fourier transform of a low-pass term and an identical band-pass term, $R_D(f,f_D)$ can be immediately written as

$$R_D(f,f_D) = \left(\sum_{i=1}^{N} B_i \, e^{-j2\pi ft_i} \right) \sqrt{\frac{\pi}{\alpha(2\pi f_D)^2}} \tag{12}$$

$$= \left\{ \left[\exp - (f-f_D)^2/4\alpha f_D^2 \right] + \exp -\left[(f+f_D)^2/4\alpha f_D^2 \right] \right\} + N_T(f)$$

The integral I_1, defined as follows

$$I_1 = \int_{-f_H}^{f_H} |S_I(f,f_D)|^2 \, df \tag{13}$$

where f_H is the upper frequency cut-off of the estimator, is required in the discussion of signal to noise ratio in Chapter IV. It is assumed that f_H is high enough that f_D falls well below f_H and I_1 can be written

$$I_1 = \int_{-\infty}^{\infty} |S_I(f,f_D)|^2 \, df \tag{14}$$

The integrand $|S_i(f,f_D)|^2$ follows from Eq. (8) as

$$|S_I(f,f_D)|^2 = \left(\sum_{i=1}^{N} B_i^2 + \sum_{\substack{i=1 \\ i \neq 1}}^{N}\sum_{k=1}^{N} B_i B_k\, e^{j2\pi f(t_i - t_k)}\right)\cdot\left(\frac{\pi}{\alpha(2\pi f_D)^2}\right) \quad (15)$$

$$\cdot\left(4\exp\left[\frac{-f^2}{2\alpha f_D^2}\right] + \exp -\left[\frac{(f-f_D)^2}{2\alpha f_D^2}\right] + \exp-\left[\frac{(f+f_D)^2}{2\alpha f_D^2}\right]\right)$$

It is assumed in Eq. (15) that f_D is large enough that the exponentials do not overlap. Substituting Eq. (15) into (14), the following is obtained

$$I_1 = \int_{-\infty}^{\infty}\left[\frac{\pi}{\alpha(2\pi f_D)^2}\right]\left[\sum_{i=1}^{N} B_i^2\right]\left[4\exp - f^2/2\alpha f_D^2 + \exp-(f-f_D)^2/2\alpha f_D^2\right. \quad (16)$$

$$\left. + \exp - (f+f_D)^2/2\alpha f_D^2\right] df + \int_{-\infty}^{\infty}\left[\left(\sum_{\substack{i=1 \\ i \neq k}}^{N}\sum_{k=1}^{N} B_i B_k\, e^{j2\pi f(t_i - t_k)}\right)\right.$$

$$\cdot\left(\frac{\pi}{\alpha(2\pi f_D)^2}\right)\left]\left[4\exp - f^2/2\alpha f_D^2 + \exp - (f-f_D)^2/2\alpha f_D^2\right.\right.$$

$$\left.\left. + \exp - (f+f_D)^2/2\alpha f_D^2\right] df\right.$$

The integrand of the first integral is a product of a constant term and a sum of exponentials. The second integrand is the product of a sum of complex exponentials and a sum of real exponentials. The contribution of the second integral of Eq. (16) can be neglected relative to the first. I_1 can now be written as

$$I_1 \approx \frac{\pi}{\alpha(2\pi f_D)^2}\sum_{i=1}^{N} B_i^2\; 6\; I_2$$

where I_2 is defined as

$$I_2 = \int_{-\infty}^{\infty} \exp\ (-f^2/2\alpha f_D^{\,2})\ df$$

The integral I_2 can be evaluated readily as

$$I_2 = \sqrt{2\pi\alpha f_D^{\,2}}$$

and I_1 becomes

$$I_1 = \sqrt{2/\pi\alpha}\,(3/2f_D) \sum_{i=1}^{N} B_i^{\,2}$$

By a similar line of reasoning, I_3 is defined as

$$I_3 = \int_{-f_H}^{f_H} |S_D(f,f_D)|^2\ df$$

$$= \sqrt{2/\pi\alpha}\left(\frac{1}{2f_D}\right) \sum_{i=1}^{N} B_i^{\,2}$$

APPENDIX E

VARIATION ON THE BOUND OF V WITH g_ℓ AND h_k

The bound on V is given by Eq. (32) of Chapter IV as

$$V \leq \sum_{\substack{k=1 \\ k \neq \ell}}^{M} \sum_{\ell=1}^{M} \left[Q(\sqrt{g_\ell}, \sqrt{h_\ell}) - \frac{1}{2} \exp - \left(\frac{g_\ell + h_k}{2} \right) \cdot I_o(\sqrt{g_\ell h_k}) \right] \tag{1}$$

It is now demonstrated that the bound on V becomes zero as g_ℓ and h_k increase. First of all, the exponential term of Eq. (1) is considered. As g_ℓ and h_k increase, the $I_o(\sqrt{g_\ell h_k})$ factor approaches the value[42]

$$I_o(\sqrt{g_\ell h_k}) \approx \frac{e^{\sqrt{g_\ell h_k}}}{\sqrt{2\pi \sqrt{g_\ell h_k}}} \tag{2}$$

The exponential term becomes

$$- \frac{1}{2} \exp \left(- \frac{g_\ell + h_k}{2} \right) I_o(\sqrt{g_\ell h_k}) = \frac{-1}{2\sqrt{2\pi \sqrt{g_\ell h_k}}} e^{-\frac{1}{2}\left[\sqrt{g_\ell} - \sqrt{h_k} \right]^2} \tag{3}$$

From Eq. (3), it is apparent that the exponential term becomes zero and g_ℓ and h_k increase.

For large values of g_ℓ and h_k, the integrand of the Q function,

defined in Eq. (31) of Chapter IV, becomes

$$x \exp - \left[\frac{g_\ell + x^2}{2}\right] I_o(x\sqrt{g_\ell}) \approx x \exp \left[- \frac{g_\ell + x^2}{2}\right] \cdot e^{x\sqrt{g_\ell}/\sqrt{2\pi x\sqrt{g_\ell}}} \tag{4}$$

The approximation for $I_o(x\sqrt{g_\ell})$ given by Eq. (2) is used in the above expression. Eq. (4) can be rewritten as

$$x \exp - \left[\frac{g_\ell + x^2}{2}\right] I_o(x\sqrt{g_\ell}) \approx \sqrt{\frac{x}{2\pi\sqrt{g_\ell}}}\, e^{-(x-\sqrt{g_\ell})^2/2} \tag{5}$$

It is apparent from Eq. (5) that, as $\sqrt{g_\ell}$ becomes arbitrarily large, the integrand of the Q function becomes arbitrarily small and hence vanishes. Since all the terms in the bound given in Eq. (1) vanish as g_ℓ and h_k increase, the bound on V also becomes zero as g_ℓ and h_k increase.

BIBLIOGRAPHY

1. James W. Bradley, "Density Determination from Axisymmetric Interferograms," AIAA Journal, June 1968, pp. 1190-1192.

2. Fisher, M. J. and Krause, F. R., "The Crossed-Beam Correlation Technique," Journal of Fluid Mechanics, Vol. 28, Part 4, 1967, pp. 705-717.

3. W. T. Mayo, Jr., Laser Doppler Flowmeters--A Spectral Analysis, Ph.D. dissertation, Georgia Institute of Technology, May 1969.

4. W. T. Mayo, Jr., "Simplified Laser Doppler Velocimeter Optics," Journal of Physics & Scientific Instruments, March 1970, Vol. 3, pp. 235-237.

5. Brayton, D. B., "A Simple Laser, Doppler Shift, Velocimeter with Self-Aligning Optics," Presented at the Electro-Optical Systems Design Conference, September 16-18, 1969, New York Coliseum.

6. Brayton, D. B. and Goethert, W. H., "A New Dual Scatter, Laser, Doppler Shift Velocity Measuring Technique," Proceedings of the Sixteenth International ISA Aerospace Instrumentation Symposium, May 11-13, 1970.

7. Laser Focus, May 1971, p. 24.

8. Y. Yeh and H. Z. Cummins, "Localized Fluid Flow Measurements with an He-Ne Laser Spectrometer," Applied Physics Letters, Vol. 4, No. 10, p. 176 (may 1964).

9. Foreman, J. W., Jr., George, E. W., and Lewis, R. D., "Measurement of Localized Flow Velocities in Gases with a Laser Doppler Flowmeter," Applied Physics Letters, Vol. 7, No. 77, August 1965.

10. Goldstein, R. J. and Kreid, D. K., "Measurement of Laminar Flow Development in a Square Duct Using a Laser Doppler Flowmeter," Journal of Applied Mechanics, Item 34, Series E, No. 4, pp. 813-818, December 1967.

11. J. W. Foremen, Jr., E. W. George, J. L. Jetton, R. D. Lewis, J. R. Thorton, and H. J. Watson, "Fluid Flow Measurements with a Laser Doppler Velocimeter," IEEE Journal of Quantum Electronics, Vol. QE-2, No. 8, 260 (August 1966).

BIBLIOGRAPHY (Continued)

12. Lading, L., "Differential Doppler Heterodyning Technique," Applied Optics, August 1971, pp. 1943-1949.

13. C. A. Greated, "Resolution and Back Scattering Optical Geometry of Laser Doppler Velocimeter Systems," Journal of Physics E: August 1971 Scientific Instruments, Vol. 4, pp. 585-588.

14. Mayo, W. T., "Spatial Filtering Properties of the Reference Beam in an Optical Heterodyne Receiver," Applied Optics, Vol. 9, No. 5, May 1970, pp. 1159-1162.

15. Siegman, A. E., "The Antenna Properties of Optical Heterodyne Receivers," Proceedings of the IEEE, October 1966, pp. 1350-1356.

16. H. Kogelnik and T. Li, "Laser Beams and Resonators," Proceedings of the IEEE, Vol. 54, 1312 (October 1966).

17. C. Orr, Particulate Technology, The MacMillan Company, New York.

18. C. N. Davies, Aerosol Science, Academic Press, New York, 1966.

19. W. B. Davenport and W. L. Root, Random Signals and Noise, McGraw-Hill Book Company, 1958.

20. W. K. Pratt, Laser Communication Systems, John Wiley & Sons, 1969.

21. E. N. Gilbert and H. O. Pollack, "Amplitude Distribution of Shot Noise," Bell Systems Technical Journal, 39, March 1960.

22. H. Hondara and N. George, "Excess Photon Noise in Multimode Lasers," IEEE Journal of Quantum Electronics, Sept. 1966.

23. H. Van Trees, Estimation of Signals in Noise, Wiley, 1968.

24. J. L. Gradshteyn and I. M. Ryzhik, Table of Integrals, Series and Products, Academic Press, New York, 1968.

25. P. M. Woodward, Probability and Information Theory with Applications to Radar, Pergamon Press, New York, 1953.

26. RCA Photomultiplier Manual, RCA Corporation, 1970.

27. S. Hongo, U. Kubo, and Y. Inuishi, "Noise in Helium-Neon Oscillators," Osaka University Technical Reports, Vol. 19, March 1969.

BIBLIOGRAPHY (Concluded)

28. L. J. Cutrona, et al., "On the Application of Coherent Optical Processing Techniques to Synthetic Aperture Radar," Proc. IEEE, 54:1026 (1966).

29. P. L. Jackson, "Diffractive Processing of Geophysical Data," Applied Optics, 4, p. 419 (1965).

30. Electronics, February 16, 1970, pp. 101-103.

31. L. J. Cutrona, et al., "Optical Data Processing and Filtering Systems," IRE Transactions on Information Theory, IT-6, page 386 (1960).

32. J. W. Goodman, Introduction to Fourier Optics, McGraw-Hill, 1968.

33. H. Van Trees, Estimation of Signals in Noise, Wiley, 1968, p. 55.

34. P. M. Woodward, Probability and Information Theory with Applications to Radar, Pergamon Press, New York, 1953, p. 31.

35. H. Van Trees, Estimation of Signals in Noise, Wiley, 1968, p. 262.

36. D. Middleton, Introduction to Statistical Communication Theory, McGraw-Hill, 1960.

37. I. S. Gradshteyn and I. M. Ryzhik, Table of Integrals, Series and Products, Academic Press, 1965.

38. H. Van Trees, Estimation of Signals in Noise, Wiley, 1968, p. 395.

39. W. W. Harmon, Principles of the Statistical Theory of Communication, McGraw-Hill, 1963, p. 184.

40. S. Stein, "Unified Analysis of Certain Coherent and Non-Coherent Binary Communication Systems," IEEE Trans. Inform. Theory, IT-10, 43-51 (January 1964).

41. W. B. Davenport and W. L. Root, An Introduction to the Theory of Random Signals and Noise, McGraw-Hill, 1958, p. 107.

42. Handbook of Chemistry and Physics, 47th Edition, Chemical Rubber Publishing Company (1966-67), p. D98.

43. H. Van Trees, Estimation of Signals in Noise, Wiley, 1968, p. 273.

44. W. W. Harmon, Principles of Statistical Theory of Communication, McGraw-Hill (1963), p. 184.

VITA

John Burton Allen was born in Detroit, Michigan on March 21, 1940. He is the son of Clarence Bertin Allen and Juanita Victoria Allen. On May 14, 1966 he was married to Mary Ann Kirkland of Moncks Corner, South Carolina and they have one son, Steven Burton Allen.

He attended public school in Detroit, Michigan where he graduated from Redford High School in 1958. In 1963 he received a B.S.E. in Physics and an M.S. in Mathematics, both from the University of Michigan. In 1969, he received an M.S. in Electrical Engineering from the Georgia Institute of Technology.

During the summers of 1959 to 1963, he was employed in the Quality Control Laboratory of the Ford Motor Company's Steel Division. After receiving his first Master's degree, he held a position as a research engineer at the Los Angeles Division of North American Aviation from 1964 to 1965. From 1965 to 1971, he was employed in the Systems Sciences Laboratory at the Lockheed-Georgia Company, where he conducted research in the fields of laser applications and communication systems. Currently, he is a member of the technical staff at the Equipment Research and Development Laboratory of the Texas Instrument Company, Dallas, Texas.